

Ink Trails

Tracking the life and death of memory T cells

ARPIT CHANDAN SWAIN

INK TRAILS

Tracking the life and death of memory T cells

Arpit Chandan Swain

Utrecht University

2023

Arpit Chandan Swain

Ink Trails

Tracking the life and death of memory T cells

PhD thesis, Utrecht University

Cover design: Priyanka Maharana and Arpit Chandan Swain

The cover is an abstract representation of a cell that emerges from rough and messy trails left behind by ‘inked’ (‘labelled’ in scientific language) memory T cells. In this thesis, we use trails like these to sketch a detailed picture of memory T cells. The blue trails signify the labelling of memory T cells with heavy water (scientific name: deuterium, see Chapters 1-3) and the red and green trails signify red and green fluorescent proteins, respectively, that were used in Chapter 4. The cover designs were made by modifying designs found on Tumblr.

Printing: Ridderprint | www.ridderprint.nl

ISBN: 978-94-6483-305-8

DOI: <https://doi.org/10.33540/1850>

Copyright © Arpit Chandan Swain, 2023

All rights reserved. No part of this thesis may be reproduced in any form without written permission of the author.

INK TRAILS

Tracking the life and death of memory T cells

Inktsporen

Leven en dood van geheugen-T-cellen

(met een samenvatting in het Nederlands)

ସଂକ୍ଷିପ୍ତ ପଥରେଖା

ସ୍ମୃତି 'ଟି' କୋଷକ ଜୀବନ ଓ ମୃତ୍ୟୁର ଅନୁଷ୍ଠାନ

(ଓଡ଼ିଆରେ ଏକ ସାରାଂଶ ସହିତ)

Proefschrift

ter verkrijging van de graad van doctor aan de Universiteit Utrecht
op gezag van de rector magnificus, prof.dr. H.R.B.M. Kummeling,
ingevolge het besluit van het college voor promoties
in het openbaar te verdedigen op

dinsdag 5 september 2023

des middags te 4.15 uur

door

Arpit Chandan Swain

geboren op 26 april 1993
te Odisha, India

Promotoren:

Prof. dr. R.J. de Boer

Prof. dr. J.A.M. Borghans

Beoordelingscommissie:

Prof. dr. R. Antia

Prof. dr. R.E. Bontrop

Dr. C. Gerlach

Prof. dr. L. Perié

Prof. dr. R. Ribeiro

The studies described in this thesis were financially supported by the Dutch Research Council (NWO), grant numbers ALWOP.265 and 09150181910016 (Vici-grant).

Table of contents

	Introduction	7
1	Turnover of murine cytomegalovirus-expanded CD8 ⁺ T cells is similar to that of memory phenotype T cells and independent of the magnitude of the response <i>Published as: Baliu-Piqué et al., J. Immunol., 2022;</i> <i>doi:10.4049/jimmunol.2100883</i>	17
2	Explaining unexpected deuterium labelling curves <i>To be submitted</i>	41
3	How are estimated cellular turnover rates of a population influenced by the dynamics of its precursor population? <i>To be submitted</i>	71
4	Replicative history marks transcriptional and functional disparity in the CD8 ⁺ T-cell memory pool <i>Published as: Bresser, Kok, Swain et al., Nat. Immunol., 2022;</i> <i>doi:10.1038/s41590-022-01171-9</i>	101
5	Effect of cellular aging on memory T-cell homeostasis <i>Published as: Swain et al., Front. Immunol., 2022;</i> <i>doi:10.3389/fimmu.2022.947242</i>	161
	Discussion	187
	Bibliography	203
	Summary	227
	Samenvatting	229
	ସାରାଂଶ	232
	Curriculum Vitae	235
	List of Publications	236
	Acknowledgements	237

Introduction

Memory T (T_M) cells are one of the protagonists of a successful immune response. They are formed after a naive T (T_N) cell (a type of white blood cell) recognizes an invading pathogen (by binding one of its molecules, referred to as the antigen) (Sprent and Surh, 2003). In a mouse, typically close to 10^2 T_N cells that are specific for the pathogen give rise to about 10^5 specific T_M cells, a 10^3 fold increase (Kaech et al., 2002; Kalia et al., 2013). Such large numbers and their semi-activated state confer upon T_M cells the ability to generate swift and effective successive immune responses (Cho et al., 1999); a property that is famously exploited during vaccination (Esser et al., 2003; Kaech et al., 2002; Todryk, 2018).

Since their discovery in 1971, a lot of progress has been made in characterizing and understanding various aspects of T_M cells (Gershon et al., 1971; Miller and Sprent, 1971; Qiu, 2022). We can now distinguish between antigen-inexperienced T_N cells and antigen-experienced T_M cells confidently, based on the expression of certain cell surface proteins (Berard and Tough, 2002). Several studies have also highlighted that the T_M -cell population is both kinetically heterogeneous with slow and fast sub-populations (Westera et al., 2013), and phenotypically heterogeneous where the responsibilities of T_M cells are shared among many different sub-populations (Roberts et al., 2005; Sallusto et al., 2004). For example, central memory T (T_{CM}) cells re-expand and generate a memory response upon re-encountering the pathogen, and effector memory T (T_{EM}) cells migrate to tissues to clear the pathogen through direct cytolytic activity (Roberts et al., 2005; Sallusto et al., 2004).

In spite of the understandings garnered, many questions warrant additional study. For example, how many functional subsets does the T_M -cell population have? Why do only ~5% of all activated cells become T_M cells? When are T_M cells formed and when do they differentiate into different subsets? The answers to these fundamental questions are required to better understand the mechanisms behind the generation of T_M cells, which would then not only aid in the design of vaccines (Ahmed et al., 2009), but also improve T-cell therapies (for example, against cancer), and limit undesired T-cell responses (for example, in auto-immune diseases and chronic inflammation). For example, if it were known whether T_M cells are generated during or after an immune response, vaccine developers could harness this knowledge to skew an immune response, upon vaccination, to generate a larger, and perhaps more potent, T_M -cell pool (Ahmed et al., 2009).

It is important that the T_M cells generated after an immune response are sustained, and that the diversity of the T_M -cell pool is maintained. For this, it is necessary to know whether T_M cells can be long-lived. It is also essential to understand the effect of new infections (or vaccinations) on previous memories. Selin and Welsh, among other researchers, have addressed this by measuring the composition of the T_M -cell repertoire before and after multiple infections (Hogan et al., 2013; Kim and Welsh, 2004; Selin et al., 1999, 1996; Vezys et al., 2008; Welsh and Selin, 2009). These studies were typically done in 'clean' (i.e., disease-free) mice and might not accurately reflect the effect of successive infections on the diversity of the T_M -cell pool (as the T_M -cell pool in these mice have limited diversity and their T_M cells, therefore, experience limited competition). Further, it is feasible to work with only a few infections in such experimental studies.

The addition or deletion of methyl groups to the DNA (DNA methylation) has been used to study the generation of T_M cells (Youngblood et al., 2017), as the DNA methylation pattern leaves behind a road map (or a trail) of a T_N cell's development into a T_M cell. The dynamics of T cells can also be tracked by labelling them and subsequently following the label over time. For example, the incorporation of compounds like deuterium into the DNA of T-cell populations has been studied to infer the turnover (division) rate of the cells in the population and to understand its maintenance mechanisms (Baliu-Piqué et al., 2018). The principle behind these techniques is analogous to carbon dating a mummy, or analysing the ink of a person's tattoo, to not only infer the age of the mummy or the tattoo, but to also pinpoint its place of origin. In this compilation of works, we focus on understanding the generation and maintenance of T_M cells by collecting time-series data of labelled T cells and analysing these "ink trails".

1. When are memory T cells generated?

Three different chronologies of T_M -cell generation have been proposed (**Figure I.1**) (Henning et al., 2018; Kaech et al., 2002; Kalia et al., 2006). The first of these, the circular pathway, postulates that T_{CM} cells are formed after (and from) T_{EM} cells, and upon restimulation differentiate into T_{EM} cells again. The second view, the linear pathway, suggests that T_{CM} cells are the precursors of T_{EM} cells. The third, the branched pathway, postulates that T_{CM} and T_{EM} cells are formed in parallel.

The circular differentiation pathway. Support for this pathway propagates the traditional Effector-First view of T_M -cell generation (Henning et al., 2018; Kaech et al., 2002; Kalia et al., 2006). In this traditional view, activated T_N cells give rise to T_{EM} cells which then differentiate into T_{CM} cells after the antigen is cleared and the immune response is resolved. These T_{CM} cells upon re-stimulation by the antigen revert back to T_{EM} cells (**Figure I.1a**) (Henning et al., 2018; Kaech et al., 2002). This idea was recently strengthened by observations made by a group of researchers who followed the DNA methylation patterns of T_N cells, and memory-phenotype T cells during and after an acute immune response (Akondy et al., 2017; Omilusik and Goldrath, 2017; Youngblood et al., 2017). As the loci of naive-associated genes in memory-phenotype T cells were demethylated during the expansion phase and methylated again during the memory phase, it was suggested that T_{EM} cells de-differentiate into T_{CM} cells (Youngblood et al., 2017), in at least some cases. This on-off-on cycle of naive- and effector-associated genes before, during and after an immune response motivated the name of this differentiation pathway.

The linear differentiation pathway. This pathway supports the Memory-First principle where an activated T_N cell goes through the T_{CM} -cell phenotype before becoming a T_{EM} cell (**Figure I.1b**) (Henning et al., 2018; Kaech et al., 2002). Unlike the circular differentiation pathway, where T_N cells differentiate into T_{EM} cells and then into T_{CM} cells regardless of the strength of the stimulation, in the linear differentiation pathway it is proposed that the fate of a T_N cell is driven by the strength and number of antigenic stimulations. Repeated and strong

stimulation drives a T_N cell into the more differentiated T_{EM} cells, whereas limited stimulation of a T_N cell results in the formation of less differentiated T_{CM} cells. Thus, the phenotypic make-up of a T_{CM} cell is in between that of a T_N and a T_{EM} cell. This progressive differentiation mechanism is also neatly in line with the fact that T_{CM} cells generate T_{EM} cells upon subsequent stimulation.

The branched differentiation pathway. By analysing the T-cell receptor repertoire and the proliferation history of T cells, it is postulated that the generation of memory-phenotype and effector-phenotype T cells is a unidirectional, but not necessarily linear, pathway (Song et al., 2005). Thus, the formation of T_{CM} and T_{EM} cells are thought to be parallel processes (**Figure I.1c**). In this pathway, T_N cells do not have to go through the T_{EM} -cell stage before becoming T_{CM} cells, as suggested by the circular differentiation pathway, and T_N cells also do not have to go through the T_{CM} phenotype in their journey to become T_{EM} cells, as suggested by the linear differentiation pathway.

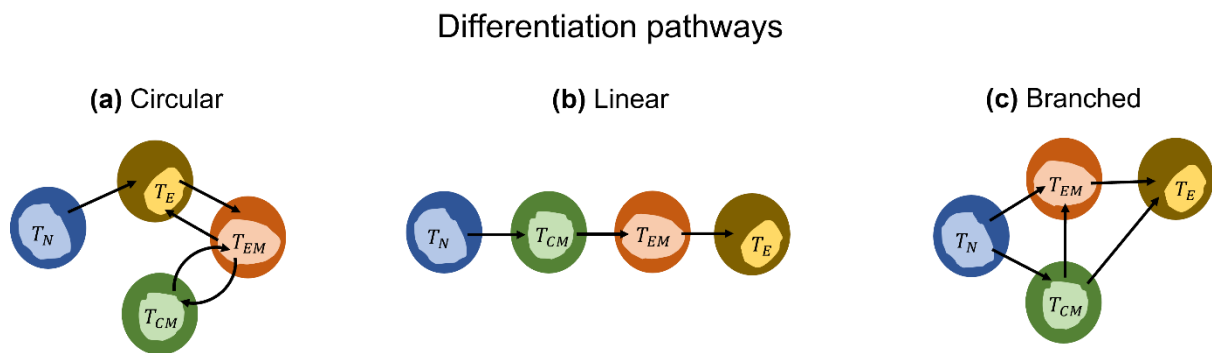


Figure I.1: The different differentiation pathways that have been postulated to underlie the generation of T_{CM} , T_{EM} and effector (T_E) T cells from T_N cells. In the circular differentiation pathway, T_E cells give rise to T_{EM} cells in absence of antigen, which revert to T_E cells upon re-encountering the pathogen. In the linear and branched differentiation pathways, T_E cells are generated from T_{EM} cells during the expansion phase.

2. How are memory T cells maintained?

The immunity imparted by T_M cells against a pathogen often spans decades (Sprent and Surh, 2003). Initially, this long-lived immunity was thought to be due to long lifespans of individual T_M cells (Gowans and Uhr, 1966; Sprent, 1997; Sprent and Miller, 1976). This view has been amended in recent times by a rich body of work showing that on average circulating T_M cells are, in fact, fairly short-lived (Baliu-Piqué et al., 2018; Gray and Matzinger, 1991; Macallan et al., 2017; Westera et al., 2013).

Measuring the lifespan of memory T cells. Estimation of division and death rates¹ of the cells in a cell population is crucial to calculate the lifespans of the cells in the population.

¹ In this thesis, the terms rate and *per capita* rate are used synonymously.

Identifying both division and death rates of the cells in a cell population simultaneously just from the changes in the population size is not possible. For example, a population that expands at a net growth rate of 2/day can have a division rate of 4/day and a death rate of 2/day, or a division rate of 3/day and a death rate of 1/day. Even if one of the rates (division or death) is known, the accuracy of the other rate that is estimated tends to be poor as the measurements of a population's size are notoriously noisy. Further, the noise in the measurements of the cell numbers makes it difficult to know whether the cell population is at steady state or not. Other techniques such as the dilution of T-cell receptor excision circles (TRECs) and the shortening of telomeres have been used to estimate cellular lifespans (De Boer and Perelson, 2013a). TRECs are small circles of DNA formed during T-cell development in the thymus and do not duplicate when cells divide (De Boer and Perelson, 2013a). This makes TRECs suitable for analysing the division history of T_N cells but not for T_M cells (as T_M cells have gone through clonal expansion). Telomeres are non-coding ends of chromosomes that are eroded when a cell divides (De Boer and Perelson, 2013a). Interpretation of telomere data is tricky as telomeres can be extended by the enzyme telomerase (Chan and Blackburn, 2004) and due to the transfer of telomeres by antigen presenting cells (APCs) to T_M cells during their interaction (Carey et al., 2022; Lanna et al., 2022). Unfortunately, the rate at which telomeres erode inform more about the division rate of their precursors than that of the population of interest (De Boer and Noest, 1998). The current state-of-the-art technique to measure the turnover rates of a cell population is to label the cells (using compounds like CFSE, BrdU or deuterium) to track their division history (see **Figure I.2** for a graphical explanation of typical deuterium labelling experiments) (De Boer and Perelson, 2013a). Analysing the time course of the fraction of labelled DNA (in BrdU and deuterium labelling experiments), then informs about the average expected lifespan of the cells (even in a population that is at steady state). The best estimates, based on deuterium labelling of cell populations, for the expected lifespans of circulating T_N cells and circulating T_M cells are 6-9 years and ~ 0.5 year, respectively, in humans (Borghans et al., 2018), and ~ 60 days (den Braber et al., 2012) and ~ 20 days (Westera et al., 2013), respectively, in mice.

Implications of short lifespans. T_M cells depend on cytokines for growth and survival (De Boer and Perelson, 1994). The relatively short lifespan of circulating T_M cells makes them prone to competitive exclusion, due to their dependence on the same cytokines. The effects of this competition can be severe. Existing T_M cells are lost (possibly due to competition) upon new infections, sometimes modestly, and at other times significantly (Vezys et al., 2008; Welsh and Selin, 2009). This erosion could impair the subsequent immune responses against a previously encountered pathogen (Huster et al., 2009). Recurrent infections by a pathogen are known to boost the number of T_M cells specific for the pathogen, strengthening the T_M -cell response. These boosts can, however, also change the phenotypic distribution within the T_M cell pool, causing a delayed response that could lead to inefficient protection of the host (Huster et al., 2009). Thus, the response of one's immune system to a pathogen can be significantly moulded by its past infection history, possibly due to erosion of short-lived T_M cells (Kim and Welsh, 2004; Selin et al., 1999, 1996; Vezys et al., 2008; Welsh and Selin, 2009). The observation that efficient immune memory over many years is successfully maintained by short-lived T_M cells, therefore, remains quite surprising.

Long-lived memory T cells. It has been postulated that long-term immunity would be compatible with short-lived T_M cells amidst competitive exclusion if these cells were progenies of long-lived T_M cells that maintain themselves (Di Rosa, 2016a; Radbruch et al., 2021). One such hypothesis suggests that during an immune response some T_M cells migrate to the bone marrow and reside in the stromal niches, becoming quiescent and long-lived (Siracusa et al., 2018, 2017). Another hypothesis proposes that stem-cell-like T_M cells could act as the source through asymmetrical division (Ahmed et al., 2009; Borsa et al., 2019; Chang et al., 2014, 2007). A long-term deuterium labelling study has shown that the T_M -cell pool becomes more quiescent (i.e., longer-lived) with time, crediting this to the presence of long-lived stem-cell-like T_M cells (Akondy et al., 2017). However, it is uncertain whether this gradual quiescence of the T_M cell pool is due to the preferential loss of the short-lived, circulating T_M cells (and the persistence of ‘true’ long-lived T_M cells), or due to the individual T_M cells becoming long-lived. Regardless of how long-lived T_M cells are formed, they would lead to the long-term maintenance of a diverse T_M -cell repertoire.

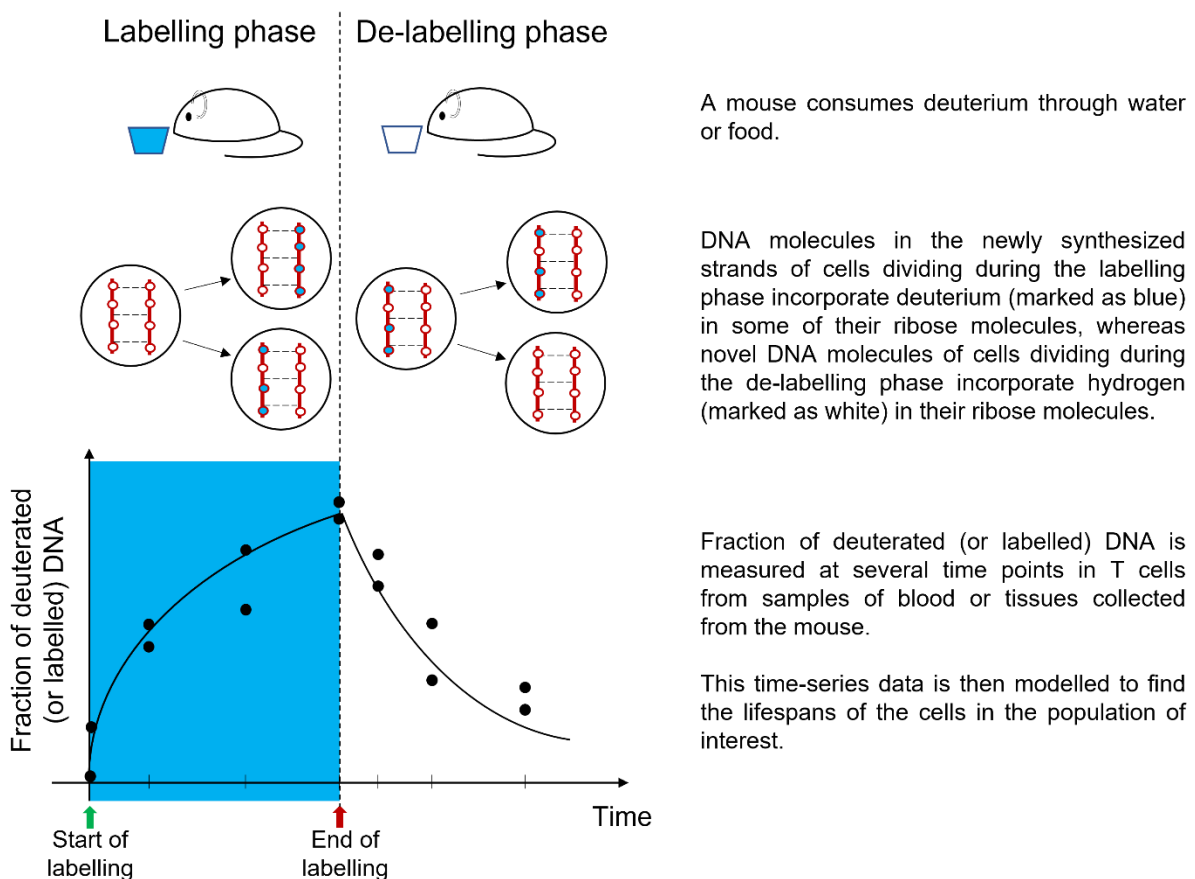


Figure I.2: A typical deuterium labelling experiment.

The discussion presented above related to the generation and maintenance of T_M cells is the focal point of this body of work. The chapters presented here not only discuss the most likely

differentiation pathways and maintenance mechanisms of T_M cells, but they also address the heterogeneity in the T_M -cell pool and the reliability of the estimates inferred from deuterium labelling data.

Thesis Outline

This thesis is a product of our efforts to better understand the ontogeny of T_M cells and their maintenance mechanisms. We do this by improving upon the theoretical analysis (**Chapter 2**), suggesting improvements in experimental design (**Chapter 3**), and in some cases, introducing new experimental and theoretical approaches (**Chapters 1, 4 and 5**) in an attempt to resolve previous debates about the generation and long-term maintenance of T_M cells.

Question 1 Do cells of an inflationary T_M -cell response that is maintained during a chronic infection live longer than those of a non-inflationary T_M -cell response? (**Chapter 1**)

Most pathogens induce acute immune responses. It has been estimated that approximately 1 out of every 100 pathogens encountered by a human, results in a chronic infection (Virgin et al., 2009). In contrast to acute infections, chronic infections can induce both non-inflationary and inflationary T_M -cell responses. The number of specific T_M cells increases over time in an inflationary T-cell response. Circulating T_M cells maintained after an acute response are known to be short-lived (< 2 months in mice) (Choo et al., 2010; Westera et al., 2013), but what about the non-inflationary and inflationary T_M cells formed and/or maintained during a chronic response? Certain epitopes of the murine cytomegalovirus (MCMV) elicit chronic responses that are inflationary. It has been suggested that this accumulation of MCMV-specific T_M cells is due to their long expected lifespans (Wallace et al., 2011). Through deuterium labelling of MCMV-specific T_M cells, we studied whether this is indeed true.

Question 2 How can the label gain rate of a population of cells be higher than its label loss rate? (**Chapter 2**)

Estimation of the label gain and loss rates of MCMV-specific T_M cells showed an unexpected behaviour i.e., the gain rate was higher than the loss rate. Such estimates would suggest that the population becomes labelled quicker than it gets unlabelled, which is unexpected for a population at steady state. This behaviour was not unique to MCMV-specific T_M cells and was also seen for human neutrophil populations in the bone marrow and murine NK cell populations in the blood. When can the estimated gain rate of label be higher than the estimated loss rate of label? We explore this question analytically and numerically using various mathematical models.

Question 3 Does a population's label gain rate truly reflect its average turnover rate? **(Chapter 3)**

Most models used to analyse deuterium labelling data assume that the population of interest has no source of progenitor cells or is preceded by a rapidly dividing population. The label gain rate of a population that is at steady state is then interpreted as its turnover rate, which is used to calculate the average lifespan of the cells in question. However, the population of interest is not always independent of its precursors, and/or does not always have a rapidly turning over precursor population. Are the estimated turnover rates significantly different when the precursors do not turnover rapidly? We further discuss the explicit source model developed in the previous chapter to comment on this question and use multiple published datasets to support our analytical results.

Question 4 Are the protective potential and division history of a T_M cell related? **(Chapter 4)**

Often the many different T_M -cell phenotypes are distinguished based on their protective potential and their ability to expand. A subset's protective potential has been shown to be related to its ability to expand upon stimulation. For example, the more protective T_{CM} cells expand more than T_{EM} cells, which have limited protective abilities. As it has been suggested that cells age with division, a cell's ability to expand is perhaps influenced by its division history. So, is the protective potential of a T_M cell directly dependent on its division history? This question has remained unexplored due to the inability of staining dyes (like CFSE) to track the division history of a cell *in vivo* for over 10 divisions. Using a Cre-lox module that can track the division history of a population over many more divisions, we explore the relation between the division history of the different T_M -cell subsets and their functional properties. With the help of mathematical models, we also discuss the most likely differentiation pathway of T-cell differentiation based on the replicative history of T_{CM} and T_{EM} cells.

Question 5 Are the relatively short lifespans of T_M cells compatible with a diverse T_M -cell pool? **(Chapter 5)**

Reports of highly diverse T_M -cell repertoires are difficult to reconcile with the fact that short-lived T_M cells depend on limiting resources for growth and survival. Resource specialization among T_M cells and the presence of long-lived T_M cells are often proposed as mechanisms to maintain the diversity of the T_M -cell repertoire in the long-term. Do these mechanisms indeed maintain a diverse T_M -cell repertoire, or are memories lost by competitive exclusion over time? We study different mechanisms using mathematical models and discuss the repercussions of both the lifespan and the age of an individual cell on the longevity of memory and the diversity of the T_M -cell pool.

Discussion The generation and maintenance of T_M cells.

Years after the discovery of T_M cells, there is still a lack of consensus on the pathways underlying their generation and the mechanisms behind their maintenance. In this section, we attempt to bring together previous findings with results presented here to build a consensus. We also connect the dots between the chapters and discuss the contrasts and parallels between the different datasets.

Turnover of murine cytomegalovirus-expanded CD8⁺ T cells is similar to that of memory phenotype T cells and independent of the magnitude of the response

Mariona Baliu-Piqué^{*,1,2}, Julia Drylewicz^{*,1}, Xiaoyan Zheng^{†,1}, Lisa Borkner[†], Arpit C. Swain[‡], Sigrid A. Otto^{*}, Rob J. de Boer[‡], Kiki Tesselaar^{*,3}, Luka Cicin-Sain^{†,§,3}, and José A. M. Borghans^{*,3}

^{*}Center for Translational Immunology, University Medical Center Utrecht, Utrecht, The Netherlands

[†]Department of Viral Immunology, Helmholtz Centre for Infection Research, Braunschweig, Germany

[‡]Theoretical Biology, Utrecht University, Utrecht, The Netherlands

[§]German Center for Infection Research, Partner Site, Hannover-Braunschweig, Germany

¹M.B.-P., J.D., and X.Z. contributed equally to this work.

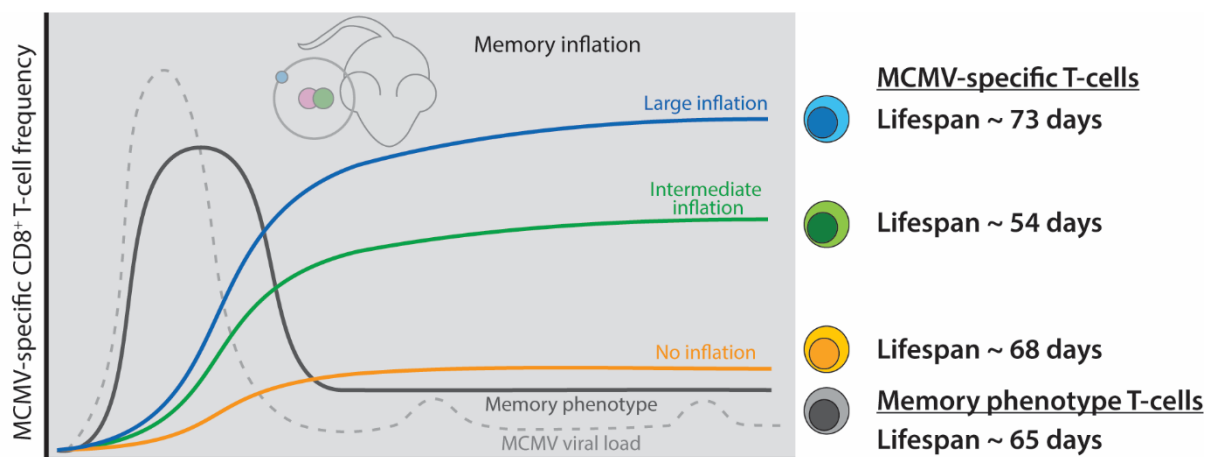
²Current address: Immunotherapy Manufacturing Center, Galara-Sergas, Santiago de Compostela, Spain.

³K.T., L.C.-S., and J.A.M.B. are co-senior authors.

Published as: Baliu-Piqué et al., J. Immunol., 2022; doi:10.4049/jimmunol.2100883

Abstract

The potential of memory T cells to provide protection against reinfection is beyond question. Yet, it remains debated whether long-term T-cell memory is due to long-lived memory cells. There is ample evidence that blood-derived memory phenotype CD8⁺ T cells maintain themselves through cell division, rather than through longevity of individual cells. It has recently been proposed, however, that there may be heterogeneity in the lifespans of memory T cells, depending on factors such as exposure to cognate Ag. CMV infection induces not only conventional, contracting T-cell responses, but also in inflationary CD8⁺ T-cell responses, which are maintained at unusually high numbers, and are even thought to continue to expand over time. It has been proposed that such inflating T-cell responses result from the accumulation of relatively long-lived CMV-specific memory CD8⁺ T cells. Using *in vivo* deuterium labelling and mathematical modelling, we found that the average production rates and expected lifespans of mouse CMV-specific CD8⁺ T cells are very similar to those of bulk memory-phenotype CD8⁺ T cells. Even CMV-specific inflationary CD8⁺ T-cell responses that differ 3-fold in size were found to turn over at similar rates.



Abbreviations used in this article: **CI**, confidence interval; **dpi**, days post-infection; **GC/MS**, gas chromatography/mass spectrometry; **KNL**, KCSRNRQYL; **MCMV**, murine CMV; **SL**, SSIEFARL; **129/Sv**, 129S2/SvPas Ctrl; **T_{CM}**, central memory T; **T_{EM}**, effector memory T; **Tet⁺**, tetramer-positive; **T_M**, total memory T; **T_N**, naive T; **YFV**, yellow fever virus.

Introduction

Memory CD8⁺ T cells are a crucial component of the adaptive immune response to viruses. Ag-specific memory CD8⁺ T cells convey immune protection against viral infections that may last for long periods of time, sometimes even life-long. There is ample evidence that memory T cells isolated from the blood and lymph nodes are relatively short-lived. Their lifespan is much shorter than that of naive T (T_N) cells, and far shorter than the long-term immune protection they convey (Borghans et al., 2018; Crotty and Ahmed, 2004; Hellerstein et al., 2003; Macallan et al., 2017, 2004, 2003; Michie et al., 1992; Vrisekoop et al., 2008; Wallace et al., 2004; Westera et al., 2013). Memory T-cell populations are heterogeneous, both phenotypically and functionally. They consist of phenotypically defined sub-populations, such as central memory T (T_{CM}) and effector memory T (T_{EM}) cells, and of subsets that differ in terms of exposure to their cognate Ag. *In vivo* deuterium labelling studies have shown that different subsets of memory T cells can have different kinetics. CD4⁺ T_{EM} cells were shown to have shorter lifespans than did T_{CM} cells (Macallan et al., 2004), and yellow fever virus (YFV)-specific memory T cells generated by vaccination, which can persist for years, were found to have longer lifespans than did bulk memory-phenotype cells (Akondy et al., 2017).

CMV infection is a persistent, chronic infection, which, in contrast to YFV vaccination, results in continual Ag presentation. CMV is under constant immune surveillance, and it triggers ongoing CD8⁺ T-cell responses that provide effective viral control for long periods of time. A hallmark of the CD8⁺ T-cell response to CMV infection is the steady maintenance or accumulation of large populations of virus-specific effector CD8⁺ T cells over time, a phenomenon termed memory inflation (O'Hara et al., 2012). Expanded CD8⁺ T-cell populations specific for unique CMV epitopes can become extraordinarily large, composing up to 20% of the total memory T (T_M) CD8⁺ cell pool (Bolinger et al., 2015; Dekhtiarenko et al., 2013; Karrer et al., 2003; Kim et al., 2015; Klenerman and Oxenius, 2016; Munks et al., 2006). These large CMV-specific T-cell responses turned out to be maintained dynamically, through continuous production of relatively short-lived cells (Snyder et al., 2008). Nevertheless, a face-to-face comparison of the *in vivo* dynamics of CMV-specific and bulk memory-phenotype CD8⁺ T cells suggested that inflating CMV-specific memory CD8⁺ T-cell responses are composed of cells that are longer-lived than other memory cells. This has led to the hypothesis that T-cell inflation arises from the accumulation of relatively long-lived CMV-specific memory T cells (Wallace et al., 2011).

In this study, we addressed this hypothesis using *in vivo* deuterium labelling and mathematical modelling, the state-of-the-art techniques to quantify lymphocyte turnover, in the setting of murine CMV (MCMV) infection, a relevant experimental model to study memory T-cell inflation (Klenerman and Oxenius, 2016). In contrast to the postulated hypothesis that CMV-specific T cells may have extended lifespans, we found no significant difference in the expected lifespans of MCMV-specific CD8⁺ T cells and bulk memory-phenotype CD8⁺ T cells. Using recombinant viruses inducing inflationary CD8⁺ T-cell

responses of different magnitudes, we found that MCMV-specific T cells composing small and large inflationary T-cell responses had very similar turnover rates.

Materials and Methods

Mice

129S2/SvPas Cr1 (129/Sv) mice were purchased from Charles River Laboratories (Sulzfeld, Germany). Mice were housed and handled in accordance with good animal practice as defined by the Federation of Laboratory Animal Science Associations and the national animal welfare body Die Gesellschaft für Versuchstierkunde (Society of Laboratory Animal Science). All animal experiments were approved by the responsible state office (Lower Saxony State Office of Consumer Protection and Food Safety, Germany; permit number 33.19-42502-04-15/1836 and by the Animal Experiments Committee of Utrecht University, IVD Utrecht, the Netherlands; DEC AVD115002016714).

Viruses

Bacterial artificial chromosome-derived recombinant viruses MCMV^{ie2SL} and MCMV^{m45SL} were generated and propagated as described previously (Dekhtiarenko et al., 2013), and the recombinant virus MCMV^{ie2KNL} was generated and propagated as described in Borkner et al. (Borkner et al., 2017).

In vivo infection

Female 8-wk-old mice were infected with 2×10^5 PFU of MCMV^{ie2SL} ($n = 40$), MCMV^{m45SL} ($n = 37$), or MCMV^{ie2KNL} ($n = 41$) and housed in specific pathogen-free conditions throughout the experiment. Non-infected sex- and age-matched mice were used as controls ($n = 10$).

Stable isotope labelling

One hundred twenty days after MCMV infection, mice received 8% deuterated water (99.8% ²H₂O, Cambridge Isotope Laboratories) in their drinking water for 28 days. At day 4, mice were given an i.p. boost injection of 15 ml/kg ²H₂O in PBS. To determine deuterium enrichment in the body water, EDTA plasma was collected during the up- and down-labelling phase and was frozen and stored at -80°C until analysis.

Sampling and cell preparation

Spleen, thymus, and blood were isolated at different time points during and after label administration. Blood was collected in EDTA tubes. Single-cell suspensions from blood, spleen, and thymus were obtained as described previously (Oduro et al., 2016).

Flow cytometry and cell sorting

To determine the fraction of SSIEFARL (SL) and KCSRNRQYL (KNL) epitope-specific T cells, single-cell suspensions from blood and spleen were stained with allophycocyanin-conjugated SL-K^b or KNL-D^b tetramers for 15 min at 4°C. Samples were further stained for 30 min at 4°C with anti-CD3-allophycocyanin-eFluor 780 (clone 17A2; eBioscience), anti-CD3e-FITC (clone 145-2C11; BD Pharmingen), anti-CD3-V500 (clone 500A2; BD), anti-CD4-Pacific Blue (clone GK1.5; BioLegend), anti-CD4-Brilliant Violet 650 (clone GK1.5; BD Horizon), anti-CD4-allophycocyanin-H7 (GK1.5; BD), anti-CD8a-PerCP/Cy5.5 (clone 53-6.7; BioLegend), anti-CD8a-Brilliant Violet 786 (clone 53-6.7; BD), anti-CD44-Alexa Fluor 700 (clone IM7; BioLegend), anti-CD44-Alexa Fluor 450 (IM7; eBioscience), anti-CD62L-eVolve 605 (clone MEL-14; eBioscience), anti-CD62L-FITC (MEL-14; eBioscience), and anti-CD127-PE/Cy7 (clone A7R34; BioLegend) mAbs. For intracellular staining, cells were subsequently fixed for 20 min at room temperature with 100 μ l of fixation/permeabilization buffer of the FoxP3 Transcription Factor Staining Set (eBioscience), permeabilized for 15 min at room temperature in 100 μ l of permeabilization buffer (eBioscience) and stained with Ki-67-PE (clone 16A8; BioLegend) in 100 μ l of permeabilization buffer for 30 min at room temperature. Cells were analyzed on an LSRFortessa flow cytometer using FACSDiva software (BD Biosciences) and FlowJo software (version 9.8.3). For infected mice, tetramer-positive (Tet⁺) (CD3⁺CD8⁺Tet⁺) T cells and tetramer-negative T_N (CD3⁺CD8⁺Tet⁻CD62L⁺CD44⁻), T_{CM} (CD3⁺CD8⁺Tet⁻CD62L⁺CD44⁺), and T_{EM} (CD3⁺CD8⁺Tet⁻CD62L⁻CD44⁺) cells were sorted from spleen on a FACS Aria II SORP (BD Biosciences), FACS Aria III (BD Biosciences), or MoFlo XDP cell sorter (**Figure S1.1a**). For uninfected mice, T_N, T_{CM}, and T_{EM} cells were sorted from spleen on a FACS Aria III (BD Biosciences).

DNA isolation

Genomic DNA was isolated from total thymocytes and from sorted T-cell subsets from MCMV-infected and uninfected mice according to the manufacturer's instructions using the NucleoSpin Blood QuickPure kit (Macherey-Nagel) and stored at -20°C until further analysis.

Measurement of ²H₂O enrichment in body water and DNA

Deuterium enrichment in plasma and DNA was analysed by gas chromatography/mass spectrometry (GC/MS) using an Agilent 5973/6890 GC/MS system (Agilent Technologies). Plasma was derivatized to acetylene (C₂H₂) as previously described (Westera et al., 2013). The derivative was injected into the GC/MS system equipped with a PoraPLOT Q 25 × 0.32 column (Varian) and measured in selected ion monitoring mode monitoring ions m/z 26 (M+0) and m/z 27 (M+1). From the ratio of ions, plasma deuterium enrichment was calculated by calibration against standard samples of known enrichment. DNA obtained from sorted lymphocytes and granulocytes was hydrolysed to deoxyribonucleotides and derivatized to pentafluoro tri-acetate (Westera et al., 2013). The derivative was injected into the GC/MS system equipped with a DB-17 column (Agilent Technologies) and measured in selected ion monitoring mode monitoring ions m/z 435 (M+0) and m/z 436 (M+1). From the ratio of ions, we calculated DNA deuterium enrichment by calibration against deoxyadenosine standards of known enrichment, as previously described (Westera et al., 2015).

Mathematical modelling of T-cell dynamics

We deduced the dynamics of tetramer-negative T_N, tetramer-negative T_{CM}, tetramer-negative T_{EM}, and tetramer-negative T_M (calculated as the weighted average of T_{CM} and T_{EM} cells) CD8⁺ cells, and of Tet⁺CD8⁺ T cells from the deuterium labelling data using previously published mathematical models (Asquith et al., 2002; Vrisekoop et al., 2008). In brief, to monitor the changing levels of deuterium in body water during the course of the experiment, a simple label enrichment/decay curve was fitted to the deuterium enrichment in plasma (Vrisekoop et al., 2008):

$$S(t) = \begin{cases} f(1 - e^{-\delta t}) + S_0 e^{-\delta t}, & t \leq \tau \\ [f(1 - e^{-\delta \tau}) + S_0 e^{-\delta \tau}] e^{-\delta(t-\tau)}, & t > \tau \end{cases} \quad (1.1)$$

where $S(t)$ is the fraction of deuterium in plasma at time t (in days), f is the predicted plateau value of deuterium enrichment in the plasma, δ is the turnover rate of body water per day, S_0 is the plasma enrichment level attained due to the i.p. ²H₂O boost, and ²H₂O administration was stopped at $\tau = 28$ days. The level of label incorporation in the different cell subsets was described by

$$\frac{dl(t)}{dt} = pcS(t) - d^*l(t) \quad (1.2)$$

Here, $l(t)$ is the fraction of labelled DNA in the cell subset, p is the average (per capita) production rate of the cells, d^* is the average (per capita) rate at which labelled cells are lost (which need not be equal to the average loss rate of cells in the population (Asquith et al.,

2002)), and c is an amplification factor, which accounts for the multiple hydrogen atoms that can be replaced by deuterium (see Ref. (Vrisekoop et al., 2008)). To estimate the value of c , we first fitted **equation 1.2** for a kinetically homogeneous population ($p = d^*$) (Westera et al., 2013) to the level of deuterium enrichment in the DNA of total thymocytes, as they are known to have a high turnover rate (Westera et al., 2013). The resulting estimated value of c was subsequently fixed to estimate the turnover rates of T_N , T_{CM} , T_{EM} , and T_M cells and Tet⁺CD8⁺ T cells. The best fits to the plasma and thymocyte data are shown in **Figure S1.2** (see **Table S1.1** for the estimated parameter values). When modelling the deuterium enrichment levels of T_N cells, a time delay (Δ) was introduced between T-cell production in the thymus and the appearance of labelled DNA in T_N cells in the spleen, based on previous observations (Westera et al., 2013). This was done by incorporating a delayed labelling curve of the deuterium enrichment in plasma [i.e., $S(t - \Delta)$] in **equation 1.2** when fitting the dynamics of T_N cells.

To estimate the rate of change in cell numbers, r , in the T_N , T_{CM} , T_{EM} , T_M , and Tet⁺ T-cell populations, we used a simple exponential growth/decay model, $\frac{dN(t)}{dt} = rN(t) = (p - d)N(t)$, which we fitted to the cell number data from the start of the experiment (i.e., 120 days post-infection (dpi)) until 550 days later (see **Table 1.2** and **Figure S1.3**). Results were very similar when r was estimated based on cell numbers during the first 140 days of the experiment. Based on the resulting value of r and the estimated value of p from **equation 1.2**, the cellular loss rates, $p - r$, were calculated (see **Table 1.2**). The expected lifespans of cells can be calculated as the inverse of their average loss rates, that is, as $1/d$.

Best fits to the labelling and cell number data were determined by minimizing the sum of squared residuals using the R function `modCost()` of the FME package (Soetaert et al., 2010). The fractions of labelled DNA, x , were transformed using the function `arcsin(sqrt(x))` before the fitting procedure. Fitting the cell number data yielded estimates for the initial cell number at the start of the experiment at 120 dpi, $N(0)$, and the exponential growth rate, r . The 95% confidence intervals (CIs) on the estimated parameters for both labelling and cell number data were determined using a bootstrap method where the data points were re-sampled 500 times. Fitting the exponential growth/decay model to these 500 data samples yielded 500 bootstrap trajectories. The 95% CI trajectories for the cell numbers were calculated by taking the 95% CI of these 500 bootstraps at each time point.

Statistical analysis

Statistical analyses were performed using GraphPad Prism. Comparisons between two and more groups were performed using Kruskal–Wallis and Dunn’s multiple comparison tests. A p -value < 0.05 was considered significant.

Results

Induction of inflationary CD8⁺ T-cell responses of different magnitude and phenotype

To study the kinetics of MCMV-specific and inflationary CD8⁺ T-cell responses during the memory phase of MCMV infection, we made use of 129/Sv mice to benefit from the well-defined H^{2b} MHC class I haplotype and the well-characterized arrays of epitopes associated with it, while circumventing a protective dominant role of NK cells in controlling the infection (Dekhtiarenko et al., 2013; Mitrović et al., 2012). The avidity of the viral epitope together with its context of gene expression define the kinetics and magnitude of the cognate inflationary CD8⁺ T-cell response (Dekhtiarenko et al., 2013). We used three well-characterized MCMV mutants expressing low-avidity or high-avidity epitopes in different genetic contexts: the recombinant MCMV^{ie2SL}, which expresses the high-avidity HSV-1 epitope SL inserted at the C terminus of the immediate-early 2 (*ie2*) gene (Dekhtiarenko et al., 2013); the MCMV^{ie2KNL} mutant expressing the low-avidity epitope KNL also inserted at the C terminus of the *ie2* gene (21); and the MCMVm45SL recombinant, which expresses the same epitope as MCMV^{ie2SL} inserted in a different genetic context, the early *m45* gene (Dekhtiarenko et al., 2013).

SL-specific and KNL-specific CD8⁺ T cells were analysed 120 dpi using tetramer staining to determine the magnitude and the phenotype of the inflating T-cell response. As previously described (Borkner et al., 2017), the SL and the KNL epitopes expressed within the *ie2* gene induced larger inflationary T-cell responses than does the SL epitope expressed within the *m45* gene (**Figure 1.1a**). MCMV^{ie2SL} induced the inflationary response of the highest magnitude; a median of 13% of total CD8⁺ T cells were SL Tet⁺. The size of the specific response to MCMV^{ie2KNL} was ~9% of the CD8⁺ T cell pool, and significantly larger than the response to MCMV^{m45SL}, which remained below 5%. Yet, even the latter recombinant virus induced a clearly detectable Tet⁺CD8⁺ T-cell population (**Figure 1.1a**).

Ag-specific CD8⁺ T cells composing an inflationary response typically present an effector phenotype and maintain their effector function (Klenerman and Oxenius, 2016). Accordingly, the vast majority (>80%) of Tet⁺CD8⁺ T cells composing large inflationary responses (MCMV^{ie2SL} and MCMV^{ie2KNL}) had a T_{EM} cell phenotype (CD44⁺CD62L⁻). In contrast, only 60% of the Tet⁺CD8⁺ T cells induced by MCMV^{m45SL} presented a T_{EM} cell phenotype, whereas the remaining 40% expressed T_{CM} cell markers (CD44⁺CD62L⁺) (**Figures 1.1b, S1.1b and S1.1c**). Less than 2% of the Tet⁺ T cells had a T_N cell phenotype (CD44⁻CD62L⁺).

Ki-67 expression pattern of CD8⁺ T cells does not differ between MCMV-induced inflationary responses of different magnitude

To study the dynamics of CD8⁺ T cells in the stable phase of chronic MCMV infection, we first determined cell proliferation by measuring Ki-67 expression. The fraction of Ki-67^{hi} cel-

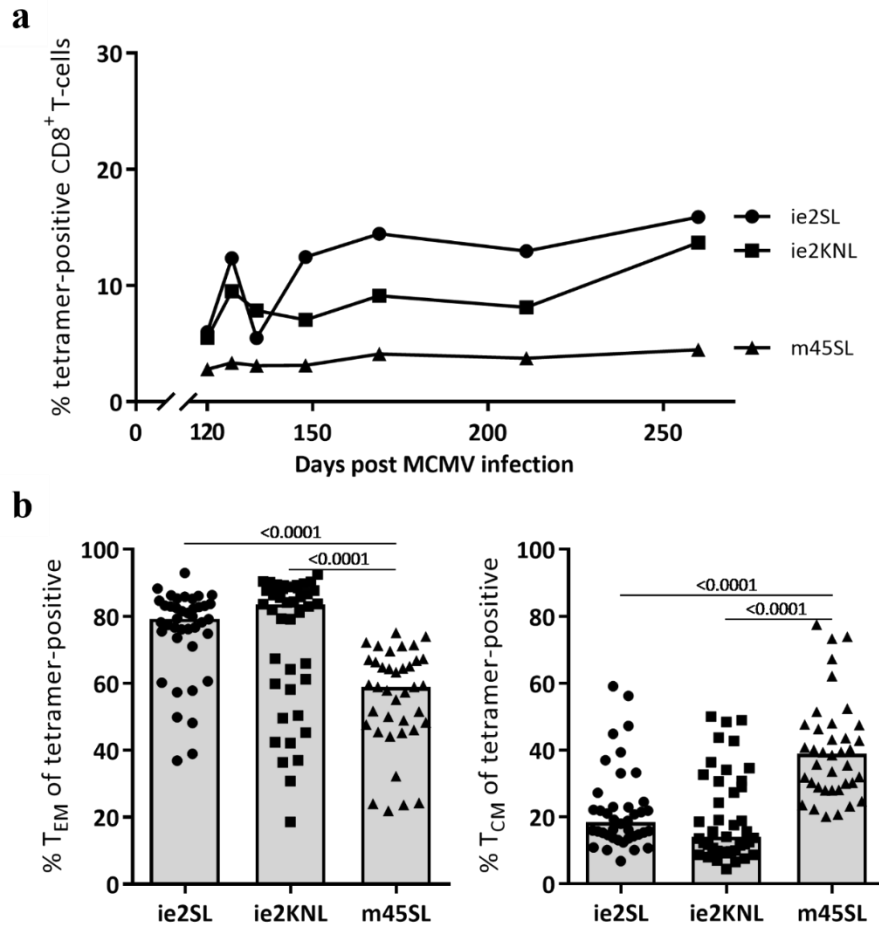


Figure 1.1: Recombinant viruses induce inflationary responses of different magnitude and phenotype. Mice (129/Sv) were infected with MCMV^{ie2SL}, MCMV^{ie2KNL}, or MCMV^{m45SL}, and at 120 dpi Tet⁺CD8⁺ T cells from spleen were characterized. **(a)** Median percentage of Tet⁺ cells within CD8⁺ T cells over time ($n = 4 - 7$ per time point per group). For significance, p -value = 0.04 for pooled time points of MCMV^{ie2SL} versus MCMV^{ie2KNL}, p -value < 0.0001 for pooled time points of MCMV^{ie2SL} versus MCMV^{m45SL}, and p -value = 0.0006 for pooled time points of MCMV^{ie2KNL} versus MCMV^{m45SL}. Pooled samples of different time points were compared using Kruskal–Wallis and Dunn’s multiple comparisons test. Data are pooled from two independent experiments. **(b)** Percentage of T_{EM} (left; CD44⁺CD62L⁻) and T_{CM} (right; CD44⁺CD62L⁺) cells within the Tet⁺CD8⁺ T-cell pool (MCMV^{ie2SL} $n = 39$, MCMV^{ie2KNL} $n = 41$, MCMV^{m45SL} $n = 38$). Data are pooled from two independent experiments. Bars represent the median percentage. For the % of T_{EM} cells, p -value > 0.999 for pooled time points of MCMV^{ie2SL} versus MCMV^{ie2KNL}, p -value < 0.0001 for pooled time points of MCMV^{ie2SL} versus MCMV^{m45SL}, and p -value < 0.0001 for pooled time points of MCMV^{ie2KNL} versus MCMV^{m45SL}. For the % of T_{CM} cells, p -value = 0.976 for pooled time points of MCMV^{ie2SL} versus MCMV^{ie2KNL}, p -value < 0.0001 for pooled time points of MCMV^{ie2SL} versus MCMV^{m45SL}, and p -value < 0.0001 for pooled time points of MCMV^{ie2KNL} versus MCMV^{m45SL}. Pooled samples of different time points were compared using Kruskal–Wallis and Dunn’s multiple comparison tests. Median percentages of T_N, T_{CM}, and T_{EM} cells within tetramer-negative and Tet⁺CD8⁺ T cells in MCMV-infected and uninfected mice are shown in **Figure S1.1b**. Changes in the median percentage of T_N, T_{CM}, and T_{EM} CD8⁺ cells over time are shown in **Figure S1.1c**.

Is within T_N, T_{CM}, and T_{EM} CD8⁺ cells was not significantly different between uninfected mice and chronically infected mice for all three viruses (**Figure 1.2**). In line with previous reports (Sun et al., 2016), we found that the percentage of Ki-67^{hi} cells was the lowest within T_N cells (median over all groups of 0.4%), intermediate within T_{CM} cells (median of 4.5%), and the highest within T_{EM} cells (median of 12%) (**Figure 1.2b**). Approximately 5% of the Tet⁺CD8⁺ T cells were Ki-67^{hi}. For each viral infection, the total fraction of Ki-67^{hi} cells within the Tet⁺ cells was not significantly different from that of memory phenotype T cells, and it was in fact between the Ki-67 expression levels of T_{EM} and T_{CM} cells (**Figure 1.2b**). Based on Ki-67 expression, we thus found no indication that inflated MCMV-specific CD8⁺ T cells have different proliferation rates than do bulk memory phenotype CD8⁺ T cells. Because Ki-67 only provides a snapshot marker of T-cell proliferation, we next studied the average production and loss rates of the cells using *in vivo* deuterium labelling.

Kinetics of T_N, T_{CM}, and T_{EM} CD8⁺ cells during chronic MCMV infection

The *in vivo* kinetics of memory CD8⁺ T cells have primarily been studied in bulk memory phenotype T cells (Westera et al., 2013). Here, we quantified the dynamics of T_N, T_{CM}, T_{EM} and T_M CD8⁺ cell subsets in chronically infected and uninfected 129/Sv mice. Mice received ²H₂O for 4 wk and were sacrificed at different time points during the labelling and the de-labelling period. We subsequently used previously published mathematical models (Westera et al., 2013) (see **Materials and Methods**) to quantify the average production and loss rates of T_N, T_{CM}, T_{EM}, and T_M CD8⁺ cells based on their deuterium labelling data.

Deuterium enrichment curves of T_N, T_{CM}, T_{EM}, and T_M cells were very similar in MCMV^{ie2SL}-, MCMV^{ie2KNL}-, and MCMV^{m45SL}- infected animals (**Figure 1.3**). In line with this, the best fits of the model to the data yielded similar estimates for the average production rates p and the average loss rates of labelled cells d^* within the T_N, T_{CM}, T_{EM}, and T_M CD8⁺ cell populations for the three different viruses (**Figure 1.4a**, **Table 1.1**). The estimated average production rate p of T_N cells during chronic MCMV infection was 0.0090 per day for MCMV^{ie2SL}, 0.0095 per day for MCMV^{ie2KNL}, and 0.0077 per day for MCMV^{m45SL}, suggesting that T_N cells turn over relatively little. In contrast, T_{CM} cells turned over significantly, with average production rates of 0.0132 per day for MCMV^{ie2SL}, 0.0151 per day for MCMV^{ie2KNL}, and 0.0139 per day for MCMV^{m45SL}. The average production rates of T_{EM} cells were consistently the highest, with 0.0204 per day for MCMV^{ie2SL}, 0.0229 per day for MCMV^{ie2KNL}, and 0.0205 per day for MCMV^{m45SL} (**Table 1.1**).

The turnover rate of MCMV-specific CD8⁺ T cells is independent of the magnitude of the inflationary response

To investigate how the size of an MCMV-specific memory T-cell response is related to its turnover (Wallace et al., 2011), we quantified the turnover rates of Tet⁺CD8⁺ T cells compos-

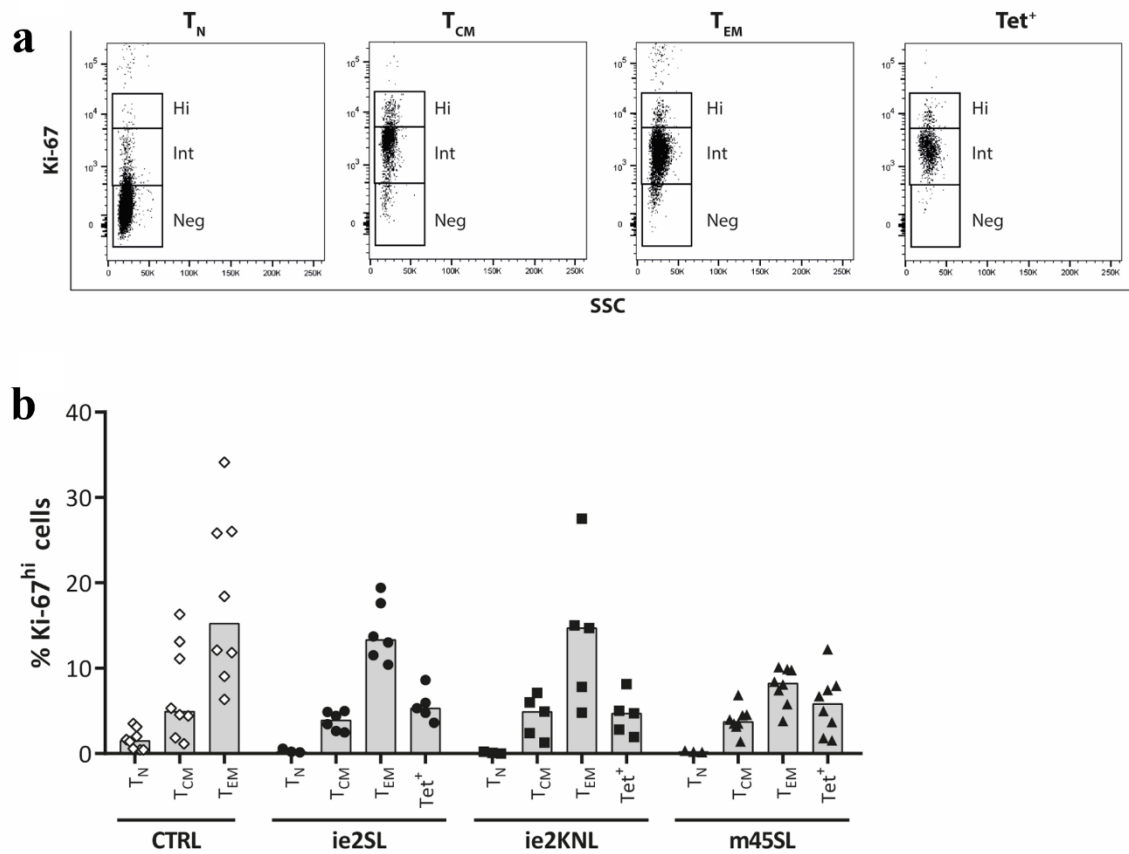


Figure 1.2: Percentage Ki-67^{hi} cells within CD8⁺ T-cell subsets in MCMV-infected and uninfected mice. (a) Representative Ki-67 staining of T_N, T_{CM}, and T_{EM} cells and Tet⁺CD8⁺ T cells from blood of an MCMV^{m45SL}-infected mouse at 17 mo post-infection. (b) Fraction of Ki-67^{hi} T_N, T_{CM}, and T_{EM} cells and Tet⁺CD8⁺ T cells from blood of MCMV^{ie2SL}-infected ($n = 4 - 6$), MCMV^{ie2KNL}-infected ($n = 4 - 5$), and MCMV^{m45SL}-infected ($n = 4 - 8$) mice and age-matched and sex-matched uninfected mice (CTRL, $n = 8$). For MCMV^{ieKNL}, p-value = 0.418 for pooled time points of % Ki-67^{hi} Tet⁺ versus T_{EM} cells, p-value > 0.999 for pooled time points of % Ki-67^{hi} Tet⁺ versus T_{CM} cells, and p-value = 0.224 for pooled time points of % Ki-67^{hi} Tet⁺ versus T_N cells; for MCMV^{ie2SL}, p-value = 0.583 for pooled time points of % Ki-67^{hi} Tet⁺ versus T_{EM} cells, p-value > 0.999 for pooled time points of % Ki-67^{hi} Tet⁺ versus T_{CM} cells, and p-value = 0.389 for pooled time points of % Ki-67^{hi} Tet⁺ versus T_N cells; for MCMV^{m45SL}, p-value = 0.938 for pooled time points of % Ki-67^{hi} Tet⁺ versus T_{EM} cells, p-value > 0.999 for pooled time points of % Ki-67^{hi} Tet⁺ versus T_{CM} cells, and p-value = 0.088 for pooled time points of % Ki-67^{hi} Tet⁺ versus T_N cells. Pooled samples of different time points were compared using Kruskal–Wallis and Dunn’s multiple comparison tests. Data are pooled from two independent experiments. Bars represent median percentages.

ing large (MCMV^{ie2SL}) and intermediate (MCMV^{ie2KNL}) inflationary responses, as well as a low inflationary response (MCMV^{m45SL}). Despite the clear differences in the height of the Ag-specific responses induced by these three viruses, the corresponding deuterium enrichment curves of Tet⁺CD8⁺ T cells were very similar (**Figure 1.3**). The best fits of the model to the deuterium-enrichment data of SL Tet⁺CD8⁺ T cells in MCMV^{ie2SL}- and

MCMV^{m45SL}-infected mice (**Figure 1.3**) confirmed that, despite the 3-fold difference in the size of these inflationary responses (**Figure 1.1a**) and their different T_{CM} and T_{EM} compositions (**Figure 1.1b**), their average production rates p and loss rates of labelled cells d^* were not significantly different (**Figure 1.4a**, **Table 1.1**). We estimated that SL Tet⁺CD8⁺ T cells had an average production rate of 0.0169 per day in MCMV^{ie2SL}-infected mice and 0.0161 per day in MCMV^{m45SL}-infected mice. For KNL-specific T cells, which comprised the intermediate inflationary response, we found an average production rate of 0.0195 per day (**Table 1.1**). Thus, there were no substantial differences in the average turnover rates of Tet⁺CD8⁺ T cells composing large, intermediate, and low inflationary responses.

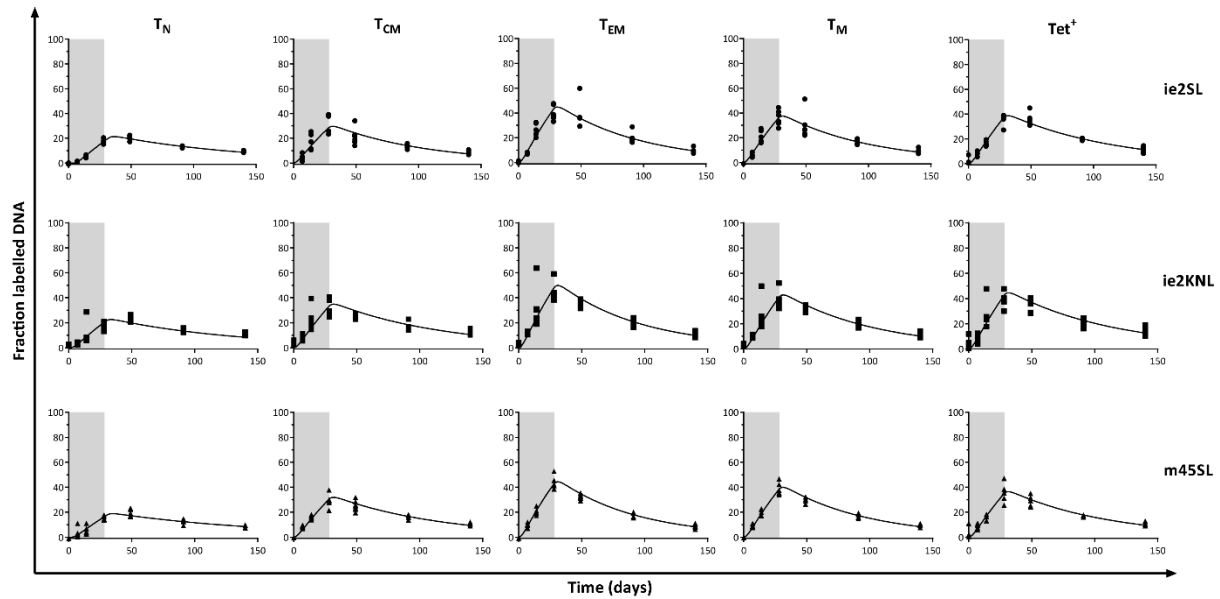


Figure 1.3: Deuterium labelling of tetramer-negative and Tet⁺CD8⁺ T cells in MCMV-infected mice. Deuterium enrichment in the DNA of T_N, T_{CM}, T_{EM}, and T_M cells and Tet⁺CD8⁺ T cells 120 d after MCMV^{ie2SL}, MCMV^{ie2KNL}, or MCMV^{m45SL} infection. The curves represent the best fits of the model (Westera et al., 2013) to the deuterium enrichment data. Label enrichment was scaled between 0 and 100% by dividing all enrichment levels by the estimated maximum enrichment level of thymocytes (**Figure S1.2**, **Table S1.1**). Parameter estimates corresponding to the best fits are given in **Table 1.1**.

MCMV-specific CD8⁺ T cells do not have significantly longer lifespans than do memory phenotype CD8⁺ T cells

Finally, to investigate the hypothesis that accumulation of inflationary responses in MCMV is due to accumulation of long-lived cells, we compared the average turnover rates of MCMV-specific (Tet⁺) CD8⁺ T cells to those of tetramer-negative T_M CD8⁺ cells (see **Materials and Methods**). When comparing the best fits of the individual datasets, we found no statistical indication that T_M cells and Tet⁺ T cells had different production rates p or loss rates of labelled cells d^* (**Figure 1.4a**, **Table 1.1**).

Since the average loss rate d^* of labelled cells may not be representative of the cell population as a whole (Asquith et al., 2002), we used additional information on absolute cell

CD8 ⁺ T-cell subset	MCMV ^{ie2SL}	MCMV ^{ie2KNL}	MCMV ^{m45SL}
Average production rate per day (p)			
T_N	0.0090 (0.0084; 0.0095)	0.0095 (0.0085; 0.0107)	0.0077 (0.0068; 0.0089)
T_{CM}	0.0132 (0.0114; 0.0154)	0.0151 (0.0133; 0.0177)	0.0139 (0.0126; 0.0153)
T_{EM}	0.0204 (0.0184; 0.0229)	0.0229 (0.0203; 0.0270)	0.0205 (0.0192; 0.0221)
T_M	0.0169 (0.0149; 0.0188)	0.0192 (0.0172; 0.0219)	0.0182 (0.0171; 0.0195)
Tet⁺	0.0169 (0.0158; 0.0182)	0.0195 (0.0175; 0.0222)	0.0161 (0.0147; 0.0176)
Average loss rate of labelled cells per day (d^*)			
T_N	0.0090 (0.0084; 0.0095)	0.0095 (0.0085; 0.0107)	0.0077 (0.0068; 0.0089)
T_{CM}	0.0131 (0.0111; 0.0160)	0.0113 (0.0093; 0.0142)	0.0115 (0.0102; 0.0130)
T_{EM}	0.0146 (0.0130; 0.0163)	0.0153 (0.0134; 0.0180)	0.0157 (0.0143; 0.0170)
T_M	0.0141 (0.0124; 0.0158)	0.0135 (0.0118; 0.0160)	0.0146 (0.0135; 0.0161)
Tet⁺	0.0116 (0.0104; 0.0128)	0.0120 (0.0100; 0.0143)	0.0126 (0.0113; 0.0140)

Table 1.1: Average production rates and loss rates of labelled cells in MCMV-infected mice. Estimated parameters and their corresponding 95% confidence intervals are shown. For T_N cells, we report the best fits of the model with $p = d$, as allowing for different values of p and d did not significantly improve the fit to the data (for significance, p-value of F-test = 1 for MCMV^{ie2SL}, p-value of F-test = 0.09 for MCMV^{ie2KNL}, and p-value of F-test = 0.54 for MCMV^{m45SL}).

numbers to compare the average loss rates d of Tet⁺ and T_M cells. Although these absolute cell numbers are notoriously noisy, we estimated a slight increase in cell numbers in the T_{CM}, T_{EM}, T_M, and Tet⁺CD8⁺ T-cell populations (**Table 1.2, Figure S1.3**). The average production rates p may thus not be equal to the average loss rates d of cells. Even when accounting for this rate of increase, r , in cell numbers, we found very similar average loss rates d (where $d = p - r$, see **Materials and Methods**) of T_M and Tet⁺ cells in MCMV^{ie2SL}-, MCMV^{ie2KNL}-, and MCMV^{m45SL}-infected mice (**Figure 1.4b, Table 1.2**). We thus found no evidence for the previously proposed idea that CMV-specific T cells are longer-lived than other memory T cells (Wallace et al., 2011).

Although an advantage of the current study is the face-to-face comparison of Tet⁺ and tetramer-negative cells in the same mouse, it is more than likely that the tetramer-negative T-cell populations still contained MCMV-specific CD8⁺ T cells specific for other MCMV epitopes (Borkner et al., 2017; Dekhtiarenko et al., 2013; Munks et al., 2006). We wondered

whether this could have masked possible differences in the turnover of MCMV-specific and non-MCMV-specific memory CD8⁺ T cells. To investigate this, we compared the deuterium enrichment levels of T_N, T_{CM}, T_{EM}, and T_M cells in MCMV-infected mice to those in uninfected mice. Because these levels were very similar (**Figure S1.4**), we conclude that the expected lifespan of MCMV-specific memory CD8⁺ T cells is not significantly different from that of other memory-phenotype CD8⁺ T cells.

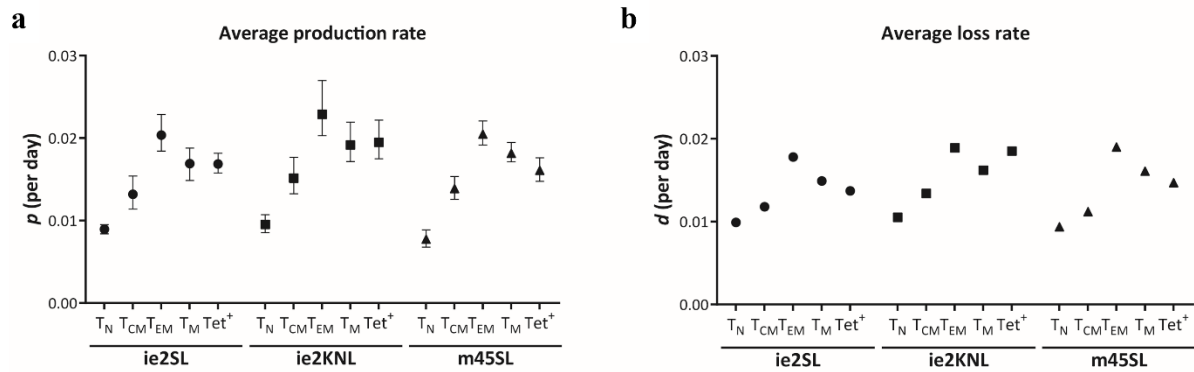


Figure 1.4: Average production and loss rates of T cells in MCMV-infected mice. **(a and b)** Estimated average production rates p per day **(a)** and average loss rates d per day **(b)** for T_N, T_{CM}, T_{EM} and T_M CD8⁺ T cells and Tet⁺ memory CD8⁺ T cells. **(a)** Average production rates (p) were based on the best fits of the deuterium labelling data of **Figure 1.3**. Their values are reported in **Table 1.1**. Whiskers represent the corresponding 95% confidence intervals. **(b)** The average loss rates (d) were calculated from $d = p - r$, using the best estimates of p (**Table 1.1**) and the estimated growth rate (r) of the specific T-cell population (**Table 1.2**). Because the average loss rates were calculated based on other parameters, they are given without 95% confidence intervals.

Discussion

During the chronic phase of MCMV infection, we found no evidence that MCMV-specific CD8⁺ T cells are longer-lived or produced at higher rates than do bulk memory-phenotype CD8⁺ T cells. These findings are in line with our recent findings in humans, which showed that CMV-specific CD8⁺ T cells had similar turnover rates as bulk memory CD8⁺ T cells (van den Berg et al., 2021). Both outcomes are remarkable in the light of a previously published deuterated-glucose labelling study in humans, which reported that CMV-specific CD8⁺ T cells incorporated less deuterium than did CD45RO⁺ (memory) T cells (Wallace et al., 2011), which led to the hypothesis that inflating responses are composed of relatively long-lived memory T cells. We found that the turnover rates of Ag-specific T cells composing inflationary responses that varied up to 3-fold in size were not significantly different. This adds further support to our conclusion that the magnitude of inflationary responses is not explained by extended lifespans of MCMV-specific T cells.

To interpret the deuterium labelling data, we used a previously proposed kinetic heterogeneity model (Asquith et al., 2002), which yields the average production rate p of cells, as well as the average loss rate d^* of labelled cells. It was previously explained that cell

populations in steady state typically yield $d^* > p$, because p is representative of all cells in the population, whereas d^* is biased toward cells that have just divided (Asquith et al., 2002).

CD8 ⁺ T-cell subset	MCMV ^{ie2SL}	MCMV ^{ie2KNL}	MCMV ^{m45SL}
Average growth/decay rate of the cell population per day (r)			
T_N	-0.00093 (-0.0028; 0.00015)	-0.00094 (-0.0039; 0.00065)	-0.0016 (-0.004; -0.0004)
T_{CM}	0.0014 (0.00032; 0.0024)	0.0017 (-0.0028; 0.0027)	0.0027 (0.0007; 0.0044)
T_{EM}	0.0026 (0.0013; 0.0037)	0.0040 (0.00025; 0.0068)	0.0015 (0.00014; 0.0028)
T_M	0.0020 (0.000895; 0.0029)	0.0030 (-0.00033; 0.0043)	0.0021 (0.00083; 0.0033)
Tet⁺	0.0032 (0.0021; 0.0045)	0.001 (-0.0021; 0.008)	0.0014 (-0.00025; 0.0029)
Calculated average T-cell loss rate per day (d)			
T_N	0.0099	0.0105	0.00939
T_{CM}	0.0118	0.0134	0.0112
T_{EM}	0.0178	0.0189	0.0190
T_M	0.0149	0.0162	0.0161
Tet⁺	0.0137	0.0185	0.0147

Table 1.2: Average population growth rates and average loss rates in MCMV-infected mice. T-cell loss rates (d) were calculated using the estimated average production rates (p) (from the deuterium labelling experiments, **Table 1.1**) and the estimated overall growth/decay rates (r) of the specific T-cell populations (followed for 550 days, **Figure S1.3**) (see **Materials and Methods**). Overall growth/decay rates of the specific T-cell populations were estimated by simultaneously estimating each population size at the start of the experiment (i.e., 120 dpi), $N(0)$, of which the values are given in **Table S1.1**. Estimated growth rates are reported with their corresponding 95% confidence intervals in brackets. Because the average loss rates were calculated based on other parameters, they are given without 95% confidence intervals.

The estimated value of p can thus safely be interpreted as the average production rate of cells, which apparently does not differ between inflationary CMV-specific T-cell responses and bulk memory T cells. The cellular production that we measured by *in vivo* deuterium labelling captures both T-cell division as well as a possible influx of cells from the naive compartment. Although it has previously been shown that naive T cells can continuously be recruited into the MCMV-specific T-cell response (Snyder et al., 2008), the contribution of this influx is probably relatively small, as memory inflation in mice was shown to be hardly affected by thymectomy (Loewendorf et al., 2011; Welten et al., 2019). Thus, assuming that the vast majority of MCMV-specific cells are formed by peripheral T-cell division, and not by continuous recruitment of new naive MCMV-specific T cells into the memory pool, the similar production rates of Tet⁺ and T_M cells imply that MCMV-specific T cells do not divide more frequently than do other memory T cells, which is supported by their similar Ki-67

expression levels. It has recently been shown that the MCMV-specific inflationary T-cell response is “fueled” by a subset of TCF1⁺ MCMV-specific T cells (Welten et al., 2020), and that continual, stochastic encounters with MCMV maintain the inflationary response (Smith et al., 2020).

To compare the average loss rates of Tet⁺ and T_M cells, we used additional information on absolute cell numbers, which confirmed that also the expected lifespans of Tet⁺ and T_M cells are very similar. We found that the expected lifespan (calculated as $1/d$) of bulk memory-phenotype T cells was ~ 65 days, whereas that of MCMV-specific T cells was 73 days for the large inflationary response in MCMV^{ie2SL}-infected mice, 54 days for the intermediate inflationary response in MCMV^{ie2KNL}-infected mice, and 68 days for the low inflationary response in MCMV^{m45SL}-infected mice. These estimates are well in line with previous studies showing the dynamic behaviour of inflating responses (Snyder et al., 2008). We thus found no evidence for the previously proposed idea that CMV-specific T cells are longer-lived than other memory T cells (Wallace et al., 2011). Instead, our data suggest that the explanation for the size differences between MCMV-specific CD8⁺ T-cell responses and for memory inflation in general should be sought earlier during infection. In line with this, several studies have shown that the inflationary potential of CMV-specific T cells is set early, during the acute phase of the response (Snyder et al., 2008; Welten et al., 2019), and is linked to the number of primed KLRG1⁻ CMV-specific CD8⁺ T cells (Baumann et al., 2019) and to the early transcriptomic profile and T_{CM} cell precursor content of the CMV-specific CD8⁺ T cells (Grassmann et al., 2020).

Non-steady cell numbers in some of the populations may explain why we sometimes found values of d^* lower than p (see **Table 1.1**). This is typically not observed in deuterium labelling experiments (Asquith et al., 2002), and it suggests that cells that have recently divided live longer than other cells in the population. Alternatively, for populations that are not in steady state, if cellular turnover is dependent on cell densities, average production rates may decrease during the labelling experiment, although cell numbers are increasing. This could explain why, contrary to what is typically observed for populations in steady state, some turnover rates during the de-labelling phase were lower than during the up-labelling phase (see Chapter 2). In this light, it is interesting to note that the T-cell repertoire against CMV has recently been shown to continuously evolve during chronic infection, in that the relative immunodominance of high-affinity clones declines during chronic infection, most likely due to cellular senescence (Schober et al., 2020).

A previous study in humans reported that YFV-specific CD8⁺ T cells triggered upon YFV vaccination divide sporadically, approximately every 666 days (Akondy et al., 2017), and less than bulk memory T cells. It was argued that the shorter intermitotic times of bulk memory T cells probably reflect their continuous Ag stimulation (Akondy et al., 2017). In line with this hypothesis, we found that MCMV-specific CD8⁺ T cells, which are repeatedly exposed to their cognate Ag, have similar life-spans as bulk memory-phenotype CD8⁺ T cells, which may also be continuously exposed to commensal and environmental Ags. However, the observation that lymphocytic choriomeningitis virus-specific memory CD8⁺ T cells transferred into naive mice had similar turnover rates to those of bulk memory-phenotype

CD8⁺ T cells (Choo et al., 2010) suggests that even Ag-specific T cells maintained in the absence of cognate Ag can turnover as fast as bulk memory-phenotype T cells. Although we cannot exclude the possibility that the differences in the maintenance of YFV-, MCMV-, and lymphocytic choriomeningitis virus-specific memory CD8⁺ T cells are due to mouse and human differences, the characteristics of different Ag-specific memory T cells may also depend on the nature of the infection, the duration of the stimulus, and the concomitant response to other Ags. It is therefore perhaps not surprising that Ag-specific T-cell responses against different infections have different dynamics (Althaus et al., 2007). Future studies into the dynamics of memory T cells specific for Ags that are presented persistently (chronic), intermittently (latent reactivating), or only once (acute) are needed to gain more insight into how Ag-specific memory T-cell responses are maintained in mice and humans.

Chronic CMV infection in both mice and humans is under constant immune surveillance and triggers ongoing CD8⁺ T-cell responses. It is thought that CMV infection modulates the peripheral lymphoid pool (Chidrawar et al., 2009; Derhovanessian et al., 2009) and affects T-cell differentiation and function (Miles et al., 2008), not only of CMV-specific T cells but also of T cells with other specificities (Lanfermeijer et al., 2021). Under this hypothesis, we directly compared the dynamics of T_N, T_{CM}, T_{EM}, and T_M cells in uninfected and chronically MCMV-infected mice (**Figure S1.4**) and found no significant differences in their kinetics. Despite differences in the composition of the T-cell pool, our results therefore suggest that the dynamics of non-MCMV-specific CD8⁺ T cells are not substantially affected during chronic MCMV infection. We previously observed that also cellular immune function was maintained during latency, as responses to heterologous virus infection and immune protection were not diminished in mice latently infected with MCMV or other herpesviruses (Marandu et al., 2015).

The large prevalence of chronic CMV infection in the human population (>50%) (Cannon et al., 2010) and its effect on healthy aging (Aiello et al., 2017; Brodin et al., 2015; Roberts et al., 2010), together with the emerging interest in CMV-based vector vaccines (Bolinger et al., 2015), highlight the need to understand how CMV-specific CD8⁺ T-cell responses are maintained. *In vivo* MCMV infection provided us with the means to address fundamental questions about the maintenance and turnover of inflated CD8⁺ T-cell responses. The finding that the maintenance of inflationary MCMV-specific CD8⁺ T cells does not differ from that of low inflationary memory CD8⁺ T cells suggests that inflationary CD8⁺ T-cell responses, such as those induced by CMV-based vector vaccines, may also result in a memory CD8⁺ T-cell response of high magnitude without substantial alterations in the dynamics of the cells.

Acknowledgments

We thank Ramon Arens for generously providing all MHC-peptide tetramers, Nienke Vriskoop for help and support with the animal experiments, Derek Macallan and Linda Hadcocks for measuring ²H₂O enrichment in the body water of the uninfected mice, and Janine Schreiber and Lothar Gröbe for technical assistance.

Author Contributions

The study was designed by K.T., J.B., R.dB. and L.C.-S.; M.B.-P., X.Z., L.B. and S.O. performed the experimental work; A.S. and J.D. performed the mathematical modelling. All authors contributed to the article and approved the submitted version.

Funding statement

This work was supported by funding from the European Union Seventh Framework Programme (FP7/2007–2013) through the Marie-Curie Action “Quantitative T Cell Immunology” Initial Training Network, with reference FP7-PEOPLE-2012-ITN 317040-QuanTI supporting M.B.-P., and European Research Council Grant 260934 to L.C.-S.. X.Z. was supported by a Chinese Scientific Council scholarship. A.C.S. was supported by Netherlands Organisation for Scientific Research Grant ALWOP.265.

Disclosures

The authors have no financial conflicts of interest.

Supplementary Information

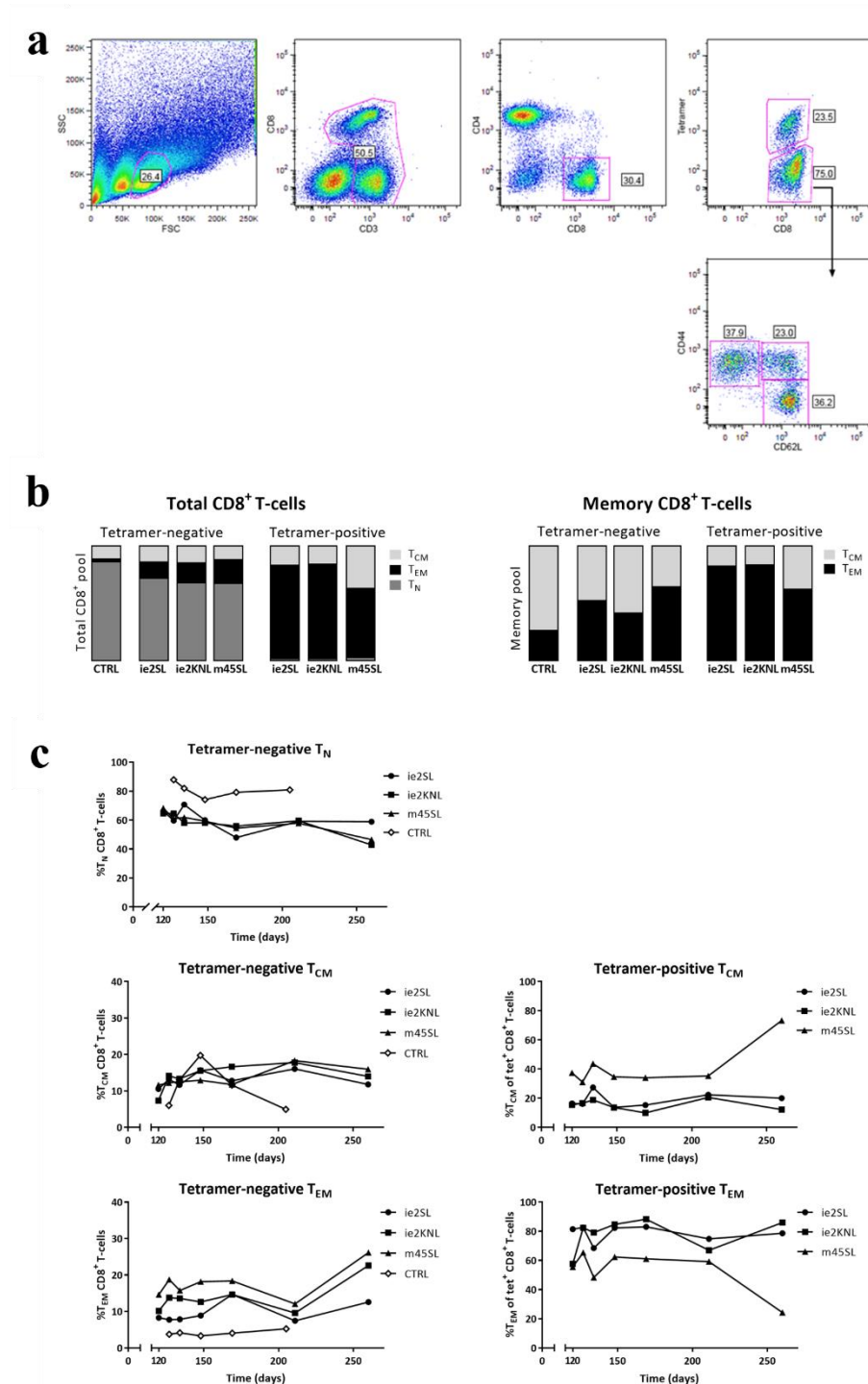
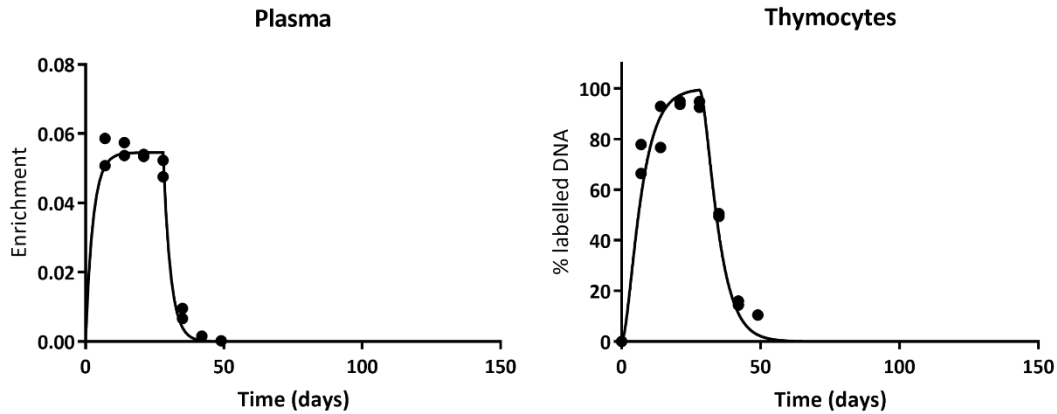


Figure S1.1: (a) **Sort gating strategy.** Strategy for sorting of tetramer-positive CD8⁺ T cells and tetramer-negative T_N (CD62L⁺CD44⁻), T_{CM} (CD62L⁺CD44⁺) and T_{EM} (CD62L⁻CD44⁺) CD8⁺ T cells. (b) **Composition of the CD8⁺ T-cell pool in MCMV-infected and uninfected mice.** Median percentage of T_N, T_{CM} and T_{EM} cells within tetramer-negative and tetramer-positive total CD8⁺ T cells (left) and median percentage of T_{CM} and T_{EM} cells within tetramer-negative and tetramer-positive memory phenotype CD8⁺ T cells (CD44⁺) (right) from MCMV-infected mice (MCMV^{ie2SL} (*n* = 39), MCMV^{ie2KNL} (*n* = 41), MCMV^{m45SL} (*n* = 38)) and age- and sex- matched uninfected mice (CTRL)

($n = 10$). (c) **Composition of the CD8⁺ T-cell pool over time in MCMV-infected and uninfected mice.** Mice (129/Sv) were infected at $t=0$ with MCMV^{ie2SL}, MCMV^{ie2KNL} or MCMV^{m45SL}, age- and sex-matched uninfected 129/Sv mice were used as controls (CTRL). From 120 dpi onwards, tetramer-negative and tetramer-positive CD8⁺ T cells from spleen were characterized. Median percentage of T_N, T_{CM} and T_{EM} cells within tetramer-negative CD8⁺ T cells and median percentage of T_{CM} and T_{EM} cells within tetramer-positive CD8⁺ T cells over time (for MCMV-infected mice, $n = 4 - 7$ per time point; for CTRL mice, $n = 2$ per time point).

a MCMV-infected mice



b Uninfected mice

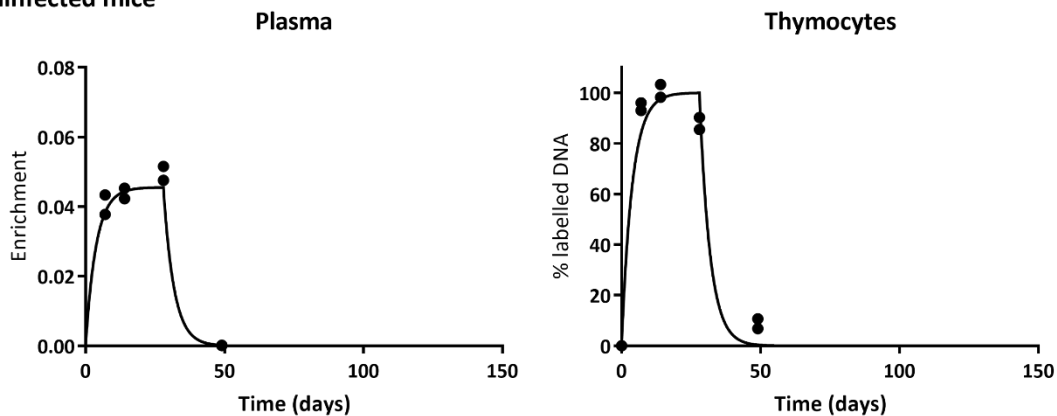


Figure S1.2: Deuterium enrichment in plasma and thymocytes. Deuterium enrichment in the body water (plasma) and thymocytes. Symbols represent individual measurements during the up- and down- labelling phases of (a) MCMV-infected mice and (b) age-matched and sex-matched uninfected mice. The labelling data of thymocytes were fitted with **equation 1.2** assuming $p = d^*$, and their label enrichment was scaled between 0 and 100% by normalizing for their estimated maximum level of deuterium enrichment. The enrichment curves of thymocytes were used to normalize the deuterium enrichment data of the different T-cell subsets (see **Material and Methods**). Parameter estimates of the best fits are given in **Table S1.1**.

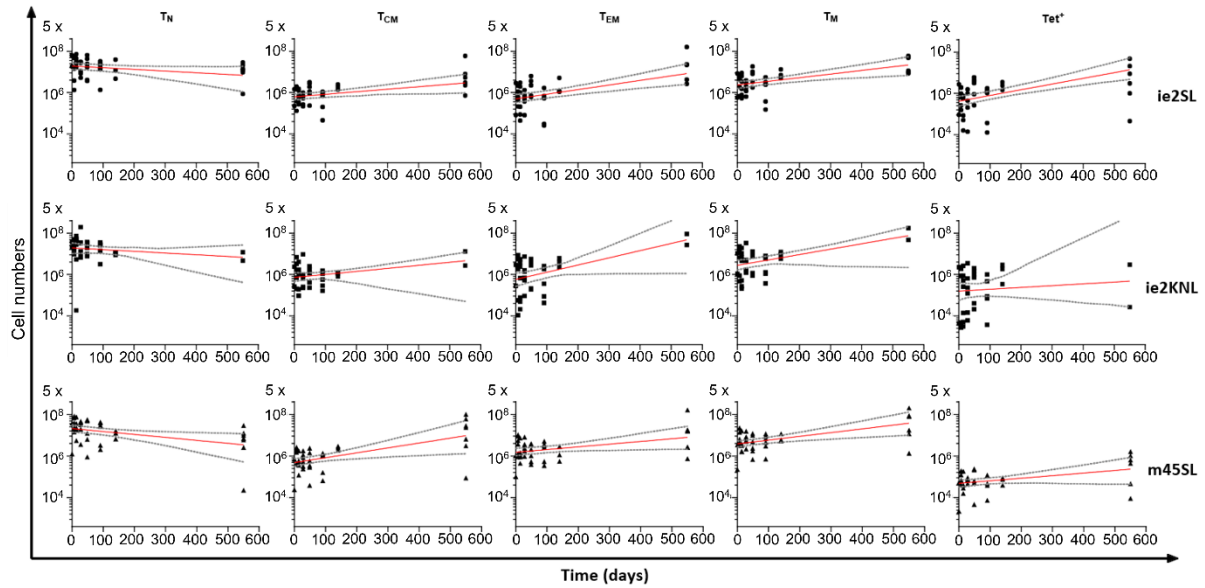


Figure S1.3: Estimation of the growth/decay rate r of the different T-cell populations. We estimated the rate of change in cell numbers, r , and the cell numbers at the start of the experiment (i.e., 120 days p.i.), $N(0)$, in the T_N, T_{CM}, T_{EM}, T_M, and Tet⁺ T-cell populations of MCMV-infected mice by fitting a simple exponential growth/decay model to the observed cell numbers in mice over 550 days (see **Material and Methods**). The best fits to the data are given by the red curves. The grey curves represent the 95% confidence intervals (CI) and were calculated by taking the 95% CI, at each time point, of 500 bootstrap trajectories (see **Material and Methods**). The estimated values of r and $N(0)$ and their 95% CI are given in **Tables 1.2** and **S1.1**, respectively.

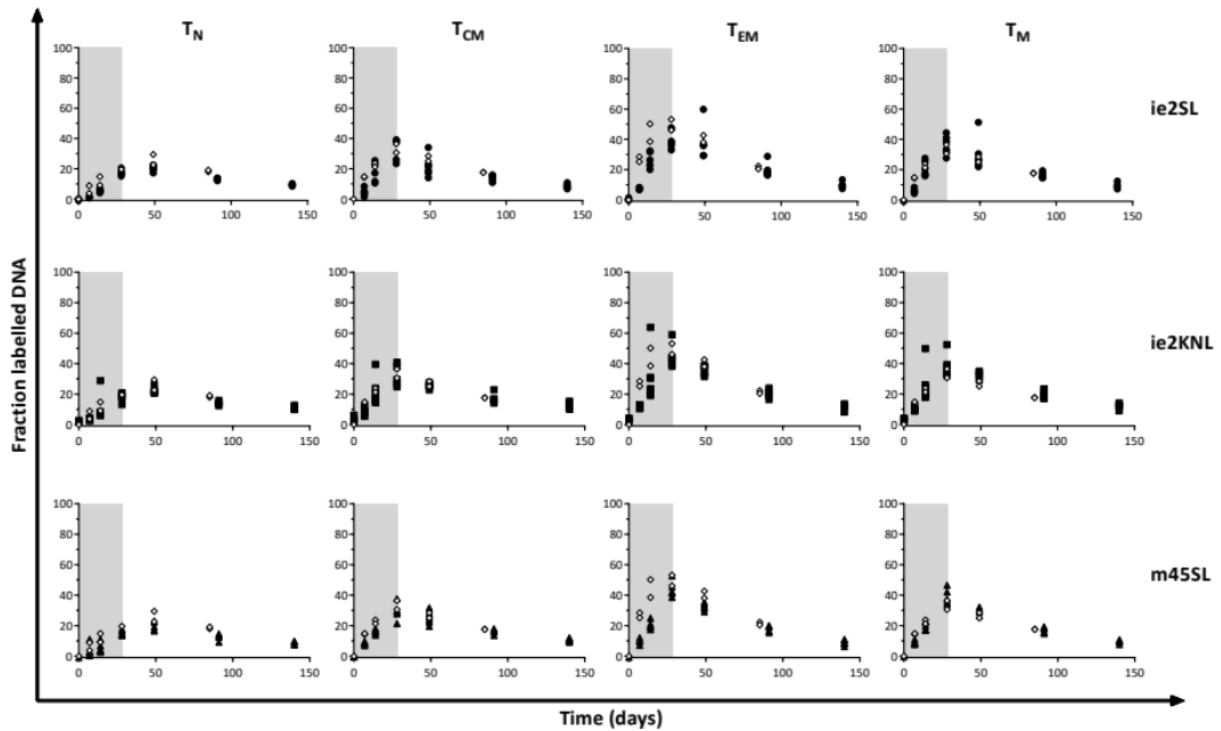


Figure S1.4: Enrichment level in T_N, T_{CM}, T_{EM} and T_M CD8⁺ T cells of uninfected mice is similar to that of MCMV-infected mice. ²H enrichment in the DNA of T_N, T_{CM}, T_{EM} and T_M of uninfected 129/Sv mice (open diamonds) and tetramer-negative T_N, T_{CM}, T_{EM} and T_M CD8⁺ T cells of MCMV^{ie2SL}, MCMV^{ie2KNL} or MCMV^{m45SL} infected mice (black symbols, which are also shown in Figure 1.3).

		MCMV-infected mice	Uninfected mice
Plasma	δ (per day)	0.3730 (0.2436; 0.3844)	0.2616 (0.1945; 0.4198)
	f (per day)	0.0545 (0.0526; 0.0829)	0.0455 (0.0430; 0.0483)
	S_0	0.0006 (0; 0.0007)	0 (0;0)
Thymocytes	c	3.0271 (2.7906; 3.2116)	3.9011 (3.5946; 4.1589)
	p	0.1839 (0.1507; 0.2314)	N.I.
Estimated population size at start of experiment, $N(0)$			
CD8⁺ T-cell subset	MCMV^{ie2SL}	MCMV^{ie2KNL}	MCMV^{m45SL}
T_N	2187085 (1800056; 2643753)	2193015 (1597846; 2908849)	2286946 (1855345; 2810501)
T_{CM}	394773 (333631; 467489)	423450 (341455; 559050)	346660 (283320; 431499)
T_{EM}	353468 (286233; 451371)	380288 (258420; 541734)	614460 (509244; 760951)
T_M	763465 (624839; 918752)	832600 (643671; 1113140)	979134 (819990; 1168923)
Tet⁺	324228 (246843; 424190)	198686 (117330; 308198)	109771 (89367; 132410)

Table S1.1: Estimated parameters and their corresponding 95% confidence intervals for deuterium enrichment in plasma and thymocytes of MCMV-infected and uninfected mice. Since allowing for different values of p and d^* did not significantly improve the description of the labelling curve of the thymocytes, we report the best fits of the model with $p = d^*$. For uninfected mice, the turnover rate of thymocytes was non-identifiable (N.I.). **Estimated values of $N(0)$.** Overall growth/decay rates r of the specific T-cell populations (**Figure S1.3** and **Table 1.2**) were estimated by simultaneously estimating each population size at the start of the experiment (i.e., 120 days p.i.), $N(0)$, of which the values are given below, with 95% CI in brackets.

Explaining unexpected deuterium labelling curves

Arpit C. Swain^{1,2}, Julia Drylewicz², Elena S. de Dios Panal², Daniela K. Korolova², Kiki Tesselaar²,
José A.M. Borghans², Rob J. de Boer¹

¹Theoretical Biology, Utrecht University, Utrecht, The Netherlands

²Center for Translational Immunology, University Medical Center Utrecht, Utrecht, The Netherlands

To be submitted

Abstract

Deuterium labelling experiments are used to infer the kinetic properties of cell populations *in vivo*. A population that is at steady state does not gain labelled DNA at a faster rate than the rate at which the labelled DNA is lost, regardless of whether the population is homogeneous or heterogeneous. However, recently obtained datasets show that some populations can gain labelled DNA faster than they lose it, which does not have any mechanistic explanation yet. We studied various mathematical models to search for mechanisms that can account for such unexpected labelling data. For a population at steady state, either temporal heterogeneity (i.e., cells become longer-lived upon division), or a continued source of labelled precursor cells can theoretically generate labelling curves with a faster gain of label compared to the rate of loss. However, the effect size (i.e., the difference between the gain and loss rates) is so small that these models fall short in describing our experimental data satisfactorily. We show that prolonged label availability, and cell populations that are increasing in size, can explain our labelling data in a quantitative manner. We subsequently experimentally addressed and confirmed both mechanisms *in vitro*.

Introduction

The use of deuterium to label cellular DNA started in the 1990s (Hellerstein and Neese, 1992). Administered either in the form of heavy (deuterated) water or deuterated glucose, deuterium provides a non-toxic way to study multiple aspects of immune cell behaviour *in vivo*, by following the kinetics of its incorporation in and loss from cellular DNA (Borghans et al., 2018; Macallan et al., 2019). Deuterium labelling has been used to quantify cell population dynamics both under normal (homeostatic) conditions and upon perturbations (Ahmed et al., 2015; Baliu-Piqué et al., 2021; den Braber et al., 2012; Patel et al., 2017). An example is the key discovery of increased rates of T-cell loss under duress from HIV, and the ability of anti-retroviral therapy to normalise this increased turnover (Hellerstein et al., 1999; Mohri et al., 2001).

Accurate estimation of the rates of cellular processes is essential for understanding how normal physiological conditions are maintained (Ahmed et al., 2020; Baliu-Piqué et al., 2018). Determination of homeostatic loss rates of T cells promises a better understanding of the mechanisms involved in the maintenance of immune memory (Baliu-Piqué et al., 2021, 2018; den Braber et al., 2012; Vrisekoop et al., 2008), which could aid the design of vaccines and inform us on how to deal with undesirable immune responses that result in chronic inflammation. Therefore, several studies have tried to characterize labelling curves in terms of their gain and loss rates, to better understand the mechanisms through which populations are maintained (Ahmed et al., 2020; Asquith et al., 2002; Baliu-Piqué et al., 2022; De Boer et al., 2012; Ganusov et al., 2010; van Grinsven, 2019; Vrisekoop et al., 2008).

In a population that is at equilibrium, the number of new cells produced in any given time interval, expressed as a fraction of the total population (i.e., the *per capita* production), equals the fraction of the population that is removed. Mathematical models developed for interpreting deuterium labelling experiments exploit this steady state assumption because labelling is typically done in populations that are thought to be at steady state. Asquith and colleagues devised a phenomenological mathematical model with parameters for the *per capita* production rate of the population, p , and the *per capita* loss rate of the labelled population, d^* (Asquith et al., 2002). They pointed out that although production and loss rates are expected to be equal in a population that is at steady state, labelling curves often yield $p < d^*$. The authors reasoned that such a behaviour is in fact expected for a kinetically heterogeneous population. Finite-term labelling results in a labelled population that is skewed towards the more rapidly dividing cell subset(s) (Asquith et al., 2002). Thus, the loss rate of the labelled population is, on average, higher than the loss rate of the total (labelled + unlabelled) population (Asquith et al., 2002). Later, more mechanistic models exploring this idea confirmed that a heterogeneous population at steady state would indeed yield estimates where $p < d^*$ (De Boer et al., 2012; Ganusov et al., 2010).

Several explanations of $p < d^*$ and $p = d^*$ labelling curves have been detailed before (Asquith et al., 2002; De Boer et al., 2012; Ganusov et al., 2010). Datasets of labelling curves with $p > d^*$ behaviour have also been observed but have not been described mechanistically. For example, labelling of MCMV-tetramer⁺ memory T cells in MCMV-infected mice (Baliu-

Piqué et al., 2022) and of neutrophil precursors (promyelocytes) in healthy humans (van Grinsven, 2019) resulted in labelling curves with $p > d^*$ behaviour. The $p > d^*$ labelling behaviour would be incompatible with a cell population consisting of a sub-population of slow cells and a sub-population of rapid cells, as it would suggest that the labelled population got enriched in cells undergoing slow turnover. In other words, it suggests that cells become quiescent (or longer-lived) upon division. Therefore, the emergence of datasets with $p > d^*$ behaviour has exposed a major gap in our understanding and interpretation of deuterium labelling curves.

In this article, we look for models that can mechanistically explain labelling curves with a gain rate that is higher than the loss rate. We begin by re-introducing the phenomenological model proposed by Asquith et al. (Asquith et al., 2002), and the datasets in which the accrual of label is faster than its loss, to precisely define what we mean by gain and loss. We then develop an analytical approach to determine the relationship between the labelling and de-labelling rates that can be applied to all models. We show that even though some models can qualitatively show the desired $p > d^*$ behaviour, they nevertheless fail to quantitatively explain the data at hand. Finally, we present two models that resolve this issue and successfully describe the data quantitatively. The first model allows for prolonged availability of label in short-term labelling studies, and the second model relaxes the steady state assumption. We provide experimental evidence for both mechanisms.

Models and Results

A basic and a phenomenological model of labelling dynamics (the pd^* model)

For a basic mechanistic model, consider a homogeneous population that is at steady state, \bar{N} , has a source of s cells/day, divides at *per capita* rate p /day and is lost at *per capita* rate d /day (**equation 2.1a**). The dynamics of the cell numbers, $N(t)$, the number, $L(t)$, and the fraction, $l(t) = \frac{L(t)}{N}$, of labelled DNA in the population is then given by (De Boer and Perelson, 2013a):

$$\frac{dN}{dt} = s + (p - d)N \quad (2.1a)$$

$$\frac{dL}{dt} = scD(t) + pcD(t)\bar{N} - dL \quad (2.1b)$$

$$\frac{dl}{dt} = d(cD(t) - l) \quad (2.1c)$$

where

$$\bar{N} = \frac{s}{(d - p)} \quad (2.1d)$$

Here $D(t)$ is the level of deuterated water or glucose in plasma (or urine), and c is the intracellular amplification or dilution factor (Ahmed et al., 2015). Note that, in this classic model, the label in the cells from the source is proportional to the deuterium concentration in plasma or urine ($D(t)$).

The labelling curve of such a population has the same gain and loss rates, d (**equation 2.1c**). To explain labelling curves where the gain rate is lower than the loss rate, the more phenomenological ‘ pd^* ’ model, which is used to model implicit kinetic heterogeneity in a population, was proposed (Asquith et al., 2002):

$$\frac{dl}{dt} = pcD(t) - d^*l \quad (2.2)$$

where p and d^* were defined as the average *per capita* production rate of the total population, and the average *per capita* loss rate of the labelled population, respectively. The difference between the estimates of p and d^* depends on the length of the labelling period (Asquith et al., 2002), as the labelled population will be enriched in cells with the faster *per capita* turnover rate after a short labelling period, implying that $d^* > p$. This averages out after a long period of labelling, i.e., over time $d^* \rightarrow p$, meaning that the fraction of labelled DNA will approach the expected asymptote ($l(t \rightarrow \infty) = \frac{pcf}{d^*} = cf$; see **equation 2.2**, where $D(t \rightarrow \infty) = f$ defines the plateau of body water/glucose enrichment).

Two datasets showing $p > d^*$ behaviour

As the pd^* model has only two parameters, it is routinely used to find an (initial) estimate for the label gain and loss rates. In recent years, a few datasets have surfaced with labelling curves that suggest $p > d^*$. In this section, we discuss the experimental design behind two of these datasets and report the estimates of p and d^* obtained for them.

Promyelocyte data

An example of $p > d^*$ behaviour can be seen in the labelling of promyelocytes in human bone marrow where p was estimated to be 86% higher than that of d^* (**Figure 2.1a**). Promyelocytes make up the earliest fully committed precursor of granulocytes and were measured as part of a short-term deuterium labelling study (with a 5.5 hour labelling period) of neutrophil differentiation in the bone marrow (van Grinsven, 2019) (see **SI** for details on experimental design and plasma enrichment).

The labelling behaviour of the promyelocytes is quite surprising. With an estimated $p = 0.26/\text{day}$, about 6% of the promyelocyte population is labelled after 5.5 hours of label administration (**Figure 2.1a**). This would indicate that the population is expected to approach its labelling asymptote (100%) in about 4 days, while the de-labelling curve with an

exponential loss rate of $d^* = 0.14/\text{day}$ indicates that the mean expected residence time of the population is about one week (**Table 2.1**). These estimates seem to suggest that either there are other mechanisms at play, or the population is not at steady state, which we regard highly unlikely since the experiment was performed under homeostatic conditions. Unfortunately, the peak of the labelling curve in this short deuterated glucose study had to be inferred (because the first data point is at day 1, which is 18 hours after the end of the labelling period). The same is true for other deuterated glucose studies, however, $p > d^*$ labelling behaviour has not been seen in any of the previous deuterated glucose studies.

MCMV-specific memory T-cell data

Murine cytomegalovirus (MCMV) is a persistent, chronic infection that is characterized by a phenomenon called memory inflation due to the accumulation of large numbers of virus specific CD8^+ memory T cells. Mice were given deuterated water for 28 days, beginning from 120 days post-infection, to study the kinetics of MCMV-specific CD8^+ T-cell responses during the memory phase of MCMV infection. ((Baliu-Piqué et al., 2022), see **SI** for details on experimental design and plasma enrichment). The labelling data of tetramer⁺ (MCMV-specific) memory T-cells generated in three different MCMV infections also showed $p > d^*$ behaviour (**Figures 2.1b-d**). The estimates of p were as much as 58% higher than those of d^* (**Table 2.1**), indicating that even after a long labelling period (4 weeks), the rate of gain of labelled DNA was much faster than the rate of loss.

		pd^*		$p = d^*$
		p (/day)	d^* (/day)	
Promyelocytes		0.26 (0.22-0.32)	0.14 (0.11-0.19)	0.27 (0.22-0.32)
Tetramer + MCMV- specific T cells	ie2SL	0.017 (0.015-0.018)	0.011 (0.01-0.012)	0.018 (0.016-0.019)
	ie2KNL	0.019 (0.017-0.022)	0.012 (0.01-0.015)	0.021 (0.018-0.024)
	m45SL	0.016 (0.014-0.018)	0.013 (0.011-0.015)	0.017 (0.015-0.019)

Table 2.1: Parameters for the best fits shown in **Figure 2.1**. The 95% confidence intervals were determined by bootstrapping the data 500 times and are reported in the parentheses.

In all cases, the data is well described by a single exponential, with an asymptote predicted to be higher than the maximum possible labelling level in a population (i.e., $p > d^*$). Although the pd^* model provides a good description of the data, the p and d^* estimates lose their mechanistic interpretation as they should vary with the length of the labelling period (i.e., ultimately $p \approx d^*$). What these data tell us is that the gain and loss rates of label are in fact not simply the proliferation and loss rates of a cell population. Therefore, moving forward, we use the pd^* model as the standard model to compare different models, but refrain from assigning any mechanistic meaning to the parameters. To make this distinction clear, we use * to denote phenomenological parameters. Henceforth, we refer to the pd^* model (Asquith et

al., 2002) as the p^*d^* model. To understand how to interpret datasets with $p^* > d^*$ labelling behaviour, we now look for mechanistic models that can explain such labelling curves.

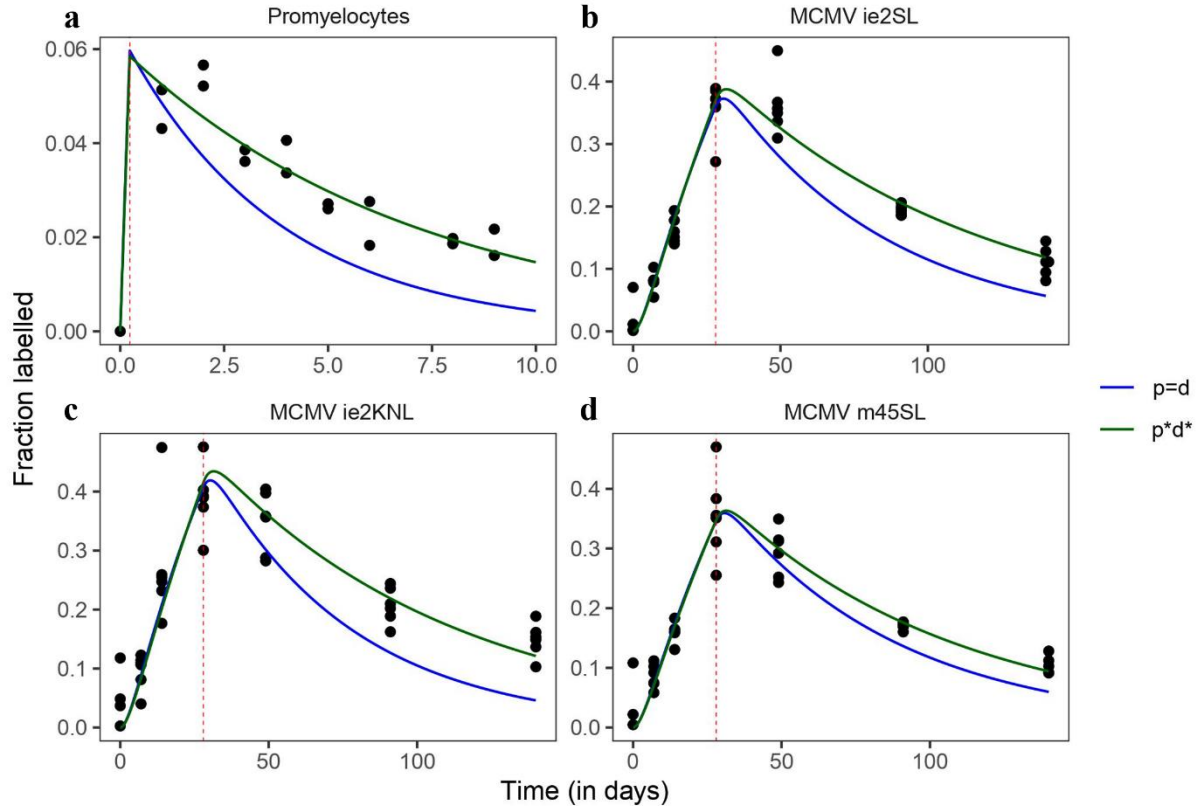


Figure 2.1: The best fits of the phenomenological pd^* model (green line, **equation 2.2**) and the homogeneous model (referred to as $p = d$) (blue line, **equation 2.1c**) to (a) the promyelocyte data and (b-d) tetramer⁺ MCMV-specific memory T-cell data for the three different viruses (ie2SL (b), ie2KNL (c), and m45SL (d)). The vertical red dashed line marks the stop of label administration.

Heterogeneity

Several mechanistic models have been proposed to describe the heterogeneity in a population of interest (POI). One is kinetic heterogeneity (KH, **Figure 2.2a**), where the POI is made up of multiple sub-populations with different kinetics (De Boer et al., 2012; Ganusov et al., 2010). Another is temporal heterogeneity (TH, **Figure 2.2b**) where the POI is a population in which quiescent and recently divided cells are lost at different rates (De Boer et al., 2012; Ribeiro et al., 2002). We first test whether these two mechanisms can account for $p^* > d^*$ behaviour.

KH cannot deliver $p^* > d^*$ labelling behaviour

Previous studies have shown that KH in a population can explain labelling data with $p^* < d^*$ behaviour (De Boer et al., 2012; Ganusov et al., 2010). This is in line with the intuition that in a finite-term labelling experiment, the labelled population gets enriched in cells with faster

turnover (Asquith et al., 2002). Here we introduce a mathematical framework to find out whether a model can generate labelling curves where $p^* > d^*$. We use this analytical approach to prove that the KH model cannot generate labelling curves with $p^* > d^*$.

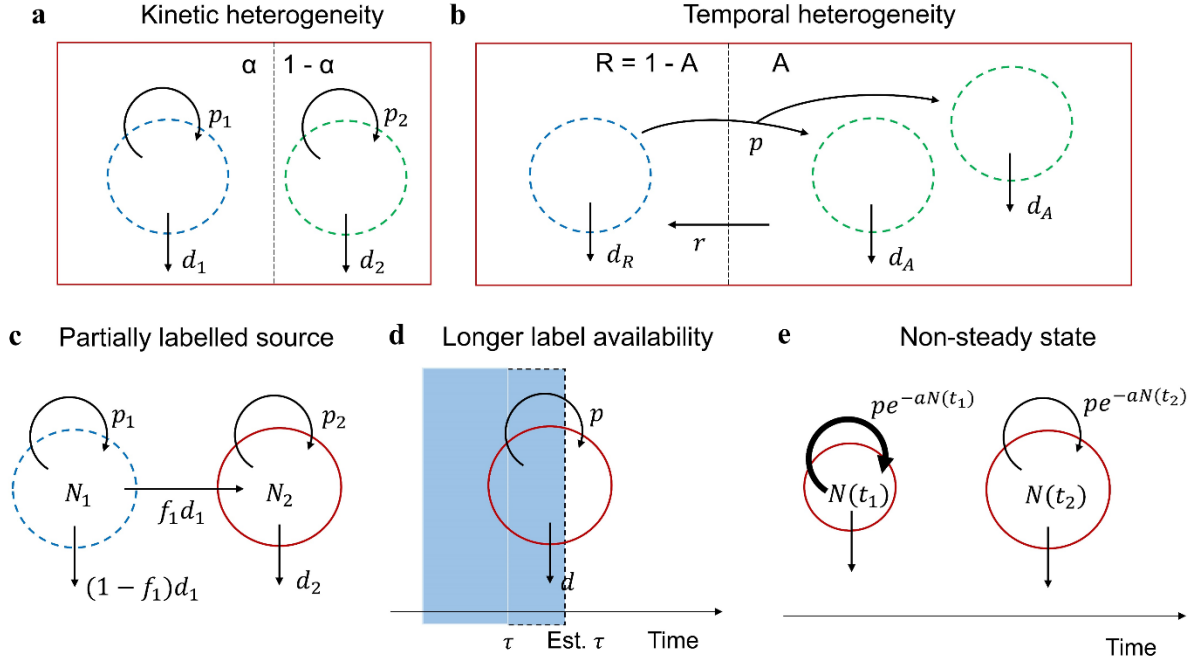


Figure 2.2: Model cartoons of the (a) KH, (b) TH, (c) Explicit source, (d) Longer label availability, and (e) Non-steady state models.

Consider a population that is at steady state and can be divided into multiple kinetically distinct homogeneous sub-populations (**Figure 2.2a**). The fraction of labelled DNA within each sub-population i , l_i , is given by (Ganusov et al., 2010):

$$\frac{dl_i}{dt} = d_i(cD(t) - l_i) \quad (2.3)$$

where, d_i is the *per capita* loss rate of sub-population i . To simplify, consider the fraction of labelled DNA within a population that has two sub-populations, each occupying α and $(1 - \alpha)$ fractions of the population, respectively (**Figure 2.2a**). The fraction of labelled DNA in that population can be written as:

$$\frac{dl}{dt} = \alpha \frac{dl_1}{dt} + (1 - \alpha) \frac{dl_2}{dt} = (\alpha d_1 + (1 - \alpha) d_2) cD(t) - (\alpha d_1 l_1 + (1 - \alpha) d_2 l_2) \quad (2.4)$$

Since the single exponential $p^* d^*$ model gives a good description of both the datasets (**Figure 2.1**), we re-write the multi-exponential KH model in the form of the $p^* d^*$ model,

with the parameter p^* as a coefficient of the deuterium term, $cD(t)$, and a time-dependent “parameter” $d^*(t)$ replacing the time-independent d^* . Thus, **equation 2.4** becomes:

$$\frac{dl}{dt} = p^*cD(t) - d^*(t)l$$

with,

$$p^* = \alpha d_1 + (1 - \alpha)d_2 \quad (2.5)$$

$$d^*(t) = \beta(t)d_1 + (1 - \beta(t))d_2$$

where, $\beta(t) = \frac{\alpha l_1(t)}{\alpha l_1(t) + (1 - \alpha)l_2(t)}$ is the fraction that the labelled DNA of the first sub-population occupies in the total labelled population at any time t .

Without loss of generality, suppose that the first sub-population has the slower loss rate i.e., $d_1 < d_2$. Defining $\rho(t)$ as the ratio of the fractions of labelled cells in the first and the second population, $\rho(t) = \frac{l_1(t)}{l_2(t)}$, we obtain that $\rho(t) < 1$ during the labelling phase (and shortly thereafter). Using this it can be shown that $\beta(t) < \alpha$ during the entire labelling phase because $\beta(t)$ increases monotonically with $\rho(t)$,

$$\beta(t) = \frac{\alpha\rho(t)}{\alpha\rho(t) + (1 - \alpha)} < \alpha \quad (2.6)$$

The de-labelling phase can be divided into two phases by the timepoint, t_{crit} , at which the fraction labelled DNA within both sub-populations becomes equal i.e., $\rho(t) = 1$, so that i) $\rho(t) < 1$, when $t < t_{crit}$, and ii) $\rho(t) > 1$, when $t > t_{crit}$.

By comparing p^* and $d^*(t)$, we can find the condition when $p^* > d^*(t)$ if $t < t_{crit}$:

$$d^*(t) - p^* = (\beta(t) - \alpha)(d_1 - d_2) < 0, \forall t < t_{crit} \quad (2.7)$$

As $d_1 < d_2$ and $\beta(t) < \alpha$, the KH model fails to satisfy **equation 2.7**. Numerical non-linear parameter estimation confirmed our analytical result that the KH model cannot explain the promyelocyte and the MCMV datasets (**Figure 2.3, Table 2.2**). Therefore, KH cannot explain the $p^* > d^*$ datasets considered in this article.

Equation 2.7 is valid when $t < t_{crit}$. As the peak of the labelling curve is attained before t_{crit} , this time range ($t \in [0, t_{crit}]$) provides information on both p^* and d^* (**equation 2.2**). Therefore, **equation 2.7** is also valid for $t > t_{crit}$, and provides a necessary and sufficient condition for a model to show $p^* > d^*$ behaviour.

An exception to the above analysis would be a dataset that is skewed in measurements towards the late time points, and therefore fails to have a well-defined peak. In such cases, the KH model can generate labelling curves with $p^* > d^*$ as the estimate of d^* would be heavily influenced by a long tail (**Figure S2.1**). Labelling datasets that have multi-exponential slopes, or are markedly skewed in their sampling times, are not considered further because these cases do not correspond to the datasets that we are trying to explain.

	Promyelocytes	Total tetramer ⁺ memory		
		ie2SL	ie2KNL	m45SL
d_1	0.27 (0-0.31)	0.017 (0.015-0.019)	0.021 (0.016-0.022)	0.017 (0.0013-0.0189)
d_2	1 (0.23-5.55)	4.01 (0.018-7.28)	5.65 (0.03-9.99)	1.08 (0.016-9.43)
α	1 (0-1)	1 (0-1)	1 (0.91-1)	1 (0-1)
d	0.27 (0.21-0.31)	0.017 (0.016-0.019)	0.021 (0.018-0.24)	0.017 (0.015-0.12)

Table 2.2: The estimates for the best fits with the KH model as shown in **Figure 2.3**. The turnover rate of the entire population, d , is defined as $\alpha d_1 + (1 - \alpha)d_2$. Note the narrow confidence range of d despite the large confidence ranges of α and d_2 .

Temporal heterogeneity is insufficient to explain the relatively slow loss of label in our data

Several studies have alluded to the possibility that activation of cells transiently changes their division and loss rates (De Boer et al., 2012; Ribeiro et al., 2002). Originally, TH was defined to model an increase in the loss rate of cells upon division. It was shown that this model, like the KH model, can account for the typical $p^* < d^*$ behaviour (De Boer et al., 2012). In contrast, $p^* > d^*$ should be achieved if cells transiently lower their loss rates following a division event. This would be in line with the intuition that for $p^* > d^*$ behaviour, the labelled population should be enriched with cells that are lost more slowly than the population average.

Consider a population, N , that can be split into a resting, R , and an activated, A , sub-population (**Figure 2.2b**). When a resting cell divides, it makes 2 activated cells at a rate p /day, while an activated cell reverts to the resting state at a rate r /day, i.e.,

$$\frac{dR}{dt} = rA - (p + d_R)R \quad (2.8)$$

$$\frac{dA}{dt} = 2pR - (r + d_A)A$$

where, d_i , $i \in \{R, A\}$ denote the *per capita* loss rates of the sub-populations. We only consider the case where cells lower their loss rates upon division i.e., $d_A < d_R$.

One parameter of the model can be removed by assuming both populations are at steady state. Solving for the division rate, we obtain $p = d_R \frac{(r+d_A)}{(r-d_A)}$, which reveals that $r > d_A$, i.e., the population is maintained if at least half of the daughter cells survive to revert to the resting state. Scaling the steady-state population size to unity i.e., $\bar{N} = 1$, we find:

$$\bar{R} = \frac{r - d_A}{r - d_A + 2d_R} \quad (2.9)$$

$$\bar{A} = \frac{2d_R}{r - d_A + 2d_R}$$

Note that the above model describes a heterogeneous population only if $d_R > 0$. The kinetics of the fraction of labelled DNA within the resting and activated populations, and within the population as a whole, are given by:

$$\frac{dl_R}{dt} = \frac{2rd_R}{(r - d_A)}(l_A - l_R)$$

$$\frac{dl_A}{dt} = \frac{(d_A + r)}{2}(cD(t) + l_R - 2l_A) \quad (2.10)$$

$$\frac{dl}{dt} = \bar{R}l_R + \bar{A}l_A = p\bar{R}cD(t) - d_R\bar{R}l_R - d_A\bar{A}l_A$$

where $p = d_R \frac{(r+d_A)}{(r-d_A)}$, leaving the TH model with three free parameters: r , d_R and d_A .

Remarkably, the TH model fails to explain the high enrichment at late timepoints seen in the promyelocyte and the MCMV datasets (**Figure 2.3**). For MCMV^{ie2KNL}, the TH model (like the KH model) preferred a solution in which the population is near-homogeneous (**Table 2.3**). In this case, the activated population had a higher turnover rate compared to the resting population. In contrast, for the other cases, the TH model preferred a solution where the population has equal proportions of activated and resting cells. In line with our intuition, the best estimate, in these cases, preferred a slower loss rate of the activated sub-population (**Table 2.3**). Thus, even a scenario where a population becomes more quiescent upon division is inadequate to explain the steep gain and slow loss of label observed in these datasets.

Puzzled that we could not explain the data even with the necessary constraint on the loss rates of the sub-populations ($d_A < d_R$), we looked for mathematical explanations. As we did for the KH model, we derived the sufficient and necessary condition for the TH model to generate labelling curves with $p^* > d^*$ behaviour (**Text S2.1**):

$$d^*(t) - p^* = (\beta(t) - \bar{R})(d_R - d_A) < 0, \text{ if } t < t_{crit}$$

$$\Rightarrow \begin{cases} d^* < p^*, & d_R > d_A \\ d^* \geq p^*, & d_R \leq d_A \end{cases} \quad (2.11)$$

As expected, in a version of TH in which cells are lost at a lower rate following division, labelling curves will exhibit $p^* > d^*$ behaviour (Text S2.1, equation 2.11, Table 2.3, Figure 2.3).

	Promyelocytes	Total tetramer ⁺ memory		
		ie2SL	ie2KNL	m45SL
d_A	0 (0-0)	0 (0-0)	0.365 (0-3.81)	0.00061 (0-5.38)
d_R	0.47 (0.37-0.55)	0.032 (0.028-0.034)	0.002 (0.0002-0.038)	0.03 (0.0001-0.033)
r	0.93 (0.75-1.10)	0.064 (0.059-0.07)	0.406 (0.068-5.47)	0.061 (0.053-7.64)
\bar{R}	0.5	0.5	0.91	0.5
\bar{A}	0.5	0.5	0.09	0.5
d	0.24 (0.18-0.27)	0.016 (0.015-0.017)	0.035 (0.017-0.041)	0.015 (0.014-0.034)
p	0.47 (0.37-0.55)	0.032 (0.028-0.034)	0.038 (0.023-0.047)	0.031 (0.02-0.036)

Table 2.3: The estimates for the best fits using the TH model as shown in Figure 2.3. The turnover rate of the entire population, d , is defined as $\bar{A}d_A + \bar{R}d_R$. Note the narrow confidence range of d despite the large confidence ranges of r and d_A . The division rate, p , is calculated as $d_R \frac{(r+d_A)}{(r-d_A)}$.

The difference between p^* and d^* depends on both the distribution of the sub-populations in the labelled population and the loss rates of the sub-populations (equation 2.11). Interestingly, for the TH model this difference is always very small compared to that between the estimates of the p^*d^* model (Figure 2.1). To understand this, consider an extreme case by setting $d_A = 0$. Although the difference between p^* and d^* seems to increase when the loss rate of the resting cells, d_R , increases (equation 2.11), the difference between p^* and d^* , in fact, decreases, because the activated sub-population, \bar{A} , starts dominating in size (as $\bar{R} \rightarrow 0$ and $\beta \rightarrow 0$, see equation S2.4), making the population nearly homogeneous (equation 2.9). The rates of both sub-populations determine their relative sizes (equation 2.9). This co-dependency of the sub-populations sets a limit on the extent of the $p^* > d^*$ behaviour. Therefore, even though labelling curves with $p^* > d^*$ behaviour can be described to some extent with the TH model, the model fails to properly describe the presented datasets (Figure 2.3).

A labelled source fails to generate sufficiently large $p^* > d^*$ behaviour

The slow loss of labelled DNA seen in the POI could be due to a trickle of labelled cells from a source, even after the end of the labelling period. In this section, we analyse a homogeneous population that has a source. As the labelling dynamics of the POI is not affected by the source in an implicit source model (equation 2.1, Chapter 3), here we explicitly consider the

dynamics of the precursor population along with that of the POI (referred to as the explicit source model).

Consider a POI, N_2 , that can proliferate (at *per capita* p_2 /day), can be lost (at *per capita* d_2 /day) and is supplemented from a precursor population, N_1 , that proliferates at *per capita* rate p_1 /day, is lost at *per capita* rate d_1 /day, of which a fraction, f_1 , is due to differentiation into the POI, N_2 (**Figure 2.2c**). If this differentiation step is not accompanied by cell division, the dynamics of these populations are given by:

$$\begin{aligned}\frac{dN_1}{dt} &= (p_1 - d_1)N_1 \\ \frac{dN_2}{dt} &= f_1 d_1 N_1 + (p_2 - d_2)N_2\end{aligned}\tag{2.12}$$

Scaling N_1 to 1 at steady state, we find:

$$\begin{aligned}\bar{N}_1 &= 1 \Rightarrow p_1 = d_1 \\ \bar{N}_2 &= \frac{f_1 d_1 \bar{N}_1}{d_2 - p_2}\end{aligned}\tag{2.13}$$

where $p_2 < d_2$. Using the above, the change in the fraction of labelled DNA can be calculated as:

$$\frac{dl_1}{dt} = d_1(cD(t) - l_1)\tag{2.14a}$$

$$\frac{dl_2}{dt} = p_2(cD(t) - l_1) + d_2(l_1 - l_2)\tag{2.14b}$$

Note that if the loss rate of the precursor population, d_1 , is comparable to or faster than the turnover rate of glucose/water (denoted as δ), the labelling equation of the POI (**equation 2.14b**) will approach that of a homogeneous population (as $l_1(t) \approx cD(t)$; see **equation 2.1b**). Therefore, we require $d_1 \ll \delta$ to study the effect of a precursor population on the POI's dynamics.

It has been postulated that naive T cells and/or stem-like memory T cells can act as precursors of the memory T-cell population (Hogan et al., 2019; Weitering et al., 2021; Welten et al., 2020). As both naive T cells (Vrisekoop et al., 2008) and stem-like memory T cells (del Amo et al., 2018) turnover at a rate that is much slower than that of water, these populations could influence the dynamics of the MCMV-specific memory T cell population.

The turnover rate of hematopoietic stem cells (HSCs), the precursor of promyelocytes, is un-

known. If HSCs are relatively faster than promyelocytes, that turnover rapidly (**Figure 2.1a**), the explicit source model would not help explain the data (as $d_1 \approx \delta$). However, if the turnover rate of HSCs (or any other intermediary population) would be relatively low, they could influence the dynamics of the promyelocytes.

The three free parameters (d_1 , p_2 , and d_2) of the model (**equation 2.14**) were estimated by fitting the model to the two datasets on MCMV-specific memory cells and promyelocytes. The explicit source model also failed to explain the observed gain and loss of label together (**Figure 2.3**). In most cases, the loss of label slowed down initially (around the peak) compared to the previous models, however, the flux of labelled DNA from the precursors was not enough to sustain this slow loss.

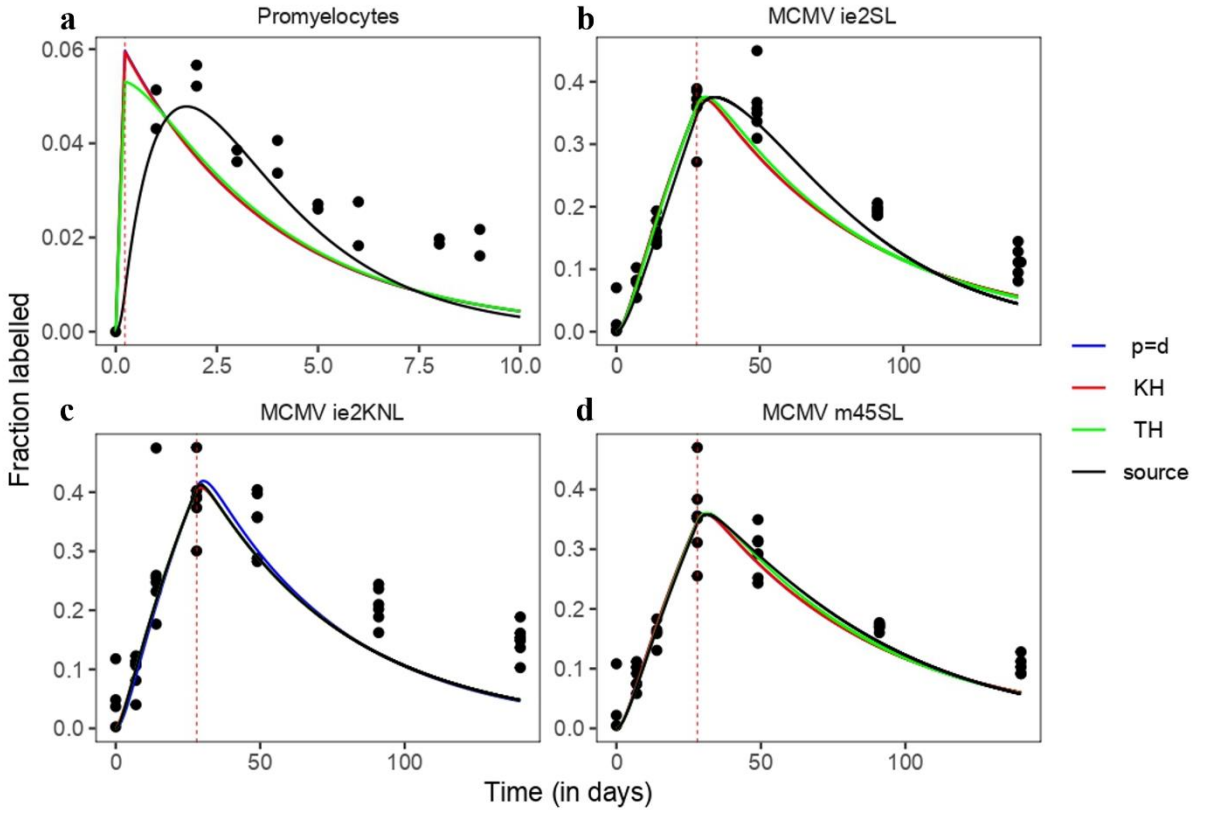


Figure 2.3: The best fits of the KH, TH, and explicit source models to **(a)** the promyelocyte data, and **(b-d)** the MCMV data for the three different viruses: **(b)** ie2SL, **(c)** ie2KNL, **(d)** m45SL. The best fits of the homogeneous model (referred to as the $p = d$ model) is shown for comparison (blue line). The vertical red dashed line marks the stop of label administration.

The sufficient and necessary condition for this model to show $p^* > d^*$ labelling behaviour yielded a simple relationship (**Text S2.2**):

$$d^*(t) - p^* = (d_2 - p_2) \left(1 - \frac{l_1(t)}{l_2(t)}\right) < 0, \text{ if } t < t_{crit} \quad (2.15)$$

$$\therefore d_1 > p_2 \Rightarrow p^* > d^*$$

i.e., only if the precursor has a higher fraction of labelled DNA than the POI ($l_1(t) > l_2(t)$), then the fraction labelled within the POI will increase, even after the stop of label administration, until the enrichment in the precursors matches that in the POI, leading to a slower loss of label relative to its gain. Interestingly, the labelled fraction in the precursor population will be higher than that in the POI if the turnover rate of the precursor is higher than the proliferation rate of the POI i.e., if $d_1 > p_2$. The estimates of the best fits confirm this relationship (**Table 2.4**). As the condition for observing the $p^* > d^*$ labelling behaviour is dependent only on the rates of the POI and its immediate precursor (**equation 2.15**), adding an explicit source to the precursor of the POI does not explain the data any better (fits not shown).

The enrichment in the POI reaches its peak at t_{crit} . The extra labelling period, $t_{crit} - \tau$, is determined by the loss rates of both the POI and the precursor. As the loss rates determine both the enrichment in the POI as well as the length of the extra labelling period, it sets a quantitative limit on the capacity of the explicit source model to explain the large difference between the p^* and d^* that were estimated from the data. In conclusion, although an explicit source model can yield $p^* > d^*$ labelling behaviour, the effect is too small to explain the labelling data of promyelocytes and MCMV-specific T cells in a satisfactory manner.

		d_1 (/day)	d_2 (/day)	p_2 (/day)
Promyelocytes		0.89 (0.37-1.54)	0.4 (0.30-1.01)	0 (0-0.06)
MCMV-specific T cells	ie2SL	0.03 (0.02-0.04)	0.03 (0.03-0.04)	0.01 (0.009-0.015)
	ie2KNL	0.02 (0.016-0.6)	0.80 (0.022-3)	0.035 (0.013-0.11)
	m45SL	0.025 (0.015-0.679)	0.025 (0.016-3)	0.015 (0.012-0.056)

Table 2.4: The estimates of the best fits found with the explicit source model as shown in **Figure 2.3**. Note that the best fit for the ie2KNL epitope does not satisfy the necessary condition to show $p^* > d^*$ behaviour.

Prolonged label availability yields $p^* > d^*$ behaviour

The washout rate of glucose in plasma might fail to convey the true deuterium availability period for cells. For example, if the newly formed promyelocytes in the bone marrow, which is a prime location for cell apoptosis (Tofts et al., 2011), can access labelled adenosine molecules through the nucleotide salvage pathway (Austin et al., 2012), after the loss of labelled cells, then the promyelocytes may continue to gain deuterated DNA after the end of the labelling period. The effective deuterium availability for cells in the bone marrow may, therefore, differ from that measured in plasma, $D(t)$.

As the first data point is only at day one, the time at which the peak of labelling was achieved might not have been at 5.5 hours. If the peak of labelling was truly achieved at a later time point, forcing the labelling period to be 5.5 hours would return an estimate of p^* that is higher

than its “true” value, to be able to explain the high enrichment observed on day 1. As the loss rate of label, d^* , which is estimated from the de-labelling phase of the labelling curve would remain unaffected, it would give rise to $p^* > d^*$ labelling behaviour. We, hence, sought to estimate the effective label availability duration, instead of forcing it to be 5.5 hours, and considered the promyelocytes to be kinetically homogeneous (**equation 2.1c, Figure 2.2d**). If the promyelocytes were homogeneous, the best fit to the promyelocyte labelling data was obtained for an estimated 10 hours of label availability and the fit was identical (in terms of the sum squared residual) to the best fit found with the p^*d^* model (where the label was available for 5.5 hours, **Figure 2.4**). Therefore, a homogeneous promyelocyte population that renews itself in about a week is perfectly compatible with the experimental data if deuterium would remain available to the cells for 10 rather than for 5.5 hours.

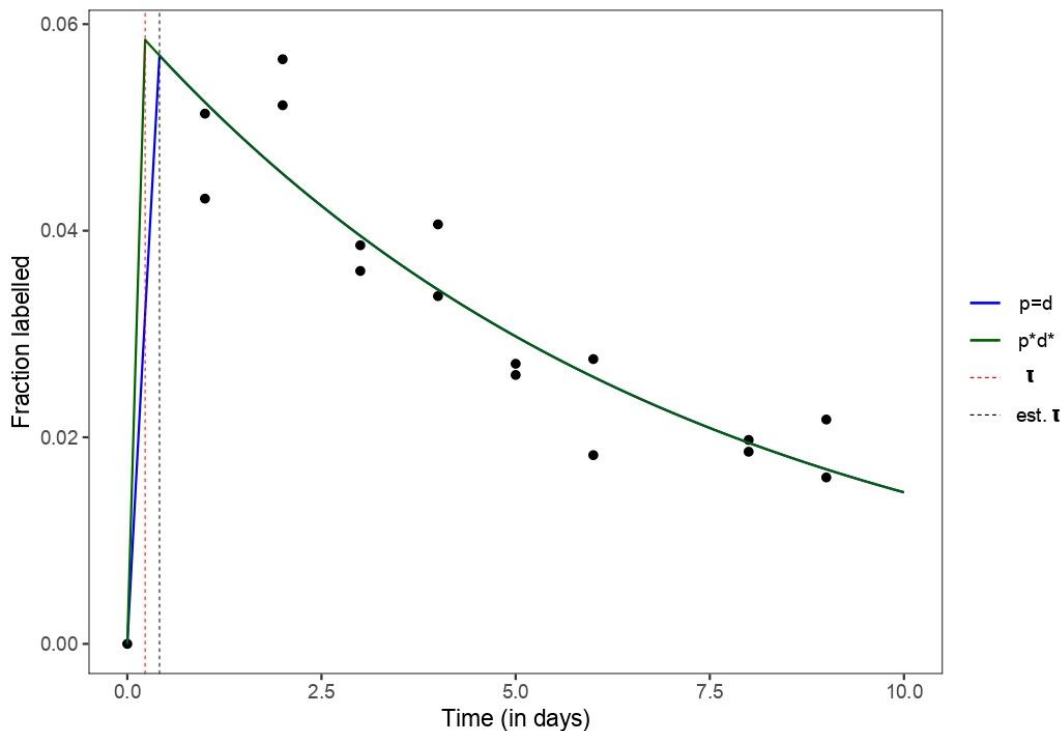


Figure 2.4: The best fits of the phenomenological p^*d^* and the $p = d$ (homogeneous POI) models to the promyelocyte data: for the phenomenological model, τ was fixed to 5.5 hours (red line), and for the homogeneous POI model, τ was free to be estimated (blue line). The estimates of the best fit were: $d = 0.14/\text{day}$ [0.11,0.19] and $\tau = 9.95$ hours [8.91,11.49]. The 95% confidence intervals are reported in square brackets.

To test the hypothesis that deuterated glucose is available for longer than the period over which it is administered, we performed *in vitro* experiments with two cell lines (see **SI** for details on the study design). The mono mac 6 cells, a monocytic cell line derived from peripheral human blood (Ziegler-Heitbroc et al., 1988), showed a notable increase in its deuterium enrichment after the stop of labelling (at 12 hours) for at least an additional 8 hours (**Figure 2.5a**). Further, the HL-60 cell line, which resembles the promyelocytes (Birnie,

1988), also showed significant deuterium uptake after the stop of labelling (**Figure 2.5d**, where hour 0 is the start of labelling and hour 6 is the stop of labelling).

The *in vitro* experiments clearly showed that deuterium was being incorporated into the cells for several hours after the cessation of label. Since the medium did not contain any deuterium during the de-labelling phase, the additional/delayed deuterium source can only be intracellular. We hypothesized that the uptake of deuterated glucose and its integration into intra-cellular compounds (like nucleotides) could add rate-limiting steps to the integration of deuterium into the DNA during cell division. We tested this hypothesis with an ‘intra-cellular’ model, tracking the enrichment in the DNA, L , of cells in a population of size N , that are expanding in a medium with a deuterium concentration D , and having an intra-cellular concentration, I (**equation 2.16**).

$$\begin{aligned}\frac{dN}{dt} &= (p - d)N \\ \frac{dI}{dt} &= \delta(D(t) - I) \\ \frac{dL}{dt} &= p(cI - L)\end{aligned}\tag{2.16}$$

Here, p and d are the division and loss rates of the cells, respectively; δ is the turnover rate of the intra-cellular rate-limiting compound; and $c = 0.65$. As no cell death was observed in the *in vitro* experiments, d was set to 0. Note that the fraction of labelled DNA depends on the division rate, p , as the population is expanding, i.e., is not at steady state ((De Boer and Perelson, 2013a), also see the next section).

The fit of the intra-cellular model (**equation 2.16**) to the labelling of the mono mac 6 data (**Figure 2.5a**) shows that an intracellular deuterium pool renewing itself every 3 hours (**Figure 2.5b**; $\delta = 7.62/\text{day}$) suffices to explain the extended labelling period observed in the *in vitro* experiments. Further, the predicted increase in the population size is in line with that observed in the experiments (**Figure 2.5c**). Interestingly, by fitting the HL-60 data we also estimate that these cells continue to accumulate label for several hours after the stop of label administration (**Figure 2.5d-e**). Together these *in vitro* experiments, thus, suggest that a population can continue to accrue label for a few hours after label cessation.

Non-steady state yields $p^* > d^*$ behaviour

It is known that MCMV infection generates T-cell responses that lead to memory inflation (O’Hara et al., 2012; Schober et al., 2020). Even though care was taken to label DNA with deuterium in the late memory phase, i.e., 120 days after infection, this does not guarantee that the tetramer⁺ population had approached steady state. We wondered whether a population that is not in steady state could have $p^* > d^*$ labelling behaviour.

Assuming that tetramer⁺ cells form an inflating population, their proliferation rate may decline over time due to competition for resources (antigen or cytokines), and/or due to an increasing dominance of low-affinity clones (Schober et al., 2020). We studied whether this could explain the observed $p^* > d^*$ labelling behaviour in the MCMV dataset, by describing the proliferation rate as a monotonically decreasing function.

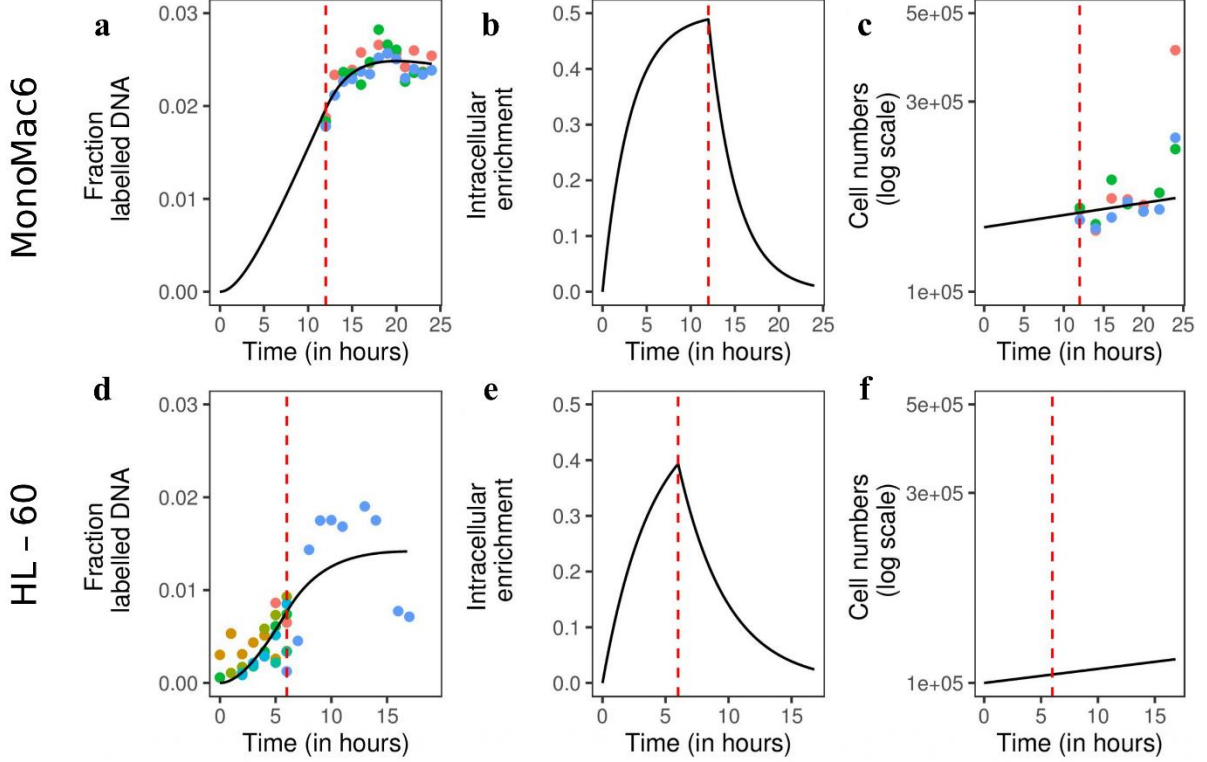


Figure 2.5: *In vitro* labelling experiments showing that the true labelling period is longer than the period of label administration. Lines depict the best fit of the intra-cellular model to the *in vitro* labelling data (a,d), the predicted deuterium enrichment in the intra-cellular compound (b,e), and the predicted increase in cell numbers (overlaid on the *in vitro* expansion of the mono mac 6 cells) (c,f). The predicted cell numbers were normalized such that they matched the mean of the measured cell numbers at the first measured time point (c). The parameters of the best fits with the intra-cellular model (equation 2.16) are: $\delta = 7.62/\text{day}$ [6.53,9.12] and $p = 0.17/\text{day}$ [0.16,0.17] for the mono mac 6 cell line; $\delta = 6.18/\text{day}$ [0.93,12.05] and $p = 0.20/\text{day}$ [0.13,0.90] for the HL-60 cell line. The 95% confidence intervals are reported in square brackets. The vertical red dashed line marks the stop of label. The colours represent different experiments.

Consider a population of MCMV-specific T cells, N , with a maximal per-capita proliferation rate, p_{max}/day and a per-capita loss rate, d/day (Figure 2.2e). If the actual proliferation rate, p , decreases exponentially due to a parameter a scaling the population density, the change in cell numbers for such a population is given by:

$$\frac{dN}{dt} = (p(N) - d)N = (p_{max}e^{-aN} - d)N \quad (2.17)$$

Hence, the change in labelled DNA in the MCMV-specific T-cell pool follows:

$$\frac{dL}{dt} = p_{max}e^{-aN(t)}cD(t)N(t) - dL \quad (2.18)$$

and the change in the fraction of labelled DNA is:

$$\frac{dl}{dt} = \frac{d(L/N)}{dt} = p_{max}e^{-aN(t)}(cD(t) - l) \quad (2.19)$$

which depends on the per-capita proliferation rate only. Therefore, regardless of whether a population is at steady state or not, the rate of change of the fraction of labelled cells is dictated by the per capita production rate, which may decrease when a population expands.

	a	p_{max}	d	r	$N(0)$
ie2SL	4.1e-06 (1.1e-06 - 9.0e-06)	0.08 (0.03 - 0.39)	8.3e-03 (6.4e-04 - 1.1e-02)	4.5e-03 (- 2.8e-03 - 9.4e-03)	3.08e+05 (2.13e+05 - 4.4e+05)
ie2KNL	7.3e-06 (1.5e-06 - 1.9e-05)	0.1 (0.03 - 1.32)	7.2e-03 (0 - 1e-02)	5.5e-03 (- 3.7e-03 - 1.3e-02)	1.67e+05 (8.96e+04 - 2.96e+05)
m45SL	2.5e-05 (1.7e-06 - 4.8e-05)	0.35 (0.02 - 6.93)	1.1e-02 (0- 1.3e-02)	8e-04 (-3.3e- 03 - 4.6e-03)	1.13e+05 (8.57e+04 - 1.45e+05)

Table 2.6: The parameter estimates for the best fits shown in **Figure 2.6**.

During the de-labelling phase ($D(t) = 0$), this simplifies into $\frac{dl}{dt} = -p_{max}e^{-aN(t)}l$, i.e., to $\frac{dl}{dt} = -d^*(t)l$, and during the initial part of the labelling phase this approaches $\frac{dl}{dt} = p^*(t)cD(t)$ where, $p^*(t) = p_{max}e^{-aN(t)}$. Thus, the rate of change of the fraction of labelled cells in the POI is not constant. It follows that a homogeneous population that increases in size over time will generate labelling curves with $p^* > d^*$ behaviour, whereas a homogeneous population that decreases over time will generate labelling curves with $p^* < d^*$ behaviour (**equation 2.19**). Additionally, if the POI had a source, its labelling dynamics would also depend on the fraction of cells that are supplemented by the source (s/N , where s is the number of cells flowing into the POI per day and N is the size of the POI). The POI, in such a case, will also show $p^* > d^*$ labelling behaviour if the POI is expanding.

The labelling data for the three different viruses are well-described by the non-steady state model due to the decreasing proliferation rates (**Figure 2.6**). Although the estimated p_{max} and a differ among the responses to the different viruses (**Table 2.6**), the actual proliferation rate, p , approaches a similar asymptotic value for the three viruses (**Figure 2.6** and **Table 2.6**). The T-cell response to the non-inflationary epitope, m45SL, was estimated to expand

much less by having a loss rate that is about 2-fold higher than that of the responses to the other viruses.

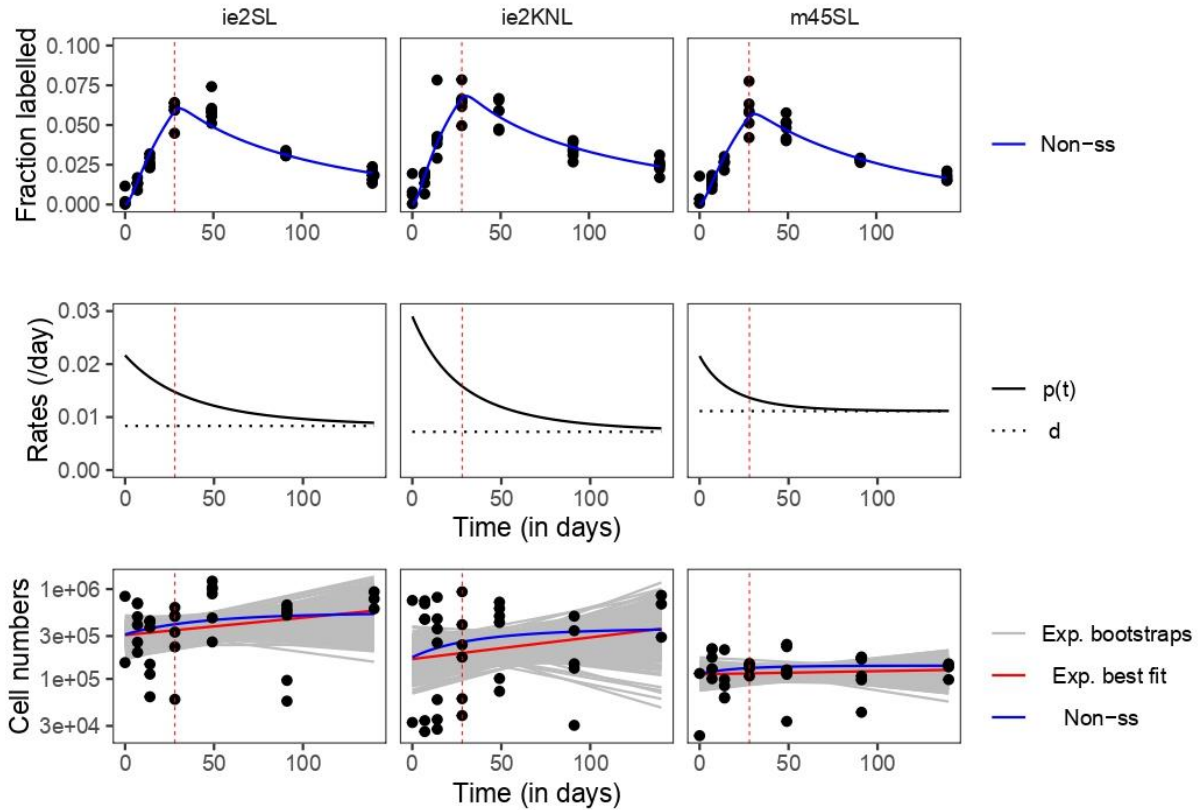


Figure 2.6: The best fits and the predictions of the non-steady state model to the MCMV data for the three different viruses: (left column) ie2SL, (middle column) ie2KNL, (right column) m45SL; the best fits (dark blue) of the non-steady state model to the labelling data (top row), the estimated proliferation, p , and loss, d , rates corresponding to the best fits to the labelling data (middle row), and the predicted change in cell numbers (dark blue) from the non-steady state model overlaid on the best fit (red) and 500 bootstraps (grey) of the exponential model to the measured cell numbers (bottom row). The vertical red dashed line marks the stop of label.

Since it was necessary to have a 1.1 to 2.5 fold expansion in the population to explain the $p^* > d^*$ behaviour of the labelling data, we tested whether there was any evidence of inflation in the MCMV-specific T-cell populations. We fitted a simple exponential growth model, $\frac{dN}{dt} = rN$, to the cell numbers measured over time. The ie2SL and ie2KNL epitope-specific populations showed an inflationary tendency, whereas the m45SL epitope-specific population barely showed an increase in size (**Table 2.6**). Bootstrapping the dataset provided wide confidence intervals due to the relatively noisy and sparse measurements (**Figure 2.6**). Approximately 90% of the bootstraps showed an increase in the population size ($r > 0$). Interestingly, in all three cases, the increase in cell numbers predicted by the best fit to the labelling data lay within the confidence intervals of the exponential growth model (**Figure 2.6**). As the predicted inflation lay well within the observed variation in cell numbers, these

data are compatible with the hypothesis that the $p^* > d^*$ labelling behaviour resulted from an expanding cell population due to the reduction of its per capita production over time.

Discussion

The datasets presented here suggest that the DNA of the POI gained more label than it lost per unit of time ($p^* > d^*$ labelling behaviour). We showed that this unusual labelling behaviour can be explained if either the POI has prolonged access to label, or if the POI was expanding and thus, reducing its *per capita* production. We provided additional *in vitro* and *in vivo* experimental support for the proposed mechanisms.

The two cell populations for which we observed $p^* > d^*$ behaviour had very disparate experimental setups. Promyelocyte curves came from human bone marrow in a short-term deuterated-glucose experiment under homeostatic conditions. In contrast, the MCMV data was derived from the spleens of mice in a long-term deuterated-water experiment in the memory phase of acute infection. This disparity suggests that the $p^* > d^*$ behaviour was the characteristic of the POI and did not originate from the commonalities in the experimental designs. In addition to the populations reported here, murine natural killer (NK) cells after an MCMV infection also showed $p^* > d^*$ behaviour in long-term labelling experiments with deuterated water. Unlike MCMV-specific T cells, NK cells could not be described as a homogeneous population with a declining *per capita* production rate (Lukas et al., manuscript in preparation).

The labelling data of the promyelocytes was well-described by a homogeneous population when the label availability period was longer than the label administration period. The fact that the washout rate of body glucose is ~1.5 hours makes this finding difficult to grasp. However, that deuterium was available to cells for longer than 5.5 hours (i.e., the label administration period) was verified by *in vitro* experiments with mono mac 6 cells and HL-60 cells, cell-lines known to be closely related to monocytes and neutrophils, respectively. If the pool of de-novo deuterated nucleotides were to be formed in the beginning of the cell cycle's S-phase instead of being generated throughout the S-phase, this pool could act as a delayed source of intra-cellular labelled nucleotides after 5.5 hours. The extended availability of label is even more likely *in vivo* due to the salvage pathway in the bone marrow, through which newly dividing cells can pick up required molecules from the surroundings after the death of neighbouring cells (Austin et al., 2012). The prolonged label availability could also be due to the maintenance of the body glucose levels by multiple pathways (Nakrani et al., 2022), where the slower pathways can act as a late source of deuterated glucose.

The possibility of a longer labelling period was disregarded in the case of MCMV-specific memory T cells as a few extra hours of label availability would be insignificant in a long-term labelling experiment (28 days in this case). Further, T cells are thought to hardly use the salvage pathway (Macallan et al., 1998). Instead, we found that the $p^* > d^*$ behaviour of MCMV-specific memory T cells may result from the inflationary behaviour of the MCMV-

specific T-cell response. Therefore, unless there is compelling evidence for it, such a population should not be assumed to be at steady state. The inflationary capacity of MCMV-specific CD8⁺ T cells is well-documented (Klenerman and Oxenius, 2016; O’Hara et al., 2012). In a recent communication, it was shown that T cells with low affinity T-cell receptors (TCRs) dominate in the later part of the chronic response to MCMV, likely due to the senescence of high-affinity clones (Schober et al., 2020). Our choice of an exponentially decreasing cell density-dependent proliferation rate would be in line with this when low-affinity clones expand slower than their high-affinity counterparts. It is important to note that the $p^* > d^*$ behaviour requires a declining per capita production, and that a change in the loss rate will not have any effect because the loss rate is absent from the labelling equation (**equation 2.19**). Alternatively, the $p^* > d^*$ behaviour of the MCMV-specific cells could be explained if the memory T-cell pool is largely maintained by a source (fits not shown). Although recent articles have proposed the presence of a TCF1⁺ stem-like cell population that maintains the memory T-cell pool (Weitering et al., 2021; Welten et al., 2020), their relative contribution to the maintenance of the memory T-cell pool has not been quantified. Here we show that a density-dependent proliferation rate is in line with both the labelling data and the inflation seen in the population size.

Interestingly, we also found models that qualify to explain the $p^* > d^*$ behaviour but nevertheless failed to satisfactorily explain the presented datasets. We developed a framework to assess the qualification of a model to yield $p^* > d^*$ behaviour, merely through algebraic manipulations. TH and explicit source mechanisms, along with longer label availability and non-steady state mechanisms, passed the selection criteria of this procedure. Although the qualification of the TH and explicit source models reinforced our intuitive understanding of the $p^* > d^*$ labelling behaviour, these models failed to explain the data presented in this paper, indicating inherent bounds on the $p^* > d^*$ estimates that can be described by any model. Quantifying these bounds accurately is difficult because approximating multi-phasic slopes with single exponentials (as in the p^*d^* model) is non-trivial. These approximations also depend strongly on the accurate estimation (and measurements) of the peak of the labelling curve.

Finally, it is important to note that we analysed the presented datasets as if they were longitudinal even though they were in fact cross-sectional. Although it is highly unlikely, we cannot formally rule out the possibility that the $p^* > d^*$ behaviour was in fact merely due to inter-individual differences. We nevertheless regard the mechanisms proposed here as the most parsimonious, because i) most data points in the de-labelling phase were higher than expected (**Figures 2.1 and 2.3**), ii) the slow loss of enrichment in the promyelocytes could be due to longer label availability, which is seen *in vitro* (**Figures 2.4 and 2.5**), and iii) the labelling dynamics of tetramer⁺ MCMV-specific memory T cells could be perfectly explained by the inflationary nature of the response (**Figure 2.6**), which is a well-documented phenomenon (Klenerman and Oxenius, 2016; O’Hara et al., 2012).

Acknowledgements

We thank Andrew Yates for his supportive feedback on this manuscript.

Author Contributions

AS performed the mathematical modelling. AS, JB, RdB designed the study. AS, JB, RdB analysed the data and wrote the manuscript. All authors contributed to the article and approved the current version.

Funding statement

ACS was supported by grant number ALWOP.265 of the Dutch Research Council (NWO) to RdB and by Vici-grant number 09150181910016 of the Dutch Research Council (NWO) to JB.

Supplementary Information

Experimental design and plasma enrichment

Deuterated water labelling is suitable for cell populations with slow turnover rates (for example, naive and memory T-cell populations) due to the relatively slow turnover rate of water, and labelling with deuterated glucose is more suitable for populations that turnover rapidly (like granulocytes) as glucose has rapid turnover (Borghans et al., 2018; Macallan et al., 2009).

Promyelocytes

Promyelocytes make up the earliest fully committed precursor of granulocytes and were measured as part of a short-term deuterium labelling study of neutrophil differentiation in the bone marrow. In this study, bone marrow samples were obtained from 12 healthy volunteers, by aspiration of a 40ml volume from the posterior iliac crest. The volunteers received deuterated glucose for 5.5 hours at different days prior to the aspiration. At each time point, ranging from 1 to 9 days after the deuterated glucose pulse, two volunteers were sampled. The samples on day 1 and day 8 after labelling were obtained from the same two donors by repeated bone marrow sampling. Similarly, the samples on day 2 and day 9 after labelling were taken from the same donors.

Due to the fast washout rate of deuterated glucose, the fraction of body glucose that is deuterated, $D(t)$, can be approximated quite accurately with a step-function, analogous to a “pulse” of deuterium:

$$D(t) = \begin{cases} f, & t \leq \tau \\ 0, & t > \tau \end{cases} \quad (\text{S2.1})$$

Here, τ (in days) is the end of the labelling period, and f is the maximum level of enrichment in the plasma, which was measured to have a mean of 0.55 and a standard deviation of 0.05. As the data is cross-sectional and the enrichment in the plasma among the donors vary, the promyelocyte dataset was scaled before the fitting procedure (such that $f = 1$), using the protocol outlined previously (where $c = 0.65$) (Macallan et al., 2009).

MCMV-specific memory T cells

Murine cytomegalovirus (MCMV) is a persistent, chronic infection that is characterized by a phenomenon called memory inflation due to the accumulation of large numbers of virus specific CD8⁺ memory T cells. Three well-characterized MCMV-mutants expressing low or high-avidity epitopes (ie2SL: large inflationary response, ie2KNL: intermediate inflationary

response and m45SL: non-inflationary response) were used for the infections. Mice were given deuterated water for 28 days, beginning from 120 days post-infection. Their spleens were isolated at different time points during and after label administration to determine the fraction of labelled DNA in tetramer⁺ (MCMV-specific) memory T-cells.

Compared to deuterated glucose, the washout rate of deuterated water is relatively slow (Macallan et al., 2009; Reinauer et al., 1990; Shimamoto and Komiya, 2000). The fraction of body water that is deuterated, $D(t)$, in this case is given by (Vrisekoop et al., 2008):

$$D(t) = \begin{cases} \beta e^{-\delta t} + f(1 - e^{-\delta t}), & t \leq \tau \\ (\beta e^{-\delta \tau} + f(1 - e^{-\delta \tau}))e^{-\delta(t-\tau)}, & t > \tau \end{cases} \quad (\text{S2.2})$$

where, $\beta = 6 \times 10^{-3}$ is the baseline enrichment in plasma due to a boost given in the beginning of the experiment, $\delta = 0.373$ is the washout rate of body water (per day) and $f = 0.0545$ is the predicted plateau of deuterium enrichment in plasma. These parameters were estimated by fitting the enrichment curves to the deuterium enrichment levels measured in plasma. Next, the fraction of labelled DNA in a rapidly dividing cell population (thymocytes, in this case) was fitted to estimate the amplification factor, $c = 3.0271$, using **equation 2.1b**. This step was essential as the amplification factor, c , signifies the fold difference between the enrichment plateaus reached in plasma and the rapidly dividing population (Vrisekoop et al., 2008). These parameters were then used to define the deuterium availability function when fitting the labelling kinetics of other cell populations.

In-vitro experiment design

Mono mac 6 cell line

The mono mac 6 cells were cultured in a medium with equal concentration of normal glucose (1g/L) and deuterated glucose (1g/L) for 12 hours. After the 12-hour labelling period, the cells were washed with and cultured in a medium containing only 2g/L normal glucose (to mimic the de-labelling phase). Hourly samples were taken during the de-labelling period (i.e., sampled every hour from 12th to 24th hour, where the 12th hour is the start of the de-labelling phase, **Figure 2.5a**) to find out the deuterium incorporation in the population. Samples were also taken on a bi-hourly basis to estimate the population size (**Figure 2.5c**).

HL-60 cell line

The HL-60 cells were cultured in a medium with equal concentration of normal glucose (1g/L) and deuterated glucose (1g/L) for 6 hours. Hourly samples were taken during the labelling period. After the 6-hour labelling period, the cells were followed for 12 more hours after being washed with and cultured in a medium containing only 2g/L normal glucose (to

mimic the de-labelling phase). Hourly samples were taken during the labelling and de-labelling period (**Figure 2.5d**) to find out the deuterium incorporation in the population.

Figure S2.1

A kinetically heterogeneous population can show $p^ > d^*$ behaviour only if the data is skewed towards the late time points*

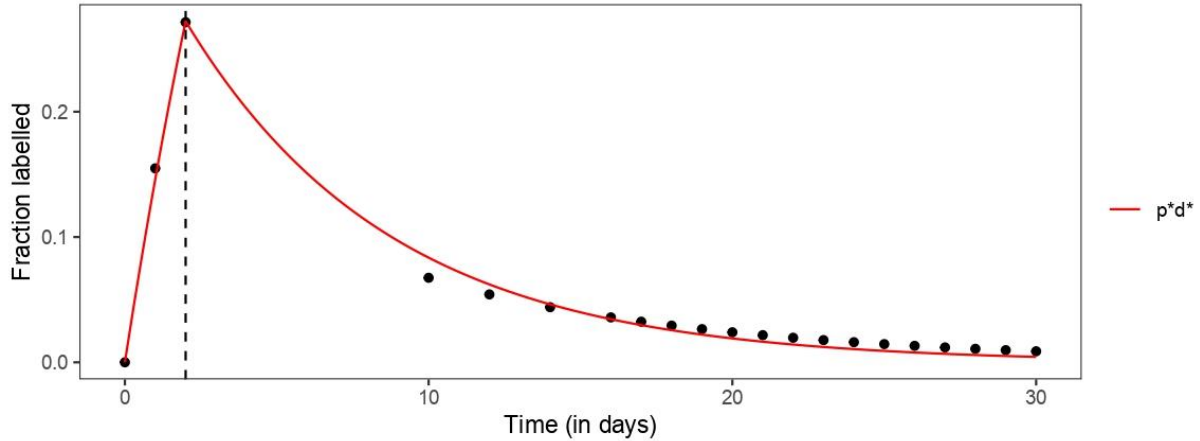


Figure S2.1: Best fit to a dataset generated with the KH model showing $p^* > d^*$ behaviour. The generated dataset is skewed towards measurements at late time points during the de-labelling period, giving unfair importance to the tail of the dataset. The parameters used to generate data with the KH model are: $d_1 = 0.1$, $d_2 = 0.5$, and $\alpha = 0.8$. The parameters of the best fit with the p^*d^* model are: $p^* = 0.16$, $d^* = 0.15$ (which is just a mild effect, that would probably be difficult to find in true data with experimental noise). The vertical black dashed line marks the stop of label.

Text S2.1: the temporal heterogeneity (TH) model

TH in a population can generate $p^ > d^*$ behaviour only if activated cells are lost at a slower rate than the resting cells*

Equation 2.10 can be re-written as:

$$\frac{dl}{dt} = p^*cD(t) - d^*(t)l$$

with,

$$p^* = p\bar{R} = d_A + \bar{R}(d_R - d_A) \tag{S2.3}$$

$$d^*(t) = d_A + \beta(t)(d_R - d_A)$$

where $\beta(t) = \frac{\bar{R}l_R(t)}{\bar{R}l_R(t) + \bar{A}l_A(t)}$ is the fraction that the labelled DNA strands of the resting sub-population occupy in the labelled population at any time t . Like for the KH model, it can be

shown that $\beta(t) < \bar{R}$ during the labelling phase, because $\beta(t)$ increases monotonically with $\rho(t)$:

$$\beta(t) = \frac{\bar{R}\rho(t)}{\bar{R}\rho(t) + 1 - \bar{R}} \quad (\text{S2.4})$$

where $\rho(t) = \frac{l_R(t)}{l_A(t)} < 1, \forall t < t_{crit}$. Thus, as expected the activated sub-population dominates the labelled population during the labelling phase. This results in a drop in the fraction labelled within the entire population as soon as the labelling is stopped even though the labelled fraction within the resting sub-population increases (**equation 2.10**). As in the KH model, t_{crit} divides the labelling curve into regions where $p^* > d^*(t)$ and $p^* < d^*(t)$. From the sufficient and necessary condition,

$$\begin{aligned} d^*(t) - p^* &= (\beta(t) - \bar{R})(d_R - d_A) < 0, \text{ if } t < t_{crit} \\ \Rightarrow \begin{cases} d^* < p^*, & d_R > d_A \\ d^* \geq p^*, & d_R \leq d_A \end{cases} \end{aligned} \quad (\text{S2.5})$$

Therefore, a population with TH will generate labelling curves with $p^* > d^*$ behaviour only if the activated sub-population has a slower loss rate than the resting sub-population.

Text S2.2: the explicit source model

A population can produce $p^ > d^*$ behaviour if it has a precursor with higher enrichment*

Equation 2.14 can be re-written in the form:

$$\frac{dl}{dt} = p^*cD(t) - d^*(t)l$$

with,

$$p^* = p_2 \quad (\text{S2.6})$$

$$d^*(t) = d_2 \left(1 - \frac{l_1(t)}{l_2(t)} \right) + \frac{p_2 l_1(t)}{l_2(t)}$$

The necessary condition becomes:

$$\begin{aligned} d^*(t) - p^* &= (d_2 - p_2) \left(1 - \frac{l_1(t)}{l_2(t)} \right) < 0, \text{ if } t < t_{crit} \\ \therefore p^* > d^* &\Rightarrow \frac{l_1(t)}{l_2(t)} > 1 \end{aligned} \quad (\text{S2.7})$$

Therefore, the POI will provide $p^* > d^*$ behaviour if the precursor population has higher fraction of labelled cells, $l_1(t) > l_2(t)$. This makes intuitive sense because the label in the POI is retained by labelled cells trickling into the population. The fraction of labelled cells within the POI would be lower than that in its precursor when $t < t_{crit}$ if:

$$l_1(t) > l_2(t) \Rightarrow \left. \frac{dl_1}{dt} \right|_{t=0} > \left. \frac{dl_2}{dt} \right|_{t=0}$$

$$\Rightarrow d_1 cD(0) > \alpha_2 d_2 cD(0) \quad (\text{S2.8})$$

$$\therefore l_1(t) > l_2(t) \Rightarrow d_1 > p_2 \Rightarrow p^* > d^* \quad (\text{S2.9})$$

where $p_2 = \alpha_2 d_2$. Therefore, if the turnover rate of the precursor population is higher than the division rate of the POI, the precursor will have a larger fraction of cells that is labelled, implying that the population can produce $p^* > d^*$ behaviour.

Note that the necessary condition (**equation S2.9**) does not always imply that the POI is majorly maintained by a source. If the POI were majorly maintained by the source, the number of cells from the source would be higher than that contributed by division (see **equation 2.12**), i.e.,

$$f_1 d_1 \bar{N}_1 > p_2 \bar{N}_2 \quad (\text{S2.10})$$

Using **equation 2.13**, the above can be simplified to

$$d_2 - p_2 > p_2 \Rightarrow d_2 > 2p_2 \quad (\text{S2.11})$$

Comparing **equations 2.13**, **S2.9** and **S2.11**, we find that the POI can show $p^* > d^*$ labelling behaviour when $d_1 > p_2$, and is not majorly maintained by the source if $p_2 < d_2 < 2p_2$. Thus, $p^* > d^*$ labelling behaviour does not require that the POI is majorly maintained by the source.

How are estimated cellular turnover rates of a population influenced by the dynamics of its precursor population?

Arpit C. Swain^{1,2}, José A. M. Borghans², Rob J. de Boer¹

¹Theoretical Biology, Utrecht University, Utrecht, The Netherlands

²Center for Translational Immunology, University Medical Center Utrecht, Utrecht, The Netherlands

To be submitted

Abstract

Estimating production and loss rates of cell populations is essential but difficult. The current state-of-the-art method to estimate these rates involves mathematical modelling of deuterium labelling experiments. Current models typically assume that the labelling in the precursors of the population of interest (POI) is proportional to that in the body water/glucose. This assumption is not always true and could have a significant effect on the rates estimated from labelling experiments. Here we quantify the effect different turnover rates of the precursors could have on the estimated proliferation and loss rates of a POI by explicitly modelling the dynamics of the precursors. We find that the labelling curve of the POI only reflects its own turnover rate if either the turnover rate of the precursors is sufficiently fast, or the contribution from the precursors is sufficiently small. We describe three other realistic scenarios where the labelling of the POI depends on both its own (proliferation and loss) rates and on the turnover rate of its precursors. Uniquely identifying the turnover rate of a POI, therefore, requires measurements (or knowledge) quantifying the contribution of label from its precursors.

Introduction

The estimation of the average production and loss rates of a cell population, and therefore of the expected lifespan of its cells, has remained challenging. Most estimation procedures either interfere with the true dynamics of the populations (as in adoptive transfer experiments or in-vitro cultures) or are toxic for the cells (for example during in-vivo labelling with compounds such as BrdU or radioactive diisopropylfluorophosphate (DFP³²)) (CARTWRIGHT et al., 1964; Gratzner, 1982). In recent decades, naturally occurring heavy isotopes (such as H², C¹³) have been proposed as alternative labelling compounds that are stable and non-toxic, and that should not alter the behaviour of the cells (Borghans et al., 2018; Macallan et al., 1998).

The current state-of-the-art technique to quantify the dynamics of cell populations involves the use of deuterium (H²) as the labelling agent. Deuterated water or glucose is ingested by human volunteers or mice and its incorporation in the DNA of a population of interest (POI) is followed over time. The kinetics of label uptake (upon labelling) and loss (after labelling is stopped) reveals information about the turnover of the POI, which is deciphered using mathematical models (Asquith et al., 2002; Borghans et al., 2018). These models often simplify all cellular processes into just gain and loss of cells in the POI (Asquith et al., 2002).

It is common practice, in studies addressing maintenance mechanisms of the POI, to distinguish between the gain of cells in the population due to i) cell division and ii) maturation from a precursor population. These are typically considered as two separate processes by using two independent parameters. Typically, the gain of label from the precursor population has been modelled implicitly, with the assumption that the enrichment of the precursor population mimics that of the body water, i.e., the precursors turn over rapidly. In such a case, the rate at which the POI gains label is dictated by its turnover rate (De Boer and Perelson, 2013a). Here, we show that the labelling dynamics of the source (precursor population) can have a significant effect on the labelling dynamics of the POI. Depending on the turnover rates of the precursors and the POI, the labelling curve of the POI could reflect its own rates, its precursors' rates, or their combination. To uniquely identify the kinetics of a POI that is (partly) maintained by a source, therefore, we propose to always consider (through prior knowledge or new measurements) the labelling curve of its immediate precursors.

Implicit source (IS) model

Any population is maintained due to gain of new cells (source from a precursor or from proliferation) and loss of resident cells (differentiation into another population or death). Consider a population, N , that is at equilibrium (denoted by \bar{N}), has a source of σ cells/day, a *per capita* proliferation rate, p /day and a *per capita* loss rate, d /day (**equation 3.1a**). The kinetics of the number of cells, N , the number of labelled DNA fragments, L , and fraction of labelled DNA, l , within this population can be described as:

$$\frac{dN(t)}{dt} = \sigma + (p - d)N(t) \quad (3.1a)$$

$$\frac{dL(t)}{dt} = \sigma D(t) + pD(t)\bar{N} - dL(t) \quad (3.1b)$$

$$\frac{dl(t)}{dt} = d(D(t) - l(t)) \quad (3.1c)$$

where

$$\bar{N} = \frac{\sigma}{(d - p)} \quad (3.1d)$$

$$D(t) = cU(t) = \begin{cases} 1, & t < 1 \\ 0, & t \geq 1 \end{cases} \quad (3.1e)$$

This model suggests that the fraction of the population that is labelled can be accurately tracked if just the loss rate, d , of the population is known (**equation 3.1c**). The turnover rate, d , is typically identifiable as the number of parameters to be estimated reduces from 3 to only 1, when dealing with the labelled fraction of a population that is at steady state (**equation 3.1a** vs **equation 3.1c**). Importantly, the precursor population (source) is assumed to label and de-label instantaneously (**equation 3.1b**).

In the model, $D(t)$ is a function denoting the probability that deuterium is incorporated into newly synthesized deoxyribose molecules ($U(t)$ is the level of deuterated water or glucose in plasma (or urine), and c is the intracellular amplification or dilution factor (Ahmed et al., 2015)). For simplicity, we treat it as a square pulse and scale time such that the labelling period (typically denoted as τ days) is 1 time unit. Scaling time scales the rates of the population. For example, if the memory T cell pool (i.e., the POI) is labelled for 28 days in mice and has been estimated to have a turnover rate of 0.02/day, the labelling period becomes 1 (scaled unit of time, reflecting about a month) and the turnover rate of the POI becomes $0.02 \times 28 = 0.56$ per scaled unit of time (i.e., approximately per month). This scaling simplifies the presentation of the results considerably.

Explicit source (ES) model

While the previous model assumed that the precursor population labels and de-labels instantaneously, in face, the dynamics of a source can have a major impact. This was illustrated by a study on the dynamics of neutrophils. The lifespan of blood neutrophils was estimated to be ~ 5 days when the precursors of neutrophils (in the bone marrow) were assumed to have a fast turnover, and ~ 0.5 day when the precursors were assumed to be slow, underlining the importance of explicitly considering the dynamics of the source (Borghans et al., 2018).

To quantify the effect of the source's dynamics on the rate estimates of the POI, consider an experiment designed to find out the rates of a POI, N_2 , that has an unobserved precursor population, N_1 . The cells of the precursors, N_1 , have a source of σ cells/scaled time unit (stu), from their immediate precursors, they divide at a rate of p_1 /stu and are lost at a rate of d_1 /stu. A fraction α of the cells leaving the precursor population mature into cells of the POI (i.e., the remaining $(1 - \alpha)$ fraction die or move elsewhere). Thus, the precursors obey the standard IS model (**equation 3.1a**). If the cells of the POI divide at a rate of p_2 /stu, and are lost at a rate of d_2 /stu, the kinetics of the precursors and the POI are written as:

$$\frac{dN_1(t)}{dt} = \sigma + (p_1 - d_1)N_1(t) \quad (3.2a)$$

$$\frac{dN_2(t)}{dt} = k\alpha d_1 N_1(t) + (p_2 - d_2)N_2(t) \quad (3.2b)$$

with,

$$\bar{N}_1 = \frac{\sigma}{(d_1 - p_1)} \quad (3.2c)$$

$$\bar{N}_2 = \frac{k\alpha d_1 \bar{N}_1}{(d_2 - p_2)} \quad (3.2d)$$

where $0 < \alpha \leq 1$ and \bar{N}_1 and \bar{N}_2 are the steady state values of the precursors and the POI, respectively. If the differentiation of the precursors into the POI is accompanied by division, the parameter $k = 2$, otherwise $k = 1$. The POI is primarily maintained by the source if $p_2 < d_2/2$ (compare **equations 3.2c and 3.2d**). For simplicity, we no longer mention the units (stu) of the parameters as they are all scaled with respect to the labelling period.

The number of labelled DNA strands in the precursors, L_1 , and in the POI, L_2 , in the ES model obey:

$$\frac{dL_1(t)}{dt} = \sigma D(t) + p_1 D(t) \bar{N}_1 - d_1 L_1(t) \quad (3.2g)$$

$$\frac{dL_2(t)}{dt} = \alpha d_1 L_1(t) + (k - 1)\alpha d_1 \bar{N}_1 D(t) + p_2 D(t) \bar{N}_2 - d_2 L_2(t) \quad (3.2h)$$

Thus, if differentiation is accompanied with division, the POI gains label due to the inflow of labelled DNA strands from the precursors as well as due to the generation of de-novo DNA strands on replication of the labelled and unlabelled DNA strands. The kinetics of the fractions of labelled DNA strands in the precursors, l_1 , and the POI, l_2 , then follow:

$$\frac{dl_1(t)}{dt} = d_1(D(t) - l_1(t)) \quad (3.2i)$$

$$\frac{dl_2(t)}{dt} = \frac{(d_2 - p_2)}{k} (l_1(t) + (k - 1)D(t)) + p_2 D(t) - d_2 l_2(t) \quad (3.2j)$$

$$= \frac{d_2}{k} (l_1(t) + (k-1)D(t) - kl_2(t)) + \frac{p_2}{k} (D(t) - l_1(t)) \quad (3.2k)$$

Transforming the system from cell numbers into fractions reduces the system to a 3-parameter model: d_1 , p_2 and d_2 (**equation 3.2**). Note that after a long labelling period (or in rapidly turning over populations), $l_1(t) \rightarrow D(t) = 1$, and that regardless of the value of k , $l_2(t) \rightarrow 1$.

The labelling curve of the POI reflects its own or its precursor's turnover rates in special cases

The ES model is a very general model, no longer requiring the assumption that the precursors are fast. In this model, every POI can have a source (of potentially recently divided cells), can divide, and has a loss rate. If $k = 2$ and $p_1 > 0$, the ES model can also represent a population of stem cells, N_1 , dividing asymmetrically into N_1 and N_2 cells (see **SI**).

Trivially, the labelling curve of the ES model is defined by the turnover rate of the POI, d_2 , if the source into the POI is negligible, i.e., if $p_2 \rightarrow d_2$ (in **equation 3.2k**). Therefore, in this section, we discuss the label gain and loss rates in two well-known cases of the ES model where the POI does have a significant source from the precursors: 1) a rapidly turning over precursor, and 2) a rapidly turning over, non-dividing POI. Throughout this article, we use label gain rate (and label loss rate) to refer to the rate at which a population gains (and loses) labelled DNA.

If the precursors turn over rapidly, e.g., $d_1 \geq 10$, the unlabelled cells in the precursor population would be rapidly replaced by labelled cells. The precursors can, in such a case, be approximated by the deuterium availability in plasma, i.e., $l_1(t) \approx D(t)$ (**equation 3.2i**). The labelling in the POI (**equation 3.2k**) will then boil down to:

$$\frac{dl_2(t)}{dt} \approx d_2(D(t) - l_2(t)) \quad (3.3)$$

which is the familiar IS model showing that the enrichment of the POI is determined by just the turnover rate of the POI, d_2 . Thus, the gain and loss rates estimated from labelling experiments where the precursors turn over rapidly (relative to the labelling period) indeed reflect the turnover rate of the POI (De Boer and Perelson, 2013a). Consequently, as rapidly dividing thymocytes are the precursors of slowly dividing naive T cells, the estimated lifespan of naive T cells can be trusted (Vrisekoop et al., 2008).

If the only source of label into the POI is due to the flow of labelled DNA from the precursors (i.e., $k = 1$ and $p_2 = 0$), the labelling dynamics in the POI (**equation 3.2k**) obeys:

$$\frac{dl_2(t)}{dt} \approx d_2(l_1(t) - l_2(t)) \quad (3.4)$$

If the cells of the POI turn over rapidly (e.g., $d_2 \gg 1$), the enrichment of the POI mimics that of the precursors (**equation 3.4**). Therefore, measuring only the POI will, in fact, reveal the turnover rate of the precursors. The neutrophils are a prime example of this case, as it is uncertain whether the slow labelling rate of mature neutrophils in blood reflects their own rate, or that of their precursors in the bone marrow (Borghans et al., 2018; Lahoz-Beneytez et al., 2016). These special cases showcase that the labelling curve of the POI sometimes reflects the turnover rate of the POI and sometimes that of its precursors.

The label gain and loss rates of the POI do not equal its turnover rate if the POI and the precursors have comparable turnover rates

Above we estimated the label gain and loss rates in a few extreme cases where either the source into the POI is negligible, or the precursors or the POI are short-lived. However, in many labelling experiments, the duration of the labelling period is comparable to the POI's lifespan, to avoid scenarios where the POI either hardly labels or becomes rapidly labelled during the labelling period. This is important as an accurate estimation of the POI's rates requires the collection of enough informative data points during the labelling period. As estimating the label gain and loss rates in these cases is not straight forward, here we derive first-order approximations for the POI's label gain and loss rates.

Denoting the label gain and loss rates as $p^*(t)$ and $d^*(t)$, respectively, the labelling curve of a POI can be written as (from **equation 3.1c**):

$$\frac{dl(t)}{dt} = p^*(t)U(t) - d^*(t)l(t) \quad (3.5)$$

The label gain rate reflects the dynamics of the entire population (Asquith et al., 2002), as de-novo labelled DNA molecules are made if a cell (with either labelled or unlabelled DNA molecules) divides during the labelling phase. The label loss rate, however, reflects the loss rate of the labelled cells only (Asquith et al., 2002), as the POI loses label only when a cell with labelled DNA is lost.

In the ES model introduced above, the fraction labelled DNA in the precursors is determined only by its loss rate, d_1 , whereas the fraction labelled DNA in the POI is dependent not just on its own rates but also on the rates of its precursor population (**equation 3.2j**). The rate of label gain in the POI, $p^*(t)$, during the labelling phase ($t \leq 1$) is (from **equation 3.2j**, with $D(t) = 1$ during the labelling phase):

$$p^*(t) = \frac{dl_2(t)}{dt} = \frac{(d_2 - p_2)}{k} (l_1(t) + k - 1) + p_2 - d_2 l_2(t) \quad (3.6a)$$

If the label gain can be approximated well by a linear increase, the expression for the gain rate (**equation 3.6a**) can be simplified by noticing that $l_1(t) = 1 - e^{-d_1 t} \approx d_1 t$, and $l_2(t) \approx p^*(t)t$. During the labelling phase ($t < 1$), the rate of label gain in the POI can then be approximated by:

$$p^*(t) \approx \frac{d_2(d_1t + k - 1) + p_2(1 - d_1t)}{k(1 + d_2t)} \quad (3.6b)$$

The initial slope (when $t \rightarrow 0$) and the slope at the end of the labelling phase (when $t \rightarrow 1$) of the POI, then, become

$$p^*(0) \approx \frac{d_2(k - 1) + p_2}{k} \quad (3.6c)$$

$$p^*(1) \approx \frac{d_2(d_1 + k - 1) + p_2(1 - d_1)}{k(1 + d_2)} \quad (3.6d)$$

As we are in a regime where the gain of label in the POI can be approximated well by a straight line, $p^*(t) \approx p^*(0) \approx p^*(1)$ (see **Figures 3.1 and 3.2**, and **Table 3.1** below). If the labelling curves of both the precursors and the POI can be approximated reasonably by a straight line, the population with the faster labelling dynamics can be identified just by comparing the initial gain rate of these populations. Hence, the gain in label in the POI (during the labelling phase) is faster than that in its precursor if

$$l_2(t) > l_1(t) \Leftrightarrow p^*(0)t > d_1t \Leftrightarrow p^*(0) > d_1 \quad (3.7)$$

As opposed to the rate of label gain, $p^*(t) = \frac{dl_2(t)}{dt}$, which is defined on the total population, the label loss rate, $d^*(t) = \frac{1}{l_2(t)} \frac{dl_2(t)}{dt}$, is only defined on the labelled fraction (see **equation 3.5**). So, the rate of label loss in the POI, $d^*(t)$, in the de-labelling phase (i.e., when $D(t) = 0$ in **equation 3.2j**, again for simplicity) is

$$d^*(t) = -\frac{\frac{(d_2 - p_2)}{k} l_1(t) - d_2 l_2(t)}{l_2(t)} \quad (3.8a)$$

$$= d_2 - \frac{(d_2 - p_2) l_1(t)}{k l_2(t)} \quad (3.8b)$$

Again, as $l_1(t) \approx d_1t$ and $l_2(t) \approx p^*(t)t$, the above expression simplifies to

$$d^*(t) \approx d_2 - \frac{(d_2 - p_2)}{k} \frac{d_1}{p^*(t)} \quad (3.8c)$$

It is important to keep in mind that the approximated downslope is accurate for only a short period of time in the de-labelling phase as the approximations of $l_1(t)$ and $l_2(t)$ are not accurate for $t > 1$.

As $p^*(0) = 0$ in some cases, for example, when $p_2 = 0$ and $k = 1$, we typically use the approximation $p^*(t) \approx p^*(1)$ for defining $d^*(t)$. Thus, the initial rate at which label is lost in the beginning of the de-labelling phase is

$$d^*(1 + \varepsilon) \approx d_2 - \frac{(d_2 - p_2)}{k} \frac{d_1}{p^*(1)} \quad (3.8d)$$

where $\varepsilon > 0$ is small.

The approximations of the gain and loss rates of label in the POI show that these rates are not dictated only by the turnover rate of the POI but also by the division rate of the POI and the turnover rate of the precursors.

Label uptake in the POI is generally lower than its true turnover rate

Models that consider an implicit source (like the IS model) predict that, in a population that is at steady state, the rate of label gain in the POI, $p^*(t)$, is the same as its death rate, i.e., d_2 (see **equation 3.1c**). To test the validity of this prediction, we compare the turnover rate of the POI analytically with the rates estimated from the more general explicit source model (**equations 3.6c-d and 3.8c, Table 3.1**), and empirically with the true gain by using numerical simulations (**Figures 3.1, 3.2 and S3.1**).

The turnover rates of the precursors and the POI are comparable

We first consider scenarios where the lifespans of the precursors and the POI are comparable to the duration of the labelling period (e.g., $0.1 \leq d_1 < 1$, $0.1 \leq d_2 < 1$), for example, labelling studies that track memory T cells, which might have a source from less-differentiated memory T-cell phenotypes, in blood (Ahmed et al., 2020). For the numerical simulations, we consider examples where the precursors' and the POI's lifespans are comparable, e.g., either 2-fold or 5-fold longer than the duration of the labelling period (**Figures 3.1 and 3.2**). Further, the POI may (left column in figures) or may not (right column in figures) divide.

Precursors are faster than the POI. If the precursors turn over faster than the POI, i.e., $d_1 > d_2 > p_2$, the labelling in the POI, during the labelling phase, cannot be higher than that in the precursors ($p^*(0) < d_1$ in **equation 3.7, Figure 3.1**).

If the differentiation of the precursors into the POI is not accompanied by division (i.e., if $k = 1$), the initial rate of label gain in the POI, $p^*(0)$, is given by its division rate, p_2 (**equation 3.6c, Figures 3.1a-b, Table 3.1**). The predicted initial label gain rate, $p^*(0) = p_2$, can have any value between 0 and d_2 (**Figures 3.1a-b**), and therefore, is not the average turnover rate of the POI, as was previously assumed. If the cells in the POI do not divide (i.e., if the gain of label in the POI is only due to the influx of labelled precursors), the labelling curve of the POI has an initial delay during which the gain of label in the POI is zero (**Figure**

3.1b). This initial delay in the gain of label is given by $p^*(0) = p_2 = 0$, which is infinitely smaller than the expected d_2 .

After the initial phase, the labelling curve is best described by $p^*(1)$, which depends on all three parameters of the model (**equation 3.6d**). The slope, $p^*(t)$, increases over time, starting at the POI's division rate, p_2 , up to $p^*(1)$, where the gain rate of label in the POI is higher than its own division rate, and is approaching its turnover rate (**Table 3.1**). The slope of the labelling curve approaches the turnover rate of the POI as cells of the POI that are lost are replaced by labelled cells from the higher enriched precursors. Numerical simulations confirm that the predicted slopes describe the true labelling curve faithfully (**Figures 3.1a-b**) and are similar to each other if the POI is a dividing population (**Figure 3.1a**).

The initial rate of label gain in the POI cannot be zero if the differentiation of precursors into the POI is accompanied by cell division (i.e., if $k = 2$ in **equation 3.6c**, **Figures 3.1c-d**). Like before (the case when $k = 1$), the approximated gain rate increases from the initial $p^*(0)$ to $p^*(1)$ due to the higher enrichment of the incoming precursors. The label gain rate of the POI is closer (relative to the case when $k = 1$) to, but still smaller than, its true turnover rate (**Figures 3.1c-d**). Thus, if the precursors are faster than the POI, the label gain rate in the POI increases over the labelling period due to an influx of precursors into the POI, provided $d_1, d_2 < 1$ and regardless of whether differentiation is accompanied by division (**Table 3.1**).

Precursors are slower than the POI. If the POI is faster than the precursors, i.e., $d_2 > d_1$, the labelling in the POI can be either faster or slower than the labelling in the precursors (**equation 3.7**, **Figures 3.2a-b**, **Table 3.1**). The labelling of the POI is faster than the precursors if the division rate of the POI is faster than the turnover rate of the precursors, i.e., $p_2 > d_1$. If the cells in the POI do not divide, the labelling in the POI can be faster than that in the precursors only if the precursors go through division-linked differentiation and the POI is at least 2-fold faster than the precursors, $d_2 > 2d_1$ (**equation 3.7**; also see **equations 3.12 and 3.13**).

Some properties stay unchanged compared to the case where precursors are faster than the POI. For example, if the precursors do not divide while differentiating into the POI ($k = 1$), the initial rate of label uptake reflects the division rate of the POI, $p^*(0) = p_2$ (**equation 3.6c**). This implies that a non-dividing POI would initially have a zero labelling rate (**Figure 3.2b**). If the differentiation of the precursors is linked with division ($k = 2$), the initial rate of label gain in the POI reflects both its division and death rates (**equation 3.6c**). The approximated slopes ($p^*(0)$ and $p^*(1)$) were, in all cases, much lower than the true turnover rate of the POI, d_2 . The slope declined over time during the labelling period, starting at a value defined by its own (division and loss) rates and moving towards the turnover rate of the precursors. The low enrichment of the precursors diluted the enrichment in the POI, causing a decline in the slope of the labelling curve. Therefore, the POI's label gain rate initially

reflects its own rates and is influenced by the rates of its precursors later in the labelling period.

Finally, to confirm these analytical results, the phenomenological model (**equation 3.5**) was used to numerically estimate the label gain and loss rates of the POI in all cases (i.e., whether the precursors are faster or slower than the POI) by non-linear parameter fitting. In all cases where the model was able to describe the artificial data, the estimated label gain rate, p^* , lay between the analytically predicted initial and final label gain rates ($p^*(0)$ and $p^*(1)$, respectively) (**Table 3.1**). The estimated label loss rate, d^* , and the predicted initial label loss rate, $d^*(1 + \epsilon)$, however, differed considerably. As the estimated label loss rate, d^* , is based upon the labelling dynamics of the POI during the entire de-labelling phase, it need not be similar to the initial gain or loss of label after the end of the labelling period (i.e., $d^*(1 + \epsilon)$, **Table 3.1**). Note that the phenomenological model (**equation 3.5**) is unable to describe the labelling curve if the precursor population differentiates without division into a non-dividing POI (see **Table 3.1**, **Figures S3.2 and S3.3**).

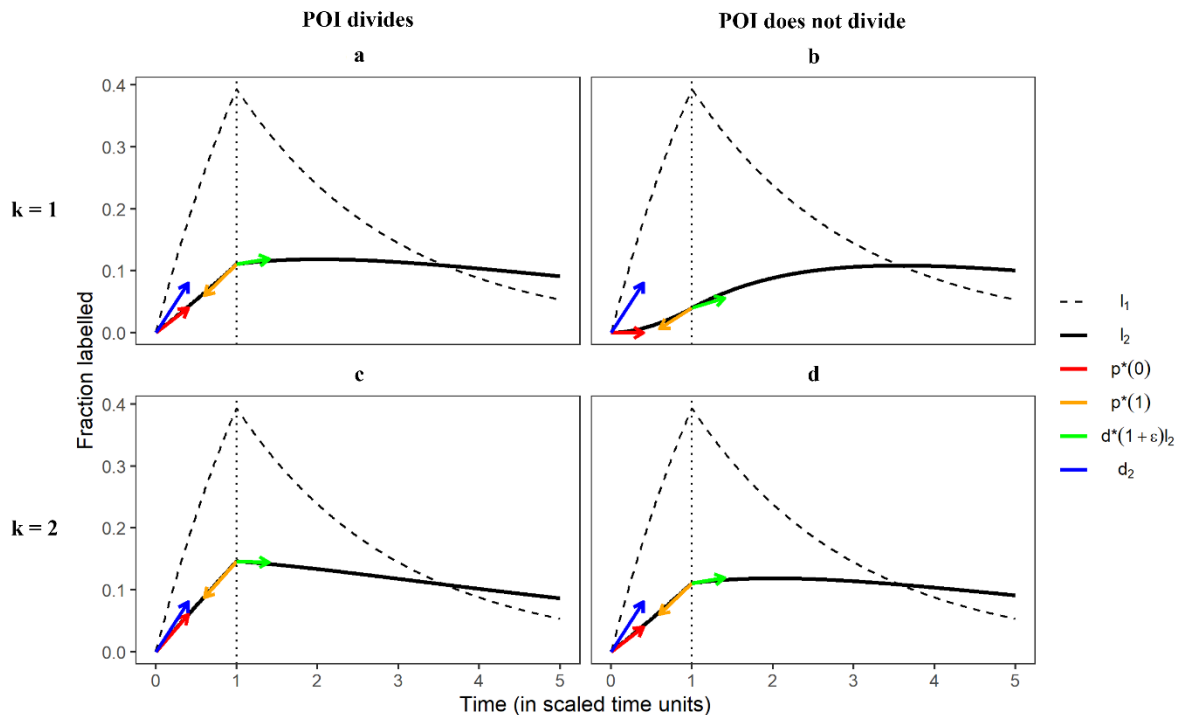


Figure 3.1: Precursors are faster than the POI. The rate of label gain is lower than the POI's turnover rate, d_2 (blue vector), if the precursors turn over faster than the POI. The coloured vectors represent the slopes identified in the legend and the arrows give the direction of extrapolation of these slopes. Note that the slopes are calculated as the label gain or loss rate multiplied by the fraction of unlabelled or labelled cells, respectively, for example, $d^*(1 + \epsilon)l_2$. The loss rate of the precursors, d_1 , and the POI, d_2 , were set to 0.5 and 0.2, respectively. The division rate of the POI, p_2 , was either set to 0.1 (in **(a)** and **(c)**) or 0 (in **(b)** and **(d)**). Note that the dynamics in **(a)** and **(d)** are identical, which can also be seen in **Table 3.1** (see the sub-section *Division-linked differentiation* below for details).

The turnover rates of the precursors and the POI are not comparable

If the POI is much faster than the precursors, the label gain rate approaches the turnover rate of the precursors, which was highlighted above as a well-known special case (Borghans et al., 2018; Lahoz-Beneytez et al., 2016). Note that the approximated slopes describe the labelling curve for a short period of time, as linear approximations do not give good descriptions of $l_1(t)$ and $l_2(t)$ when $d_1, d_2 > 1$ (see **Figure S3.1** and **Table S3.1**). Similarly, if the precursors are faster than the POI, the label gain rate in the POI approaches its own turnover rate as the label gain rate in the POI cannot be higher than its turnover rate, which was also reported above as a special case. Therefore, the approximated rates give a good description of the gain and loss of label in a population.

Condition	d_1	d_2	p_2	k	$p^*(0)$	$p^*(1)$	$d^*(1 + \epsilon)$	p^*	d^*
Faster precursors	0.5	0.2	0.1	1	0.10	0.13	-0.20	0.12	0.04
				2	0.15	0.15	0.03	0.16	0.13
			0	1	0	0.08	-1	-	-
				2	0.10	0.13	-0.20	0.12	0.04
Slower precursors	0.2	0.5	0.25	1	0.25	0.20	0.25	0.24	0.27
				2	0.38	0.27	0.41	0.37	0.40
			0	1	0	0.07	-1	-	-
				2	0.25	0.20	0.25	0.24	0.27

Table 3.1: The true proliferation and turnover rate (d_1 , d_2 , and p_2), and the predicted label gain and loss rates (i.e., $p^*(0)$, $p^*(1)$, and $d^*(1 + \epsilon)$) using **equations 3.6c-d and 3.8c** corresponding to the simulations shown in **Figures 3.1 and 3.2**. The parameters (p^* and d^*) of the best fits (shown in **Figures S3.2 and S3.3**) of the phenomenological model (**equation 3.5**) to the labelling data of the POI. The estimated label gain rate initially (see $p^*(0)$) reflects the proliferation rate of the POI (when $k = 1$) and then changes to reflect the influence of the precursor's rate (captured by $p^*(1)$). The estimates of p^* and d^* are not reported for the cases in which the phenomenological model fails to describe the data (see **Figures S3.2 and S3.3**). Note that the estimated loss rate, $d^*(1 + \epsilon)$, gives the rate at which the labelled population loses labelled DNA soon after the end of the labelling period (ϵ is a very small positive number). The negative sign indicates that the population, in fact, gains labelled DNA for a short period after the end of labelling (see **equation 3.5**). The rates (expressed as stu) are scaled with respect to the labelling period.

The label gain rate can maximally be the turnover rate of the POI. The examples above showed that the rate at which the POI gains label was invariably lower than the POI's turnover rate. Here we show that this is always the case, provided that the lifespans of the POI and the precursors are comparable to the duration of the labelling period.

If the precursors are not fast, i.e., if $d_1 < 1$ (and hence, $l_1(1) < 1$), both the slopes, $p^*(0)$ and $p^*(1)$, are smaller than the expected value, d_2 , as

$$p^*(0) \approx \frac{d_2(k-1) + p_2}{k}$$

$$\text{and} \quad = \frac{d_2(k - (1 - \alpha_2))}{k} < d_2 \quad (3.9)$$

$$p^*(1) \approx \frac{d_2(d_1 + k - 1) + p_2(1 - d_1)}{k(1 + d_2)}$$

$$= \frac{d_2(k + (d_1 - 1)(1 - \alpha_2))}{k(1 + d_2)} < d_2$$

as $\frac{(k+(d_1-1)(1-\alpha_2))}{k(1+d_2)} < 1$, when $d_2 > \frac{(d_1-1)(1-\alpha_2)}{k}$, which always holds true as $d_1 < 1$. Here $p_2 = \alpha_2 d_2$, with $0 \leq \alpha_2 < 1$. Thus, the rate at which the POI gets labelled is always lower than its turnover rate, d_2 , provided $d_1, d_2 < 1$. Interpreting the label gain rate as the true turnover rate would, therefore, overestimate the POI's lifespan whenever the precursors are not very fast and/or play a significant role in the maintenance of the POI.

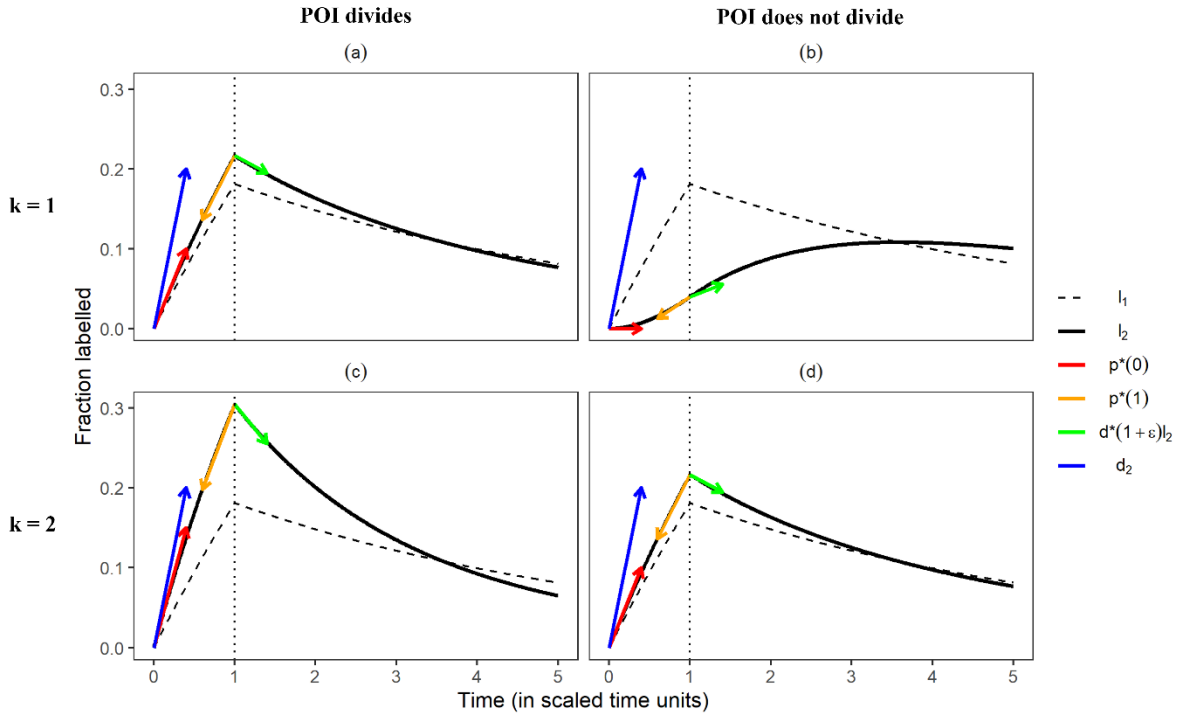


Figure 3.2: Precursors are slower than the POI. The rate of label gain is lower than the POI's true turnover rate, d_2 (blue vector), if the precursors turn over slower than the POI. The coloured vectors represent the slopes identified in the legend and the arrows give the direction of extrapolation of these slopes. Note that the slopes are calculated as the label gain or loss rate multiplied by the fraction of unlabelled or labelled cells, respectively, for example, $d^*(1 + \epsilon)l_2$. The loss rate of the precursors, d_1 , and the POI, d_2 , were set to 0.2 and 0.5, respectively. The division rate of the POI, p_2 , was either set to 0.1 (in (a) and (c)) or 0 (in (b) and (d)). Note that the dynamics in (a) and (d) are identical, which can also be seen in **Table 3.1** (see the sub-section *Division-linked differentiation* below for details).

The initial label loss in the POI is accurately predicted

We have shown that the estimated gain rates tend to be reasonable predictors of the enrichment in the precursors and the POI. As the relative enrichment of populations at the end of the labelling period influences the rate at which label is lost (**equation 3.8b**, **Chapter 2**), the initial rate at which label is lost, $d^*(1)$, can be approximated well by using the estimated gain rates (**equation 3.8c**).

When the lifespans of the POI and the precursors are comparable to the labelling period, the estimated gain and loss rates give a good description of the labelling curves (**Figures 3.1 and 3.2**). The estimated loss rates predicted whether the POI started to lose or continued to accrue label at the end of the labelling phase (**Table 3.1**). If the precursors are more enriched compared to the POI, the labelling of the POI continues after the labelling period in most cases (4 out of 5 cases, see **Figures 3.1a,b,d** and **Figure 3.2b**). In these cases, the gain of label in the POI is primarily due to the inflow of highly labelled precursor cells (also see the subsection *Timing of the peak*). In the other four cases (see **Figure 3.1c** and **Figures 3.2a,c,d**), the label gain in the POI was driven by proliferation.

Note that even when the cells in the POI are very short-lived, the estimates of the initial loss rate accurately informed on whether the POI gained or lost label after the labelling period (**Table S3.1**). So, the estimated rates do provide a faithful description of the de-labelling curve, but only for a very short period of time (**Figure S3.1**). Thus, the predicted label gain rate, $p^*(1)$, can be used to find a good approximation of the initial loss rate (**equation 3.8c**).

The POI can have four different labelling behaviours

Unlike the IS model where the labelling of the POI is determined only by the death rate of the POI (**equation 3.1c**), in the ES model the POI can have four qualitatively different slopes at which the POI gains and loses label (summarized in **Table 3.2**). The labelling of the POI is determined by:

1) its own turnover rate, d_2 , if the precursors turn over rapidly. In this case, the labelling in the precursors approximates the label availability in the plasma. In this case, the ES model approximates the IS model, and the rates of labelling and de-labelling are primarily driven by the POI's loss rate. An example of this case are naive T cells, that have the rapidly dividing thymocytes as their precursors (Vrisekoop et al., 2008).

2) the turnover rate of the precursors, d_1 , if the POI is fast. An example would be mature neutrophils in blood, which are thought to mimic the labelling curve of their precursors in the bone marrow (Borghans et al., 2018; Lahoz-Beneytez et al., 2016). The POI, here mature neutrophils, are probably much faster than their precursors in the bone marrow. They attain the enrichment of the precursors as they are replaced (by the cells flowing in from the precursors, post-mitotic pool) much faster than the change in the enrichment of the precursors.

3) its division rate, p_2 , if differentiation is not accompanied by division ($k = 1$). This is because the increase in enrichment due to the division in the POI would initially be the major contributor compared to the label flowing in from the precursors. Note that the precursors and the POI should have lifespans that are comparable to the length of the labelling period. A likely example for such a case would be central memory T cells undergoing homeostatic differentiation into effector memory T cells (Restifo and Gattinoni, 2013; Sallusto et al., 2004).

4) the average of its division and death rates, $(p_2 + d_2)/2$, if the precursors go through division-linked differentiation ($k = 2$). Here, along with the label gain due to the division in the POI, the source from the precursors also has a significant contribution of labelled cells as the precursor cells also divide and pick up label when they differentiate into the POI. Thus, if a naive T cell were to undergo homeostatic differentiation into memory T cells (Gossel et al., 2017), the gain of label by memory T cells would reflect both its division and death rates.

Since the labelling in the POI depends on the enrichment of its immediate precursors only (**equation 3.2j**), it is sufficient to have knowledge or data on the immediate precursors (and not the precursors' precursor) to distinguish the rates of the POI from that of its precursors. So, even a phenomenological description of the precursors' labelling curve, $l_1(t)$, would suffice to correctly estimate the turnover rate of the POI. Therefore, it is essential and sufficient to measure and model the immediate precursor population of the POI to reliably interpret the estimated rates.

The peaks of the labelling curves can help distinguish scenarios

Timing of the peak. It is possible to infer some properties of the precursors and the POI just by comparing both the height and the time of their peaks. The POI reaches its peak enrichment either 1) at the end of the labelling period, or 2) after the end of the labelling period.

In general, the peak of the POI will be at the end of the labelling phase if the cells flowing into the POI from the precursors have lower enrichment than the cells in the POI, i.e.,

$$l_2(1) > l_1(1) \Leftrightarrow p^*(0) > d_1 \quad (3.10)$$

Consider two specific scenarios where the POI reaches its peak enrichment at the end of the labelling period. First, if the precursors differentiate without dividing (i.e., when $k = 1$),

$$p^*(0) > d_1 \Leftrightarrow p_2 > d_1 \quad (3.11)$$

i.e., if the division rate of the cells in the POI is higher than the loss rate of the precursors. Second, if the differentiation of the precursors is accompanied by division (i.e., when $k = 2$),

$$p^*(0) > d_1$$

(3.12)

$$\Rightarrow \begin{cases} p_2 > d_1, \text{ or} \\ d_2/2 > d_1 > p_2 \end{cases}$$

i.e., the loss rate of the precursors is less than either the division rate or half of the loss rate of the POI. In summary, the peak of the POI is at the end of the labelling period only when the enrichment of the POI is largely due to division (within the POI or by differentiating precursors).

There are two corollaries of this finding. One, a non-dividing POI always achieves its peak labelling after the stop of labelling. Two, the peak of the POI will be after the end of the labelling phase if the precursor cells flowing into the POI after the end of the labelling phase have higher enrichment than the cells in the POI, i.e.,

$$\begin{aligned} l_1(1) > l_2(1) &\Rightarrow d_1 > p^*(0) \\ &\Rightarrow \begin{cases} d_1 > d_2, \text{ or} \\ d_2 > d_1 > p_2 \end{cases} \text{ when } k = 1 \\ &\Rightarrow \begin{cases} d_1 > d_2, \text{ or} \\ 2d_1 > d_2 > d_1 > p_2 \end{cases} \text{ when } k = 2 \end{aligned} \quad (3.13)$$

Complementary to the previous conclusion, the peak of the POI is after the end of the labelling phase only when differentiating precursors (without division) are the major contributor of label in the POI. Therefore, the population architecture underlying a labelling curve can be partially realized by comparing the location of the peaks of the POI and its precursors (provided the dataset is sufficiently dense).

Division-linked differentiation. To further pinpoint the properties of the precursors and the POI, it is important to be able to distinguish between labelling curves where differentiation is accompanied by division from those where it is not. Unfortunately, whether a population goes through division-linked differentiation is, in general, unidentifiable (i.e., curves with $k = 1$ and $k = 2$ are indistinguishable). To demonstrate this, we compare the labelling equations of the POI when $k = 1$ and $k = 2$ (**equation 3.2j**). Denoting the division rate of the POI, p_2 , as p_{21} when $k = 1$, and as p_{22} when $k = 2$, we find

$$\left. \frac{dl_2(t)}{dt} \right|_{k=1} = \left. \frac{dl_2(t)}{dt} \right|_{k=2} \quad (3.14a)$$

$$\Rightarrow d_2(l_1 - l_2) + p_{21}(D(t) - l_1) = \frac{d_2(l_1 + D(t) - 2l_2) + p_{22}(D(t) - l_1)}{2} \quad (3.14b)$$

$$\Rightarrow p_{22} = 2p_{21} - d_2 \quad (3.14c)$$

where $p_{21} \geq d_2/2$. Therefore, the labelling curve of any population whose precursor goes through division-linked differentiation can also be explained by a scenario where the

precursors differentiate without division (see **Table 3.1** for examples). On the other hand, the labelling curve of a population whose precursors do not go through division-linked differentiation cannot be described with $k = 2$ if more than half of the production of the POI is due to the source, i.e., $p_2 < d_2/2$. Thus, one can conclude that the influx into the POI is not accompanied by division if $p_2 < d_2/2$ in the estimates of the best fit. In a scenario where it is not known whether differentiation is linked with division, it is safe to conclude that the POI is primarily maintained by self-proliferation only if $p_2 \geq 3d_2/4$. Fortunately, the above transformation (**equation 3.14**) does not affect the turnover rate of the POI, d_2 . Therefore, the turnover rate of the POI is identifiable if (and only if) the labelling in the precursors is known.

Scenarios	$p^*(0)$	$p^*(1)$	$d^*(1 + \varepsilon)$	Constraints
General cases				
Differentiation without division	p_2	$\frac{d_2 d_1 + p_2(1 - d_1)}{(1 + d_2)}$	$d_2 - (d_2 - p_2) \frac{d_1}{p^*(1)}$	$k = 1$
Division-linked differentiation	$\frac{(d_2 + p_2)}{2}$	$\frac{d_2(d_1 + 1) + p_2(1 - d_1)}{2(1 + d_2)}$	$d_2 - \frac{(d_2 - p_2)}{2} \frac{d_1}{p^*(1)}$	$k = 2$
Special cases				
Precursors turn over about as fast as deuterated water/glucose OR The source is negligible	d_2	d_2	d_2	$1 \ll d_1$ OR $d_1 \approx 0$
Rapidly turning over, non-dividing POI with precursors that do not divide while differentiating	d_1	d_1	d_1	$0 < d_1 < d_2$ $1 \ll d_2$ $p_2 = 0$ $k = 1$

Table 3.2: A POI with a precursor population has 4 qualitatively different gain and loss rate scenarios. Knowledge about the precursor helps and is crucial to identify the turnover rate of the POI.

Intersecting labelling curves. Consider a simple scenario where precursors differentiate without division into a non-dividing POI, i.e., $k = 1$ and $p_2 = 0$ (see above). We have seen above that the peak enrichment in the POI will then be reached after the end of the labelling

phase (where $D(t > 1) = 0$). More importantly, the peak occurs when $l_2(t) = l_1(t)$ (equation 3.4, see Figure 3.3a). This provides a cardinal property of a chain of populations:

$$l_2(t) = l_1(t) \Leftrightarrow k = 1, p_2 = 0 \quad (3.15)$$

i.e., if during the de-labelling phase, a population reaches its peak when its labelling curve intersects that of its precursors, then this is proof that the POI is not dividing, and its precursors differentiate into the population without division. This immediately implies that such a population ($k = 1, p_2 = 0$) has a lower peak than its precursor (Figure 3.3a).

The above discussions have all focused on scenarios where cells are lost or are produced randomly (i.e., the times to death or division are exponentially distributed and are independent of the cell's age). However, several cellular processes may require a minimum length of time. If the cells of the POI were to have an 'internal clock' programming their departure time, i.e., if cells would require a fixed amount of time to mature or die, then the peak of labelling achieved in the POI can be higher than that in the precursors (Figure 3.3b). For example, the maturation process of promyelocytes into mature neutrophils in the bone marrow has been shown to be a conveyor-belt-like process, where each maturation stage has a pre-determined time. Consider the kinetics of this 3-population system:

$$\frac{dN_1(t)}{dt} = \sigma - d_1 N_1(t) \quad (3.16a)$$

$$\frac{dN_2(t)}{dt} = d_1 N_1(t) - d_1 N_1(t - \Delta_2) \quad (3.16b)$$

$$\frac{dN_3(t)}{dt} = d_1 N_1(t - \Delta_2) - d_1 N_1(t - \Delta_2 - \Delta_3) \quad (3.16c)$$

with, $\bar{N}_1 = 1, \bar{N}_2 = d_1 \bar{N}_1 \Delta_2$, and $\bar{N}_3 = d_1 \bar{N}_1 \Delta_3$ (3.16d)

The residence times in N_1, N_2 and N_3 are $1/d_1, \Delta_2$ and Δ_3 , respectively. The dynamics of the labelled fraction are defined as

$$\frac{dl_1}{dt} = d_1(D(t) - l_1) \quad (3.16e)$$

$$\frac{dl_2}{dt} = \frac{l_1(t) - l_1(t - \Delta_2)}{\Delta_2} \quad (3.16f)$$

$$\frac{dl_3}{dt} = \frac{l_1(t - \Delta_2) - l_1(t - \Delta_2 - \Delta_3)}{\Delta_3} \quad (3.16g)$$

where $l_1(t - \Delta) = 0$, if $t < \Delta$ (3.16h)

Here a population, N_1 , governed by random cellular processes (i.e., an exponentially distributed loss rate, d_1) differentiates into a population, N_2 , that with fixed maturation time (Δ_2) differentiates into a successive stage, N_3 , that also has a fixed maturation time (Δ_3).

As the cells only mature in the 2nd and 3rd populations (the non-random populations) and do not divide, the gain of label in these populations is solely due to differentiation of the 1st population (with random cellular processes). The 2nd population gathers label as soon as labelling starts, as there is no fixed time in the 1st population before which a cell can mature. However, the 3rd population gains label only after the labelled cells in the 2nd population have matured, i.e., after Δ_2 units of time.

The dynamics of an analogous system where the three populations have random cellular processes is:

$$\begin{aligned}\frac{dN_1(t)}{dt} &= \sigma - d_1 N_1(t) \\ \frac{dN_2(t)}{dt} &= d_1 N_1(t) - d_2 N_2(t) \\ \frac{dN_3(t)}{dt} &= d_2 N_2(t) - d_3 N_3(t) \\ \bar{N}_1 &= \frac{\sigma}{d_1}; \bar{N}_2 = \frac{d_1}{d_2} \bar{N}_1; \bar{N}_3 = \frac{d_2}{d_3} \bar{N}_2\end{aligned}\tag{3.17}$$

$$\frac{dl_1(t)}{dt} = d_1(D(t) - l_1(t))$$

$$\frac{dl_2(t)}{dt} = d_2(l_1(t) - l_2(t))$$

$$\frac{dl_3(t)}{dt} = d_3(l_2(t) - l_3(t))$$

In a 3-population system that only has populations with random cellular processes (**Figure 3.3a**), the successive populations (2nd and 3rd) attain their peak where their labelling curves intersect with their immediate precursors, and therefore, the peak of a successive population cannot be higher than its immediate precursor. This property, however, does not hold in a system that has populations on a conveyor belt (**Figure 3.3b**), as the peak of the 3rd population can be higher than that of the 2nd. Of note, the peak of the 2nd and 3rd population cannot be higher than that of the 1st population (i.e., the source of their labelling). In the simulation presented here (**Figure 3.3b**), as the maturation time in the 3rd population is shorter than that of the 2nd, the 3rd population has a higher fraction that is labelled at its peak (even though the total amount of labelled cells going through them is the same). Since these curves are different, one would obtain different parameter estimates if such labelling data were fitted with **equations 3.16 and 3.17**. For example, we have estimated the residence time

of mature neutrophils in blood to be ~ 10 hours or ~ 1.6 days, depending on whether the mature blood neutrophils are assumed to undergo random or conveyor-belt-like cellular processes, respectively (van Grinsven et al., manuscript in preparation). Therefore, it is also important to know whether the measured populations undergo non-random cellular processes.

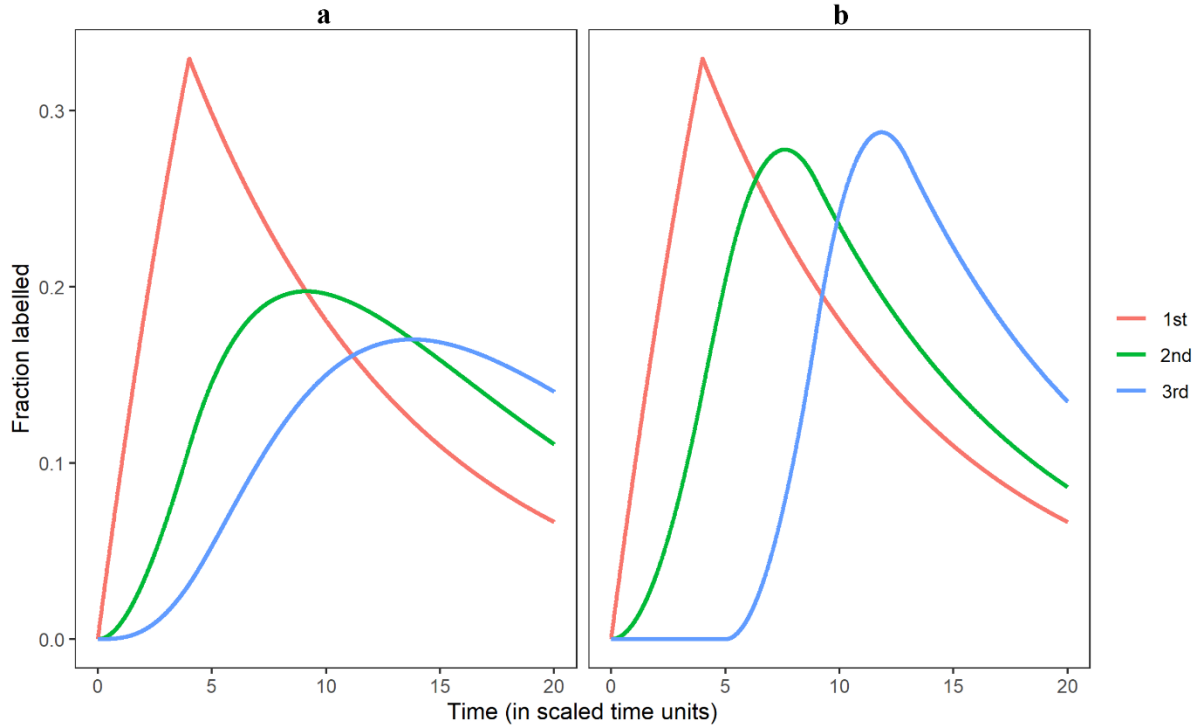


Figure 3.3: Non-dividing populations with the same differentiation properties show different behaviours if they have pre-programmed cellular processes. A 3-population system is shown where cells of either all populations (**a**, **equation 3.17**) or only the first population (**b**, **equation 3.16**) have random cellular processes. The parameters of the models are: $d_1 = 0.1$, $\frac{1}{d_2} = \Delta_2 = 5$, $\frac{1}{d_3} = \Delta_3 = 4$. The values are scaled with respect to the labelling period.

In certain cases (for example, the case shown in **Figure 3.3b**), it is possible to infer the model architecture from the labelling curves. In this example, the 3rd population has a delayed gain of label (therefore, no proliferation) and peaks well after the stop of the labelling period (so, the source, i.e., the 2nd population, is the major contributor of label). Moreover, its peak is higher than that of its precursor population, which is not possible for populations with random cellular processes. In such a case, one should choose **equation 3.16** to explain the data. So, it is safe to conclude that the cells in a population are not governed by random processes if the peak of the population is higher than its precursor and the peak is reached after the end of the labelling period (see above and **equation 3.2j**). Finally, it is also clear from the marked delay in the labelling of the 3rd population, that the 2nd population is a ‘waiting box’.

The estimated turnover rate of a POI can depend on its assumed underlying maintenance mechanism

The ES model can explain a wide variety of labelling curves, including the curves generated by the IS model. Both $p^* \leq d^*$ and $p^* > d^*$ labelling behaviour can be explained by the ES model (**Table 3.2**; also see **Chapter 2**). This generality of the ES model is troubling, however. Most current estimates of cell lifespans are based on IS-like models that do not consider a precursor population, and the estimated rate at which label is gained is generally interpreted as the average turnover rate of the POI (Asquith et al., 2002; De Boer and Perelson, 2013a). Since in the ES model, the same estimate could be reflecting the rate of the precursors (d_1), of the POI (d_2, p_2) or anything in between, this questions some of the current interpretations. We illustrate this using two examples.

Labelling of CD8⁺ memory T cells by Westera et al. (2013)

In the study by Westera et al. (2013) (Westera et al., 2013) murine CD8⁺ memory T cells were measured in a deuterium labelling experiment. The mice were drinking deuterated water for 1, 4 or 8 weeks. Using IS-like models (where the labelling in the source is the same as that in the body water), it was concluded that the CD8⁺ memory T-cell pool is heterogeneous, because the data was best described with the kinetic heterogeneity (KH) model (Westera et al., 2013). Above, we showed that a population whose label gain rate is slower than its loss rate can also be described by the ES model (**Table 3.2**), and hence as alluded to previously (Westera et al., 2013), is not conclusive evidence for heterogeneity in the POI. Further, recent reports have claimed that the memory T-cell pool in laboratory mice is partly (~10%) maintained by a continuous influx from naive T cells (Gossel et al., 2017). Therefore, we re-analysed the data from Westera et al. by fitting the data both to the KH model (with 3 parameters: d_1, d_2 and α) and to the ES model with $k = 1$ (again with 3 parameters d_1, d_2 and p_2); see **Figure 3.4**. Disturbingly, a homogeneous POI with a source (i.e., the ES model in **equation 3.2**) explains the Westera et al. data (Westera et al., 2013) equally well, but with very different estimates for the turnover rate of the POI (**Figure 3.4, Table 3.3**). The ES model estimated a turnover rate of $\bar{d} = d_2 = 0.24/\text{day}$ (i.e., a lifespan of 4 days) of the POI, which is about 5-fold higher than the average turnover rate of $\bar{d} = 0.046/\text{day}$ (i.e., a ~20-day lifespan) estimated using the KH model (**Table 3.3**). Thus, the presence of a source that does not get instantaneously labelled can have a remarkable influence on the estimated lifespan of the POI (**Table 3.3**). However, since the estimated division rate of the POI, i.e., $p_2 = 0.04/\text{day}$, would suggest that only a mere ~17% (calculated as p_2/d_2) of the POI is replaced by self-replication, one would require a much larger contribution from the naive T cell pool than the estimated ~10% (Gossel et al., 2017). Thus, although it is possible that CD8⁺ memory T cells are maintained by an influx from a precursor population, it is not very likely.

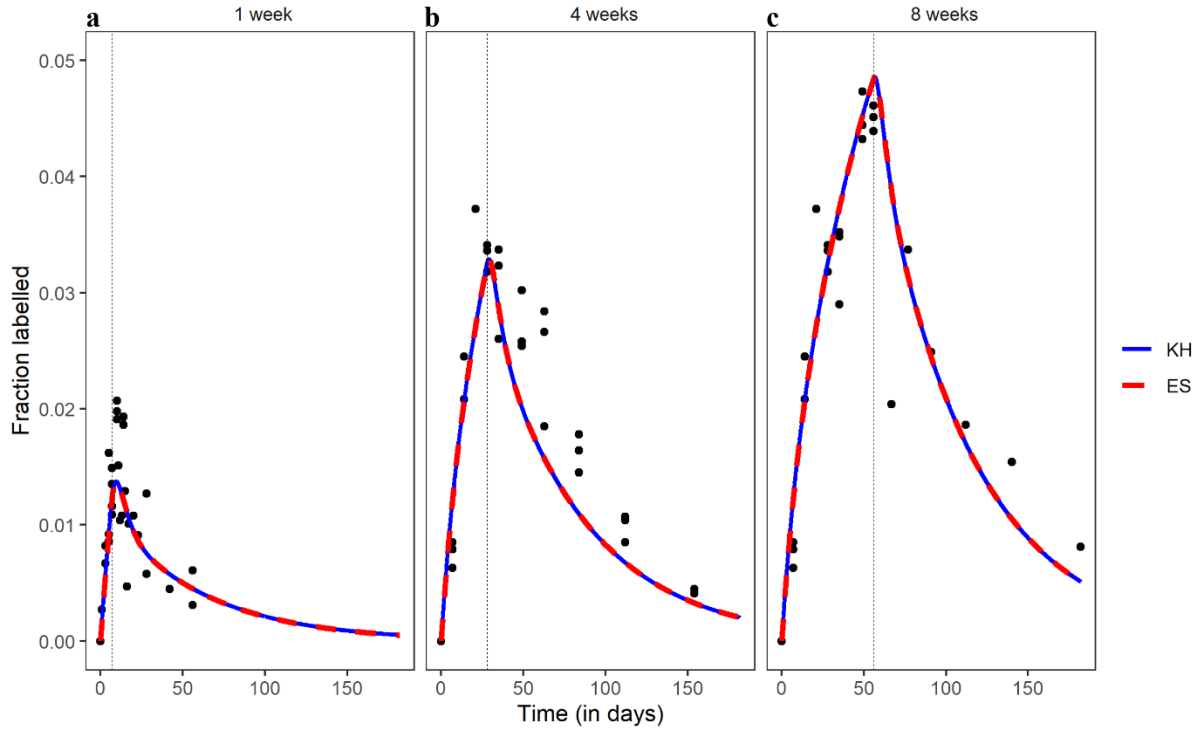


Figure 3.4: The best fits to the data from Westera et al. (2013) (Westera et al., 2013) with the KH model and the ES model with $k = 1$. The data shows the labelling of the CD8⁺ memory T cells in 1-week (a), 4-week (b) and 8-week (c) labelling experiments with deuterated water.

KH	d_1	d_2	α	$\bar{d} = \alpha d_1 + (1 - \alpha)d_2$	
	0.239	0.017	0.116	0.043	
ES	d_1	d_2	p_2	$\overline{N_2/N_1}$	$\bar{d} = d_2$
	0.017	0.239	0.043	0.1	0.239

Table 3.3: The estimates of the models for the best fits shown in **Figure 3.4**. The size of the total population in the KH model can be scaled to any value. Note the large difference in the estimated turnover rates of the POI, \bar{d} , in the KH model and the ES model.

Labelling of CD57⁺ memory T cells by Ahmed et al. (2020)

A dataset that seems uniquely suited for our analysis was generated by Ahmed et al. (2020) who measured the label gain and loss in both the POI, i.e., CD57⁺CD4⁺ memory T cells, and their precursor population, i.e., CD57⁻CD4⁺ memory T cells (Ahmed et al., 2020). To find out the dynamics of the POI, they used a phenomenological chain of two populations describing both the POI and the precursors (see (Ahmed et al., 2020) for their model). Their analysis showed that the POI was maintained largely ($\sim 95\%$) by division rather than by the source from the precursors ($\sim 5\%$). Hence, the POI and the precursors were maintained independently.

To re-analyse these data, we considered a three population chain model where the $CD57^+CD4^+$ cells are fed by the $CD57^-CD4^+$ population, that is in turn fed by an unknown precursor population. The labelling dynamics of both the $CD57^+CD4^+$ and the $CD57^-CD4^+$ populations were well-described by this three population chain model (**Figure 3.5a**). Both populations were estimated to have fast turnover rates (d_0 , d_1 and d_2 signify the turnover rates of the precursors of $CD57^-CD4^+$, $CD57^-CD4^+$ and $CD57^+CD4^+$ populations, respectively. See the legend of **Figure 3.5**) and a similar size, with $\sim 14\%$ (p_1/d_1) of the $CD57^-CD4^+$ cells and $\sim 33\%$ (p_2/d_2) of the $CD57^+CD4^+$ cells being maintained by division. If either the $CD57^-CD4^+$ cells (in a two population chain model, **Figure 3.5b**) or the $CD57^+CD4^+$ cells (i.e., modelled as a single compartment model, **Figure 3.5c**) were described with the implicit source model, the description of the labelling data became significantly worse (**Figures 3.5b-c**).

Notably, the turnover rate of the two POI, $CD57^-CD4^+$ and $CD57^+CD4^+$ memory T cells, estimated from a two population chain model and a three population chain model differed by 2-fold. This was due to the poor description of the precursors, $CD57^-CD4^+$ memory T cells. If the description of the labelling dynamics of the $CD57^-CD4^+$ memory T cells would have stayed the same, the estimates of the $CD57^+CD4^+$ memory T cells would have also remained unchanged.

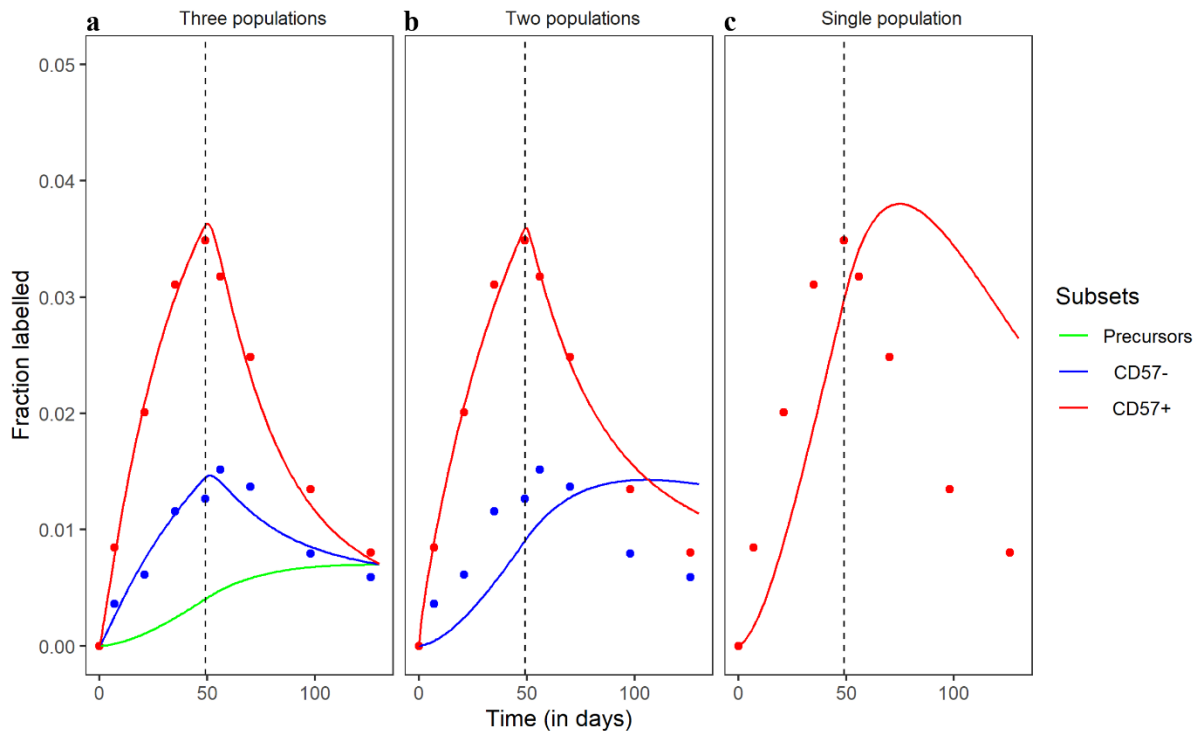


Figure 3.5: The best fits of the three population ES model (**a**), two population ES model (**b**), and IS model (**c**) to the data from Ahmed et al. (2020) (Ahmed et al., 2020). The data shows the labelling of $CD57^-CD4^+$ and $CD57^+CD4^+$ memory T cells in labelling experiments with deuterated water. The estimates of the best fit of the three population ES model are: $d_0 = 0.001/\text{day}$, $d_1 = 0.28/\text{day}$, $d_2 = 0.4/\text{day}$, $p_1 = 0.04/\text{day}$, and $p_2 = 0.13/\text{day}$.

Note that both examples are from labelling experiments with deuterated water and the body water enrichment approaches its asymptote slowly. Therefore, even a population that is entirely self-renewing can have an initial delay in gaining label (**Figure 3.5**).

Both examples demonstrate that the estimated parameters can strongly depend on the underlying model, and hence that one should always test whether the estimates change when a precursor with a realistic turnover rate is added. In the first example, one could argue that the previous KH model provides the best explanation, as the ES model requires an unrealistically large contribution from the naive T-cell compartment. In the second example, however, the estimates found from the ES model could be realistic, as they are in line with previous estimates stating that as much as a quarter of the CD4⁺ memory T-cell population could be maintained by a source from naive T cells (Gossel et al., 2017).

Discussion

Deuterium labelling is hailed as the current best technique to accurately measure the turnover rates of a cell population *in vivo*. In this article, we share some disturbing insights in the current modelling approaches. We show that models that fail to consider a slow source of label can severely underestimate the true turnover rate of the POI. The rate at which the POI gains label is not simply its average turnover rate but can be markedly influenced by the rate at which its precursors gain label. We also show that typically one cannot tell from the labelling data whether cells divide while differentiating into the POI. Therefore, unless one is convinced that 1) the precursors are much faster, or 2) hardly play any role in maintaining the POI, a source should be modelled explicitly (with the ES model) and ideally be matched with the labelling data of the precursors.

We found that the rate at which the POI gains label is always lower or equal to the true turnover rate of the POI. Depending on the dynamics of its precursor, the labelling in the POI can follow 4 different scenarios. In cases where the lifespans of both the precursors and the POI are comparable to the labelling duration, the rate of labelling varies with time and is not given by the rates of any single population. So, we defined two label gain rates, one at the beginning of the labelling period, $p^*(0)$, and the other at its end, $p^*(1)$. We showed that these approximated gain rates tend to be in good agreement with each other, and that both are smaller than the turnover rate, d_2 , of the POI. Thus, interpreting the label gain rate as the turnover rate can markedly overestimate the lifespan of the measured population.

There are two cases where one can be certain that the estimated rate reflects a POI's true turnover rate. First, when the source population's turnover rate is sufficiently fast, the labelling in the POI is largely dictated by its own turnover rate. For example, thymocytes, that act as a precursor to slowly turning-over naive T cells, turn over rapidly. Therefore, estimating the true turnover rate of naive T cells does not require measuring the labelling in the thymocytes. Second, when the population is largely maintained by proliferation (i.e., when the source into the POI is negligible). Memory T cells are a likely example of this

scenario as they are thought to be largely maintained by proliferation. Therefore, although measuring the label incorporation in the precursors should be treated as the standard procedure, it may not be necessary in all deuterium labelling experiments.

Using two case studies as examples, we showed how estimates can become very different when the assumption of a rapid source population is released. A study that focused on the labelling dynamics of the CD8⁺ memory T cells was originally explained by a kinetically heterogeneous population and concluded that these cells had a ~20 day lifespan (Westera et al., 2013). The ES model, in contrast, suggested that the CD8⁺ memory T-cell pool could be homogeneous, where cells lived only ~4 days and were maintained by a much larger influx. Although some studies have estimated that circulating CD8⁺ memory T cells could be short-lived (Bresser et al., 2022; Gossel et al., 2017), a very short-lived memory T-cell population that is primarily maintained by an influx from a large precursor population is not in line with many previous studies and can probably be discarded. Nevertheless, it remains important to study the possibility of a slow precursor, as in other cases this may provide a realistic description. In the second example that dealt with the maintenance mechanism of CD4⁺CD57⁺ memory T cells (Ahmed et al., 2020), the ES model suggested that these cells were only partly maintained by influx, as opposed to the original interpretation that suggested that they were largely maintained by self-replication. This is similar to previous conclusions on CD4⁺ memory T cell pool, that are maintained by an influx from the naive CD4⁺ T cell pool (Gossel et al., 2017). Additionally, in contrast to the original conclusion where the differentiation of CD4⁺CD57⁻ cells was accompanied by a clonal burst, the ES model preferred a solution where differentiation is not accompanied by division. As very little is known about these two POIs, it is difficult to favour one of these solutions, underlying the importance of considering an explicitly modelled source when analysing deuterium labelling data.

Here we show that even deuterium labelling, the current state-of-the-art method to estimate a population's lifespan, can be prone to error. For several populations, it is essential to have information on the dynamics of the precursors to not undermine the reliability of the estimates of the POI found from deuterium labelling experiments.

Author Contributions

AS performed the mathematical modelling. AS, JB and RdB designed the study. AS, JB and RdB analysed the data and wrote the manuscript. All authors contributed to the article and approved the current version.

Funding statement

ACS was supported by grant number ALWOP.265 of the Dutch Research Council (NWO) to RdB and by Vici-grant number 09150181910016 of the Dutch Research Council (NWO) to JB.

Supplementary Information

The ES model describes both non-stem-like and stem-like populations

The ES model makes only the most fundamental assumptions (of a possible source, of possible division in the population, and of loss from the population), that should be true for any population and, thus, is very general. With a few substitutions, we can express the system of equations (**equations 3.2a-d**) in the classical form of stem cells (Lander et al., 2009), i.e.,

$$\begin{aligned} \frac{dN_1}{dt} &= \sigma + (p_1 - d_1)N_1 \\ &= \sigma - (1 - \alpha)d_1N_1 - \alpha d_1N_1 - p_1N_1 + 2p_1N_1 \\ &= \sigma - (1 - \alpha)d_1N_1 + (2\beta - 1)\delta N_1 \end{aligned} \tag{S3.1a}$$

$$\begin{aligned} \frac{dN_2}{dt} &= 2\alpha d_1N_1 + (p_2 - d_2)N_2 \\ &= 2(1 - \beta)\delta N_1 + (p_2 - d_2)N_2 \end{aligned} \tag{S3.1b}$$

where $\delta = p_1 + \alpha d_1$ is the total division rate of the precursor population, and $\beta = \frac{p_1}{\delta} < 1$ is the fraction of the daughter cells that replenish the precursor population. The fraction $(1 - \beta)$ of daughter cells differentiate into the next population, N_2 . Therefore, the ES model is general enough to describe both non-stem-like and stem-like populations.

The initial gain and loss rates are well-described even when the POI is very short-lived

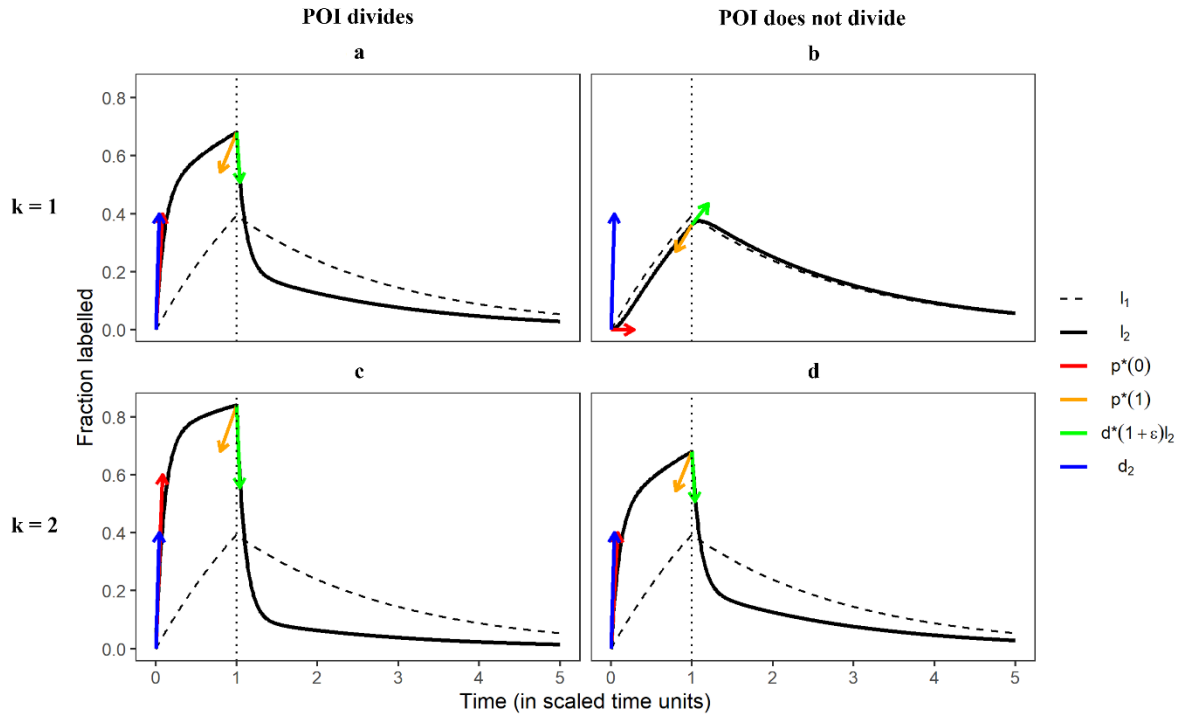


Figure S3.1: The estimated labelling rates when the POI is very short-lived. The loss rate of the POI was chosen to be 20 times higher than that of the precursors ($d_1 = 0.5$, $d_2 = 10$). Note that the slopes are calculated as the label (gain or) loss rate multiplied by the fraction of (un)labelled cells, for example, $d^*(1 + \epsilon)l_2$. The division rate of the POI, p_2 , was either set to 5 (in (a) and (c)) or 0 (in (b) and (d)).

d_1	d_2	p_2	k	$p^*(0)$	$p^*(1)$	$d^*(1 + \epsilon)$
0.5	10	5	1	5	0.68	6.33
			2	7.5	0.80	8.43
		0	1	0	0.46	-1
			2	5	0.68	6.33

Table S3.1: The true and calculated rates corresponding to the simulations shown in **Figure S3.1**. The rates (expressed as stu) are scaled with respect to the labelling period.

The best description of the labelling in the POI by the phenomenological p^*d^* model

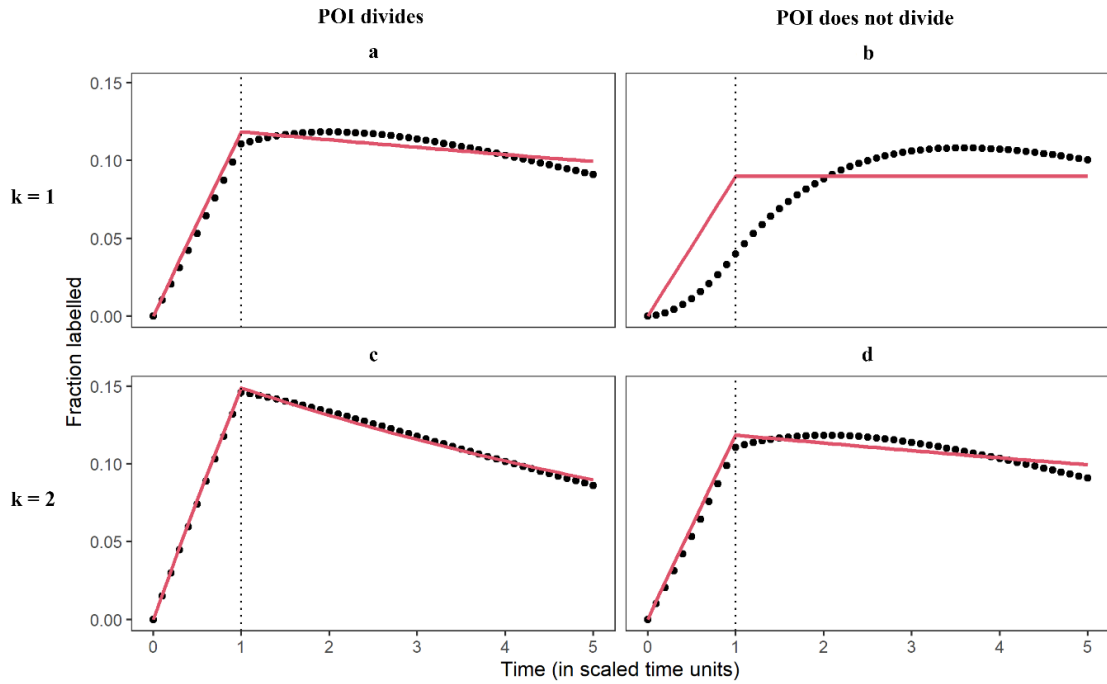


Figure S3.2: The best fits of the phenomenological model (equation 3.5 in the main text) to the labelling curve of the POIs shown in Figure 3.1. The black circles show the data, and the red trajectory shows the best fit.

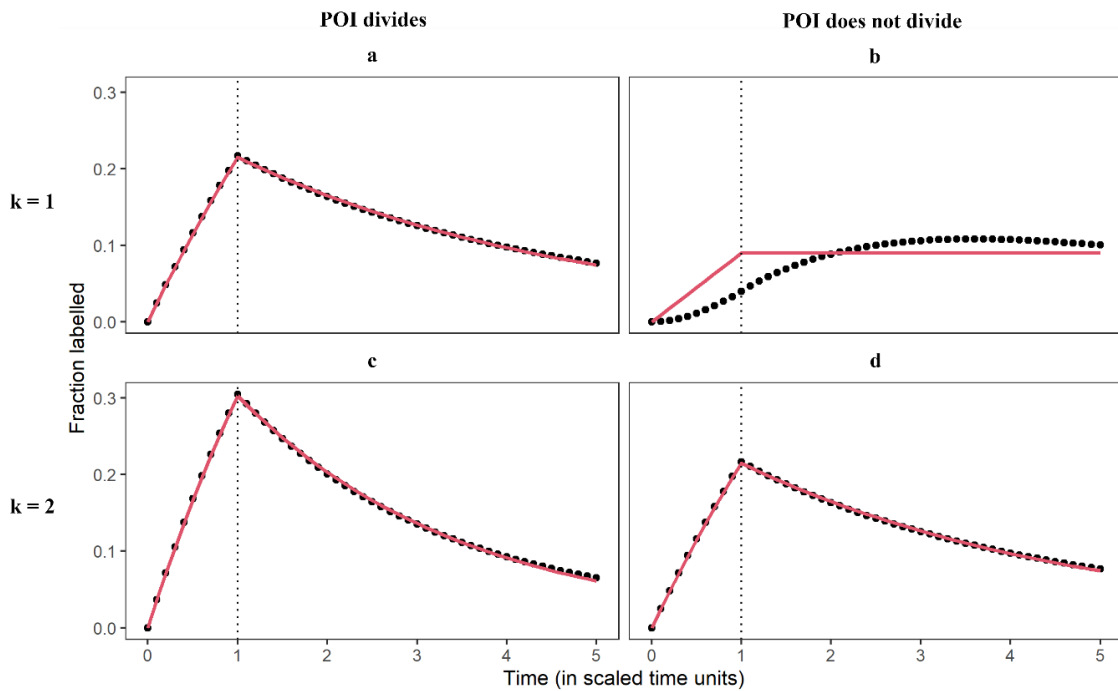


Figure S3.3: The best fits of the phenomenological model (equation 3.5 in the main text) to the labelling curve of the POIs shown in Figure 3.2. The black circles show the data, and the red trajectory shows the best fit.

Replicative history marks transcriptional and functional disparity in the CD8⁺ T cell memory pool

Kaspar Bresser^{1,10}, Lianne Kok^{1,10}, Arpit C. Swain², Lisa A. King^{1,9}, Laura Jacobs¹, Tom S. Weber^{3,4},
Leila Perié⁵, Ken R. Duffy⁶, Rob J. de Boer², Ferenc A. Scheeren⁷ and Ton N. Schumacher^{1,8}

¹Division of Molecular Oncology & Immunology, Oncode Institute, The Netherlands Cancer Institute, Amsterdam, The Netherlands.

²Theoretical Biology and Bioinformatics, Utrecht University, Utrecht, The Netherlands.

³The Walter and Eliza Hall Institute of Medical Research, Melbourne, Victoria, Australia.

⁴The Department of Medical Biology, The University of Melbourne, Melbourne, Victoria, Australia.

⁵Institut Curie, Université PSL, Sorbonne Université, CNRS UMR168, Laboratoire Physico Chimie Curie, Paris, France.

⁶Hamilton Institute, Maynooth University, Maynooth, Ireland.

⁷Department of Dermatology, Leiden University Medical Center, Leiden, The Netherlands.

⁸Department of Hematology, Leiden University Medical Center, Leiden, The Netherlands.

⁹Present address: Department of Medical Oncology, Amsterdam UMC, Vrije Universiteit Amsterdam, Cancer Center Amsterdam, Amsterdam, The Netherlands.

¹⁰These authors contributed equally to this work.

Published as: Bresser, Kok, Swain et al., Nat. Immunol., 2022; doi:10.1038/s41590-022-01171-9

Abstract

Clonal expansion is a core aspect of T-cell immunity. However, little is known with respect to the relationship between replicative history and the formation of distinct CD8⁺ memory T-cell subgroups. To address this issue, we developed a genetic-tracing approach, termed the DivisionRecorder, that reports the extent of past proliferation of cell pools *in vivo*. Using this system to genetically ‘record’ the replicative history of different CD8⁺ T-cell populations throughout a pathogen-specific immune response, we demonstrate that the central memory T-cell (T_{CM}) pool is marked by a higher number of prior divisions than the effector memory T-cell pool, owing to the combination of strong proliferative activity during the acute immune response and selective proliferative activity after pathogen clearance. Furthermore, by combining DivisionRecorder analysis with single-cell transcriptomics and functional experiments, we show that replicative history identifies distinct cell pools within the T_{CM} compartment. Specifically, we demonstrate that lowly divided T_{CM} cells display enriched expression of stem-cell-associated genes, exist in a relatively quiescent state, and are superior in eliciting a proliferative recall response upon activation. These data provide the first evidence that a stem-cell-like memory T-cell pool that reconstitutes the CD8⁺ T-cell effector pool upon reinfection is marked by prior quiescence.

Keywords: proliferation dynamics; lineage tracing; probabilistic labelling; replicative history; T-cell memory.

Introduction

The CD8⁺ T-cell compartment serves to provide protection against intracellular pathogens and also acts as a modifier of cancer growth. Upon antigen encounter, naive T cells (T_N) undergo extensive gene-expression alterations, while entering a highly proliferative state, dividing every 4 to 6 hours (Hwang et al., 2006; Yoon et al., 2010) in mice. This phase of clonal expansion gives rise to a phenotypically and functionally diverse pool of effector T cells (T_{EFF}) that exceeds its precursor population size by > 10,000-fold (Blattman et al., 2002; Obar et al., 2008). Unlike T_N cells, these T_{EFF} cells have the capacity to disseminate to peripheral tissues and can scan for and kill infected or transformed cells. Upon antigen clearance, around 95% of the T_{EFF} pool succumbs to apoptosis, leaving behind a small long-lived pool of memory T cells (T_M) that is equipped to provide long-term protection against recurring pathogens.

The central role of proliferation in the T-cell response has inspired many to study the relationship between replication and T-cell state. While earlier work hinted that memory precursor T cells have undergone limited clonal expansion (Buchholz et al., 2016; Restifo and Gattinoni, 2013), more recent work studying acute T-cell responses in humans demonstrated that T_M cells, as a whole, are derived from precursor cells that have undergone an extensive number of divisions (Akondy et al., 2017). Furthermore, prior work has shown that cell cycle speed can differ substantially between phenotypically distinct T-cell subsets at different time points in the T-cell response. Specifically, T_{CM} cells, a subgroup of memory cells that are endowed with a high level of multipotency, have been documented to undergo homeostatic proliferation after pathogen clearance, while effector memory T cells (T_{EM}) have a low turnover rate (Obar and Lefrançois, 2010; Sarkar et al., 2008). In contrast, during the effector phase, a T_{CM}-like state has been linked to lower division speed and reduced clonal burst size compared with that of their T_{EM}-like and terminally differentiated counterparts (Buchholz et al., 2013; Gerlach et al., 2013; Kinjyo et al., 2015; Kretschmer et al., 2020).

The phase-dependent association of proliferative activity within specific cell states, in combination with the reported phenotypic instability of certain T-cell subsets (Gerlach et al., 2016; Herndler-Brandstetter et al., 2018), makes it difficult to deduce the replicative history (i.e., the cumulative number of prior divisions) of different T_M cell populations and the possible relationship between replicative history and functional properties. Here, we develop a genetic-tracing approach - termed DivisionRecorder - that allows for the measurement of prior division of cell pools over extensive rounds of division, and we apply this approach to determine to what extent replicative history identifies distinct T_M cell states and behaviours. In this effort, we focus on three central issues: (1) What are the differences in replicative history between (precursor-)T_{CM} and T_{EM} cells in the effector and memory phase? (2) Is there heterogeneity in prior division within the T_{CM} pool? (3) If so, does replicative history of cells within the T_{CM} pool predict their capacity to mount a secondary T-cell response?

Results

Division-linked genetic labelling of cell pools

The genome contains a large number of hypervariable short tandem nucleotide repeats (STRs) that accumulate intra-allelic length mutations through DNA polymerase slippage during cell division. Such slippage mutations in endogenous STRs have been used to study lineage trees in various organisms and tissues (Reizel et al., 2011; Shlush et al., 2012), and synthetic STRs have previously been employed in a probabilistic-labelling approach to define stem cells in the intestinal epithelium and the mammary gland (Davis et al., 2016; Kozar et al., 2013). To investigate the replicative history of T_M cells, we engineered a synthetic STR-reporter system to continuously ‘record’ proliferation in cell pools. This genetically encoded system, termed DivisionRecorder, utilizes a synthetic STR domain to achieve a division-linked low-probability acquisition of a fluorescent mark (**Figure 4.1a**). The DivisionRecorder consists of two separate elements: (1) a retroviral-vector encoded module that contains a synthetic STR linked to an out-of-frame CRE recombinase gene; and (2) a CRE-activity reporter module that irreversibly induces the expression of a red fluorescent protein (RFP). In its base configuration, all cells that contain the DivisionRecorder express only GFP (hereafter referred to as DR^{GFP} cells). As cells undergo successive divisions, slippage mutations that occur within the synthetic STR yield in-frame variants of the downstream CRE recombinase gene at a fixed, division-dependent, probability (p). The resulting CRE activity induces an irreversible activation of the RFP gene, giving rise to GFP^+RFP^+ cells (hereafter referred to as DR^{RFP}) that pass this genetically encoded label on to subsequent generations, resulting in a cumulative increase in the DR^{RFP} cell fraction within the $DivisionRecorder^+$ (DR^+ , i.e., the sum of DR^{GFP} and DR^{RFP}) population as the cell pool expands (**Figure 4.1b**, **Supplementary Note 4.1**). Importantly, when p is small (< 0.01) the DivisionRecorder yields a near-linear relationship between the DR^{RFP} fraction and the average number of divisions over dozens of population doublings (**Figure 4.1c**) (Weber et al., 2016), thereby allowing analysis of replicative history - at the population level - far beyond what can be achieved with classical cell-labelling dyes (Tempany et al., 2018) (**Figure 4.1d**).

To test the utility of the DivisionRecorder, we established a reporter cell line carrying a lox-STOP-lox-RFP cassette. Following retroviral introduction of the GFP-STR-CRE module, a progressive increase in DR^{RFP} cells was observed over time, whereas no label acquisition was observed when the STR was replaced with a stable DNA sequence (**Figure 4.1e-f**). Moreover, the rate at which DR^{RFP} cells accumulated was dependent on the sequence stability of the STR (Koole et al., 2013; Lai and Sun, 2003), underpinning that p is linked to the likelihood of STR slippage (**Figure 4.1g**). Similarly, upon introduction of the DivisionRecorder into immortalized embryonic fibroblasts from the Ai9 mouse strain - which carries an endogenous lox-STOP-lox-RFP cassette (Madisen et al., 2010) - a low and predictable DR^{RFP} cell acquisition was observed, with a [G]33 STR conferring a p of 0.0052 ± 0.00074 (**Figure 4.1h-i**), thereby enabling the measurement of replicative history over many cell divisions (in theory $> 1,500$ population doublings, **Figure 4.1d**).

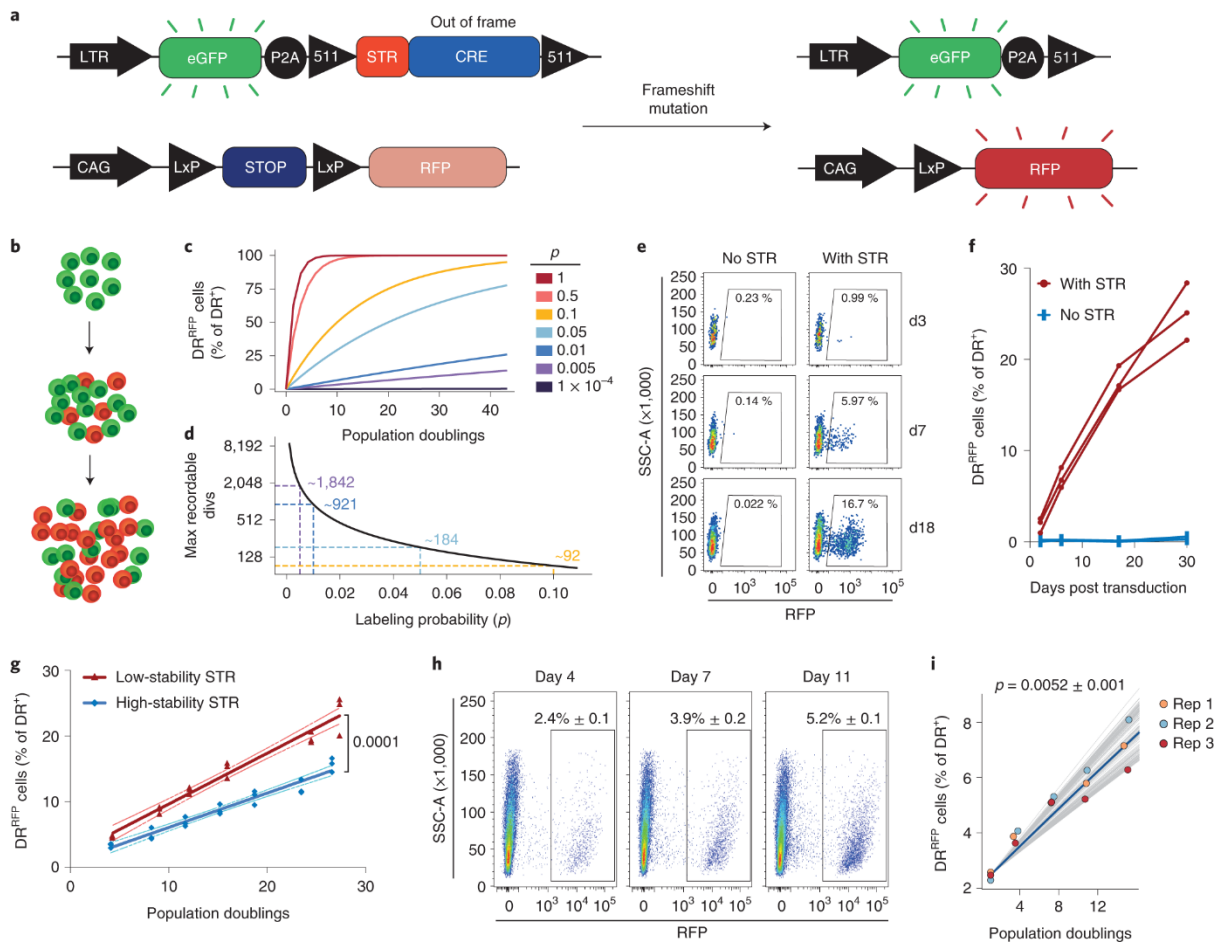


Figure 4.1: DivisionRecorder activation is a proxy for replicative history. **a**) Schematic overview of the DivisionRecorder system, **b**) Cartoon depicting progressive DivisionRecorder activation in a proliferating cell pool, **c**) Simulation of the minimal ODE model (see **Supplementary Note 4.2** for detailed description and equations), depicting DR^{RFP} acquisition as a function of population doublings for the indicated values of DR^{RFP} acquisition probability (p), **d**) Maximal number of theoretically recordable population doublings, approximated by calculating the number of division events required to reach a 99% DR^{RFP} population. Approximate maximums for selected values of p are indicated, colors correspond to legend in panel **c**, **e, f**) Percentage of DR^{RFP} cells over time in cultured DivisionRecorder⁺ (DR⁺) CRE-activity reporter HEK 293T cells ($n = 3$ replicates per group) in which the CRE recombinase gene was preceded by either a stable nucleotide region (indicated as 'no STR') or a repeat of 24 guanines (indicated as 'with STR'). Representative plots (**e**) and summarizing line graphs (**f**) are shown, **g**) Percentage of DR^{RFP} cells across population doublings in DR⁺ CRE-activity reporter HEK 293T cells ($n = 3$ replicates per group) in which the CRE recombinase gene was preceded by either a low-stability STR ([G]24) or a high-stability STR ([CA]30). Dots indicate individual samples, lines represent fitted linear regression, dotted lines indicate bounds of the 95% confidence interval, **h, i**) Percentage of DR^{RFP} cells across population doublings in immortalized DR⁺ mouse embryonic fibroblasts. Representative flow cytometry plots (**h**) and summarizing graph (**i**) are shown. Best fits of the minimal ODE model are depicted (100 bootstraps per experimental replicate, **Supplementary Note 4.2**). The blue line represents the median of the bootstraps, grey lines represent individual fits, dots indicate experimental measurements ($n = 3$ replicates). p indicates the estimated DR^{RFP} acquisition probability. Depicted experimental data are representative of at least two independent experiments. The p value in **g** was determined by two-sided analysis of covariance (ANCOVA).

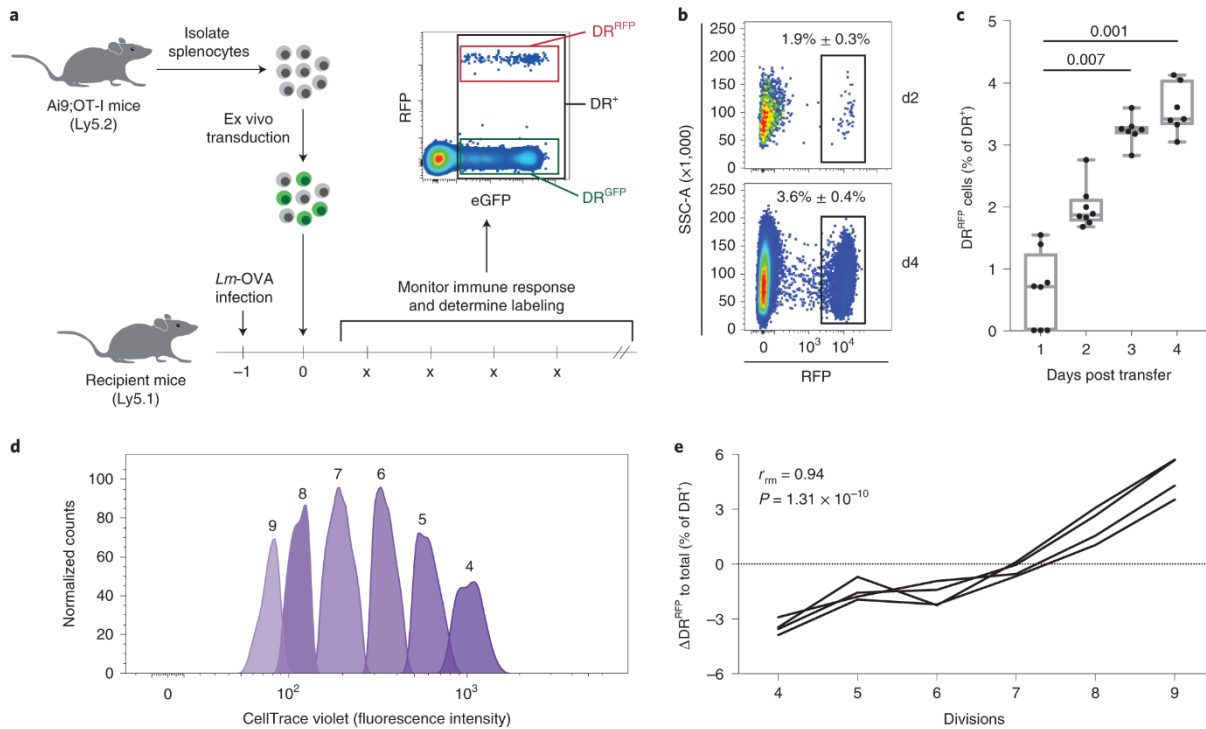


Figure 4.2: The DivisionRecorder can be applied to study T-cell division kinetics *in vivo*. **a)** Overview of experimental setup, **b,c)** DR⁺ OT-I T cells were transferred into recipient mice 24 hours post infection with *Lm*-OVA. Spleen samples were analyzed for the percentage of DR^{RFP} cells at day 1-4 post cell transfer. Representative pseudo-color density plots (**b**), and boxplots (**c**) in which the boxes indicate group median and 25th/75th percentiles, whiskers represent min/max, dots represent individual samples ($n = 8$ mice for day 1 and 2; $n = 7$ mice for day 3 and 4), **d,e)** CTV-stained OT-I T cells were retrovirally transduced with the DivisionRecorder and transferred into recipient mice ($n = 4$) 24 hours following infection with *Lm*-OVA. At 48 hours after transfer, splenic DR⁺ OT-I T cells were assessed for CTV dilution (**d**), and the percentage of DR^{RFP} cells within each division peak was analyzed (**e**). All depicted data are representative of at least two independent experiments; lines and symbols indicate individual mice or samples. p values were determined by two-sided Kruskal-Wallis test, with Dunn's multiple-comparisons test (**c**), or two-sided repeated-measurement correlation test (**e**).

To test whether the DivisionRecorder can be used as a proxy for replicative history in the CD8⁺ T-cell compartment *in vivo*, we generated Ai9;OT-I mice, in which all T cells recognize the OVA₂₅₇₋₂₆₄ epitope, thereby allowing examination of T-cell pools in the context of equal TCR affinity. Ai9;OT-I T cells were isolated, modified with the DivisionRecorder to obtain DR⁺ OT-I T cells and transferred into *Listeria monocytogenes*-OVA (*Lm*-OVA) infected mice, and the fraction DR^{RFP} cells was measured over time (**Figure 4.2a**). At early timepoints following cell transfer (d1-d4), a rapid increase in DR^{RFP} cells was observed (**Figure 4.2b-c**), coinciding with the proliferative burst of the antigen-specific CD8⁺ T-cell pool. To determine whether the observed accumulation of DR^{RFP} cells formed an accurate measure of prior cell division, DR⁺ OT-I T cells were stained with CellTrace Violet (CTV) prior to cell transfer. Notably, analysis of the fraction DR^{RFP} cells within cell pools with different degrees of CTV dilution revealed a close correlation (**Figure 4.2d-e**, $r_{rm} = 0.94$),

providing direct evidence that *in vivo* DR^{RFP} acquisition reflects the extent of past division in the CD8⁺ T-cell pool. In conclusion, these data establish that the DivisionRecorder allows for long-term measurement of division history in cell pools *in vivo*, in a way that is compatible with downstream methodologies such as single-cell sequencing (see below).

CD8⁺ T_{CM} cells are derived from replicative mature T cells

Having validated the utility of the DivisionRecorder to record T-cell division, we next sought to determine the replicative history of the total CD8⁺ T_M pool relative to that of the T_{EFF} pool. Analysis of the size of the DR⁺ OT-I T-cell compartment in blood following *Lm*-OVA infection showed the characteristic rapid expansion phase, with T-cell numbers peaking around day 6, and subsequent contraction into a stable memory pool (**Figure 4.3a**). Notably, DR^{RFP} cells remained detectable following formation of T-cell memory, thus allowing analysis of replicative history at late time points after infection (**Figure 4.3b**).

If T_M cells are primarily derived from T cells that underwent limited proliferation upon first encounter of the antigen, the fraction of DR^{RFP} cells would be expected to decay during the contraction phase, owing to the decline in the number of clonally expanded T_{EFF} cells (**Supplementary Figure 4.1** and **Supplementary Note 4.3**). However, analysis of DR^{RFP} frequencies in blood demonstrated that the fraction of DR^{RFP} cells did not decline, but instead continued to increase during the contraction and memory phase (an increase of 2.07% ± 0.77% between day 13 and 59, **Figure 4.3c**). This increase in DR^{RFP} frequencies following pathogen clearance was not restricted to T-cell responses induced by *Lm*-OVA infection, but was also observed upon infection with LCMV-OVA (Kallert et al., 2017) (**Figure 4.3d**), and was not due to anatomical redistribution of cells with distinct division histories, as the fraction of DR^{RFP} cells increased concurrently in peripheral blood and the primary sites of *Lm*-OVA infection (spleen/liver; **Figure 4.3e-f**). Thus, in line with work by Akondy et al. (Akondy et al., 2017), our results support the notion of a replicative ‘mature’, rather than ‘nascent’, CD8⁺ T_M pool, and extend this observation beyond the peripheral blood compartment to the sites of infection.

It has been well-documented that T_{CM} cells are able to maintain the memory pool through infrequent homeostatic cell division (Becker et al., 2002; Gerlach et al., 2016; Wherry et al., 2003), and recent work has shown that precursor-T_{CM} cells slow down their replicative cycle early during the expansion phase (Kretschmer et al., 2020), suggesting limited clonal expansion of these cells during the early phase of the T-cell response. However, it is difficult to translate cell cycle activity at a given timepoint into cumulative proliferative history, and we therefore wished to directly test the relationship between cell state (e.g., T_{CM} or T_{EM}) and replicative history during different stages of the T-cell response. To this end, the fraction of DR^{RFP} cells within the T_M pool was calculated at varying expression levels of proteins associated with either multipotency or terminal differentiation (**Figure 4.3g**). This analysis revealed a positive correlation between replicative history and the expression of the T_{CM}-associated proteins CD27 ($r_{rm} = 0.81$, $p = 6.2 \times 10^{-14}$) and CD62L ($r_{rm} = 0.62$, $p = 5.6 \times 10^{-14}$).

⁷) (Gerlach et al., 2016; Graef et al., 2014; Olson et al., 2013), and a negative relationship between prior division and the expression of the T_{EM}-associated proteins KLRG1 ($r_{rm} = -0.83$, $p = 9.0 \times 10^{-15}$) and CX3CR1 ($r_{rm} = -0.75$, $p = 4.5 \times 10^{-11}$) (Gerlach et al., 2016; Herndler-Brandstetter et al., 2018; Youngblood et al., 2017). Likewise, defining multipotent T_{CM} and terminally differentiated T_{EM} subsets by joint expression or absence of CD62L and CD27, respectively, (**Supplementary Figure 4.2a**), and further partitioning on the basis of the expression of KLRG1 or CX3CR1 revealed a positive association between division history and a less differentiated cell state (**Supplementary Figure 4.2b**). Furthermore, the division history of CD27^{hi}KLRG1^{lo} T_{CM} cells present in lymph nodes equalled that of T_{CM} cells in the spleen, implying that division history is dictated by cell state rather than anatomical location (**Supplementary Figure 4.2c**).

Next, to delineate at which point the divergence in replicative history between T cells with a T_{CM}-like multipotent and T_{EM}-like terminally differentiated phenotype developed, we assessed the link between phenotypic marker expression and DR^{RFP} fractions throughout the T-cell response. Notably, replicative history varied minimally across T_{EFF} cell states at the peak of the antigen-specific T-cell response (d6 post transfer, **Figure 4.3h** and **Supplementary Figure 4.2d-f**), followed by selective accumulation of DR^{RFP} within the CD27^{hi}KLRG1^{lo} early-T_{CM} pool directly after the peak of the expansion phase (**Figure 4.3h-i** and **Supplementary Figure 4.1g**), owing to continued replicative activity of this subset (**Figure 4.3j-k**). The observation that the division history of CD27^{lo}KLRG1^{hi} T cells stays constant after the effector phase (**Figure 4.3i**) suggests that, in addition to the previously documented lack of proliferative activity of this cell pool (Gerlach et al., 2016; Voehringer et al., 2001; Wherry et al., 2003), this terminally differentiated subset does not receive notable replenishment by the replicative active CD27^{hi}KLRG1^{lo} T-cell pool (**Supplementary Figure 4.1h**). The substantial number of divisions that we observe in the CD27^{hi}KLRG1^{lo} cell pool at the peak of the response appears at odds with proposed limited clonal expansion of precursor-T_M cells. However, these observations may either be reconciled by the reported trans-differentiation between T_{EFF} cell states (Gerlach et al., 2016; Herndler-Brandstetter et al., 2018; Youngblood et al., 2017), or by the fact that a reduced proliferative activity may form a property of only a small part of the memory precursor pool (Kinjyo et al., 2015; Kretschmer et al., 2020; Lin et al., 2016). In summary, the above data indicate that the high amount of prior division of the T_{CM} pool results from both strong proliferative activity during the effector phase and selective proliferative activity after pathogen clearance.

Replicative history identifies distinct T_{CM} cell states

Increasing evidence suggests that the T_{CM} pool is highly heterogeneous in terms of both gene-expression profiles and prior and ongoing replicative behavior (Gerlach et al., 2016; Herndler-Brandstetter et al., 2018; Johnnidis et al., 2021), providing an incentive to test for possible associations between division history and transcriptional states within this cell pool. To this end, we carried out single-cell mRNA sequencing (scRNAseq) on DR^{GFP} and DR^{RFP} memory OT-I T cells (75-85 days following *Lm*-OVA infection **Supplementary Figure 4.3**).

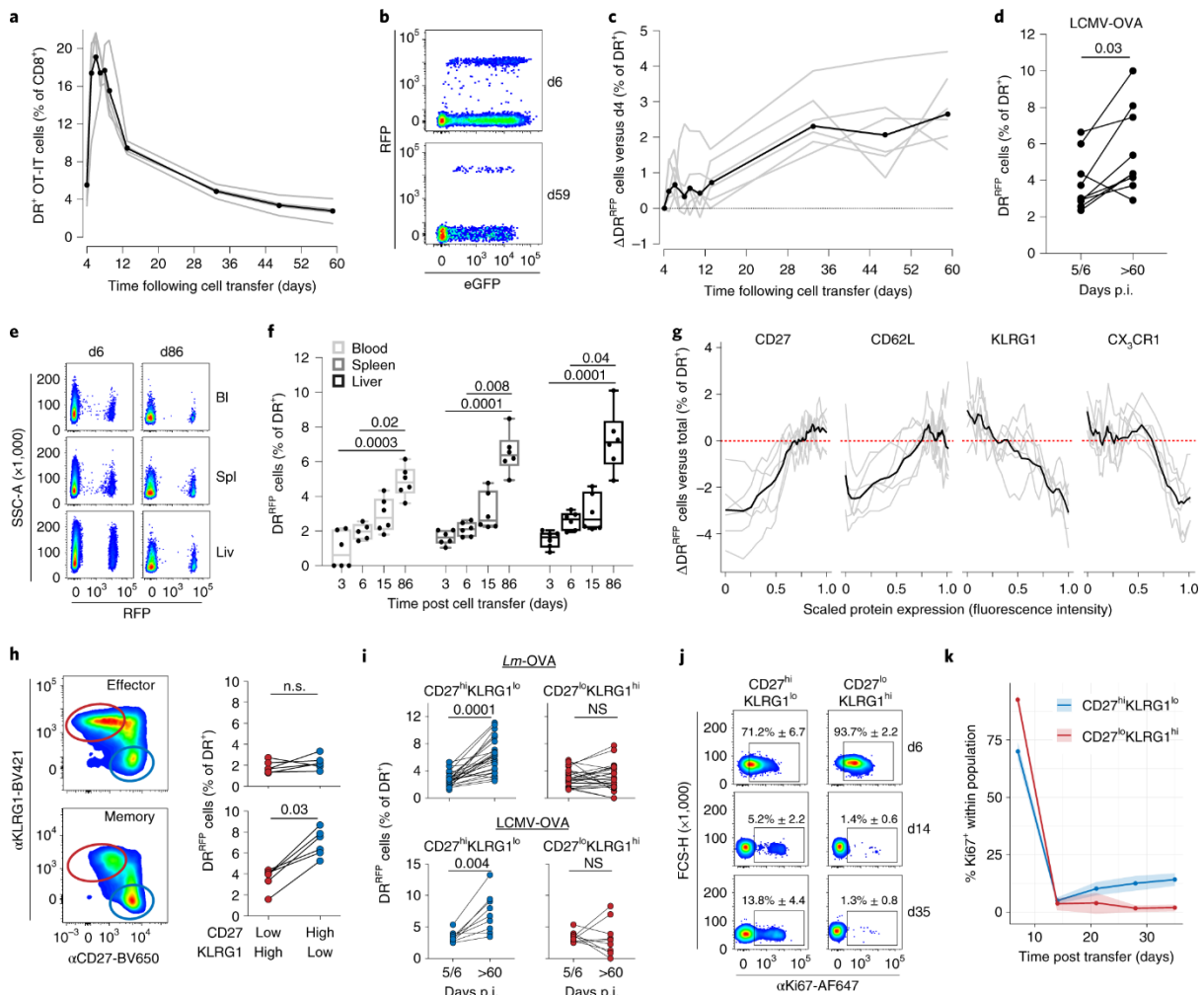


Figure 4.3: The multipotent T_M cell pool is formed by replicative ‘mature’ cells. **a-c)** Kinetics of DR^+ OT-I T cells (**a**) and the percentage of DR^{RFP} relative to day 4 (**c**) in response to *Lm*-OVA, measured in peripheral blood ($n = 6$ mice). Representative flow cytometry plots (**b**) showing DR^{RFP} and DR^{GFP} frequencies at indicated time points, and line graphs (**a,c**) depicting kinetics of single mice (grey) and group median (black), **d**) DR^{RFP} percentages within blood at day 5/6 (T_{EFF}) and day > 60 (T_M) following LCMV-OVA infection ($n = 7$), **e**) Representative plots depicting DR^{RFP} frequencies in blood (Bl), spleen (Spl) and liver (Liv), **f**) Percentage of DR^{RFP} cells detected in the indicated organs of recipient mice at the indicated time points ($n = 6$ mice per time point; response to *Lm*-OVA). Boxplots indicate the group median and 25th and 75th percentiles, whiskers represent the minimum and maximum, and dots represent individual samples, **g**) Moving average of surface marker expression level on splenic DR^+ cells plotted against the percentage of DR^{RFP} cells within each window during memory phase (day 86; $n = 6$); means are shown in black. DR^{RFP} percentages within each window are corrected for the total percentage of DR^{RFP} cells detected in that sample, **h**) Gating strategy (left) and DR^{RFP} percentages (right) of $CD27^{hi}KLRG1^{lo}$ and $CD27^{lo}KLRG1^{hi}$ cells in spleen during the effector (d6, top) and memory phase (d86, bottom; $n = 6$) in response to *Lm*-OVA, **i**) DR^{RFP} percentages within the $CD27^{hi}KLRG1^{lo}$ and $CD27^{lo}KLRG1^{hi}$ cell populations in blood, comparing effector (day 5/6) and memory (day > 60) phases. Data are shown for *Lm*-OVA (top; $n = 22$) and LCMV-OVA (bottom; $n = 7$) infections. Lines connect data from individual mice, **j,k**) Ki67 expression by $CD27^{hi}KLRG1^{lo}$ and $CD27^{lo}KLRG1^{hi}$ OT-I cells in blood in response to *Lm*-OVA. Representative flow cytometry plot (**j**), and line graphs (**k**) in which solid lines indicate population means and shaded areas indicate the 95% confidence interval ($n = 11$ mice). All depicted data are representative of at

least two independent experiments; lines and symbols indicate individual mice or samples. p values were determined by two-sided Kruskal-Wallis test with Dunn's multiple comparisons test (**f**), or two-sided Wilcoxon's signed-rank test (**d,h,i**).

In addition, to test whether DR⁺ OT-I T_M cells assume the same spectrum of transcriptional states as non-modified T cells, we performed scRNAseq on OT-I T_M cells that were generated through adoptive transfer of a small number (2,000) of naive OT-I T cells, followed by *Lm*-OVA infection 24 hours later. DR⁺ OT-I and unmodified OT-I T_M cells were jointly grouped into 23 transcriptionally distinct MetaCells (MCs) (Baran et al., 2019), including 4 T_{EM} and 19 T_{CM} MCs, on the basis of the expression of a small set of multipotency- and effector-associated genes (**Figure 4.4a,b**). Notably, while T_M cells derived from small numbers of unmodified OT-I T cells showed a proportionally greater contribution to T_{EM} MCs - consistent with the relationship between precursor frequency and T_{EM} formation (Badovinac et al., 2007) - DR⁺ OT-I T cells and unmodified OT-I T cells were equal in their potential to yield the 19 distinct T_{CM} MCs (**Supplementary Figure 4.4**), indicating that the introduction of the DivisionRecorder did not measurably impact the ability of T cells to differentiate into different T_{CM} states.

Among the observed T_{CM} MCs, two transcriptionally distinct subgroups could be identified (**Figure 4.4b**). Specifically, while all T_{CM} cells showed the expected high expression of *Bcl2*, *Sell*, and *Cd27* and minimal expression of *CX3CR1*, *Zeb2*, *Gzma*, and *Prdm1* (**Figure 4.4c**, **Supplementary Figure 4.5a**), a dichotomy was observed in the expression of multipotency-associated (e.g., *Myb* and *Ccr7*) and effector-associated (e.g., *Tbx21* and *Lgals1*) genes within the T_{CM} pool (denoted as T_{CM}(mult.) and T_{CM}(eff.), respectively in the figures; **Figure 4.4b**, **Supplementary Figure 4.5a**). Next, we assessed the relationship between transcriptional state and replicative history within the T_M cell pool. In line with the flow cytometry data, the replicative history of T_{CM} - as a whole - exceeded that of T_{EM}, thereby validating the scRNAseq approach. Strikingly, T_{CM} cells enriched for effector genes had overall higher DR^{RFP}/DR^{GFP} ratios compared with T_{CM} cells enriched for multipotency genes, demonstrating that stemness-related transcriptomic features are inversely associated with division history within the T_{CM} pool (**Figure 4.4d**). Correspondingly, comparison of the three T_{CM} MCs with the highest and lowest level of prior division (hdT_{CM} and ldT_{CM}, respectively) revealed that ldT_{CM} cells were marked by the expression of key multipotency-associated genes, including *Tcf7*, *Sell*, *Myb*, and *Eomes*, and several survival factors (*Gimap* and *Birc* family members, **Supplementary Figure 4.5b-c**). Moreover, one ldT_{CM} MC was highly enriched for transcripts involved in inhibitory function (*Lag3*, *Cd160*, *Tox*), suggesting a possible analogy with the inhibitory signalling-dependent T_{CM}-precursor subset identified by Johnnidis et al. (Johnnidis et al., 2021) (**Supplementary Figure 4.5c**). In contrast, hdT_{CM} cells commonly expressed genes related to terminal differentiation, such as *Lgals1* and *S100* family members, and showed increased transcript levels for cytotoxicity-associated genes (*Nkg7*, *Ctsw*; **Supplementary Figure 4.5b-c**). This link between replicative history and a multipotency versus effector-associated gene expression signature within the T_{CM} pool was further validated by differential gene expression analysis and gene set enrichment analysis (**Figure**

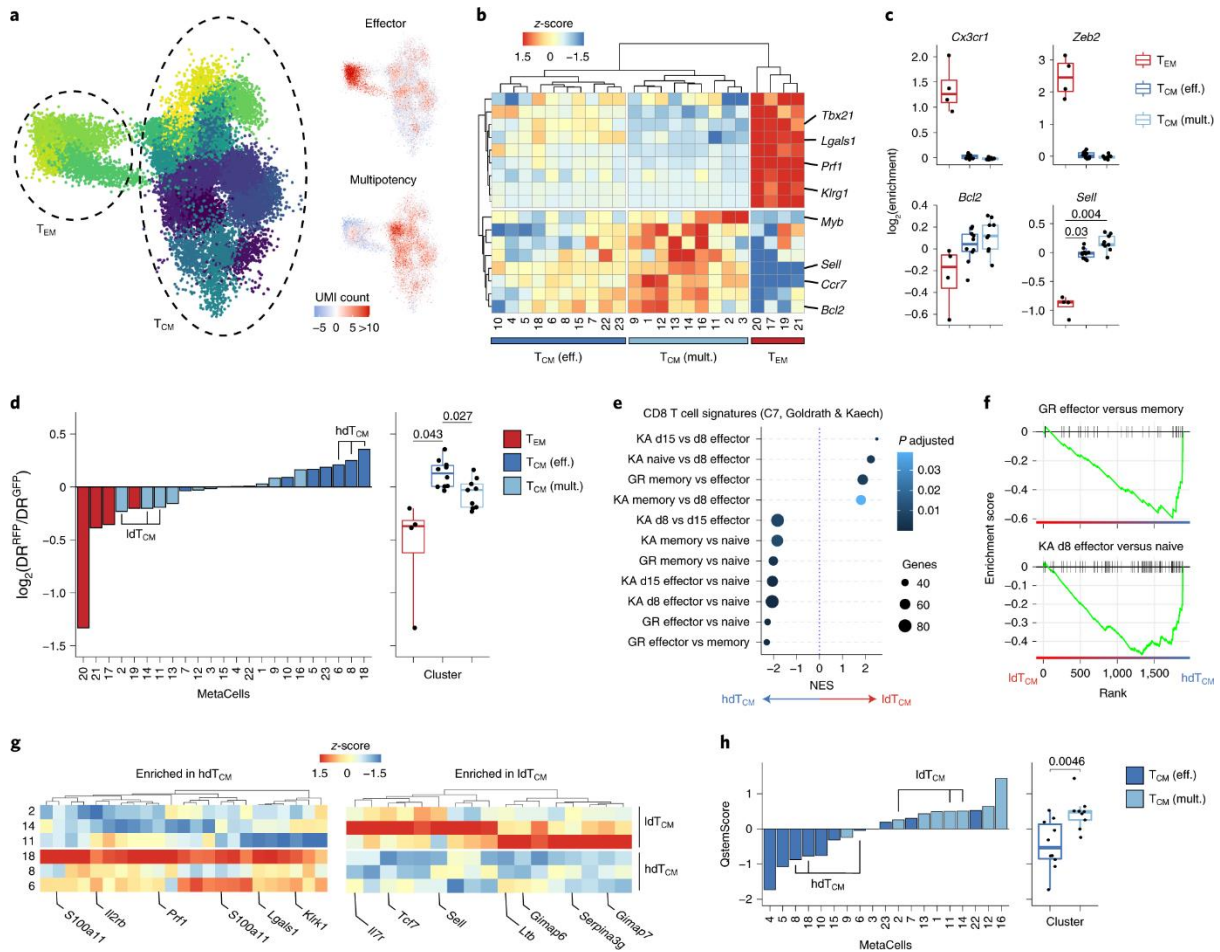


Figure 4.4: Replicative history identifies distinct transcriptional states within the T_{CM} pool. Single-cell transcriptomics profiling of DR⁺ T cells obtained from spleen in memory phase (day 75 and day 85 after *Lm*-OVA infection). **a**) 2D projection of all profiled cells. Colors indicate MCs (left) or relative expression of effector- and multipotency-associated genes (right). Gene list in **Supplementary Table 4.1**, **b**) Hierarchical clustering of MCs by their expression of effector- and multipotency-associated genes used in **a**. MCs are divided into three clusters on the basis of Euclidean distance, **c**) Expression of selected genes by each MC cluster, **d**) DR^{RFP}/DR^{GFP} ratio within each MC, depicted as waterfall plot (left) and boxplot (right), **e, f**) Enrichment of gene signatures from MsigDB (C7, collections deposited by Goldrath (GR) and Kaech (KA), **Supplementary Table 4.2**) by gene set enrichment analysis comparing IdT_{CM} and hdT_{CM} (**e**) and enrichment plots (**f**) of two representative gene sets. NES, normalized enrichment score, **g**) Heatmaps depicting genes involved in immune function that were significantly ($p < 0.05$) depleted (left) or enriched (right) within IdT_{CM} (see **Supplementary Figure 4.4d** and **Supplementary Table 4.3**). Selected genes are annotated; complete gene lists are provided in **Supplementary Table 4.4**, **h**) QstemScore of all T_{CM} MCs depicted as waterfall plot (left) and boxplot (right). QstemScore is based on marker genes of quiescent stem cells (**Supplementary Table 4.5**) (Youngblood et al., 2017), see methods for calculation. Data depicted were accumulated in two independent experiments (3-4 mice per experiment). Boxplots (**c, d, h**) indicate group median and 25th and 75th percentiles, whiskers indicate the interquartile range multiplied by 1.5, and dots signify individual MCs. The phenotype clusters T_{EM}, T_{CM} (eff.), and T_{CM} (mult.) contain four, nine, and ten MCs, respectively. p values were determined by two-sided Tukey's HSD test (**c**), two-sided Student's t test with false-discovery rate correction (**d, h**), the FGSEA algorithm followed by the Benjamini-Hochberg procedure (**e**), or two-sided Wilcoxon rank-sum test with Bonferroni correction (**g**). Significant p values (< 0.05) are indicated in the plots.

4.4e-g, Supplementary Figure 4.5d). In line with this association, *ex vivo* antigen stimulation of DR⁺ T_{CM} cells collected from mice > 60 days post *Lm*-OVA infection showed that T_{CM} cells that had undergone more prior divisions were more likely to degranulate and less likely to produce IL-2 than their less divided T_{CM} counterparts (**Supplementary Figure 4.5e-f**).

The observed divergence in replicative history between distinct T_{CM} states potentially reflects the selective quiescence of a subset of T_{CM} cells with a less differentiated state. Of note, IdT_{CM} showed reduced expression of Myc targets and genes involved in cell metabolism (**Supplementary Figure 4.5g**), suggesting that these cells exist in a transcriptionally enforced replicative quiescent state. To test for such a transcriptional state, we scored the expression of a core gene set of quiescent stem cells from various tissues (Cheung and Rando, 2013) (hereafter referred as QstemScore). Notably, T_{CM} cells that showed increased expression of multipotency-associated genes were marked by a higher QstemScore than that of T_{CM} cells with increased expression of effector-associated genes (**Figure 4.4h**). Moreover, variation in QstemScore could also be detected in gp33-specific P14 T_{CM} cells from an external dataset (Kurd et al., 2020), and those P14 T_{CM} cells that prominently expressed this gene set transcriptionally resembled the multipotency-signature^{hi}effector-signature^{lo} OT-I IdT_{CM} described here (**Supplementary Figure 4.6**). Together, these data suggest a link between T_{CM} quiescence and the expression of multipotency-associated genes, driving the divergence in replicative history between distinct T_{CM} states.

To directly test whether replicative behaviour in the T_{CM} pool is associated with a multipotency-associated state and relates to the functional capacity of T_{CM} to re-expand upon secondary activation, we established a DivisionRecorder-independent, CTV-based serial-transfer approach (**Figure 4.5a**). Naive OT-I and GFP;OT-I T cells were transferred into primary recipients that were subsequently exposed to *Lm*-OVA infection. At day 30 post-infection, early T_M cells were collected, CTV labelled and transferred into infection-matched secondary recipients. At 75 days later, CTV^{hi} (div0-2) and CTV^{lo} (div5+) T_{CM} cells were isolated, and the resulting T_{CM} populations were then profiled by scRNAseq or were transferred at a 1:1 ratio into tertiary recipients that were subsequently challenged with *Lm*-OVA. Strikingly, comparison of quiescent (div0-2) cells and proliferative (div5+) T_{CM} cells by gene set enrichment analysis revealed a clear negative association between quiescence and an effector-like transcriptional state, while quiescence was positively associated with multipotency-associated gene expression (**Figure 4.5b-c, Supplementary Figure 4.7a**). Likewise, inspection of MCs (**Supplementary Figure 4.7b-e**) that were enriched in the div0-2 cells, showed a prominent expression of multipotency-associated genes (*Myb*, *Tcf7*, *Id3*), whereas those enriched in div5+ cells showed increased expression of effector-associated genes (*Id2*, *S00a4*, *Lgals1*) (**Figure 4.5d-e**). Furthermore, comparison of the expansion potential of div0-2 and div5+ T_{CM} cells demonstrated that quiescent T_{CM} cells were superior in generating offspring upon renewed infection (**Figure 4.5f-g**), further demonstrating that replicative heterogeneity in the T_{CM} pool is both linked to transcriptional state and functionality.

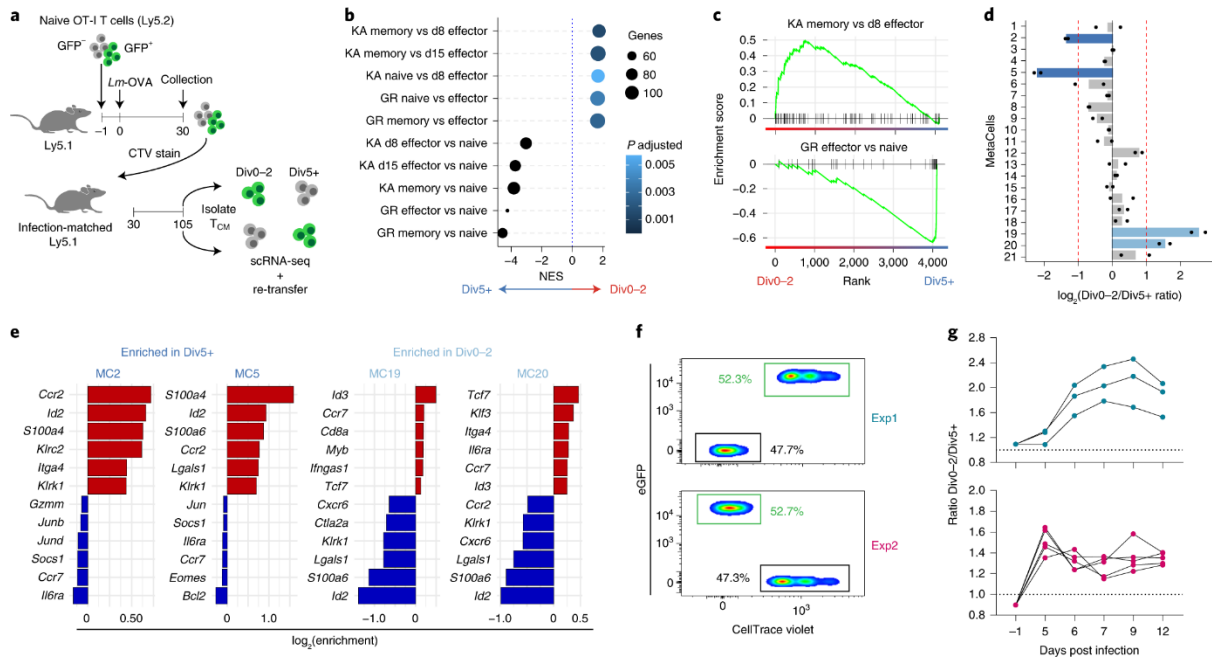


Figure 4.5: Replicative history is linked to recall potential within the T_{CM} pool. **a**) Experimental setup. Primary recipient mice received 5×10^5 naive OT-I and 5×10^5 naive GFP⁺/OT-I T cells. Thirty days after *Lm*-OVA challenge, CD8⁺ T cells were enriched, labelled with CTV, and transferred into infection-matched secondary recipient mice (one primary recipient per secondary recipient). At d105 after infection, splenic CD27⁺KLRG1⁻ T_{CM} cells that had either divided 0-2 or 5+ times and were either GFP⁺ or GFP⁻ were isolated by FACS, **b**) Enrichment of gene signatures from MsigDB (C7, collections deposited by Goldrath (GR) and Kaech (KA), **Supplementary Table 4.2**) between div0-2 and div 5+ cells. Top and bottom 5 pathways are depicted, **c**) Enrichment plots of representative pathways detected by gene set enrichment analysis, **d**) Ratio of normalized counts between div0-2 and div5+ cells within each MC separately calculated for GFP⁺ and GFP⁻ populations. Bars indicate averages, dots indicate ratios of either GFP⁺ or GFP⁻ OT-I T cells. Red dotted lines indicate a fold change of 2, **e**) Waterfall plots depicting top and bottom six marker genes for selected MCs, filtered for genes involved in immune function (**Supplementary Table 4.3**), **f**) Flow cytometry plots depicting pre-transfer mixes of div0-2 and div5+ T_{CM} cells, **g**) T_{CM} cells (8,000-12,000 total) as described in **f** were transferred into infection-naive mice, followed by *Lm*-OVA challenge 24 hours later. Ratios between div0-2- and div5+-derived cells were determined from peripheral blood samples at indicated days post infection. Lines connect populations from individual mice (experiment 1, $n = 3$; experiment 2, $n = 5$). Depicted scRNAseq data were collected from four mice, data describing recall potential was obtained from eight mice. p values were determined by the FGSEA algorithm followed by the Benjamini-Hochberg procedure (**e**).

Re-expansion potential of T_{CM} cells is linked to prior division

Having observed a link between prior division and recall potential in adoptive transfer experiments, we set out to verify this relationship without disruption of the T_{CM} niche, through re-challenge of recipient mice carrying DR⁺ memory OT-I T cells. In case the capacity for renewed expansion would primarily be restricted to replicative quiescent T_{CM} cells, the fraction of DR^{RFP} cells should show an initial decay upon reinfection - due to the increased

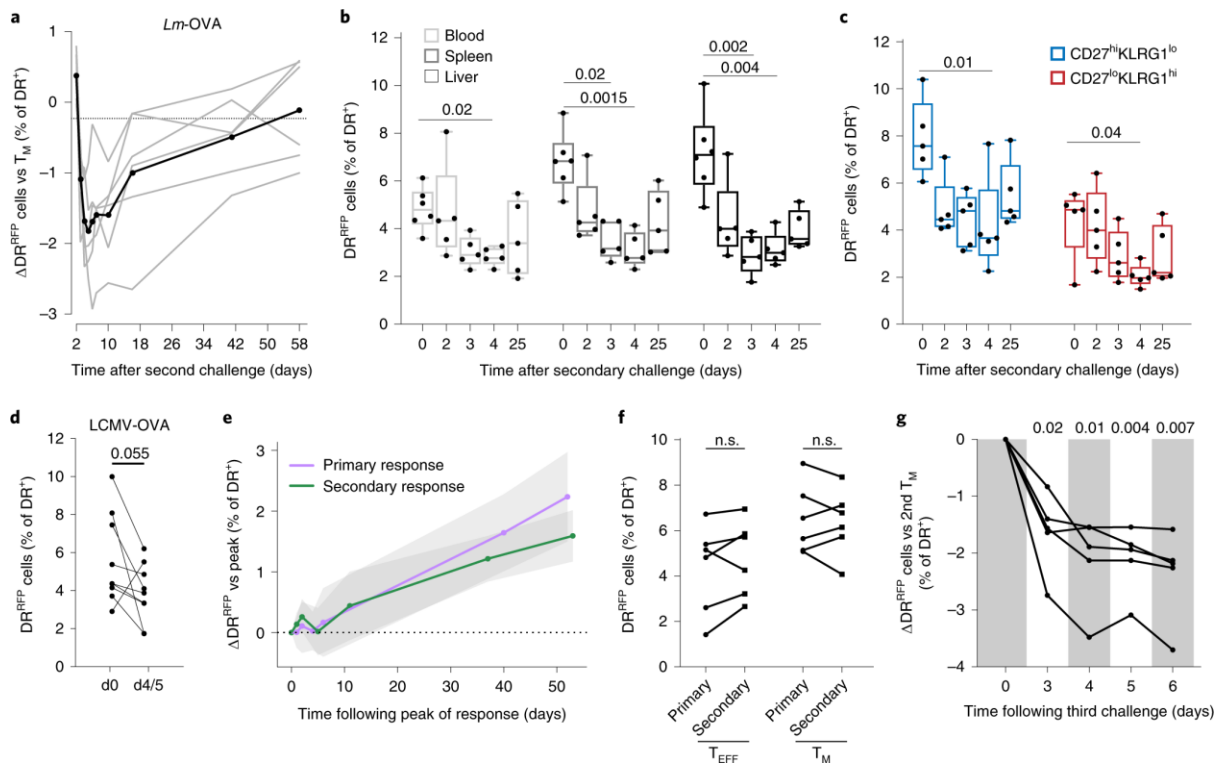


Figure 4.6: The secondary T_{EFF} pool is predominantly generated by previously quiescent memory T cells. **a**) Kinetics of the percentage of DR^{RFP} cells in blood upon secondary *Lm*-OVA infection. Values are relative to the DR^{RFP} percentage within the respective memory pools ($n = 6$ mice); the black line represents the group mean, **b,c**) DR^{RFP} percentages in the indicated organs (**b**) or within splenic CD27^{lo}KLRG1^{hi} and CD27^{hi}KLRG1^{lo} populations (**c**) at indicated time points ($n = 6$ mice per time point) following secondary infection. Boxplots indicate group median and 25th and 75th percentiles, whiskers represent the minimum and maximum, and dots represent individual samples, **d**) DR^{RFP} percentages in blood during the memory phase (day > 60) and at the peak of the secondary response (day 4/5 post-recall). Memory pools were generated with LCMV-OVA, recall infection was performed with *Lm*-OVA, **e**) DR^{RFP} acquisition in blood following primary and secondary infection. Values are relative to DR^{RFP} percentage at the peak of the primary or secondary response. Lines represent group medians ($n = 6$ mice per group), and greyed areas represent 95% confidence intervals, **f**) DR^{RFP} percentages in blood during effector and memory phases of the primary and secondary responses. Lines connect data from individual mice ($n = 6$), **g**) DR^{RFP} percentages in blood ($n = 5$ mice) upon tertiary infection. Mice were challenged twice with *Lm*-OVA with a > 60 day interval and were subsequently infected with LCMV-OVA > 60 days after secondary infection. Depicted data are representative of at least two independent experiments. p values were determined by two-sided Kruskal-Wallis test with Dunn's multiple-comparisons test (**b,c**), two-sided Wilcoxon signed-rank test (**d,f**), or repeated-measures one-way ANOVA followed by Dunnett correction (**g**).

preponderance of offspring derived from this previously quiescent population - followed by a gradual recovery throughout the contraction phase, as a result of novel division-dependent label acquisition. Notably, analysis of the fraction DR^{RFP} T cells in blood revealed a steep decline during the first days following secondary infection, followed by a gradual recovery during secondary memory formation (**Figure 4.6a**, **Supplementary Note 4.4**). This transient

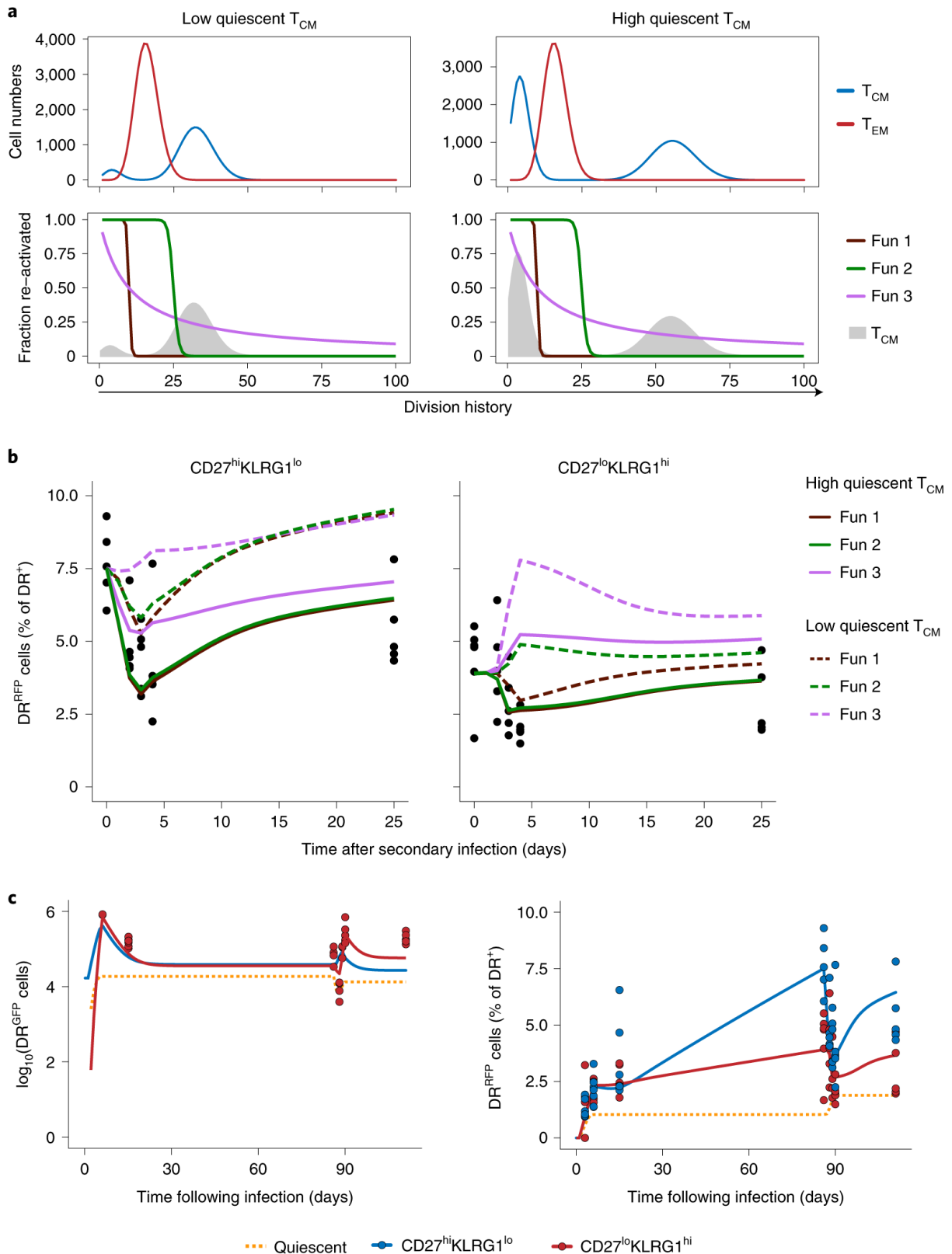


Figure 4.7: Modelled T-cell responses are consistent with the presence of a replication-competent quiescent T_{CM} population. **a**) Division history of T_{CM} and T_{EM} pools generated by modelled T-cell responses (see **Supplementary Note 4.5**) during which a high (capped at 1% of the T_{EFF} pool size) or low (capped at 0.1% of the T_{EFF} pool size) fraction of T cells acquire quiescence during the effector phase (top). Three re-expansion functions were used to restrict which fraction of

T_{CM} with a given number of prior divisions will re-expand during recall (bottom). For reference, the division history of T_{CM} is shown as a shaded area, **b**) Modelled DR^{RFP} percentages within the $CD27^{lo}KLRG1^{hi}$ and $CD27^{hi}KLRG1^{lo}$ populations during secondary responses, with each re-expansion function applied to a memory pool containing either a high or low number of quiescent T_{CM} cells. Black dots indicate experimental measurements, **c**) Best fit of the modelled T-cell response (number of quiescent T cells capped to 1% of T_{EFF}) experimental data obtained from spleen, depicting either cell numbers (left) or DR^{RFP} percentages (right). See **Supplementary Note 4.5** for details. Lines indicate the modelled populations; dots indicate experimental measurements.

reduction in the DR^{RFP} fraction was observed in multiple anatomical compartments (blood, spleen, liver), occurred independent of cell phenotype, and was also observed in LCMV-OVA-induced T_M pools responding to secondary challenge (**Figure 4.6b-d**). Of note, DR^{RFP} cell accumulation during the secondary contraction phase occurred at a comparable rate as observed during the primary response (**Figure 4.6e**), yielding a secondary T_M pool that - despite extensive renewed clonal expansion - had undergone a similar number of divisions as the initial memory pool (**Figure 4.6f**, median fold difference = 1.03). Thus, the replicative histories of the T_{EFF} and T_M pools of the secondary T-cell response mimic those of the primary T-cell response, supporting the notion that the secondary expansion wave is mounted by a group of T_{CM} cells that has undergone limited prior division. Furthermore, this low-division T_{CM} pool is able to repeatedly reconstitute the effector T-cell pool, as the same decrease in the fraction of DR^{RFP} cells was observed upon tertiary infection of mice (**Figure 4.6g**).

To determine whether the observed data are consistent with re-expansion being driven by a T_M -cell subset that becomes quiescent early in the immune response, we simulated T-cell responses in which a fraction of T_{CM} precursors acquires replicative quiescence during the primary T-cell response (see **Supplementary Note 4.5**, **Supplementary Figure 4.8a**). Specifically, T-cell responses were simulated that yielded quiescent T cells at a frequency of either $\sim 0.1\%$ or $\sim 1\%$ of the T_{EFF} pool, resulting in T_M pools in which quiescent T_{CM} cells accounted for $\sim 3\%$ and $\sim 25\%$ of the memory population (**Figure 4.7a**). Modelling of DR^{RFP} labelling rates during recall responses in which the potential to re-expand was either abruptly lost as a function of the number of prior divisions (fun 1 and 2), or was lost more gradually across division history (fun 3), demonstrated that the transient drop in DR^{RFP} fractions is consistent only with models in which the capacity to re-expand is restricted to cells that have undergone limited clonal expansion (**Figure 4.7b**). Furthermore, the stringency of this relation is strongly dependent on the relative size of the quiescent T_{CM} pool (**Figure 4.7b**).

Taken together, our data establish that replicative state is not homogeneously distributed within the T_{CM} pool and is linked to distinct transcriptional and functional properties. Specifically, our observations are consistent with a dichotomy in the T_{CM} pool in which a self-renewing T_{CM} population maintains the T_M pool but marginally contributes to secondary expansion, and a replication-competent quiescent T_{CM} population is required to form the T_{EFF} pool that arises upon renewed infection (**Figure 4.7c**, **Supplementary Figures 4.8 and 4.9**).

Discussion

Here, we report the development and application of the DivisionRecorder to dissect the replicative history of cell pools *in vivo*. We show that this approach allows longitudinal examination of division history, and how it may be combined with technologies such as flow cytometry and scRNAseq to couple cell state to division history. In the application presented here, the DivisionRecorder requires viral transduction to introduce one of its modules. While this did not considerably disrupt cell behaviour in our study, development of a fully germline-encoded DivisionRecorder system will be attractive, for instance, to follow replicative behaviour of cell pools that are not amenable to adoptive transfer.

Using the DivisionRecorder, we demonstrate that, as a whole, the multipotent CD8⁺ T-cell pool has undergone substantial proliferation at the peak of the expansion phase, and continues to proliferate following pathogen clearance, resulting in a cumulative replicative age of the T_{CM} pool that exceeds that of the T_{EFF} and T_{EM} pool. Previous work has shown that a fraction of CD62L^{hi} precursor-T_M cells divide at a lower rate than do terminally differentiated effector subsets (Kinjyo et al., 2015; Kretschmer et al., 2020; Lin et al., 2016). In line with this, we observed a lower fraction of Ki67^{hi} cells within the multipotent effector pool than in the terminally differentiated pool, early post infection. At the same time, our data indicate that this difference does not result in a reduced cumulative number of past divisions within the entire CD62L^{hi} T_{EFF} pool. Conceivably, these findings may be reconciled by the ability of highly proliferative CD62L^{lo} T_{EFF} cells to phenotypically convert to a less differentiated CD62L^{hi} state (Gerlach et al., 2016; Herndler-Brandstetter et al., 2018; Youngblood et al., 2017). Alternatively, the precursor-T_{CM} pool may harbour a heterogeneity in replicative history that is not revealed by the phenotypic markers used.

In line with the latter possibility, by combining the DivisionRecorder with scRNAseq we reveal that, although the T_{CM} pool has undergone substantial prior division as a whole, replicative history is heterogeneous within this pool and is associated with specific transcriptional states. First, our data demonstrate the presence of T_{CM} cells that bear transcriptional similarities to T_{EM} cells but, in contrast to T_{EM} cells, remain highly proliferative in the absence of inflammation (**Supplementary Figure 4.9**). Second, we identify a population of quiescent T_{CM} cells that expresses reduced levels of effector-associated genes, and high levels of pro-survival genes and genes associated with quiescent stem cells (Cheung and Rando, 2013). Several recent studies have reported the early emergence of TCF-1^{hi} and CD62L^{hi} effector cells that develop into T_M cells exhibiting stemness features (Grassmann et al., 2020; Pais Ferreira et al., 2020). Moreover, Johnnidis et al. (Johnnidis et al., 2021) propose early expression of inhibitory receptors as a mechanism preserving hallmark memory features. Although these early T-cell subsets bear similarities to the quiescent T_{CM} observed here, further investigations into the developmental origin of distinct T_{CM} states are necessary to better understand the lineage relationships between the T_{CM} states described here and those present during the early phases of the T-cell response.

A hallmark of immunological memory is the ability to efficiently generate a new wave of T_{EFF} upon renewed infection. Our data demonstrate that this ability is predominantly confined

to a subgroup of replicative nascent T_M cells. The combined observations of a less differentiated quiescent T_{CM} population, and the reconstitution of the secondary and tertiary T_{EFF} pool by the output of these nascent progenitors, make a compelling argument for the presence of a bona fide stem-cell population within the T_M pool. A growing body of work has examined a stem-cell-like T_M cell (T_{SCM}) population (Gattinoni et al., 2011, 2009), generally using cell phenotype to enrich and study these cells *ex vivo*. Using a function-driven, phenotype-agnostic, approach that does not require removal of cells from their niche, we observe a cell behaviour that fits the profile of stem-cell-like T_M cells *in situ*.

In high-turnover tissues, such as the bone marrow (Laurenti et al., 2015; Wilson et al., 2008), the intestinal epithelium (Schepers et al., 2011; Yan et al., 2012), and skin epidermis (Clayton et al., 2007; Ito et al., 2005), two distinct behaviours of multipotent progenitor cells have been described: actively dividing cells that promote normal tissue homeostasis, and quiescent cells that have been documented to break their dormancy upon tissue injury and exhibit profound re-population capacity (An et al., 2018; Laurenti et al., 2015; Sugimura et al., 2012; Yan et al., 2012). We propose that the two T_{CM} behaviours we describe provide the T-cell compartment with the same capacity for renewal. Thus, the T-cell pool can be viewed as an autonomous tissue that abides by organizing principles akin to those of the hematopoietic system and solid organs.

Methods

DivisionRecorder vector generation

In order to prevent expression of Cre recombinase during bacterial cloning, a synthetic intron - containing a splice donor, a branch site, a pyridine rich region, and a splice acceptor - was inserted into the Cre gene through three-fragment isothermal assembly. To prevent low-level Cre translation occurring from alternative start sites, two ATG codons (position 78 and 84) were replaced by TGT codons. Finally, the Cre start codon was replaced by an EcoRI-spacer-XhoI site, to facilitate subsequent introduction of synthetic STRs. To generate the DivisionRecorder vector, two lox511 sites were introduced into the multiple cloning site of the pMX retroviral vector. Subsequently, an eGFP gene and the modified Cre recombinase gene were introduced directly upstream and downstream of the 5' lox511 site, respectively. Finally, a P2A element was inserted directly in between the eGFP gene and the 5' Lox511 site. Together, this resulted in a cassette comprising from, 5' to 3': Kozak, an eGFP gene, a P2A site, a lox511 site, an EcoRI restriction site, spacer, an XhoI restriction site, a Cre recombinase gene, and a lox511 site. In its base configuration, Cre recombinase is out of frame. Synthetic STR domains were ordered as oligonucleotides (Invitrogen) and subsequently dimerized. STR dimers were inserted via the EcoRI and XhoI sites. Full sequences of all oligonucleotides are supplied in **Supplementary Table 4.6**. The retroviral expression vector of the DivisionRecorder is available from Addgene (Plasmid #179446).

Cre-activity reporter vector generation

LoxP sites were introduced into the multiple cloning site of the pCDH-CMVp-MCS-PGK-BlastR vector. In addition, a Katushka open reading frame was introduced, resulting in a vector containing from 5' to 3'; the CMV promoter, a floxed scrambled open reading frame, a Katushka open reading frame, the PGK promoter, and a blasticidin resistance gene. The Cre-activity reporter plasmid is available from Addgene (Plasmid #179457).

Establishment of cell lines

The Cre-activity reporter cell line used in **Figure 4.1** was generated by retroviral transduction of HEK 293T cells (ATCC) with the Cre-activity reporter plasmid and subsequent Blasticidin selection (2 µg/ml, InvivoGen). Transduced cells were seeded at 1% confluency, and resulting single cell-derived colonies were transferred to individual wells. Clones were then examined for efficiency of induction of Katushka expression upon transfection with Cre recombinase, and the best-performing clone was selected. Cre-activity reporter cells were cultured in IMDM (Gibco) supplemented with 8% FCS (Sigma), 100 U/ml penicillin (Gibco), 100 µg/ml streptomycin (Gibco) and 2 mM glutamax (Gibco). A mouse embryonic fibroblast (MEF) cell line from the Ai9 mouse strain was generated by modification of E14.5 embryonic fibroblasts with a retroviral vector encoding short-hairpin RNA directed against the p53 mRNA. Resultant cells were cultured in IMDM supplemented with 8% FCS, 100 U/ml penicillin, 100 µg/ml streptomycin and 2 mM glutamax.

Mice

C57BL/6J-Ly5.1, OT-I, UBC-GFP and Ai9 mice were obtained from Jackson Laboratories, and strains were maintained in the animal department of The Netherlands Cancer Institute (NKI). Ai9 and OT-I mice, and UBC-GFP and OT-I mice were crossed to obtain the Ai9;OT-I and GFP;OT-I strains, respectively. Between 5-10 mice, both male and female aged 6 to 15 weeks, were used for each experiment. All animal experiments were approved by the Animal Welfare Committee of the NKI, in accordance with national guidelines.

Generation of DivisionRecorder⁺ OT-I T cells

Platinum-E cells (Cell Biolabs) cultured in IMDM supplemented with 8% FCS, 100 U/ml penicillin, 100 µg/ml streptomycin, and 2 mM glutamax were transfected with the DivisionRecorder vector using FuGene6 (Promega). Retroviral supernatant was collected 48 hours after transfection and stored at -80°C. Spleens from Ai9;OT-I mice were collected and mashed through a 70-µm strainer (Falcon) into a single cell suspension and resulting splenocytes were subsequently treated with NH₄Cl to remove erythrocytes. Subsequently, splenocytes were cultured in T cell medium (RPMI (Gibco Life Technologies) with 8% FCS,

100 U/ml penicillin, 100 µg/ml streptomycin, glutamax, 10mM HEPES (pH 7.4), MEM non-essential amino acids (Gibco), 1 mM sodium pyruvate (Gibco), 50µM 2-mercaptoethanol, supplemented with 1ng/ml recombinant murine IL-7 (PeproTech) and 2 µg/mL ConcanavalinA (Merck)). After 48 hours, splenocytes were re-seeded on RetroNectin (Takara)-coated plates in T cell medium supplemented with 60 IU/mL human IL-2 and DivisionRecorder virus and were centrifuged for 90min at 400g to allow spinfection. Virus concentration was chosen such that a transduction efficiency of approximately 10-15% was achieved, in order to minimize the occurrence of multiple retroviral integrations (**Supplementary Note 4.6**). Cells were collected 24 hours later, and a small aliquot was stained with anti-CD8-PercpCy5.5, anti-Vb5-PeCy7, anti-CD45.2-AF700 and DAPI to determine the fraction of viable OT-I T cells (DAPI⁻CD8⁺Vb5⁺CD45.2⁺) by flow cytometry (Fortessa, BD Bioscience), which generally was around ~ 80%. CD8⁺Vb5⁺CD45.2⁺ cells that expressed GFP were considered DivisionRecorder⁺ OT-I cells. Within the initial population of DivisionRecorder⁺ OT-I cells, the fraction of cells that already showed reporter activation (as inferred by tdTomato expression) 24 hours after transduction was consistently between 0.4 and 0.8%. Activated splenocytes were prepared for adoptive transfer (see below).

Infection, adoptive transfer and cell recovery

C57BL/6J-Ly5.1 mice were infected with 5,000-10,000 CFU of a recombinant *Listeria monocytogenes* strain that expresses ovalbumin or with 5,000 PFU artLCMV-OVA (Kallert et al., 2017). Approximately 24 hours later, infected mice received 5,000-40,000 DivisionRecorder⁺ OT-I T cells through intravenous tail vein injection. For secondary challenge experiments, mice were infected with a 10-fold higher *Lm*-OVA does compared to primary infection (that is, 50,000-100,000 CFU) at indicated time points. To analyse OT-I T-cell responses in peripheral blood over time, 25- to 50-µL blood samples were obtained from the tail vein at the indicated time points and were treated with NH₄Cl supplemented with 0.2 mg/ml grade-II DNaseI (Roche) to remove erythrocytes (see ‘Flow cytometric analysis’). To obtain spleen and liver samples, mice were euthanized, organs were collected, and single-cell suspensions were prepared by means of mashing through a 100-µM or 70-µm strainer (Falcon), respectively. Subsequently, erythrocytes were removed by treatment with NH₄Cl. To purify leukocytes from single-cell suspensions of liver tissue, cell suspensions were separated over a 37.5% Percoll (Sigma) density gradient. Obtained blood, spleen and liver samples were further processed for flow cytometric analysis, scRNAseq or functional in vitro assays, as indicated. Samples were monitored for the occurrence of retroviral silencing, which was not observed in any of the examined samples (**Supplementary Note 4.7**).

Validation of DivisionRecorder functionality

To assess the ability of the DivisionRecorder to faithfully report on the replicative history of T-cell populations using dilution of cell dyes as a reference, as described in **Figure 4.2d-e**,

we employed an experimental approach that was optimized to obtain sufficient DR^{RFP} events within the limited number of cell divisions that can be followed using cell dyes such as CTV (i.e., by transferring a high number of cells modified at a high transduction efficiency). Conclusions from this experiment are restricted to the validation of the functionality of the DivisionRecorder in dividing CD8⁺ T cells. Splenic CD8⁺ T cells were isolated using the Mouse CD8 T Lymphocyte Enrichment Set (BD Biosciences) and were subsequently stained with CellTrace Violet (Thermo Fisher). Next, cells were activated for 16 hours in T-cell medium supplemented with 0.05 µg/mL SIINFEKL peptide and 60 IU/mL IL-2. Following this activation step, cells were seeded onto RetroNectin (Takara Bio)-coated plates and were transduced with DivisionRecorder virus by spinfection for 4 hours in the presence of IL-2 and SIINFEKL peptide. Analysis of CellTrace Violet signal by flow cytometry indicated that the cells had not undergone a full cell division post labelling. Subsequently, 6×10⁶ OT-I T cells were transferred into *Lm*-OVA infected recipients. Spleens were collected 48 hours after adoptive transfer, processed into single-cell suspensions and prepared for flow cytometric analysis. In order to accurately determine the fraction of DR^{RFP} cells per division during the initial stages of the proliferative burst when cumulative switching rate is still low, analysis of a large number of DivisionRecorder⁺ OT-I T cells events is required. For this reason, a transduction efficiency of ~ 60% was chosen in these experiments, instead of the 10-15% transduction efficiency used in other experiments. Note that a high transduction efficiency will result in the more frequent occurrence of cells that carry multiple retroviral integrations. The presence of cells with multiple integrations will result in a higher, yet stable, DR^{RFP} acquisition rate, as compared to the experimental setup used in the remainder of the study.

***Ex vivo* analysis of degranulation and cytokine secretion potential of memory T cells**

Spleens were collected from recipient mice at > 60 days post-infection, and CD8 T cells were isolated using the Mouse CD8 T Lymphocyte Enrichment Set (BD Biosciences). Following isolation, T cells were plated at 1×10⁶ cells per well in 96-well round bottom plates in T-cell medium supplemented with 0.05 µg/mL SIINFEKL peptide to selectively activate OVA-specific T cells. Following a 4-hour incubation, capacity of indicated T-cell populations to either produce the indicated cytokines or to degranulate was assessed. To allow analysis of cytokine production, Brefeldin A (GolgiPlug, BD Biosciences) was added 30 minutes after initiation of T-cell stimulation. To allow analysis of degranulation, T-cell medium was supplemented with anti-CD107a and anti-CD107b antibodies at the initiation of T-cell stimulation, and Brefeldin A (GolgiPlug, BD Biosciences) and Monensin (GolgiStop, BD Biosciences) were added 30 minutes after initiation of T-cell stimulation. At the end of the T-cell stimulation period, cells were stained for KLRG1 and CD27 and prepared for flow cytometric analysis (see below).

Flow cytometric analysis

Cells were taken up in PBS (Invitrogen) supplemented with 0.5% BSA (Fisher Scientific) and stained with antibodies directed against the indicated cell surface proteins (1:200 dilution), for 30 minutes on ice. To allow detection of intracellular cytokine production, cells were fixed and permeabilized with CytoFix/CytoPerm (BD Biosciences) according to the manufacturer's protocol and were subsequently stained using antibodies against IL-2, TNF α and IFN γ . To detect intranuclear Ki67 expression, the Foxp3/Transcription factor Staining buffer set (eBioscience) was used. See **Supplementary Table 4.7** for list of antibodies used in the study. All samples were acquired on a BD LSR Fortessa (BD Bioscience); DR^{GFP} and DR^{RFP} cells were identified as CD8⁺V β 5⁺CD45.2⁺GFP⁺tdTomato⁻ and CD8⁺V β 5⁺CD45.2⁺GFP⁺tdTomato⁺, respectively. Flow cytometry data analysis was performed using FlowJo V10. An example of the used gating strategy is depicted in **Supplementary Figure 4.10**.

For the moving average analysis depicted in **Figure 4.3g** and **Supplementary Figure 4.2e**, CD8⁺V β 5⁺CD45.2⁺GFP⁺ events were exported and further processed using the R package flowCore (Hahne et al., 2009). In brief, outlier events (i.e., antibody aggregates/cell doublets) were removed, fluorescence intensities of each of the cell surface proteins were normalized using an inverse hyperbolic sine transformation and subsequently scaled between 0 and 1. To obtain the depicted moving averages, the fraction of DR^{RFP} cells was calculated within windows that each contained 10% of total cells, starting with the 10% of cells with the lowest expression levels for the indicated marker, and with subsequent windows moving up by steps of 2.5%.

Single-cell RNA sequencing and data analysis of DivisionRecorder modified cells

The scRNAseq dataset of DivisionRecorder modified and unmodified OT-I T_M cells was obtained in two independent experiments, comprising 11 mice in total (See **Supplementary Figure 4.3**). Experiment 1 included 3 mice containing DR⁺ T_M cells (mouse 1-3), which were processed in a single batch. Experiment 2 included 4 mice containing DR⁺ T_M cells (mouse 4-7) and 4 mice containing T_M cells derived from naive OT-I T cells (unmodified, mouse 8-11), which were processed in two separate batches (batch 1: mouse 4-5 and mouse 8-9, batch 2: mouse 6-7 and mouse 10-11).

Spleens of mice that received DivisionRecorder⁺ OT-I T cells ($n = 7$) or mice that received naive OT-I T cells ($n = 4$) were collected > 65 days following infection. Splenocytes were stained with fluorochrome-conjugated antibodies directed against CD8, CD45.2 and V β 5 (See **Supplementary Table 4.7**), to allow purification of transferred cells by FACS using the BD FACSAria Fusion Flow Cytometer (BD Biosciences). DR⁺ cells were subsequently FACS purified on the basis of their expression of RFP and GFP. Following the isolation of DR^{GFP} and DR^{RFP} T_M cells by FACS (FACSAria Fusion, BD Biosciences), obtained cell

populations were barcode-labelled with distinct anti-mouse TotalSeq Hashtag antibodies (TotalSeq-A0301-0306, Biolegend), and pooled, with an equal number of cells from each mouse to form the total pool of cells for scRNAseq. If the amount of sorted DR^{RFP} cells from a particular sample was limited, it was pooled together with another DR^{RFP} sample to reduce cell loss during cell hashing (as indicated in **Supplementary Figure 4.3**). Single-cell RNA isolation and library preparation was performed according to the manufacturer's protocol of the 10X Genomics Chromium Single Cell 3' kit, and the cDNA library was sequenced on a NextSeq 550 Sequencing System (Illumina). Cumulative data tallied to a total of ~ 39,500 cells. Feature-barcode matrices were generated using the Cell Ranger software of the 10X Genomics Chromium pipeline. Cells that could be ascribed to multiple samples or to no sample (inferred from the detection of multiple or no Hash tags), cells with a transcript (UMI) count lower than 1,500 and cells with a mitochondrial-gene fraction higher than 0.12 were excluded from downstream analysis. Next, cells were further filtered based on gene counts, setting upper and lower thresholds separately for each sample-batch to control for differences in sequencing depth (gene-count-thresholds: experiment 1, 1,200-3,000; experiment 2 batch 1, 800-2,500; experiment 2 batch 2, 1,000-3,000). Subsequent analysis of the remaining 27,559 cells was performed using the Seurat (Butler et al., 2018) and MetaCell (Baran et al., 2019) R packages.

To examine enrichment or depletion of DR^{RFP} cells within the different MetaCells, cell counts were first normalized across hashtags. Data obtained from the different mice were subsequently aggregated and used to calculate the ratio of DR^{RFP} versus DR^{GFP} cells in each MetaCell. The immune signature gene list used in several analyses was composed of gene clusters involved or proposed to be involved in T-cell function. The full gene list is described in **Supplementary Table 4.3**.

Differential gene-expression testing was performed using the FindMarkers function (Wilcoxon rank-sum test) implemented in Seurat, comparing all ldT_{CM} to all hdT_{CM}. Significantly differentially expressed genes ($p < 0.05$) were subsequently used for gene-set enrichment analysis using the R package fgsea (Korotkevich et al., 2021), testing for enriched gene-sets from the C7 immunologic or the H Hallmark gene-sets from Molecular Signatures Database (only including sets that consisted of > 10 genes). Results from this analysis were filtered for collections deposited by Kaech and Goldrath (**Supplementary Table 4.2**), focusing on relevant CD8⁺ T-cell biology.

To calculate the QstemScore, the log₂ enrichment values of genes that were positively or negatively associated with stem cell quiescence (**Supplementary Table 4.5**) were first summed within each MetaCell resulting in a positive and a negative score. QstemScore was then obtained by subtracting the negative score from the positive score.

Re-analysis of LCMV-specific T_M cell scRNAseq dataset

Single-cell transcriptomes from P14 T_M cells (collected from spleen at day 90 post infection) were obtained from the Gene Expression Omnibus (accession GSE131847, sample

GSM3822202). All single cells from this dataset were clustered by applying the MetaCell algorithm. Next, T_{CM} MetaCells were determined on the basis of the expression levels of core effector- and multipotency-related genes (**Supplementary Table 4.1**). QstemScores were then calculated for each of the T_{CM} MetaCells, and the two highest- and two lowest-scoring MetaCells were selected. Pearson correlations were subsequently calculated between each of these four T_{CM} MetaCells and all of the T_{CM} MetaCells from the OT-I dataset described here.

CTV-based serial transfer experiment and analysis

Spleens from OT-I and GFP;OT-I mice were collected and CD8⁺ T cells were isolated using the Mouse CD8 T Lymphocyte Enrichment Set (BD Biosciences), according to the manufacturer's protocol. The obtained cells were mixed in a 1:1 ratio and transferred to 4 primary recipient C57BL/6J-Ly5.1 mice (1.5×10^6 T cells per recipient), and 24 hours later recipients were infected with 5,000-10,000 CFU *Lm*-OVA. At 30 days following infection, spleens and lymph nodes were collected and CD8⁺ T cells were enriched using the Mouse CD8 T Lymphocyte Enrichment Set (BD Biosciences), replacing the supplied antibody-cocktail with a mixture of anti-mouse CD19, CD20 and CD4 biotinylated antibodies (used 1:200 each, see **Supplementary Table 4.7** for information on antibody clones). The enriched cell pool was subsequently stained with CellTrace Violet (Thermo Fisher) and re-transferred into four infection-matched secondary C57BL/6J-Ly5.1 recipients. At 74 days after secondary transfer (104 days post-infection), spleens and lymph nodes were collected from the secondary recipients and stained with anti-mouse KLRG1-PE, CD27-APC, and CD45.2-AF700 (see **Supplementary Table 4.7** for information on antibody clones). Next, stained cell pools were first enriched for transferred cells (i.e., CD45.2⁺) through FACS using the BD FACSAria Fusion Flow Cytometer (BD Biosciences), and subsequently sorted again to obtain 4 populations of T_{CM} cells based on both GFP expression and CTV dilution: KLRG1⁻CD27⁺GFP⁺div0-2, KLRG1⁻CD27⁺GFP⁺div5+, KLRG1⁻CD27⁺GFP⁻div0-2, and KLRG1⁻CD27⁺GFP⁻div5+. These cell pools were then further processed for tertiary transfer or single-cell RNA sequencing.

For tertiary transfer, GFP⁻div0-2 cells were mixed 1:1 with the GFP⁺div5+ cells (experiment 1), or GFP⁺div0-2 cells were mixed 1:1 with GFP⁻div5+ cells (experiment 2), thereby controlling for potential confounding effects of the donor strain. Next, 10,000 cells from each pool were transferred in naive tertiary recipient C57BL/6J-Ly5.1 mice (3 mice for experiment 1, 4 mice for experiment 2). Twenty-four hours later, recipients were infected with 10,000 CFU *Lm*-OVA and the ratio of GFP⁺ over GFP⁻ cells within the transferred population (Ly5.2⁺) in blood was monitored by flow cytometry over time.

For scRNAseq analysis, cell pools obtained by cell-sorting were barcode-labelled with distinct anti-mouse TotalSeq Hashtag antibodies (TotalSeq-A0301-0304, Biolegend) and subsequently pooled. Single-cell mRNA isolation and library preparation was performed according to the manufacturer's protocol of the 10X Genomics Chromium Single Cell 3' kit, and the cDNA library was sequenced on a NextSeq 550 Sequencing System (Illumina).

Feature-barcode matrices were generated using the Cell Ranger software of the 10X Genomics Chromium pipeline, resulting in 13,064 single-cell transcriptomes. Cells that could be ascribed to multiple samples or to no sample (inferred from the detection of multiple or no hashtags), cells with a transcript (UMI) count lower than 2,000 and cells with a mitochondrial-gene fraction higher than 0.12 were excluded from downstream analysis. Finally, cells with a gene-count of $> 2,800$ were additionally excluded from further analysis. Subsequent analysis of the remaining 9,702 cells was performed using the Seurat (Butler et al., 2018) and MetaCell (Baran et al., 2019) R packages.

Differential gene-expression testing was performed using the FindMarkers function (Wilcoxon rank-sum test) implemented in Seurat, comparing all CTV^{hi} (div0-2) cells to all CTV^{lo} (div5+) cells. Significantly differentially expressed genes ($p < 0.05$) were subsequently used for gene-set enrichment analysis using the R package fgsea (Korotkevich et al., 2021), testing for enriched gene-sets from the C7 immunologic gene-sets (including only sets that consisted of > 10 genes). Results from this analysis were filtered for collections deposited by Kaech and Goldrath (**Supplementary Table 4.2**), focusing on relevant CD8⁺ T-cell biology.

For the MetaCell-based analysis, the number of cells within each hashtag-MetaCell combination was counted, and subsequently normalized to 1,000 cells within each hashtag. The ratios of CTV^{hi} over CTV^{lo} was then calculated separately for the GFP;OT-I- and OT-I-derived cells.

Statistical analysis

Flow cytometric data were acquired using BDFACSDiva (v8.0) software. Flow cytometric data were analysed using FlowJo (v10.4.2), R (v6.3.1, 'Action of the Toes'), and FlowCore (v1.52.1). Single-cell RNA sequencing data were analysed using R (v6.3.1), Seurat (v3.1.1), and MetaCell (v0.3.41). Data were visualized using Graphpad (V8.4.1, Prism software) and GGplot (v3.2.1). No statistical methods were used to predetermine sample sizes, and sample sizes were chosen on the basis of those reported in previous publications (Gerlach et al., 2013; Kok et al., 2020). Data distribution was assumed to be normal, but this was not formally tested. Mice were stratified according to age and sex where appropriate. Data collection and analysis were not performed blind to the conditions of the experiments. No data points were excluded from the analyses.

Data availability

Transcriptomic data presented in the manuscript have been deposited to the Gene Expression Omnibus (GEO), and can be accessed under the GEO accession numbers GSE169154 and GSE184947. The gp33-specific P14 T cell scRNAseq dataset was retrieved from GEO (accession GSE131847, sample GSM3822202). All statistical source data of the figures

presented in the present study can be found online (<https://doi.org/10.1038/s41590-022-01171-9>). Indicated gene sets used in gene set enrichment analyses were retrieved from the Molecular Signatures Database (MSigDB) at <http://www.gsea-msigdb.org/gsea/msigdb>. Any additional data supporting the findings of this study are available from the corresponding author upon request. Source data can be found online (<https://doi.org/10.1038/s41590-022-01171-9>).

Code availability

R scripts that were used to produce the main and supplementary figures in the manuscript are available from GitHub (https://github.com/kasbress/DivisionRecorder_analysis).

Acknowledgements

We would like to thank M. C. Wolkers (Sanquin, Amsterdam), C. Gerlach (Karolinska Institute, Stockholm) and K. van Gisbergen (Sanquin, Amsterdam) for helpful discussions regarding experimental procedures and sharing biological material, and D. Merkle (University of Geneva, Geneva) for kindly providing the artLCMV-OVA. In addition, we would like to thank the NKI Genomics Core Facility and Flow Cytometry Core Facility for providing experimental support. This work was supported by ERC AdG Life-his-T (Grant agreement ID: 268733) to T.N.S. and an NWO grant (ALWOP.265) to R.J.d.B.

Author contributions

The study was designed by K.B., L.K., F.A.S. and T.N.S., and supervised by T.N.S. and F.A.S.; K.B. and L.K. jointly performed, analysed, and visualized all experimental work included in the manuscript; F.A.S. and K.B. designed and developed the retroviral DivisionRecorder construct. L.A.K. and L.J. performed optimization and validation experiments integral to the design of the DivisionRecorder; A.C.S. and R.J.d.B. performed mathematical modelling, together with T.S.W, L.P. and K.R.D.; K.B. and L.K. wrote the manuscript with the input of co-authors; T.N.S. and F.A.S. critically reviewed and revised the manuscript.

Competing interests

The authors declare no competing interests.

Additional information

Peer review reports can be found online at <https://doi.org/10.1038/s41590-022-01171-9>.

Supplementary Information

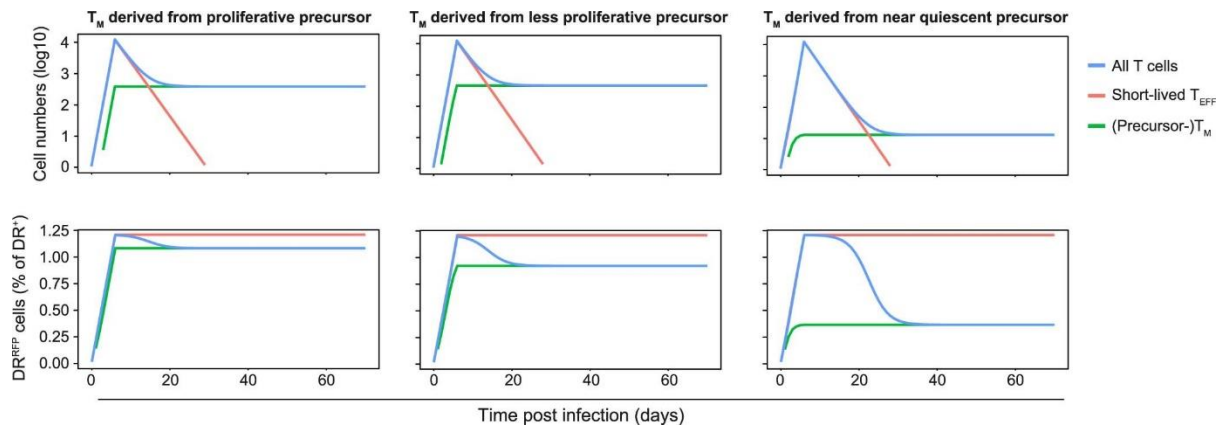


Figure S4.1: Simulation of different scenarios of memory T-cell formation. Simulated data depicting a responding antigen-specific T-cell population (blue), comprised of T_{EFF} undergoing clonal expansion and subsequent contraction (red), plus memory precursor T cells (MP, green) that develop into T_M . Activated T_{EFF} are modelled to divide rapidly for 6 days (expansion phase), die at a fixed rate throughout the response, and can differentiate into MP cells only during the expansion phase. Cell numbers (top row) and DR^{RFP} percentages (bottom row) are shown for three scenarios: (left) T_{EFF} can give rise to MP cells during the entire expansion phase, irrespective of the number of prior divisions, (middle) only T_{EFF} that have gone through at most 24 divisions can give rise to MP cells, or (right) only T_{EFF} that have gone through at most 10 divisions can give rise to MP cells. Note the strong decay in DR^{RFP} percentage that is observed during memory formation in case T-cell memory is founded by T cells that have undergone few divisions. See **Supplementary Note 4.3** for detailed description and equations.

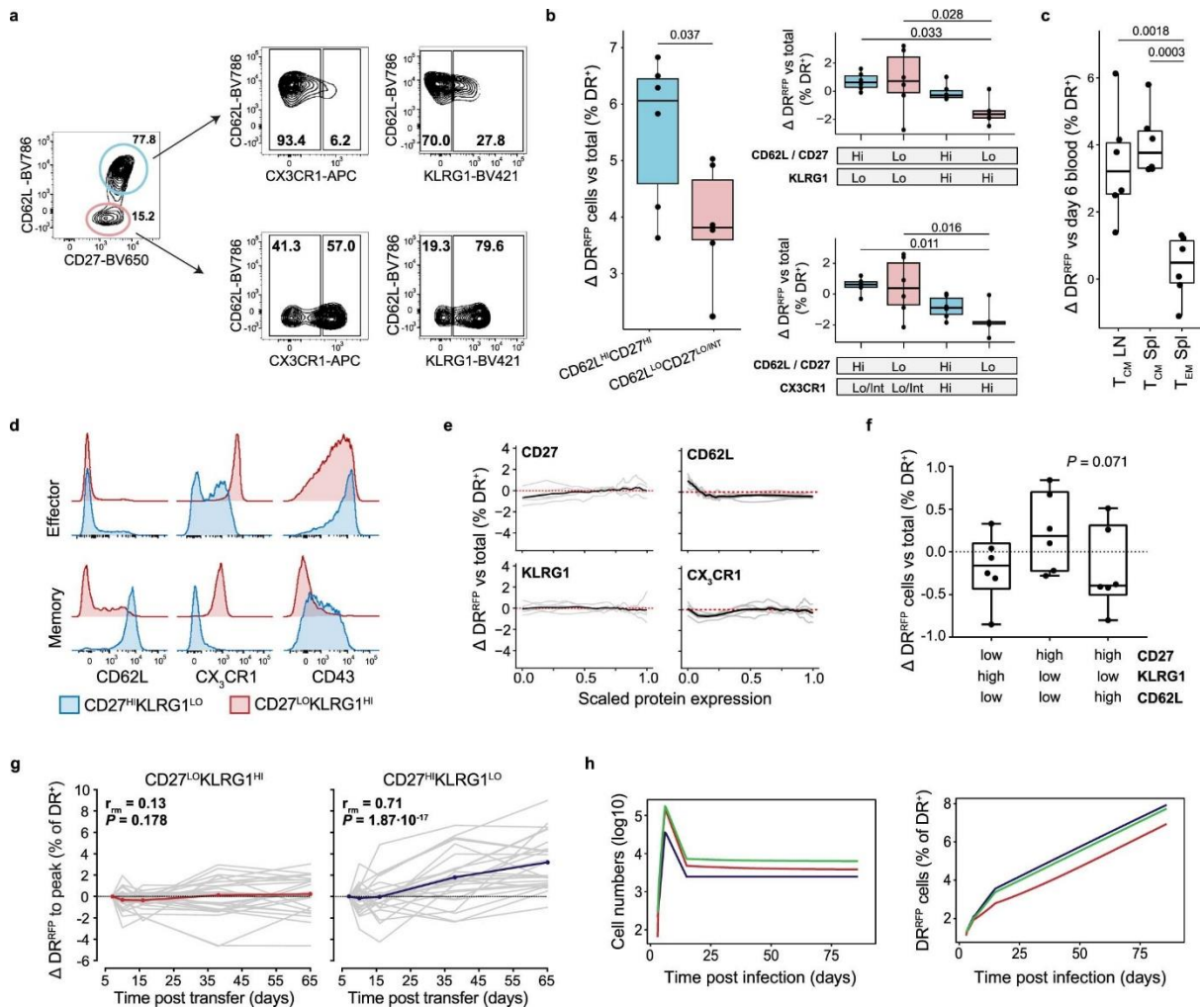


Figure S4.2: Evaluation of the division history of T-cell subsets throughout a response to *Lm*-OVA. **a**) Gating strategy used to identify indicated T_M populations (d86) in spleen samples, **b**) DR^{RFP} percentages within splenic T_M populations ($n = 6$ mice) as identified in panel **a**, **c**) DR^{RFP} percentages within the CD27^{hi}KLRG1^{lo} T_{CM} subset in spleen and lymph nodes (LN) and within the CD27^{lo}KLRG1^{hi} T_{EM} subset in spleen, **d**) Cell surface expression of CX3CR1, CD62L, and CD43 within splenic CD27^{lo}KLRG1^{hi} and CD27^{hi}KLRG1^{lo} populations at the peak of the T_{EFF} phase (day 6 post infection) and in memory phase (day 86 post infection), **e**) Moving-average of surface marker expression of splenic DR^{RFP} OT-I T cells during effector phase (day 6), depicted as in **Figure 4.3g**, **f**) Boxplots depicting DR^{RFP} percentages within T_{EFF} (day 6 post infection) subsets in spleen ($n = 6$ mice), relative to the total DR^{RFP} percentage, **g**) Kinetics of DR^{RFP} percentages within CD27^{lo}KLRG1^{hi} (left) and CD27^{hi}KLRG1^{lo} (right) DR^{RFP} OT-I T-cell populations in blood. Values are relative to the percentage of DR^{RFP} cells detected at the peak of the response (day 6). Grey lines represent individual mice ($n = 22$), red and blue lines indicate group mean, **h**) Simulation of the phenotype model (See **Supplementary Note 4.5** for details) illustrating a scenario in which conversion of CD27^{hi}KLRG1^{lo} to CD27^{lo}KLRG1^{hi} cells occur only after the peak of the response at a low rate. Depicted are the overall cell numbers (left), and the percentage DR^{RFP} cells of DR^{RFP} OT-I T cells (right) in CD27^{hi}KLRG1^{lo} cells (blue), CD27^{lo}KLRG1^{hi} cells (red) and the total T-cell population (green). Note that in this scenario the fraction DR^{RFP} within the terminally differentiated CD27^{lo}KLRG1^{hi} population would increase to almost twice the experimentally observed frequency. All depicted data are representative of at least two independent experiments. Boxplots (**c,d,g**) represent group median and 25th/75th percentiles, whiskers indicate the interquartile range multiplied

by 1.5 (**c,d**) or min/max (**g**), dots indicate individual samples. p values were determined by one-way ANOVA followed by Tukey's HSD post-hoc test (**c** and **d**), two-sided Student's *t* test (**c**), two-sided repeated measurement correlation test (**h**), or two-sided Friedman test (**g**). All significant (< 0.05) p values are indicated in the plots.

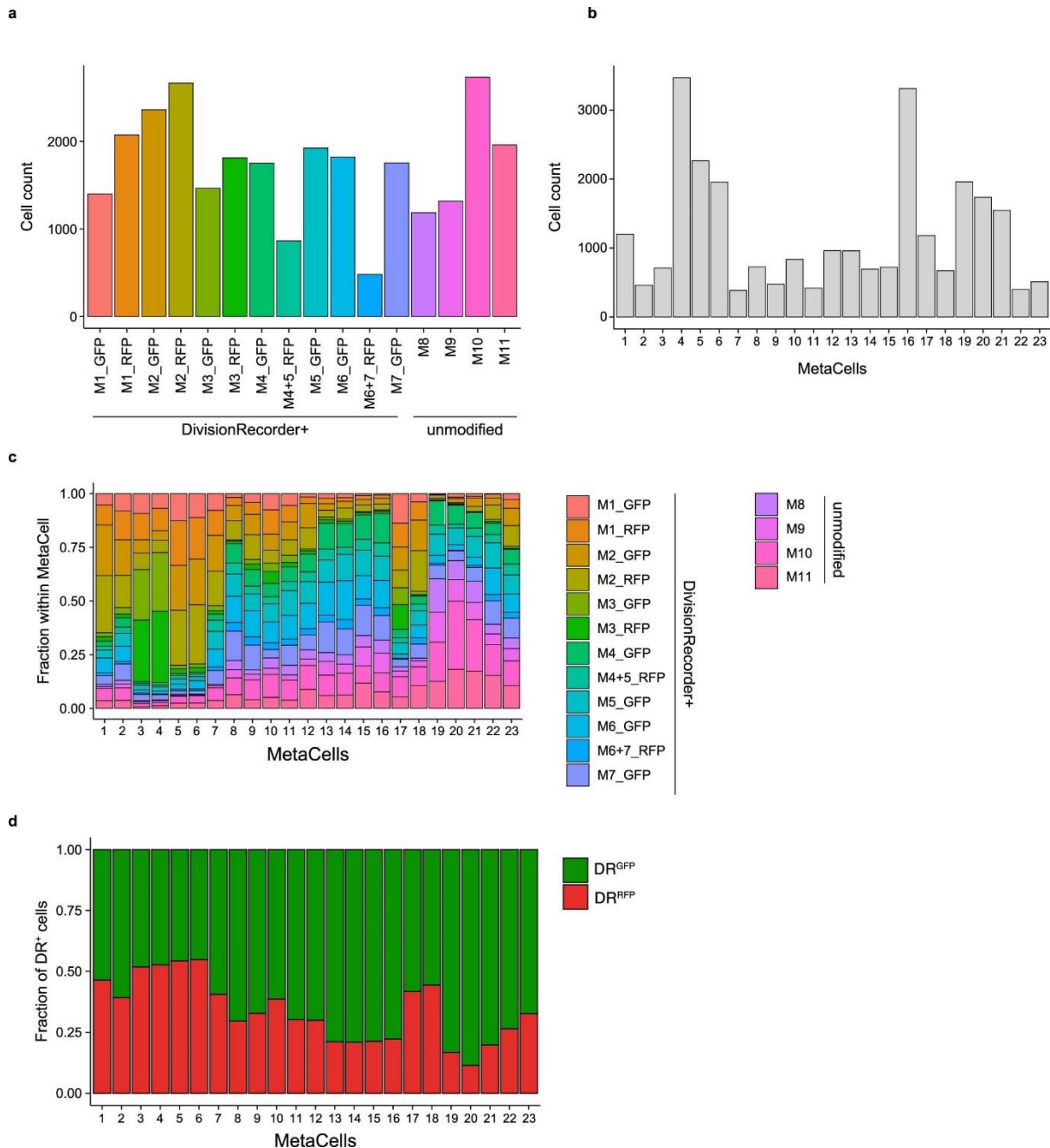


Figure S4.3: Single cell mRNA sequencing of DivisionRecorder⁺ memory T cells. Single cell mRNA sequencing was performed on DivisionRecorder modified and unmodified OT-I memory T cells (day 75 and 85 post *Lm*-OVA infection), isolated from spleens ($n = 7$ mice with DR⁺ memory T cells; $n = 4$ with unmodified memory T cells). Obtained data were aggregated from two independent experiments (experiment 1: M1-3; experiment 2: M4-11). All cells were jointly analyzed and clustered. **a**) Cell count per sample, **b**) Total cell count per MC, **c**) Sample composition of each MC, **d**) Relative contribution of DR^{GFP} and DR^{RFP} to the total DR⁺ pool within each MC.

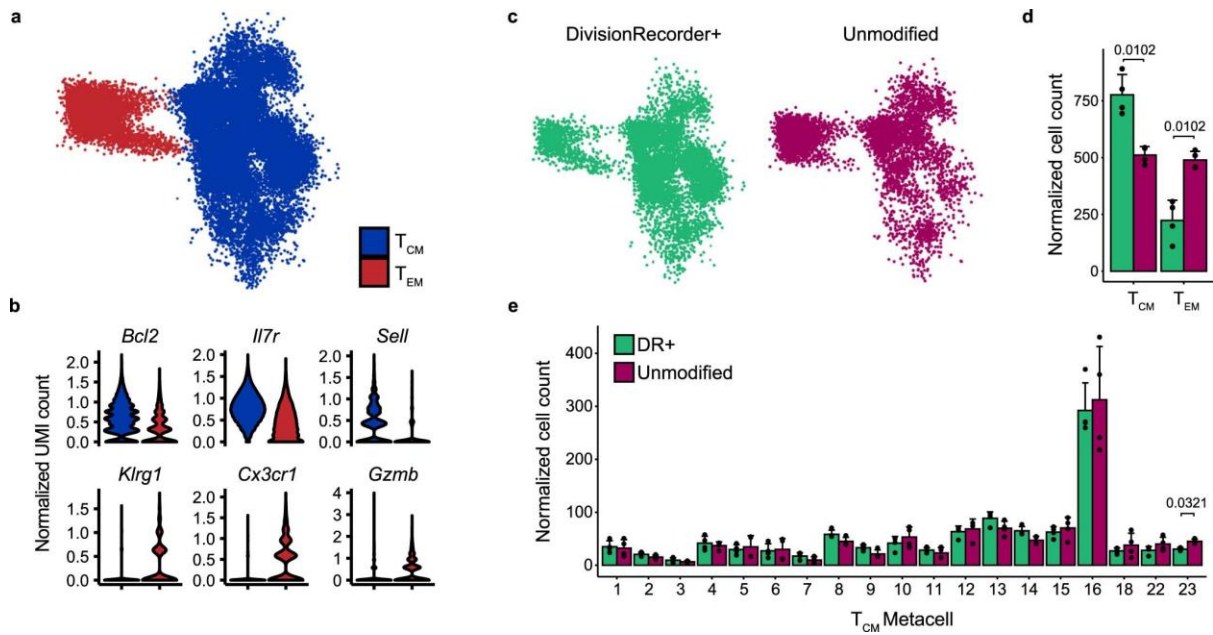


Figure S4.4: T_{CM} transcriptional states are preserved in DR⁺ OT-I T cells. Comparison of transcriptional states of splenic memory T cells generated by either DivisionRecorder modified, or unmodified OT-I T cells (day 75 and 85 post *Lm*-OVA infection). **a,b**) Memory OT-I T cells cluster into T_{CM} (blue) and T_{EM} (red). 2D projection colored by subset (**a**), and violin plots depicting normalized UMI counts of selected genes (**b**) are shown, **c**) 2D projection of either DR⁺ (left) or unmodified (right) memory OT-I T cells, **d**) Contribution of DR⁺ and unmodified memory T cells to the T_{CM} and T_{EM} subsets, **e**) Contribution of DR⁺ and unmodified OT-I T cells to the 19 MCs that jointly make up the T_{CM} subset. Dots indicate individual mice ($n = 3$ per condition). Note that all T_{CM} states are generated in near-equal proportions by DR⁺ and unmodified memory T cells. Depicted scRNAseq data was obtained from six individual mice and was aggregated from two independent experiments. p values were determined by two-sided student's t test followed by Bonferroni correction for multiple testing (**d** and **e**). p values < 0.05 are indicated.

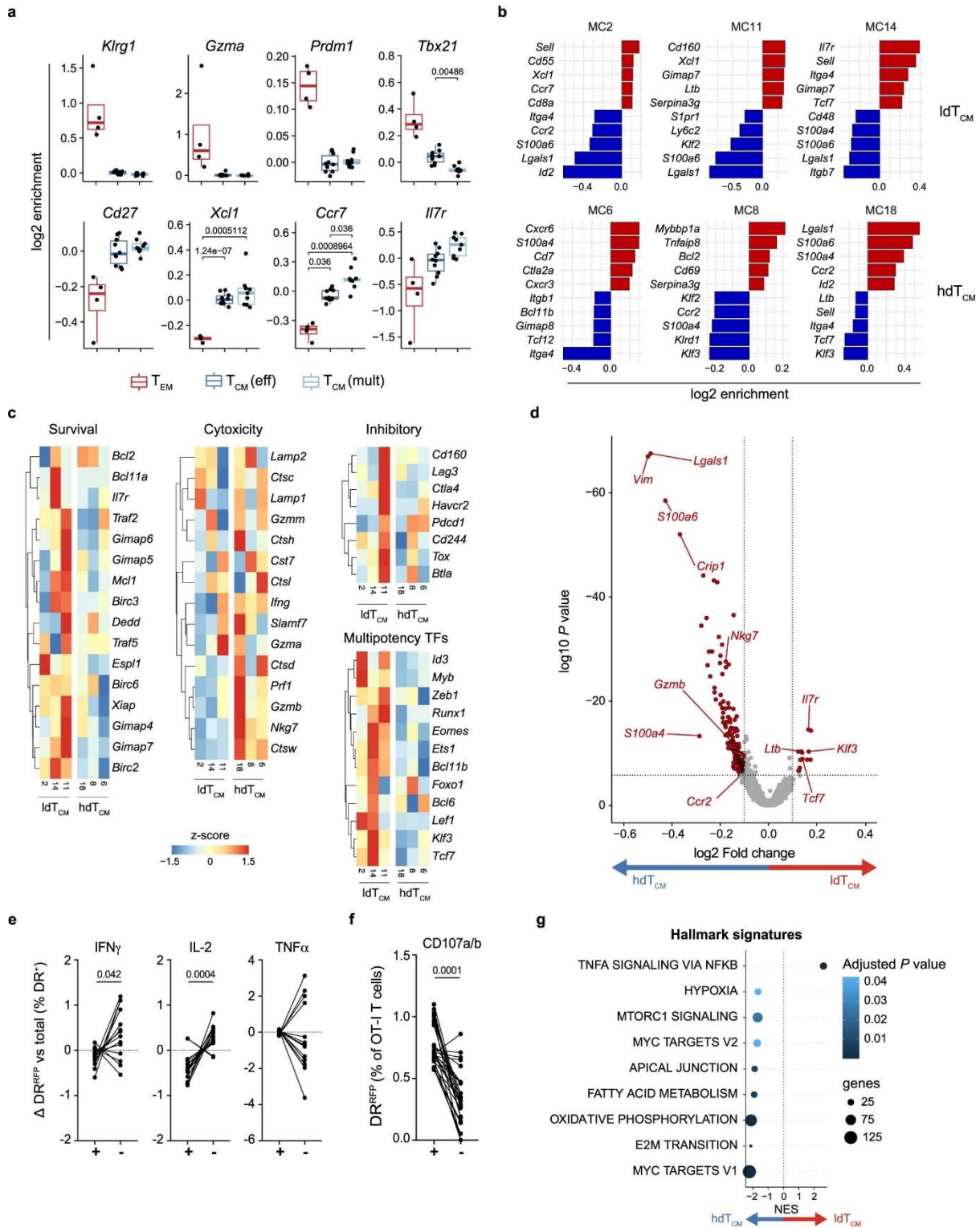


Figure S4.5: Replicative history identifies distinct transcriptional states within the T_{CM} pool. Single cell transcriptomic profiling of DR⁺ T cells obtained from spleen in memory phase (day 75 and 85 post *Lm*-OVA infection). **a**) Log₂ enrichment of selected genes in each MC cluster. Boxplots indicate group median and 25th/75th percentiles, whiskers indicate the interquartile range multiplied by 1.5, dots signify individual MCs. The phenotype clusters T_{EM}, T_{CM} (eff.) and T_{CM} (mult.) contain 4, 9 and 10 MCs, respectively. For definition of T_{CM} (eff.) and T_{CM} (mult.), see **Figure 4.4b**, **b**) Top and bottom marker genes of IdT_{CM} (top, MC2, 11, 14) and hdT_{CM} (bottom, MC6, 8, 18), see **Figure 4.4d** for IdT_{CM} and hdT_{CM} definitions, **c**) Heatmaps depicting z-score transformed enrichment values of

genes related to cell survival (left), cytotoxicity and effector function (middle), inhibitory markers (top-right), and transcription factors involved in T-cell multipotency (bottom-right). Expression is depicted for the three ldT_{CM} and three hdT_{CM} MCs, **d**) Volcano plot depicting differentially expressed genes in ldT_{CM} versus hdT_{CM}. Significantly (adjusted p-value < 0.05) differentially expressed genes are depicted in red. Selected genes are highlighted, **e**) Cytokine release of CD27^{hi}KLRG1^{lo} DR⁺ T cells (isolated from spleen at day > 60 post infection) 4 hours post *ex vivo* stimulation. Percentage DR^{RFP} cells within cytokine producers (+) and non-producers (-), relative to the average DR^{RFP} percentage within each sample, is depicted. Lines connect individual *ex vivo* stimulated samples ($n = 12$), obtained from three mice, **f**) *Ex vivo* degranulation of CD27^{hi}KLRG1^{lo} DR⁺ T cells (isolated from spleen at day > 60 post infection) 4 hours post *ex vivo* stimulation. Percentage DR^{RFP} cells within the CD107a/b positive (+) or negative (-) cell populations is depicted. Lines connect individual *ex vivo* stimulated samples ($n = 17$), obtained from five mice, **g**) Enrichment of gene signatures from MsigDB (Hallmark) by gene set enrichment analysis comparing ldT_{CM} and hdT_{CM}. Data depicted was accumulated in two independent experiments (3-4 mice per experiment). p values were determined by Tukey's HSD test (**a**), Wilcoxon rank-sum test with Bonferroni correction (**d**), two-sided Wilcoxon signed-rank test (**e,f**), the FGSEA algorithm followed by Benjamini-Hochberg procedure (**g**). p values < 0.05 are indicated.

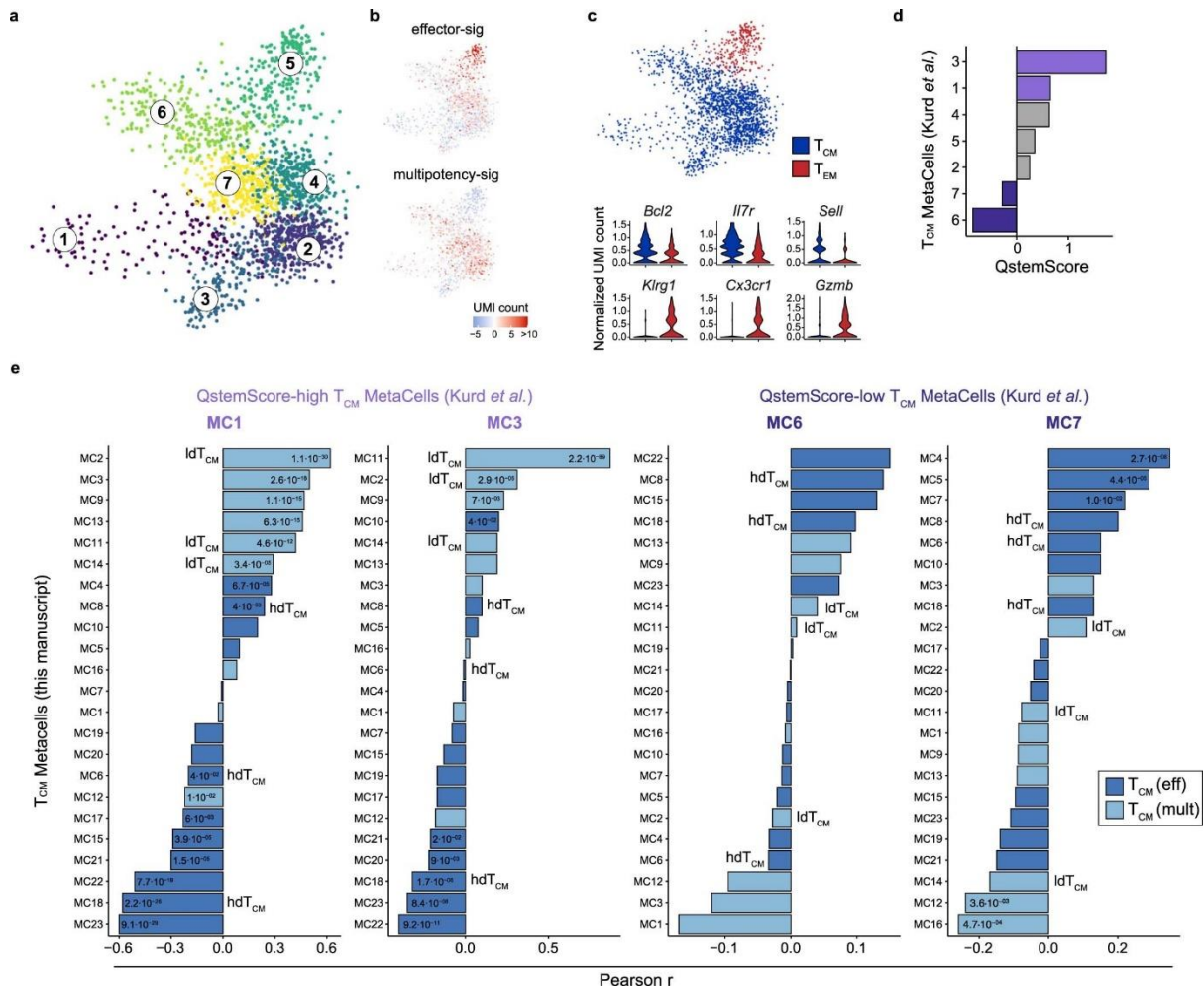


Figure S4.6: gp33-specific P14 T_{CM} with increased expression of genes associated with replicative quiescence resemble OT-I IdT_{CM}. Re-analysis of scRNAseq profiled splenic P14 memory T cells, published in Kurd *et al.* (Kurd *et al.*, 2020). **a,b**) 2D projection of P14 memory T cells 90 days post LCMV infection, colors indicate individual MCs (**a**), or the relative expression of effector- and multipotency-associated genes (**b**). Gene list in **Supplementary Table 4.1**, **c**) P14 memory T cells cluster into T_{CM} (blue) and T_{EM} (red). 2D projection colored by subset (top), and violin plots depicting normalized UMI counts of selected genes (bottom) are shown, **d**) QstemScore of all T_{CM} MCs in the Kurd *et al.* (Kurd *et al.*, 2020) dataset, **e**) Pearson correlations between the Kurd *et al.* (Kurd *et al.*, 2020) P14 T_{CM} MCs that score high (MC1,3) or low (MC6,7) for QstemScore, and all OT-I T_{CM} MCs described here. Data are depicted as waterfall plots and asterisks indicate significant correlations. T_{CM} (eff.), T_{CM} (mult.), IdT_{CM} and hdT_{CM} MCs are defined in **Figure 4.4**. p values were determined by two-sided Pearson correlation test followed by Bonferroni correction (**e**). p values < 0.05 are indicated in the plots.

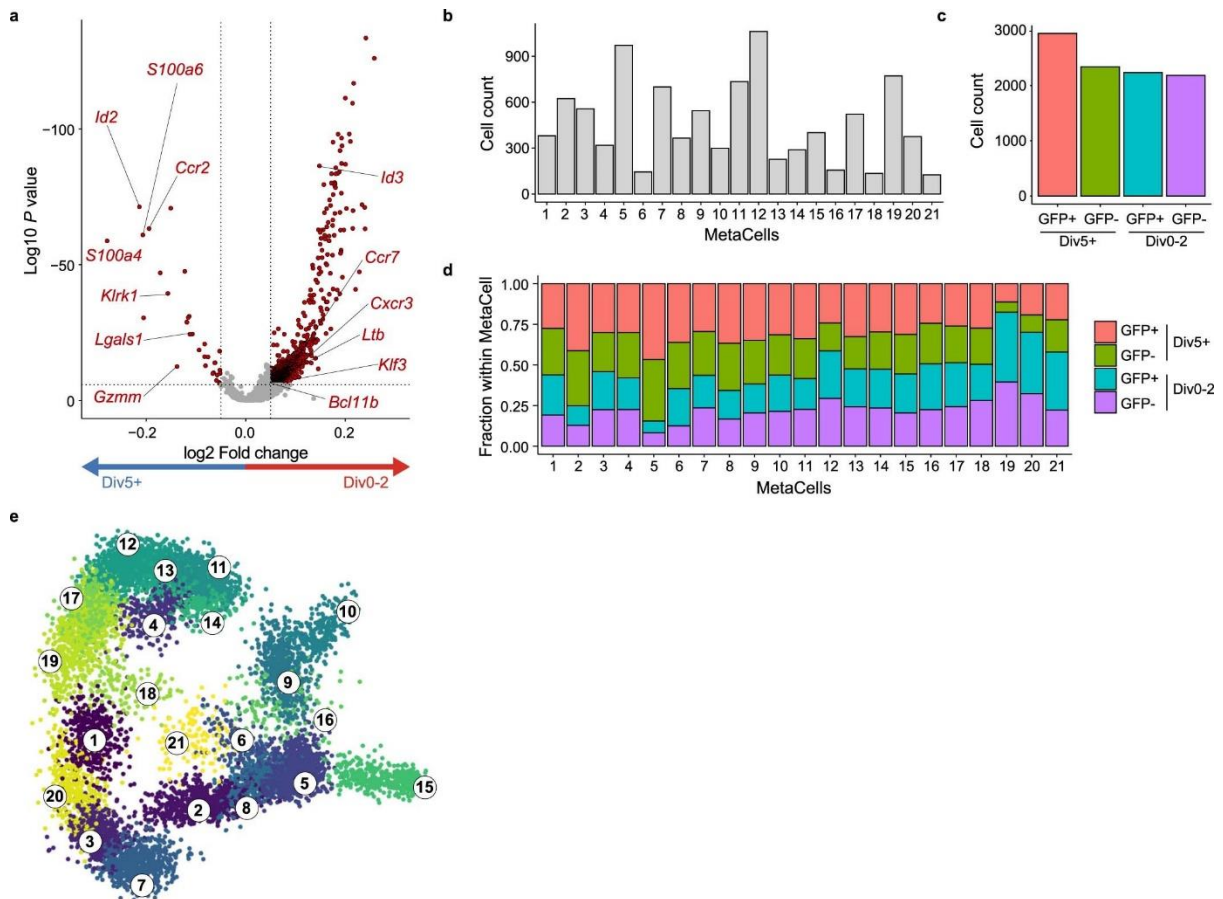


Figure S4.7: Single cell mRNA sequencing analysis of highly divided and less divided splenic T_{CM} . **a)** Volcano plot depicting differentially expressed genes in div0-2 versus div5+ T_{CM} . Significantly differentially expressed genes (adjusted $p < 0.05$) are depicted in red. Selected immune-related genes are highlighted, **b)** Cell count per MC, **c)** Number of sequenced cells per sample included in the analysis, **d)** Sample composition of each MC, **e)** 2D projection, colours indicate different MCs. Depicted scRNAseq data was collected from 4 individual mice. p values were determined by Wilcoxon rank-sum test with Bonferroni correction (**a**).

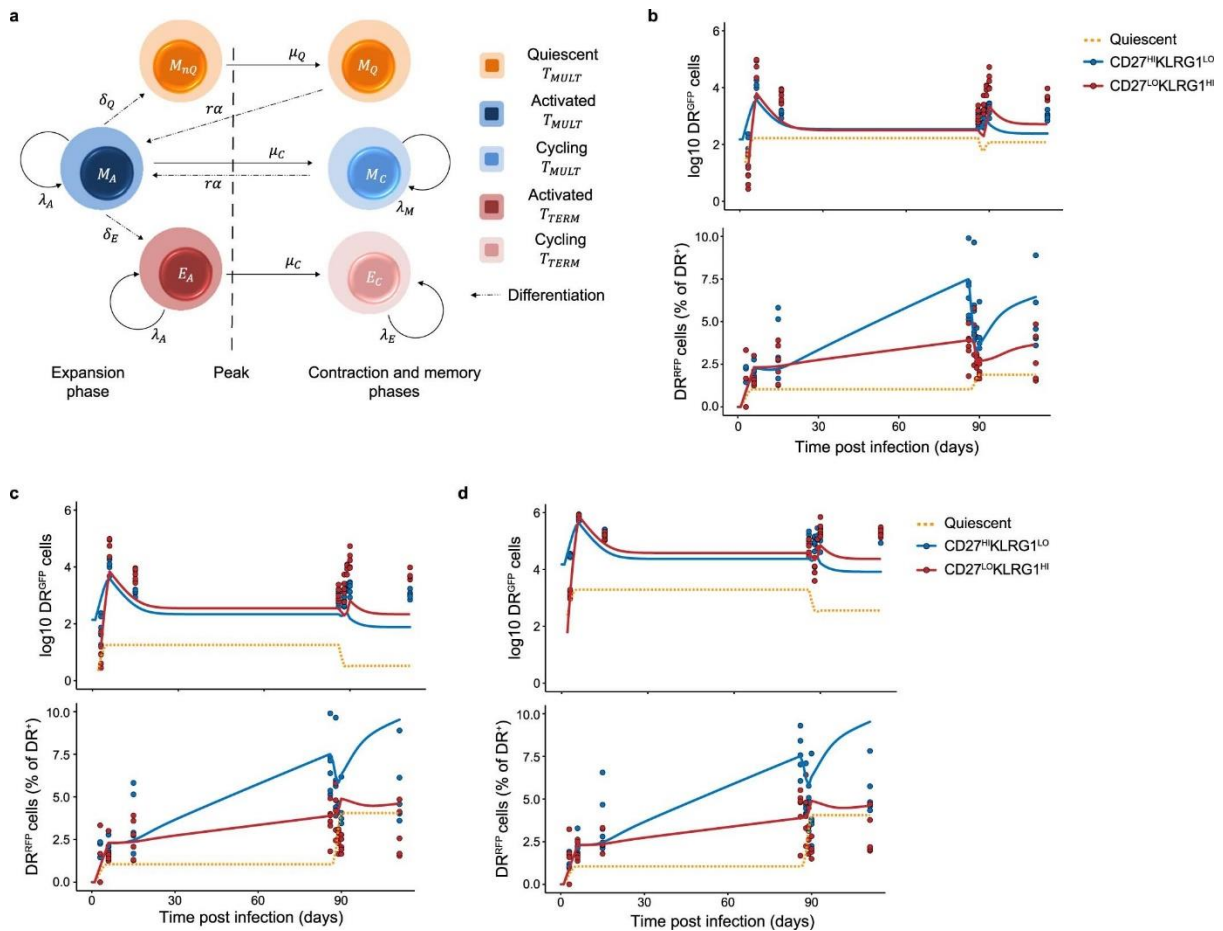


Figure S4.8: Modelled T-cell responses are consistent with the presence of a replication-competent quiescent T_{CM} population. **a**) Cartoon of the phenotype model depicting phenotypes, the considered interactions among them and the parameters associated with the interactions. Arrows indicate various events occurring during the response, such as cell division (denoted with λ), differentiation to a different phenotype (denoted with δ), cell death during contraction (denoted with μ), and recruitment toward the secondary response during recall infection (denoted with r). Subscripts indicate the phenotype of the cell that the parameter is affecting. Full list of parameters can be found in **Supplementary Note 4.5**, **b-d**) Best fit of the modelled T-cell response to the experimental measurements depicting either cell numbers (top plot in each panel), or DR^{REP} percentages (bottom plot in each panel). The total number of quiescent T cells generated was either capped at 1% (**b**) or 0.1% (**c,d**) of the T_{EFF} pool. Lines depict the modelled populations; dots indicate the experimental measurements obtained from peripheral blood (**b,d**) or spleen (**c**). See **Supplementary Note 4.5** for more details and calculations. Experimental data points are representative of at least two independent experiments, dots indicate individual mice ($n = 6$ mice per time point).

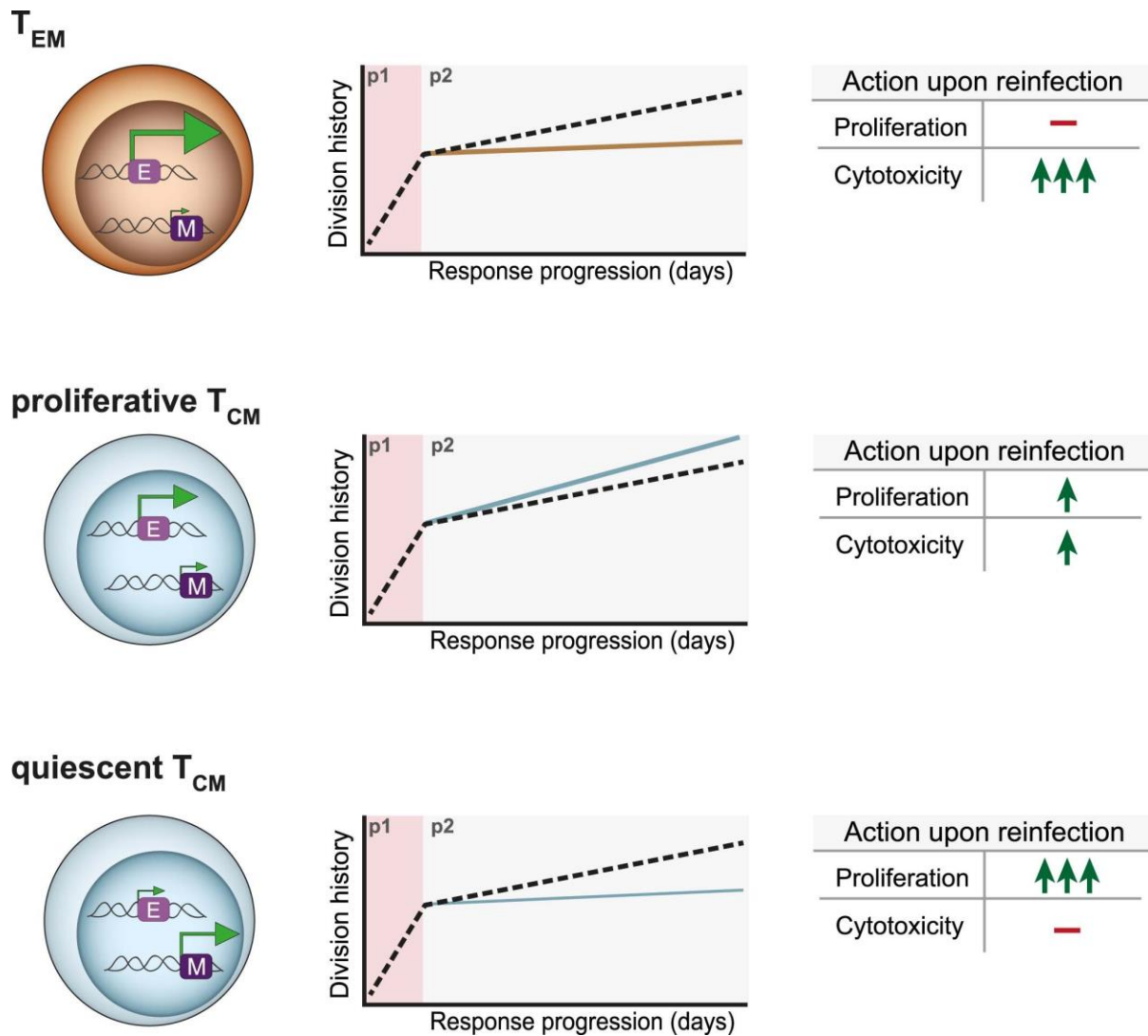


Figure S4.9: Model describing replicative behaviors in the CD8⁺ memory T-cell pool. Upon infection, antigen-specific CD8⁺ T cells activate and rapidly expand (phase 1, p1). Following pathogen clearance (p2), a subset of memory T cells continues to divide, resulting in a progressive increase in the replicative history of the overall T-cell memory pool (dotted line). Within this population, three separate behaviors of transcriptionally disparate memory T-cell pools can be distinguished. **Top)** Terminally differentiated T_{EM} cells that cease division after the inflammation phase (p1) and that are marked by high transcription of effector- and minimal expression of multipotency-associated genes ([E], [M]). Upon reactivation, these cells exert rapid effector functions, but lack the potential to re-expand. **Middle)** A subgroup of T_{CM} that continues to proliferate in the memory phase, exhibits diminished levels of multipotency-associated transcripts, and that abundantly expresses effector-associated genes. Although the functionality of these cells upon reinfection requires further study, their heightened expression of effector-associated genes suggests that these cells exert cytotoxic activity upon reinfection. The contribution of these cells to the secondary T_{EFF} pool is limited. **Bottom)** A subgroup of T_{CM} cells that shows low expression of effector-associated genes but increased expression of multipotency-associated genes, and that exists in a near-quiescent state after the inflammation phase. Upon renewed infection, this cell pool is primarily responsible for the generation of a new wave of secondary T_{EFF}. Based on their transcriptional profile, these cells are expected to have limited immediate cytotoxic functions.

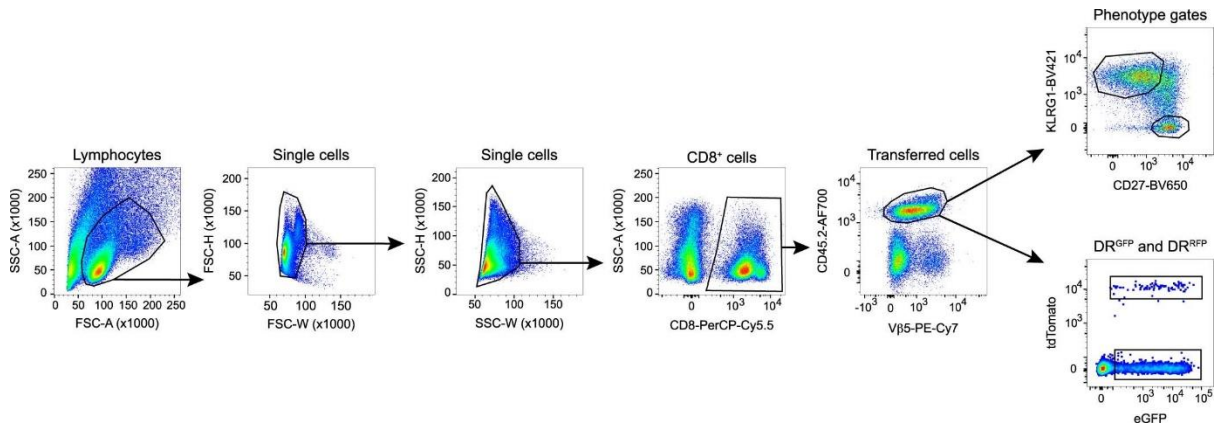


Figure S4.10: Gating strategy. General gating applied to flow cytometry data presented in the study. Single lymphocytes were first selected using morphology gates and were subsequently gated on CD8⁺ T cells and transferred OT-I T cells (Vβ5⁺CD45.2⁺). Next, DR^{RFP} and DR^{GFP} could be directly selected, or first separated by phenotype depending on the analysis. The data presented here was analyzed from blood of a recipient of DR⁺ cells and was acquired 6 days post infection with *Lm*-OVA. Phenotype gates other than those shown here are defined in their respective figures.

Supplementary Notes

Supplementary Note 4.1: Division-coupled stochastic labelling as a proxy of division history

If we would consider a hypothetical T-cell response comprising of two independent populations (A and B; see **Figure SN4.1** below): Both populations start dividing at timepoint 1 with the same amount of RFP label. Population A undergoes a large amount of expansion, and subsequently stops dividing and contracts significantly. Population B undergoes a low level of proliferation but experiences no contraction. At the timepoint of measurement (timepoint 3), population A and B have an equal size.

Due to the high level of proliferation in population A, it accumulates a larger amount of RFP⁺ cells at time-point 2 as compared to its counterpart. As population A stops dividing, it stops accumulating RFP⁺ cells. Next, because RFP labelling occurred stochastically, contraction will occur to the same extent in the labelled and the unlabelled cell pool. As a result, the two equally sized populations that are analysed at timepoint 3 will contain different fractions of RFP⁺ cells, which reflect the difference in division history between these populations.

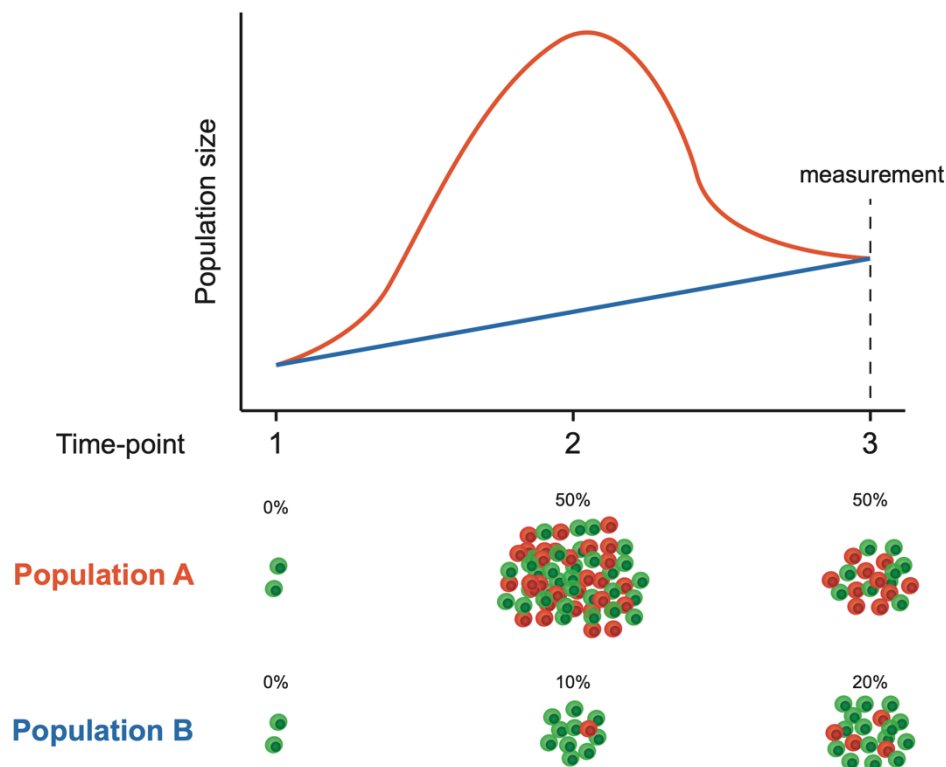


Figure SN4.1: The proportion of RFP⁺ cells in a population reflects only the division history of the population. The illustration shows two populations, A and B, that have the same size and the same proportion of RFP⁺ cells in the beginning. Population A divides much more than population B but also goes through a large contraction such that the sizes of populations A and B are the same at the end. In such a scenario, population A has a higher proportion of RFP⁺ cells, as cells of population A did more divisions.

Supplementary Note 4.2: Minimal ODE model (Figure 4.1b-d, i)

We detail the results from Weber et al. (Weber et al., 2016), as originally shown for a branching process for a system of ordinary differential equations (ODEs). As in Weber et al. (Weber et al., 2016), the average generation number is defined as the mean of the generation numbers of all the cells in the population.

For cells dividing at a rate λ /day and dying at a rate d /day, according to the ODE $\frac{dN}{dt} = (\lambda - d)N$, the equations for change in unlabelled (DR^{GFP}, G) and labelled (DR^{RFP}, R) cells with time can be written as

$$\frac{dG}{dt} = (2 - k)\lambda G + k\lambda(1 - p)G - \lambda G - dG \quad (4.1)$$

$$\frac{dR}{dt} = k\lambda p G + 2\lambda R - \lambda R - dR$$

the fraction of DR^{RFP} labelled cells, f_R at time t is

$$f_R(t) = 1 - f_G(0)e^{-k\lambda p t} \quad (4.2)$$

where, p is the labelling probability and k is the number of daughter cells that get labelled. $k = 1$ is the asymmetric case when only one daughter cell can be labelled during cell division, and $k = 2$ is the symmetric case when both daughters can get labelled during cell division.

In such a model, the average generation number, $\mu_t = 2\lambda t$, is independent of the death rate (De Boer and Perelson, 2013a). For this ODE, the relationship between the fraction of DR^{RFP} labelled cells in a population and its average generation number at some timepoint t is

$$\mu_t = 2\lambda t = -\frac{2}{kp} \ln\left(\frac{f_G(t)}{f_G(0)}\right) \quad (4.3)$$

MEF experiment described in Figure 4.1h-i

Linear regression on the cell number data from the MEF experiment was used to infer the division rate λ (Figure SN4.2). Using the same minimal ODE and assuming no cell death, the estimate for the division rate in the MEF data is $\lambda = 0.698$ /day. The 95% confidence interval for the fit is 0.673-0.723.

With the division rate known, **equation 4.2** was fitted to the fraction of DR^{RFP} labelled cells to estimate the switching probability p . **Figure 4.1i** shows the fits of 300 bootstraps (100 per MEF experiment) on the MEF data. The basic statistics of the switching probability estimates from these fits are $p = 0.0053$ (mean), 0.0052 (median), 0.0043-0.0063 (95% CI).

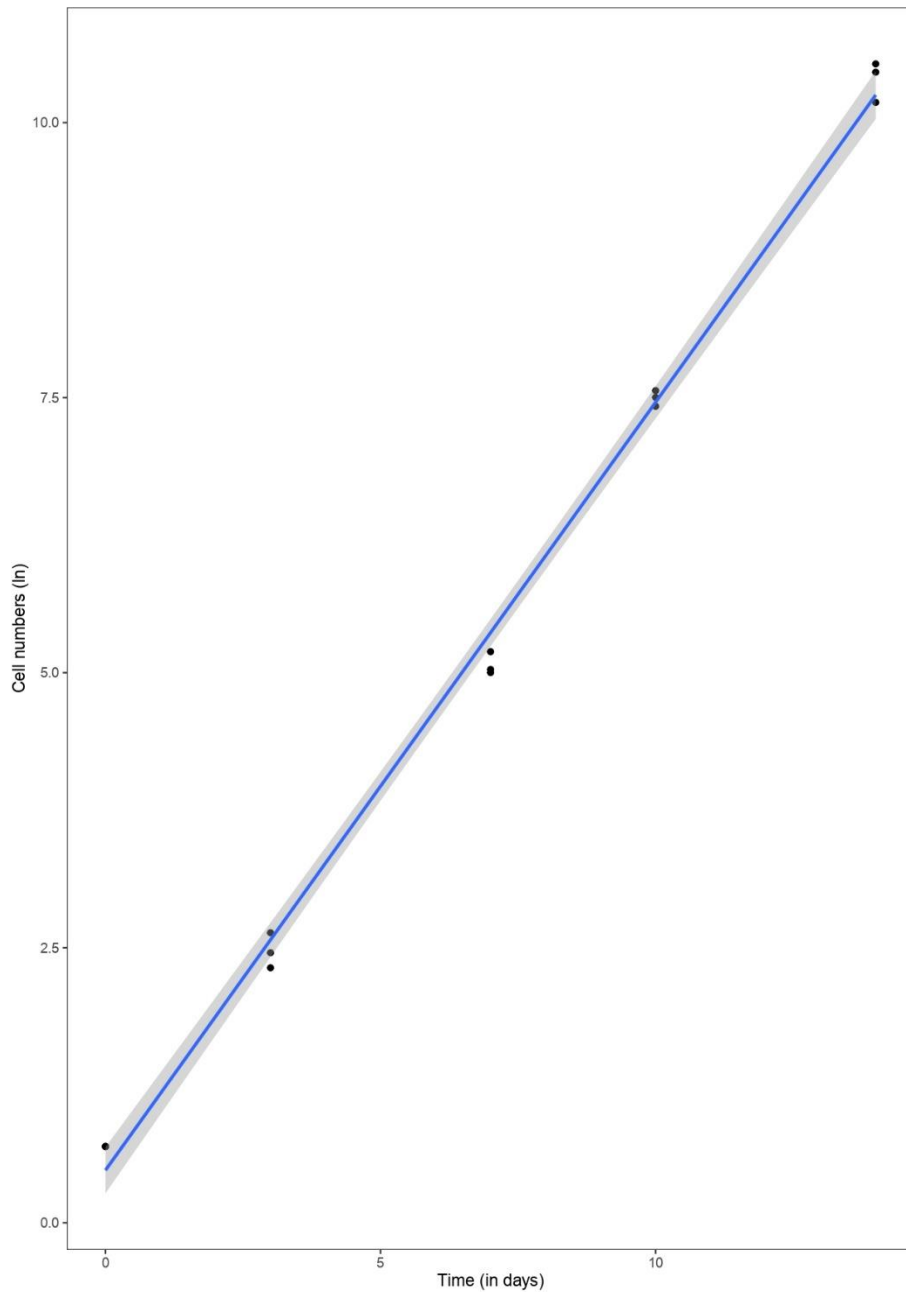


Figure SN4.2: Immortalized DivisionRecorder⁺ (DR⁺) mouse embryonic fibroblasts were cultured, counted, and analyzed every 3-4 days. Natural log of the number of DR⁺ cells is shown for three experimental replicates. Black dots represent the experimental data, the best fit of the linear regression is depicted by the blue line. The slope of this regression line is the division rate of the cells in the MEF experiment.

Supplementary Note 4.3: Expected DR^{RFP} fraction in the memory T-cell pool (Supplementary Figure 4.1)

In **Supplementary Figure 4.1** we model the expected DR^{RFP} fractions in the memory T-cell pool for a several scenarios where memory is generated from a subset of T cells that have undergone different number of divisions during the effector phase.

Consider the clonal expansion and subsequent contraction of a T-cell population with two phenotypes: activated A cells and quiescent Q cells. Activated cells divide at a rate $\lambda_A = 2/\text{day}$ for 6 days (expansion phase), die at a rate $d_A = 0.2/\text{day}$ throughout, and can differentiate into quiescent cells at a rate α_i during the expansion phase. One daughter cell of a dividing unlabelled cell (DR^{GFP}, X_G) can become permanently labelled (DR^{RFP}, X_R) with a switching probability $p = 0.0013$. The labelling is genetic i.e., the daughters of a labelled cell cannot be unlabelled. In the model below, $i \geq 0$ denotes the division number.

$$\begin{aligned}
 A'_{G_{i+1}} &= \lambda_A A_{G_i} + (1-p)\lambda_A A_{G_i} - (\alpha_i + \lambda_A + d_A)A_{G_{i+1}} \\
 A'_{R_{i+1}} &= p\lambda_A A_{G_i} + 2\lambda_A A_{R_i} - (\alpha_i + \lambda_A + d_A)A_{R_{i+1}} \\
 Q'_{G_{i+1}} &= \alpha_i A_{G_{i+1}} \\
 Q'_{R_{i+1}} &= \alpha_i A_{R_{i+1}}
 \end{aligned} \tag{4.4}$$

We analyse two variants of the model. In the first variant, activated cells can only become quiescent when they have completed less than or equal to n divisions. In the second variant, we allow quiescent cells to be formed from activated cells throughout the expansion phase regardless of their prior division number (referred to as 'all'). To create a similar number of quiescent cells in all cases we adjust the rate at which quiescent cells are formed. We depict two examples of the first variant in **Extended Data Figure 4.1** (left and middle panels): $n = 10$ and $n = 24$ (i.e., in the left panel we set $\alpha_i = 0.25/\text{day}$ when $i < 10$ (and $t < 6$ days), and $\alpha_i = 0$ otherwise, and in the middle panel we set $\alpha_i = 0.1/\text{day}$ when $i < 24$ (and $t < 6$ days), and $\alpha_i = 0$ otherwise). The second variant shown in **Extended Data Figure 4.1** (right panel) has the lowest rate at which quiescent cells are formed, $\alpha_i = 0.05/\text{day}$ for all i .

By numerical integration of **equation 4.4**, we show in **Extended Data Figure 4.1** that if the population that is persisting during the memory phase were composed of quiescent cells only, the percentage of DR^{RFP} labelled cells would decrease after the peak, regardless of when quiescent cells appear. Naturally, the decrease in the percentage of DR^{RFP} labelled cells after the peak is smaller when more quiescent cells are formed during the expansion phase. Note that we would not obtain much more quiescent cells if we would increase α_i in the $n = 10$ scenario because a too large α_i cripples the expansion of the activated cells.

Supplementary Note 4.4: Reduction in DR^{RFP} fractions during recall responses (Figure 4.6)

In **Figure 4.6** we apply the DivisionRecorder to assess the replicative recall potential of high- and low-division memory T cells, *in situ*. Based on the reduction in the fraction of DR^{RFP} cells that we reproducibly observe early upon recall, we conclude that secondary T_{EFF} cells predominantly derive from low-division T_{CM}, a conclusion that is in line with the data obtained using a CTV-based serial transfer approach (**Figure 4.5**).

As a potential alternative explanation for the observed reduction in DR^{RFP} fractions, it could be proposed that recall responses would be based on the output of only a very small pool of memory T cells, and the numerical dominance of GFP-positive cells over RFP-positive cells (92.5% versus 7.5%, respectively) would make it likely that such cells would all be GFP-positive, even if replicative recall potential was identical for GFP-positive cells and RFP-positive cells. To determine how small the responding cell pool would have to be to achieve a reproducible drop in the fraction of DR^{RFP} cells without occasional 'jackpot events', in which one of the early responders would be RFP-positive (thereby resulting in a secondary T_{EFF} pool that is largely RFP-positive, something that is not experimentally observed), we modelled memory pools with 7.5% RFP-positive cells, responding to a secondary infection, allowing various numbers of these cells to expand, and then assessed the DR^{RFP} fractions within the resulting T_{EFF} pools (**Figure SN4.3**). This analysis indicates that secondary T_{EFF} pools generated from a very small precursor pool (< 20 cells) would show a reduction in DR^{RFP} fraction in the majority of mice, even if replicative recall potential would be equal between low-division and high-division T_{CM} populations. However, models that assume such a tight bottleneck do show the occurrence of jackpot events, an observation that is inconsistent with the experimental data (**Figure 4.6**). In addition, an assumption of a responding cell pool of < 20 cells is inconsistent with the widely held view that recall responses are more rapid because of the larger pool of responding cells. Based on this analysis, we conclude that the observed drop in labelling rate during recall responses cannot be explained by T-cell expansion during recall responses being driven by a very small pool of reactivated T cells.

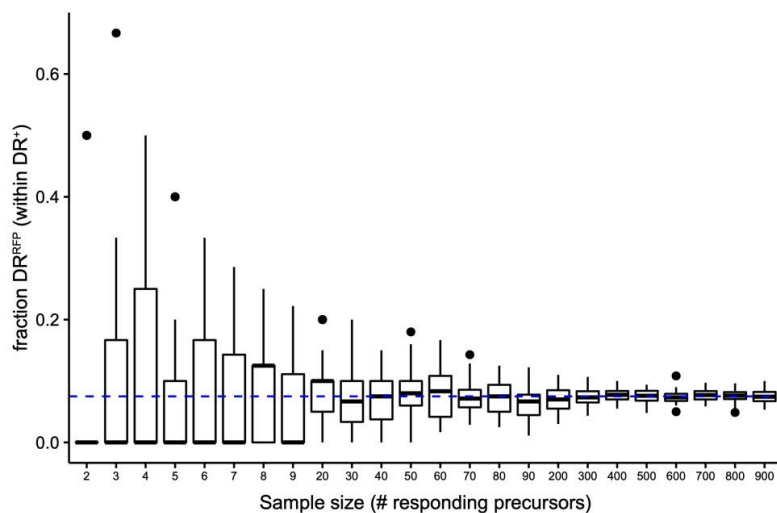


Figure SN4.3: Random sampling of precursor cells initiating the recall response. Expected DR^{RFP} fractions in secondary T_{EFF} pools (vertical axis) when a random sample of responding cells of a particular size (horizontal axis) is selected from a memory population that contains 7.5% DR^{RFP} cells (marked by horizontal dashed line). Selected responding cells expand to an equal degree to form the secondary T_{EFF} pool. Simulations were repeated 39 times (i.e., the number of mice in which recall experiments were performed in this manuscript). Boxplots indicate group median and 25th/75th percentiles, whiskers indicate the interquartile range multiplied by 1.5. Outliers are shown as dots.

Supplementary Note 4.5: Phenotype model (Supplementary Figure 4.2h, Figure 4.7a-c, Supplementary Figure 4.8)

In the main text, we argue that the observed drop in DR^{RFP} percentages is due to the preferential recruitment of lowly divided cells into subsequent responses. Here, we provide support for this proposition by demonstrating that a similar transient drop in DR^{RFP} frequencies is observed in mechanistic mathematical models that have a preferential recruitment of lowly divided cells into the secondary response. In the modelled T-cell responses described below, we consider two major phenotypic subsets; CD27^{hi}KLRG1^{lo} (hereafter referred to as T_{MULT}) and CD27^{lo}KLRG1^{hi} (hereafter referred to as T_{TERM}).

For an experiment in which DR^{RFP} label flow is asymmetrical and permanent, the DR^{RFP} accumulation in a population can be modelled by **equation 4.5**; see the cartoon in **Supplementary Figure 4.8a**. We model five phenotypes: clonally expanding activated T_{MULT} cells (M_A), clonally expanding activated T_{TERM} cells (E_A), cycling T_{MULT} cells (M_C), cycling T_{TERM} cells (E_C) and quiescent T_{MULT} cells (M_Q , M_{nQ}). The variable M_{nQ} (for newQ) keeps track of newly formed quiescent cells to prevent them from becoming re-activated during the same expansion phase. These cells become M_Q during the contraction and memory phase and can be re-activated during the secondary expansion phase.

Upon encountering antigen, a naive T cell becomes activated, starts dividing and gives rise to a continuum of phenotypically different populations. The phenotype model (**Supplementary Figure 4.8a**) broadly classifies this continuum into the five phenotypes introduced above. An activated T_{MULT} can either differentiate into an activated T_{TERM} or can stop dividing and become a quiescent T_{MULT}. After the peak of the response, a small part of the activated T_{MULT} and T_{TERM} populations becomes cycling T_{MULT} cells and long-lived T_{TERM} cells, respectively. During the recall response, we model a scenario in which a fraction of the cells engages in renewed expansion. Upon secondary antigen encounter (set at day 86 post primary infection, in concordance with the recall experiment presented in **Figure 4.6b**), the model undergoes a second sequence of expansion, contraction, and memory formation.

To examine the scenario in which lowly divided cells are preferentially recruited, it was important to know the division history of cells prior to the re-expansion. We, therefore, formulated a division-indexed model (similar to **equation 4.4**) to track the number of divisions of the DR^{GFP} and DR^{RFP} cells of each phenotype over time. The model is described in full in the supplementary R codes. For readability we here present a collapsed version of the

model, which can be obtained by summing over the division numbers as well as the DR^{GFP} and DR^{RFP} cells (compare the full model equations shown in **equation 4.6** to the collapsed equation in **equation 4.5** for a single phenotype, E_A):

$$\begin{aligned}\frac{dM_A}{dt} &= \alpha(i)r(M_C + M_Q) + 2\lambda_A M_A - (\lambda_A + d_A + \delta_E(t) + \delta_Q(t) + \mu_C)M_A \\ \frac{dE_A}{dt} &= \delta_E(t)M_A + 2\lambda_A E_A - (\lambda_A + d_A + \mu_C)E_A \\ \frac{dM_C}{dt} &= \mu_C M_A + 2\lambda_M M_C - (\lambda_M + d_M + \alpha(i)r + (1 - \alpha(i))d_C)M_C \\ \frac{dE_C}{dt} &= \mu_C E_A + 2\lambda_E E_C - (\lambda_E + d_E + d_C)E_C \\ \frac{dM_{nQ}}{dt} &= \delta_Q(t)M_A - \mu_Q M_{nQ}\end{aligned}\tag{4.5}$$

$$\frac{dM_Q}{dt} = \mu_Q M_{nQ} - (\alpha(i)r + (1 - \alpha(i))d_C)M_Q$$

$$\delta_E(t) = \delta_{E_{max}}(1 - e^{-e_a t_{exp}})$$

$$\delta_Q(t) = \delta_{Q_{max}} e^{-m_q t_{exp}}$$

$$\alpha_i = \left(1 + \left(\frac{i}{h}\right)^m\right)^{-1}; \quad i = 1, \dots, n$$

where t_{exp} (for time in expansion) is the time since the most recent challenge. The fraction of cells that is expected to be re-activated, $0 \leq \alpha(i) \leq 1$, is a function of the division number, i . Each phenotype is actually indexed by the number of divisions completed, i , and is subdivided into an unlabelled (DR^{GFP}, G) and a labelled (DR^{RFP}, R) subtype. For instance, the full division-indexed model for activated T_{TERM} cells is:

$$\frac{dE_{AG_i}}{dt} = \delta_E(t)M_{AG_i} + (2 - p)\lambda_A E_{AG_{i-1}} - (\lambda_A + d_A + \mu_C)E_{AG_i}\tag{4.6}$$

$$\frac{dE_{AR_i}}{dt} = \delta_E(t)M_{AR_i} + p\lambda_A E_{AG_{i-1}} + 2\lambda_A E_{AR_{i-1}} - (\lambda_A + d_A + \mu_C)E_{AR_i}$$

where p is the switching probability. A complete list of division-indexed phenotype specified equations can be found in the R code. Below, we explain the stepwise parameter estimation procedure of this model.

Fitting the model and estimating the parameters

Two phases of immune response were inferred from the experimental data: the expansion phase (day 0-6 for the primary response and day 86-90 for the secondary response), and the non-expansion phase, i.e., the contraction and memory phases (day 6-86 for the primary response and day 90-111 for the secondary response). The percentages of DR^{RFP} cells in blood and spleen were found to be highly similar. Additionally, the ratio of the number of DR^{GFP} cells in spleen to that in blood was similar across all time points. The blood and spleen data were, therefore, fitted simultaneously under the assumption that both compartments are well-mixed (**Figure 4.7a-c, Supplementary Figure 4.8**).

Our primary interest was to find a realistic division history of all phenotypes on day 86, to subsequently test whether the preferential recruitment of lowly divided cells can explain the kinetics of labelling rate during recall responses. The number of free model parameters was reduced to 6 using a few simplifying assumptions:

- (i) The division rate during the expansion phase is the same for T_{MULT} and T_{TERM} cells,
- (ii) The death rate of cells during the expansion phase is negligible,
- (iii) The formation of quiescent cells decreases with time post antigen encounter,
- (iv) The rate at which T_{TERM} cells are formed increases with time (instead of division number),
- (v) Only 5% of the activated cells survive after the expansion phase, i.e., $\mu_C = \frac{d_A}{19}$, and
- (vi) T_{MULT} and T_{TERM} cells maintain constant numbers during the memory phase, i.e., $\lambda_M = d_M$ and $\lambda_E = d_E$.

The free parameters were estimated by fitting the collapsed model sequentially to the data obtained during the primary expansion and non-expansion phases. First, the initial number of cells that were activated among the engrafted cells in blood and spleen, the division rate of the activated cells, and the differentiation rate of the activated cells into the different phenotypes were estimated using the experimental data obtained during the expansion phase. Next, these estimated parameters were used to estimate the division rates of the cycling cells from the experimental data obtained during the non-expansion phase. Because the estimation of the re-activation function was infeasible, as it would require fitting the full division-indexed model to the data, this function was tuned manually to obtain an optimal description of the data with the full model. The estimated parameters for the best description of the data are listed in **Table SN4.1**.

Expansion of adoptively transferred DR⁺ cells is expected to occur after a short delay, covering both the time required to identify an antigen-positive APC and to initiate cell division after TCR triggering. This delay was fixed to 1 day as our dataset lacked the appropriate information for this parameter to be estimated. The loss rate of activated cells was fixed to $d_A = 0.3/\text{day}$. The rate at which the formation of quiescent cells declines was tuned such that only 1% of the quiescent population formed during the primary response would be DR^{RFP}. As antigen-experience is known to influence secondary memory formation,

e.g., the expansion phase occurring on a shorter timescale and a considerably slower contraction phase, the rates during the secondary response differ from those during the primary response (Masopust et al., 2006). Therefore, m_q and μ_C were set to 0.5/day and $\frac{d_A}{4}$, respectively.

The maximum rate at which quiescent cells were formed was fixed to different values ($\delta_{Q_{max}} \in \{0.01, 0.1\}$) to generate different numbers of quiescent cells ($10^3, 10^4$) at the peak of the primary response (day 6) (**Figure 4.7a**). Unsurprisingly, formation of a larger number of quiescent cells during the primary response, resulted in a larger drop in DR^{RFP} frequencies during secondary expansion (**Figure 4.7b**). Higher numbers of quiescent T_{CM} also generated secondary responses that were higher in magnitude, providing a better explanation of the data (**Supplementary Figure 4.8b-d**). Three different re-activation functions, signifying either an abrupt (fun 1-2) or gradual loss (fun 3) of re-expansion potential based on the number of prior divisions, were tested (**Figure 4.7a**). The experimental data was only congruent with scenarios where re-expansion potential was restricted to cells that had undergone limited clonal expansion (**Figure 4.7a-b**). Furthermore, higher numbers of quiescent T_{CM} correlated positively with larger drops in DR^{RFP} frequencies upon re-expansion (**Figure 4.7b**).

Parameter	Description	Value	Units	On (1)/Off (0) during phases	
				Expansion	Non-expansion
t_{on}	Time delay before the first division	1 (F)	days	-	-
λ_A	Division rate of activated T _{MULT} and T _{TERM} cells	0.89	/day	1	0
d_A	The rate at which (re-) activated T _{MULT} and T _{TERM} cells leave circulation	0.3 (F)	/day	0	1
d_C				1	0
$\delta_{Q_{max}}$	Maximum differentiation rate of the activated T _{MULT} into quiescent T _{MULT} cells	0.1 (F)	/day	1	0
m_q	The rate at which $\delta_Q(t)$ changes	0.25 (F)	/day	-	-
$\delta_{E_{max}}$	Maximum differentiation rate of the activated T _{MULT} into activated T _{TERM} cells	2 (F)	/day	1	0
e_a	The rate at which $\delta_E(t)$ changes	0.15	/day	-	-

$\lambda_M = d_M$	Division and death rate of the cycling T_{MULT} cells	0.3	/day	1	1
$\lambda_E = d_E$	Division and death rate of the cycling T_{TERM} cells	0.04	/day	1	1
r	The rate of re-activation of quiescent and cycling T_{MULTS}	1 (F)	/day	1	0
h	Cut-off of the fraction re-activated function	25 (F)	-	-	-
m	Slope of the fraction re-activated function	30 (F)	-	-	-
$M_{AG}(0)$	Initial number of naïve cells at day 0	16748.72 (Spleen)	Cells (avg.)	-	-
		149.30 (Blood)			

Table SN4.1: The estimated parameters for the best fit of the phenotype model to the data. The parameter values in this table were obtained by fitting the phenotype model to the blood and spleen data simultaneously using the pseudorandom-search algorithm (see pseudoOptim) in the modFit function of the FME R package (Soetaert and Petzoldt, 2010). F signifies that these parameters were set to a fixed value.

Supplementary Note 4.6: Analysis of DivisionRecorder single integration frequency

As the DivisionRecorder is retrovirally introduced into the genome, a fraction of the modified cells may carry multiple integrations. As each DivisionRecorder has an independent probability of slippage - and hence creation of an in-frame Cre gene - during cell division, this means that cells that contain more than 1 integration will have a 'faster clock', resulting in the more rapid labelling of these cells. However, as the DivisionRecorder is applied as a population-based metric, and conclusions are based on comparison of different timepoints and/or different cell populations within individual mice, the presence of a fraction of cells with multiple integration events will not influence the interpretation of the obtained data. Nevertheless, to minimize variation in the fraction of cells with > 1 integration event between experiments, we aimed for a low and standardized transduction efficiency, in which the occurrence of multiple integration events will be minor. To determine which fraction of single integrations could be expected as a factor of transduction efficiency, Ai9 mouse embryonic fibroblasts (MEFs) or *ex vivo* activated Ai9;OT-I cells were transduced with a mixture of 2 retroviruses encoding either GFP or Katushka. The fraction of single and double-positive cells could subsequently be used to estimate the relationship between transduction efficiency and the percentage of single integrations. This analysis shows that at a transduction efficiency of $\sim 10\text{-}15\%$ (the transduction efficiency used for *in vivo* experiments), approximately 85-90% of the modified cells contain a single integration, and

this percentage is comparable between the two cell types assessed (**Figure SN4.4**). Thus, the large majority of switch events we observe in our experiments derives from cells carrying a single reporter.

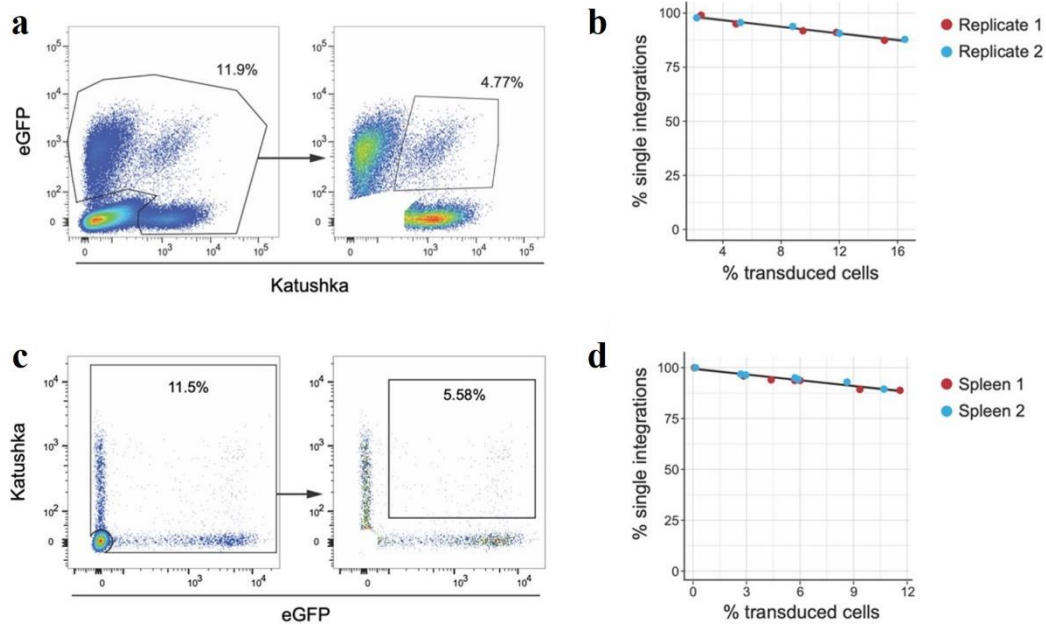


Figure SN4.4: Frequency of multiple retroviral integration events. GFP and Katushka encoding retroviruses were mixed 1:1, and subsequently used to transduce either Ai9 MEF cells (**a-b**) or *ex vivo* activated Ai9;OT-I cells (**c-d**). Ai9 MEF and Ai9;OT-I cells were assessed for fluorescent protein expression at day 7 or 24 hours post transduction, respectively. The percentage of cells carrying a single integration was calculated as $100 - (2 \times \text{fraction of GFP}^+\text{Katushka}^+ \text{ cells})$. **a**) Gating strategy to determine the percentage of GFP⁺Katushka⁺ cells within the transduced Ai9 MEF cell population. **b**) Plot depicting the percentage of Ai9 MEF cells carrying a single retroviral integration at different transduction efficiencies. **c**) Gating strategy to determine the percentage of GFP⁺Katushka⁺ cells within the transduced Ai9;OT-I cell population. **d**) Plot depicting the percentage of Ai9;OT-I cells carrying a single retroviral integration at different transduction efficiencies. Depicted data was obtained in a single experiment consisting of two experimental replicates. Dots indicate individual samples, lines represent a linear regression fitted to the data points (**b,d**).

Supplementary Note 4.7: Retroviral silencing of the DivisionRecorder does not occur

As the GFP-Cre module of the DivisionRecorder is introduced retrovirally, there is a potential risk of retroviral transcriptional silencing or attenuation. Such silencing events could influence interpretation of the data, as the fraction of DR^{RFP} cells over DR^{GFP} cells may become skewed. As only the GFP-Cre module is retrovirally introduced, whereas the RFP reporter that is switched on upon Cre activity is germline encoded, the extent of retroviral silencing can be experimentally determined by measuring the occurrence of cells that do show RFP expression (and hence did at some point express the GFP-Cre module) but lack GFP expression. As depicted in **Figure SN4.5**, virtually no RFP⁺GFP⁻ cells are observed within recipient mice, either during the acute phase or in the memory phase, demonstrating that retroviral silencing is extremely rare.

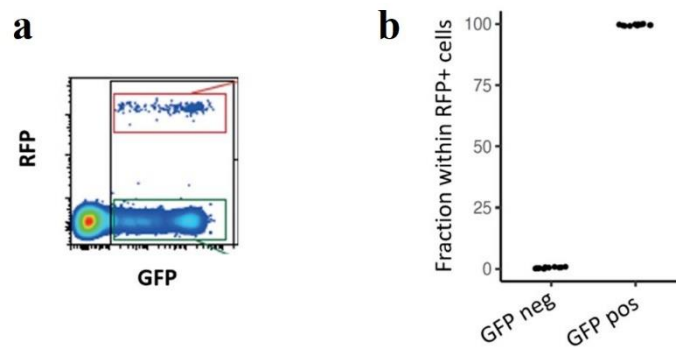


Figure SN4.5: GFP expression of RFP⁺ cells. *Lm*-OVA-infected recipient mice received 20,000 DR⁺ cells and the occurrence of GFP⁻RFP⁺ cells was assessed in spleen on day 6 and 86 after adoptive cell transfer. **a**) Flow cytometry plot, gated on CD45.2⁺ cells, depicting RFP and GFP expression. **b**) Fraction of GFP⁻ and GFP⁺ cells within the RFP⁺ cell population ($n = 12$ mice).

Supplementary Tables

Effector-sig	Multipotency-sig
<i>Id2</i>	<i>Myb</i>
<i>Ifng</i>	<i>Tcf7</i>
<i>Tbx21</i>	<i>Bach2</i>
<i>Lgals1</i>	<i>Eomes</i>
<i>Gzmb</i>	<i>Sell</i>
<i>Prfl</i>	<i>Ccr7</i>
<i>Prdm1</i>	<i>Il7r</i>
<i>Klrg1</i>	<i>Bcl2</i>
<i>Cx3cr1</i>	

Table S4.1: Manually curated effector-associated and multipotency-associated gene signatures. Listed in order of appearance (top-to-bottom) in the heatmap depicted in **Figure 4.4b**.

gs_name	gs_id	gs_pmid	gs_exact_source	gs_description
GOLDRATH_EFF_VS_MEMORY_CD8_TCELL_DN	M3044	16492737	GSE1000002_1582_200_DN	Genes downregulated in comparison of effector CD8 T cells relative to memory CD8 T cells.
GOLDRATH_EFF_VS_MEMORY_CD8_TCELL_UP	M3041	16492737	GSE1000002_1582_200_UP	Genes upregulated in effector CD8 T cells relative to memory CD8 T cells.
GOLDRATH_NAIVE_VS_EFFECTOR_CD8_TCELL_DN	M3036	16492737	GSE1000002_1580_200_DN	Genes downregulated in naive CD8 T cells relative to effector CD8 T cells.
GOLDRATH_NAIVE_VS_EFFECTOR_CD8_TCELL_UP	M3035	16492737	GSE1000002_1580_200_UP	Genes upregulated in naive CD8 T cells relative to effector CD8 T cells.
GOLDRATH_NAIVE_VS_MEMORY_CD8_TCELL_DN	M3039	16492737	GSE1000002_1581_200_DN	Genes downregulated in naive CD8 T cells relative to memory CD8 T cells.

GOLDRATH_NAIVE_VS_MEMORY_CD8_TCELL_UP	M3038	1649 2737	GSE1000002_1581_200_UP	Genes upregulated in naive CD8 T cells relative to memory CD8 T cells.
KAECH_DAY15_EFF_VS_MEMORY_CD8_TCELL_DN	M3032	1252 6810	GSE1000001_1579_200_DN	Genes downregulated in effector CD8 T cells at contraction phase (day 15 after LCMV-Armstrong infection) relative to memory CD8 T cells (day 40+ after LCMV-Armstrong infection).
KAECH_DAY15_EFF_VS_MEMORY_CD8_TCELL_UP	M3030	1252 6810	GSE1000001_1579_200_UP	Genes upregulated in effector CD8 T cells at contraction phase (day 15 after LCMV-Armstrong infection) relative to memory CD8 T cells (day 40+ after LCMV-Armstrong infection).
KAECH_DAY8_EFF_VS_DAY15_EFF_CD8_TCELL_DN	M3025	1252 6810	GSE1000001_1577_200_DN	Genes downregulated in effector CD8 T cells at the peak expansion phase (day 8 after LCMV-Armstrong infection) relative to effector CD8 T cells at contraction phase (day 15 after LCMV-Armstrong infection).
KAECH_DAY8_EFF_VS_DAY15_EFF_CD8_TCELL_UP	M3023	1252 6810	GSE1000001_1577_200_UP	Genes upregulated in effector CD8 T cells at the peak expansion phase (day 8 after LCMV-

				Armstrong infection) relative to effector CD8 T cells at contraction phase (day 15 after LCMV-Armstrong infection).
KAECH_DAY8_EFF_VS_MEMORY_CD8_TCELL_DN	M3028	12526810	GSE1000001_1578_200_DN	Genes downregulated in effector CD8 T cells at the peak expansion phase (day 8 after LCMV-Armstrong infection) relative to memory CD8 T cells (day 40+ after LCMV-Armstrong infection).
KAECH_DAY8_EFF_VS_MEMORY_CD8_TCELL_UP	M3027	12526810	GSE1000001_1578_200_UP	Genes upregulated in effector CD8 T cells at the peak expansion phase (day 8 after LCMV-Armstrong infection) relative to memory CD8 T cells (day 40+ after LCMV-Armstrong infection).
KAECH_NAIVE_VS_DAY15_EFFECTIVE_CD8_TCELL_DN	M3017	12526810	GSE1000001_1575_200_DN	Genes downregulated in naive CD8 T cells relative to effector CD8 T cells at contraction phase (day 15 after LCMV-Armstrong infection).
KAECH_NAIVE_VS_DAY15_EFFECTIVE_CD8_TCELL_UP	M3014	12526810	GSE1000001_1575_200_UP	Genes upregulated in naive CD8 T cells relative to effector CD8 T cells at

				contraction phase (day 15 after LCMV-Armstrong infection).
KAECH_NAIVE_VS_DAY8_EFF_CD8_TCELL_DN	M3013	12526810	GSE1000001_1574_200_DN	Genes downregulated in naive CD8 T cells relative to effector CD8 T cells at the peak expansion phase (day 8 after LCMV-Armstrong infection).
KAECH_NAIVE_VS_DAY8_EFF_CD8_TCELL_UP	M3012	12526810	GSE1000001_1574_200_UP	Genes upregulated in naive CD8 T cells relative to effector CD8 T cells at the peak expansion phase (day 8 after LCMV-Armstrong infection).
KAECH_NAIVE_VS_MEMORY_CD8_TCELL_DN	M3022	12526810	GSE1000001_1576_200_DN	Genes downregulated in naive CD8 T cells relative to memory CD8 T cells (day 40+ after LCMV-Armstrong infection).
KAECH_NAIVE_VS_MEMORY_CD8_TCELL_UP	M3020	12526810	GSE1000001_1576_200_UP	Genes upregulated in naive CD8 T cells relative to memory CD8 T cells (day 40+ after LCMV-Armstrong infection).

Table S4.2: Gene-sets used from the MSigDB collection C7.

Ly96	Cd38	Tlr3	Itga5	Fbxo10	Tgfbr2	Prdm2
Il1r2	Tlr1	Il12rb1	Il1rap	Tgfbr1	Cx3cr1	Prdm16
Il1r1	Tlr6	Jak3	Itgb5	Nr4a3	Clec3b	Klf3

Il18r1	Il12rb2	Il15	Cd86	Fbxo42	Fbxo48	Ezh2
Il18rap	Cd8b1	Il27ra	Cd80	Fbxo6	Bcl11a	Prdm5
Cd28	Cd8a	Itgb1	Cd200r1	Fbxo44	Havcr2	Tcf7l1
Cxcr4	Il17ra	Il3ra	Cd200r4	Tgfbr3	Serpinf2	Foxp1
Cd55	Klrg1	Il17rd	Cd200	Fbxo21	Traf4	Sox5
Tnfsf4	Cd163	Il17rb	Cd96	P2rx7	Lgals9	Klf13
Sell	Cd4	Tox4	Cd47	P2rx4	Fbxo47	Myb
Xcl1	Cd27	Ltb4r1	Il10rb	Bcl7a	Lgals8	Foxo3
Cd247	Tnfrsf1a	Gzmc	Ifngr2	Bcl7b	Serpinb1a	Prdm1
Cd244	Cd9	Gzmb	Tnfrsf12a	Fbxo24	Serpinb6b	Icosl
Ly9	Klrb1c	Tnfrsf10b	Cd320	Kdelr2	Serpinb9	Tcf3
Cd48	Klrb1f	Cxcr5	Ly6g5b	Gimap8	Serpinb6a	Klf16
Cd84	Cd69	Cd3g	Ltb	Gimap9	Prr7	Prdm4
Cd46	Klre1	Cd3d	Tnf	Gimap4	Tgfbi	Socs2
Il2ra	Klrd1	Cd3e	Cd2ap	Gimap6	Ctla2b	Stat6
Il15ra	Klrk1	Il10ra	Tnfrsf21	Gimap7	Ctla2a	Stat2
Cd302	Klrc3	Il18	Tnfaip8l1	Gimap1	Fbxo33	Jund
Ly75	Klrc2	Il20rb	Tnfsf9	Gimap5	Serpina12	Klf2
Itga6	Klrc1	Ccr9	Tnfsf14	Gimap3	Serpina3f	Junb
Itga4	Klri2	Cxcr6	Tnfaip8	Bcl2l13	Serpina3g	Tcf25
Itgav	Klra4	Ccr3	Cd74	Clec4a1	Bcl11b	Socs4
Cd82	Klra8	Ccr2	Cd226	Clec4a3	Traf3	Klf12
Cd44	Klra9	Ccr5	Cd5	Clec4a2	Fbxo4	Dnmt1
Il1b	Klra7	Tnfrsf13b	Cd6	Clec4n	Fbxo32	Prdm10
Cd93	Klra3	Cd68	Jak2	Lag3	Lgals1	Tcf12
Cd40lg	Klra2	Tnfsf13os	Cd274	Clec2i	Nr4a1	Eomes
Cd99l2	Cd3eap	Itgae	Tgfbrap1	Clec2g	Clec16a	Tcf7
Il2rg	Cd79a	Tnfaip1	Ctla4	Clec2d	Bcl6	Mybbp1a
Itgb1bp2	Ltbp4	Itga3	Serpine2	Clec12a	Fbxo45	Tbx21
Cxcr3	Cd22	Ccr7	Fbxo36	Bcl2l14	Fbxo40	Socs7
Tlr7	Il4i1	Ccr10	Pdcd1	Fbxo46	Traf7	Stat3
Il7	Cd37	Itga2b	Bcl2	Bcl3	Fbxo11	Socs3
Tnfsf10	Il16	Itgb3	Serpinc1	Tgfb1	Fbxo38	Klf6
Il2	Il18bp	Cd79b	Fasl	Fbxo27	Pdcd1lg2	Sox4
Tlr2	Il4ra	Cd300a	Fbxo28	Fbxo17	Fas	Klf11
Cd1d1	Il21r	Cd300c2	Tgfb2	Lgals4	Pdcd11	Id2
Cd5l	Cd19	Cd300lf	Traf5	Clec11a	Mybl1	Klf10
Il6ra	Cd2bp2	Itgb4	Fbxo18	Bcl2l12	Stat4	Tcf20
Tnfaip8l2	Itgal	Cd7	Traf2	Kdelr1	Stat1	Socs1
Itga10	Itgam	Ly86	Traf1	Lat	Icos	Runx1

Cd160	Itgax	Cd83	Nr4a2	Bcl7c	Klf7	Prdm15
Cd101	Itgad	Cd180	Traf6	Tgfb1i1	Gata3	Prdm9
Cd2	Cd163l1	Il6st	Fbxo3	Fbxo5	Zeb2	Tcf19
Cd53	Cd151	Gzma	Bcl2l11	Fbxo30	Zeb2os	Runx2
Tox	Cd81	Gzmk	Bcl2l1	Fbxo7	Prdm11	Runx2os2
Il11ra1	Tnfrsf26	Itga2	Pdcd10	Tgfb3l	Sox12	Runx2os1
Cd72	Tnfrsf22	Itga1	Serpini1	Fbxo25	Id1	Foxp4
Tnfsf8	Tnfrsf23	Itgb1bp1	S100a1	Fbxo8	Mybl2	Socs5
Tlr4	Tnfaip3	Il7r	S100a13	Fbxo31	Foxp3	Zeb1
Itgb3bp	Ifngr1	Ly6d	S100a3	Lgals3	Foxo4	Gata6
Jak1	Cd164	Ly6k	S100a2	Fbxo34	Klf8	Tcf4
Tlr12	Cd24a	Ly6e	S100a4	Bcl2l2	Foxo1	Socs6
Cd52	Prf1	Ly6i	S100a5	Bcl9l	Bach2	Klf9
Tnfrsf1b	Itgb2	Ly6a	S100a6	Fbxo22	Bach2os	Tcf7l2
Tnfrsf9	Gzmm	Ly6c1	S100a11	Fbxo9	Klf4	S1pr1
Tnfrsf25	Ifng	Ly6c2	S100a10	Bcl2a1d	Jun	Jakmip1
Tnfrsf14	Ifngas1	Il2rb	Bcl9	Bcl2a1a	Junos	S1pr4
Tnfrsf4	Cd63	Tnfrsf13c	Bcl2l15	Bcl2a1b	Runx3	S1pr2
Tnfrsf18	Tnfsf13b	Itgb7	Bcl10	Bcl2a1c	Id3	S1pr5

Table S4.3: Full list of immune-associated genes used in scRNAseq data analysis.

Up in IdT _{CM}	Up in hdT _{CM}
Il7r	Ccr2
Stat4	S100a11
Tcf7	Tbx21
Klf3	Klrc1
Foxp1	Il2rb
Sell	Jund
Itga4	Cd52
Cd84	Cd48
Eomes	Gzmb
Ltb	Prf1
Gimap6	Pdcd10
Cd28	Itgb7
Serpina3g	Cd2
Xcl1	Cd3g
Gzmk	S100a10
Gimap7	S100a4

Stat1	Cd8b1
	Lgal1
	S100a13
	S100a6
	Klrk1
	Ly6c2
	Klf2

Table S4.4: Full gene lists from heatmap depicted in **Figure 4.4g** in order of appearance (left-to-right).

Positive association		Negative association	
<i>Ccnd3</i>	<i>Phf1</i>	<i>Anln</i>	<i>Birc5</i>
<i>Pdk1</i>	<i>Ctdsp1</i>	<i>Ccna2</i>	<i>Ccnb1</i>
<i>Smarca2</i>	<i>Thrashings</i>	<i>Ccne2</i>	<i>Ccne2</i>
<i>Foxo3</i>	<i>Tef</i>	<i>Sgol1</i>	<i>Mcm4</i>
<i>Ezh1</i>	<i>Dicer1</i>	<i>Pcna</i>	<i>Rrm2</i>
<i>Prdm5</i>	<i>Bcas3</i>	<i>Top2a</i>	<i>Cyts</i>
<i>Ptov1</i>	<i>Ddx3y</i>	<i>Mtch2</i>	<i>Slc25a5</i>
<i>Zfp30</i>	<i>Gabarapl1</i>	<i>H2afz</i>	<i>Capza1</i>
<i>Zbtb20</i>	<i>Gltscr2</i>	<i>Hadhb</i>	<i>ldh3a</i>
<i>Phf1</i>	<i>Itm2a</i>	<i>Kpna2</i>	<i>Pgk1</i>
<i>Il18</i>	<i>Gstk1</i>		
<i>Ddt</i>	<i>Chkb</i>		
<i>Ivd</i>	<i>Pink1</i>		
<i>Fhl1</i>	<i>Ulk2</i>		
<i>Ndrp2</i>	<i>Dnajb9</i>		
<i>Grina</i>	<i>Pfdn5</i>		
<i>Pik3r1</i>	<i>Ctsf</i>		
<i>Fyn</i>	<i>Crim1</i>		
<i>Ephx1</i>	<i>Sepp1</i>		
<i>Clstn1</i>	<i>Gabbr1</i>		
<i>Igf2r</i>	<i>Rnf167</i>		
<i>Selenbp1</i>	<i>Map1lc3a</i>		

Table S4.5: Quiescent stem cell gene signature as described in Cheung & Rando et al. (Cheung and Rando, 2013).

Name	Sequence
------	----------

		d			Human	Quality tested
anti-KLRG1- Brilliant Violet 421	2F1/KLR G1	Biolegen d	138413	1:200	Mouse, Human	Flow cytometry - Quality tested
anti-KLRG1-PE	2F1/KLR G1	Biolegen d	138408	1:200	Mouse, Human	Flow cytometry - Quality tested
anti-CD62L- Brilliant Violet 785	MEL-14	Biolegen d	104440	1:200	Mouse	Flow cytometry - Quality tested
anti-CX3CR1- APC	SA011F1 1	Biolegen d	149008	1:200	Mouse	Flow cytometry - Quality tested
anti-CD43- APC/Cy7	1B11	Biolegen d	121220	1:200	Mouse	Flow cytometry - Quality tested
anti-IL2-Alexa Fluor 647	JES6- 5H4	Biolegen d	503814	1:200	Mouse	Intracellular Staining for Flow Cytometry - Quality tested
anti-IFN γ - Brilliant Violet 785	XMG1.2	Biolegen d	505837	1:200	Mouse	Intracellular Staining for Flow Cytometry - Quality tested
anti-TNF α - Brilliant Violet 650	MP6- XT22	Biolegen d	506333	1:200	Mouse	Intracellular Staining for Flow Cytometry - Quality tested
anti-CD107a- Alexa Fluor 647	1D4B	Biolegen d	121610	1:200	Mouse	Flow cytometry - Quality tested
anti-CD107b- Alexa Fluor 647	M3/84	Biolegen d	108512	1:200	Mouse	Flow cytometry - Quality tested; Immunocytochem istry - Verified
anti-Ki67- AF647	B56	BD Bioscienc es	561126	1:50	Human (QC Testing), Mouse (Tested in Developme nt), Rat, Rhesus (Reported)	Intracellular staining (flow cytometry) (Routinely Tested)
anti-CD19-	6D5	Biolegen	115504	1:200	Mouse	Flow cytometry -

biotin		d				Quality tested
anti-CD20- biotin	SA275A1 1	Biolegen d	150414	1:200	Mouse	Flow cytometry - Quality tested
anti-CD4- biotin	GK1.5	Biolegen d	100404	1:200	Mouse	Flow cytometry - Quality tested

Table S4.7: Antibodies used in this study.

Reagent	company	catalogue number
Golgiplug	BD biosciences	555029
Golgistop	BD Biosciences	554724
Mouse CD8 lymphocyte Enrichment set	BD biosciences	558471
Blasticidin	InvivoGen	ant-bl-1
IMDM	Gibco	12440061
FCS	Sigma	F7524-500ML
penicilin / streptomycin	Gibco	15140122
Glutamax	Gibco	35050061
Fugene	Promega	E2311
RPMI	Gibco	21875091
MEM non-essential AA	Gibco	11140035
Sodium pyruvate	Gibco	11360070
IL7	Peprotech	217-17
Concanavalin A	Merck	C5275-5MG
Retronectin	Takara	T100B
DNAaseI	Roche	4536282001
Percoll	Sigma	P4937-500ML
Celltrace Violet	Thermofisher	C34557
PBS	Invitrogen	003002
Cytofix/Cytoperm	BD biosciences	554714
Foxp3/Transcription factor kit	eBiosciences	00-5523-00
Bovine Serum Albumin (BSA)	Fisher Scientific	11413164
Totalseq-A0301	Biolegend	155801
Totalseq-A0302	Biolegend	155803
Totalseq-A0303	Biolegend	155805
Totalseq-A0304	Biolegend	155807
Totalseq-A0305	Biolegend	155809
Totalseq-A0306	Biolegend	155811

Table S4.8: Commercially available reagents used in the study.

Effect of cellular aging on memory T-cell homeostasis

Arpit C. Swain^{1,2}, José A.M. Borghans², Rob J. de Boer¹

¹Theoretical Biology, Utrecht University, Utrecht, The Netherlands

²Center for Translational Immunology, University Medical Center Utrecht, Utrecht, The Netherlands

Published as: Swain et al., Front. Immunol., 2022; doi:10.3389/fimmu.2022.947242

Abstract

The fact that T-cell numbers remain relatively stable throughout life, and that T-cell proliferation rates increase during lymphopenia, has led to the consensus that T-cell numbers are regulated in a density-dependent manner. Competition for resources among memory T cells has been proposed to underlie this ‘homeostatic’ regulation. We first review how two classic models of resource competition affect the T-cell receptor (TCR) diversity of the memory T-cell pool. First, ‘global’ competition for cytokines leads to a skewed repertoire that tends to be dominated by the very first immune response. Second, additional ‘cognate’ competition for specific antigens results in a very diverse and stable memory T-cell pool, allowing every antigen to be remembered, which we therefore define as the ‘gold-standard’. Because there is limited evidence that memory T cells of the same specificity compete more strongly with each other than with memory T cells of different specificities, i.e., for ‘cognate’ competition, we investigate whether cellular aging could account for a similar level of TCR diversity.

We define cellular aging as a declining cellular fitness due to reduced proliferation (or increased death). We find that the gradual erosion of previous T-cell memories due to cellular aging allows for better establishment of novel memories and for a much higher level of TCR diversity compared to global competition. A small continual source (either from stem-cell-like memory T cells or from naive T cells due to repeated antigen exposure) improves the diversity of the memory T-cell pool, but remarkably, only in the cellular aging model. We further show that the presence of a source keeps the inflation of chronic memory responses in check by maintaining the immune memories to non-chronic antigens. We conclude that cellular aging along with a small source provides a novel and immunologically realistic mechanism to achieve and maintain the ‘gold-standard’ level of TCR diversity in the memory T-cell pool.

Introduction

It is well-accepted among immunologists that homeostatic mechanisms are crucial in regulating immune cell numbers. T-cell homeostasis is the phenomenon by which the T-cell population maintains its relatively stable numbers, despite considerable perturbations, such as a decline in thymic output with age and repeated exposure to antigenic challenges (Surh and Sprent, 2008). The maintenance of CD8⁺ memory T cells generated during acute immune responses is largely cytokine-dependent, although some studies suggest that it also requires interaction with major histocompatibility complex (MHC) molecules, albeit without cognate antigen (Choo et al., 2010; Freitas and Rocha, 2000; Hashimoto et al., 2019; Ku et al., 2000; Surh and Sprent, 2008; Tan et al., 2002; Tanchot et al., 1997). In a lymphopenic host, increased homeostatic (density-dependent) T-cell proliferation drives the expansion of memory T cells (Murali-Krishna et al., 1999; Tanchot et al., 1997). Homeostasis need not be perfect, as in both mice and humans, depleted T-cell pools do not always recover to normal levels (Bouvy et al., 2013; Voehringer et al., 2008). Notably, after autologous stem-cell transplantation, even patients with reconstituted T-cell pools experienced significantly increased T-cell proliferation and loss rates when compared to healthy age-matched controls (Baliu-Piqué et al., 2021). These studies highlight our incomplete understanding of the homeostatic process. A better understanding of T-cell homeostasis is central to understanding the long-term maintenance of immunological memory.

All CD8⁺ memory T cells compete for the same cytokines. Interestingly, the maintenance of chronic immune responses to persisting pathogens is not only dependent on their interaction with cognate antigen (Virgin et al., 2009), but also on the same cytokine(s) that the memories from acute responses depend on (Baumann et al., 2018; Block and Jameson, 2021; Cupovic et al., 2021; Hashimoto et al., 2019; Sandalova et al., 2010; Virgin et al., 2009). Due to the dependence of all memory T cells on the same resource(s), every new immune response disrupts the homeostatic balance. Responses with superior proliferative capacity (e.g., due to a higher affinity for a resource) outcompete other responses dependent on the same resource (De Boer and Perelson, 1994; Hogan et al., 2013; Ku et al., 2001; Yates et al., 2008). This competition among memory T cells from different immune responses leads to moderate to severe attrition of existing memory T cells, and has been noted multiple times using both repeated vaccinations with heterologous viruses, as well as in prime-boost immunization strategies in mouse experiments (Huster et al., 2009; Schmidt and Harty, 2011; Selin et al., 1999; Vezys et al., 2008; Welsh and Selin, 2009). Early studies have postulated this attrition to be an effect of limited ‘space’ by showing that the total memory T-cell pool remained constant in size after consecutive infections (Selin et al., 1999; Welsh and Selin, 2009). Interestingly, a few recent studies report an increase in the total memory T-cell pool upon successive infections (Huster et al., 2009; Vezys et al., 2008), suggesting weaker attrition of existing memories, leading to a more diverse memory T-cell repertoire.

The mechanisms governing the maintenance of T-cell memory remain unclear. Mathematical modelling studies have assumed that memory T cells undergo global and cognate competition, concepts that correspond to well-studied ideas of inter-species and intra-species

competition for resources in ecology. In mouse models, competition for cytokines, antigens, and ‘space’ in antigenic or survival niches, have been held responsible for the attrition of existing memory T cells (Borghans et al., 1999; Cupovic et al., 2021; Freitas and Rocha, 2000; Kedl et al., 2000; Selin et al., 1999; Siracusa et al., 2017; Welsh and Selin, 2009; Yates et al., 2005). Competition for cytokines or physical niches leads to a non-cognate, i.e., ‘global’, form of competition between memory T cells (Freitas and Rocha, 2000; Siracusa et al., 2017). Conversely, antigen-dependent competition, is confined to all cells that recognize the same cognate antigen (we refer to this as ‘cognate’ competition) (Borghans et al., 1999; Callard et al., 2003; De Boer and Perelson, 1994, 2013b; Kedl et al., 2000). Low-level reactivation by cognate antigens has been suggested to have a positive effect on memory T-cell maintenance and homeostasis (Fraser et al., 2013; Masopust et al., 2006; Welsh and Selin, 2009; Yates et al., 2005). Several mathematical modelling studies have discussed the implications of global and cognate competition (Borghans et al., 1999; Callard et al., 2003; De Boer and Perelson, 1994, 2013b; Gaimann et al., 2020; Mayer et al., 2019; Yates et al., 2005). It was shown that global competition leads to competitive exclusion of all but the T-cell clone with the highest affinity for the resources the cells are competing for (De Boer and Perelson, 1994; Gaimann et al., 2020). Global competition can be further regulated by cognate competition, even in the presence of persistent antigenic stimulation, due to competition among memory T cells sharing the same specificity (Borghans et al., 1999; De Boer and Perelson, 1994, 2013b; Mayer et al., 2019). Other modelling studies showed that fratricide among memory T cells crowding around the same antigen-presenting cells (APCs) can give rise to cognate competition among them, due to Fas-FasL mediated apoptosis, which provides a mechanism through which memory T-cell pools can be regulated (Callard et al., 2003; Yates et al., 2005). Therefore, succinctly put, most current literature exploring the mechanisms underlying memory T-cell homeostasis fits in either the global or the cognate competition framework.

In this article, we propose cellular aging as an alternative mechanism that may play a role in T-cell homeostasis. That cells age is irrefutable (DiLoreto and Murphy, 2015; Mays Hoopes, 2010; Mittelbrunn and Kroemer, 2021). For instance, cellular aging has implications in cancer (“Handb. Immunosenescence,” 2020; Mays Hoopes, 2010; Mittelbrunn and Kroemer, 2021; Thoma et al., 2021), and vaccination of the elderly is affected by the poor responsiveness of their aged T cells (Ferrando-Martínez et al., 2011; Goronzy and Weyand, 2019; “Handb. Immunosenescence,” 2020; Haynes and Swain, 2012; Lanfermeijer et al., 2020; P. Chou and B. Effros, 2013; Szabo et al., 2000). Yet, due consideration has not been given to the aging of cells in models of memory T-cell homeostasis. Traditionally, models of T-cell homeostasis assume that cells can perform an infinite number of cell divisions, and are bounded only by the resources available at the time (Yates et al., 2005). However, a cell’s inherent division and loss rates change over time due to age, differentiation stage and division history (Akondy et al., 2017; Baliu-Piqué et al., 2022; Bresser et al., 2022; Rane et al., 2018; Reynaldi et al., 2019; Vibert and Thomas-Vaslin, 2017). We, therefore, investigate the role that cellular aging may play in homeostasis and the long-term maintenance of T-cell memory.

We start with a review of the existing global and cognate competition models of T-cell homeostasis, and later move on to explore the additional effect of cellular aging on the maintenance of memory T cells. Throughout the article, we use previously described attributes of the memory T-cell pool (e.g., attrition of existing memories and expanding population size) as guides to ascertain the suitability of these three different models in generating realistic memory T-cell pools. We demonstrate that, contrary to our intuition, cellular aging helps maintain memory T-cell diversity for extended periods of time. Further, we observe that a small source, from either stem-cell-like memory T cells or from naive T cells, together with cellular aging is sufficient to maintain a diverse memory T-cell repertoire that is robust to the presence of dominant competitors (e.g., chronic immune responses to persistent pathogens). We also discuss the potential disadvantages of longevity of memory T cells, and the effect of cellular aging on the phenotypic composition of the memory T-cell pool.

Models of memory T-cell maintenance

Three different mathematical models for the maintenance of memory T cells were defined. To keep the models simple, we considered three elements: (a) a source into the memory T-cell population (if any), (b) the most fundamental processes of any population of cells, i.e., cell division and cell death, and (c) the resources that have been demonstrated to be essential for the maintenance of memory T cells, i.e., cytokines such as IL-15, and antigens (for chronic responses). We consider both acute and chronic immune responses, where all memory T cells depend on the same homeostatic cytokine(s).

Global competition model

The cytokines, C (concentration, in mol/L), have a steady source, σ (in mol/L/day), from the stromal cells located across the body of a host (Cui et al., 2014; Krishnamurty and Turley, 2020). Although there are other, transient sources of cytokines during inflammation, stromal cells are the major contributors during homeostatic circumstances (Block and Jameson, 2021; Cui et al., 2014; Nitta and Takayanagi, 2021). These cytokines are either utilized by memory T cells in a fixed amount, ϵ , during each cell division, or are degraded at a rate δ /day (**equation 5.1a**). The dependence of all memory T cells on the same growth resource (cytokines), C , gives rise to global competition among the cells. The sizes of the memory T-cell populations, M_i , in a host having experienced n different antigen-specific immune responses are given by (**equation 5.1b, Figure 5.1a**):

$$\frac{dC}{dt} = \sigma - \delta C - \epsilon \frac{C}{h + C} \sum_i p_i M_i \quad (5.1a)$$

$$\frac{dM_i}{dt} = s_i + p_i M_i \frac{C}{h + C} - d_i M_i \quad (5.1b)$$

where $i = 1, \dots, n$ (here n is the number of unique antigens encountered sequentially), and h is the cytokine concentration at which the homeostatic (i.e., density-dependent) proliferation rate is half-maximal. Cells of immune response M_i have a death rate d_i , and a maximal homeostatic proliferation rate p_i (also referred to as the fitness). The source term, s_i , defines the daily influx of memory T cells, which could be either from infrequent divisions of stem-cell-like memory T cells in the bone marrow, or from antigen-driven expansion of naive T cells (only for chronic responses) (Snyder et al., 2008; Utzschneider et al., 2018). T cells downregulate their T-cell receptors after interactions with cytokines and are thus ‘non-greedy’ consumers of cytokines (Gao et al., 2015). Therefore, cytokine consumption was modelled to be proportional to proliferation of the memory T-cell population (**equation 5.1**). The effective homeostatic division rate of memory T cells was set by a saturation function of the global cytokine concentration. An inverse dependence of the death rate on the cytokine concentration would give similar qualitative results (simulations not shown).

We assume that the timescales for production and degradation of cytokines are much faster than the timescales for division and death of memory T cells. Therefore, we consider the cytokines to be in quasi-steady state (**equation 5.2**):

$$C = \frac{-(h + \gamma \sum_i p_i M_i - 1) + \sqrt{(h + \gamma \sum_i p_i M_i - 1)^2 + 4h}}{2} \quad (5.2)$$

The cytokine concentration was normalized to its maximal concentration (i.e., we set $\frac{\sigma}{\delta} = 1$), and $\gamma = \frac{\epsilon}{\delta}$ was set to 10^{-6} so that the size of the memory T-cell pool was in the order of 10^7 .

Cognate competition model

Global competition due to sharing of growth resources leads to competition between different immune responses. Cognate competition defines the competition among the memory T cells generated during the same immune response, i.e., cells sharing the same antigen specificity (but not necessarily the same T-cell receptor). For ‘acute’ immune responses to pathogens that are eliminated, cognate competition has been proposed to follow from limited ‘space’ in specific survival niches in the bone marrow (Sercan Alp et al., 2015), or from limited availability of cross-reactive antigens (Borghans et al., 1999; Callard et al., 2003; Kedl et al., 2000). Allowing for both global and cognate competition (**Figure 5.1b**), the memory T-cell pools resulting from n different immune responses can be given by:

$$\frac{dC}{dt} = \sigma - \delta C - \epsilon \frac{C}{h + C} \sum_i \frac{p_i M_i}{1 + \beta_i M_i} \quad (5.3a)$$

$$\frac{dM_i}{dt} = s_i + \frac{p_i M_i}{1 + \beta_i M_i} \frac{C}{h + C} - d_i M_i \quad (5.3b)$$

for $i = 1, 2, \dots, 100$ antigens, and where all memory T cells specific for antigen i are considered to have a similar affinity for that antigen.

This extends the global competition model (**equation 5.1**) with a cognate competition parameter, β_i , defining the size of the M_i population at which its division rate halves (which happens when $M_i = 1/\beta_i$). All other parameters remain the same, i.e., we have in fact added an intra-specific competition term to the global competition model. As h was estimated before (Mugwagwa, 2010), the parameter β_i was used to tune the relative strength of the global and cognate competition. Note that global competition weakens as $h \rightarrow 0$ and that cognate competition declines as $\beta_i \rightarrow 0$. Again, due to the very different turnover timescales of cytokines and memory T cells, the cytokines were assumed to be in quasi-steady state:

$$C = \frac{-\left(h + \gamma \sum_i \frac{p_i M_i}{1 + \beta_i M_i} - 1\right) + \sqrt{\left(h + \gamma \sum_i \frac{p_i M_i}{1 + \beta_i M_i} - 1\right)^2 + 4h}}{2} \quad (5.4)$$

Cellular aging model

The properties of a cell may change with cell division. It is well-known that telomere shortening during division stunts a cell's ability to divide forever (De Boer RJ, 1998; Goronzy et al., 2006; Hayflick and Moorhead, 1961). However, in the global and cognate competition models, the cells have a constant fitness (p_i) and, by not aging, can expand indefinitely. To account for cellular ageing, we rewrote the global competition model (**equation 5.1**) into a division-indexed model, where we used $j = 1, \dots, m$, for the number of divisions a cell has completed (i.e., j is the 'generation' number of a cell, and m is the maximal number of divisions it can go through, which is commonly referred to as the 'Hayflick limit'). In our simulations, $m = 100$ was chosen to be large enough so that in practice a cell never reaches its Hayflick limit. The model for the number of cells specific to antigen i in the j^{th} division, $M_{i,j}$ (see **Figure 5.1c**), is given by:

$$\frac{dM_{i,j}}{dt} = s_{i,j} + 2p_{i,j-1}M_{i,j-1} \frac{C}{h+C} - d_i M_{i,j} - p_{i,j} M_{i,j} \frac{C}{h+C} \quad (5.5a)$$

$$p_{i,j} = \frac{p_{i,1}}{1 + (j/k)^5} \quad (5.5b)$$

where $p_{i,j}$ is the maximal homeostatic division rate of cells specific for antigen i that have completed j divisions; $k = 25$ marks the generation number where $p_{i,j} = p_{i,1}/2$; and $M_i = \sum_j M_{i,j}$ defines the total number of cells in the i^{th} immune response. For the special case where the division rates remain independent of the division number, i.e., when $p_{i,j} = p_i$ (i.e., $k \rightarrow \infty$), this model is identical to the global competition model (it would only track the

division histories of cells). Otherwise, division rates decline with the division number (**equation 5.5b, Figure 5.1d**).

Since in the scenarios with a source, each memory T-cell population was assumed to be seeded every day with s_i cells, we described their division history with a Poisson distribution, i.e.,

$$s_{i,j} = s_i \frac{\mu^j e^{-\mu}}{j!} \quad (5.6)$$

Here, μ is the average generation number of a population. It is defined as $\mu = 2\lambda\tau$, where τ is the typical length of the expansion phase (in days), and $\lambda = 2/\text{day}$ is the rate of division during the expansion phase (De Boer and Perelson, 2013a). Two variations of the age-distribution of the source were modelled: ‘young’ cells ($\mu = 1$, or $\tau = 0.25$ days, i.e., cells that became quiescent after having completed one division, on average, during the expansion phase) or ‘old’ cells ($\mu = 20$, or $\tau = 5$ days, i.e., cells that divided extensively throughout the expansion phase). For simplicity, the T-cell death rate was kept the same across division numbers. Qualitatively similar results were found when implementing an increase in the death rate with increasing division number (simulations not shown). However, as less differentiated cells possess a higher expansion potential (Geginat et al., 2003; Hinrichs et al., 2009), we chose to decrease the division rate with the division number.

Chronic responses

To model chronic responses, we introduced extra terms specific to only chronic responses. As chronic responses are subject to additional proliferative signals due to their interaction with antigen (Yates et al., 2008), chronic immune responses have an additional maximal antigen-driven proliferation rate, ρ_i , and a cognate (antigen-driven)-competition parameter, g_i . The models allowing for chronic responses are, therefore, extensions of the models defined above. In case of chronic immune responses, the global and cognate competition models described by **equations 5.1 and 5.3** are extended with a second proliferation term:

$$+ \frac{\rho_i M_i}{1 + g_i M_i} \quad (5.7a)$$

The cellular aging model requires two terms to achieve a similar extension:

$$+ \frac{2\rho_{i,j-1} M_{i,j-1}}{1 + g_i M_i} - \frac{\rho_{i,j} M_{i,j}}{1 + g_i M_i} \quad (5.7b)$$

with

$$\rho_{i,j} = \frac{\rho_{i,1}}{1 + (j/k)^5} \quad (5.7c)$$

The cognate competition parameter, g_i , defines the strength of the cognate competition among memory T cells specific for antigen i . Notice that the antigen-driven proliferation rate follows the same cellular aging function as the homeostatic (density-dependent) proliferation rate.

Parameter choices

For a fair comparison across the models, we used the same parameter values throughout this manuscript. CD8⁺ memory T cells were found to be maintained at steady state with an intermitotic interval of ~50 days in an adoptive transfer experiment of LMCV-specific CD8⁺ memory T cells into naive mice after being CFSE labelled (Choo et al., 2010). Reports of in vivo deuterium labelling of non-specific CD8⁺ memory T cells supported this time scale by showing that the CD8⁺ memory T-cell pool is renewed, on an average, every ~ 66 days (Baliu-Piqué et al., 2022). Therefore, the death rate of memory T cells, d_i , was set to 0.02/day, irrespective of the immune response. The maximal homeostatic proliferation rate, p_i , of 0.5/day and the coefficient for global competition, h , of 10^{-5} were estimated based on temporal data of murine memory CD8⁺ T cells (Mugwagwa, 2010). As all cells in the models have the same expected life span of 50 days, and differ only in their maximum homeostatic proliferation rate, p_i , we also refer to this proliferation rate as the ‘fitness’ of the immune response. Disparate immune responses differ in their fitness values. In the simulations, the fitness values were drawn from a normal distribution with a mean of 0.5 and a standard deviation of 0.05. The effective proliferation rate decreases as the memory T-cell pool increases and will approach $d_i = 0.02$ when the memory of a particular response is at steady state. The coefficient for cognate competition, β_i (in the cognate competition model) and g_i (for chronic responses), were set to be 10^{-6} and 5×10^{-5} for all i , respectively, so that the total mouse memory CD8⁺ T-cell pool was realistically in the order of 10^7 cells.

Simpson’s Diversity Index

Simpson’s diversity index has many variations. Here, we used a variation that provides an intuitive interpretation of the diversity in the memory T-cell pool. The index, based upon the relative abundances, $f_i = M_i / \sum_i M_i$, of all immune responses, gives an indication of the effective number of immune responses in a population. The index is defined as

$$\frac{1}{\sum_{i=1}^n f_i^2} \quad (5.8)$$

A memory T-cell pool with an index of n denotes a pool with n evenly abundant immune responses whereas an index of 1 denotes a scenario with a single, dominant immune response in the pool of immune responses.

Results

Three models of homeostasis were formulated based on the different competition schemes: global competition (**Figure 5.1a**), cognate competition (**Figure 5.1b**) and cellular aging (**Figure 5.1c**, see the **Models** section). The global and cognate competition models are conventional models differing only in the absence or presence of intra-specific competition among memory T cells, respectively. The cellular aging model is a novel variant of the global competition model, which we propose as an alternative because there is limited evidence for cognate (intra-specific) competition among memory T cells. As this manuscript focuses on the long-term maintenance of the memory T-cell pool, we abstained from modelling the short expansion phase after an antigenic challenge. Instead, in all the simulations, we assumed that after the introduction of each antigen, the memory T-cell pool is expanded with a random number of cognate memory T cells (drawn from a normal distribution centred around 10^5 with a 10% standard deviation), to model the beginning of a new memory phase. The simulations below reflect $CD8^+$ T cells in a representative mouse (i.e., parameter values used are specific to mice).

To realize the effect of the three different mechanisms on the immune dynamics over a simulated mouse's lifetime, we recorded and compared model simulations over 1000 days (**Figure 5.2**). To this end, the host was successively exposed to 100 different antigens that gave rise to 100 acute immune responses with different fitness levels (see **Models** for details). The 100 antigens were introduced over 1000 days in 10-day time intervals from day 0 until day 990. The number of an immune response marks the time point at which (and antigen by which) it was triggered. For example, immune response M_i was triggered by antigen i on day $10 \times (i - 1)$.

Under global competition, the memory T-cell pool is dominated by a single immune response

The cytokine IL-15 is thought to be necessary for the expansion and maintenance of all memory T cells, thereby leading to global competition between the cells (De Boer and Perelson, 1994), irrespective of their antigen specificity (**Figure 5.1a**; see **Models**). In such a setting, the immune memory to the first encountered antigen, M_1 , in a new-born mouse, expanded to fill up the memory T-cell pool almost entirely, simply by the virtue of being the only immune response depending on the abundantly available growth factor (**Figure 5.2a**). The size of M_1 increased, unabated, until the death in the population balanced the reduced growth of the population due to the depleted cytokine availability (i.e., $p_1 \frac{c}{h+c} = d_1 = 0.02$).

M_1 started to decline only when the mouse was exposed to enough antigens of comparable, or higher, fitness (M_2, M_6, M_{71}). Nevertheless, M_1 dominated the memory T-cell pool almost throughout the entire lifetime of the mouse, because the rate of exclusion was very slow. At steady state, the actual division rate of the memory T cells with the highest fitness was close to their death rate $d_i = 0.02$. The division rate of memory cells with 10% lower fitness (corresponding to the standard deviation of our distribution) would then be 10% lower, leading to a net loss rate of just 0.002 per day. With a half-life of about a year, it would therefore take longer than the lifespan of a mouse to lose a large population of specific memory T cells, even for T cells with a relatively low fitness.

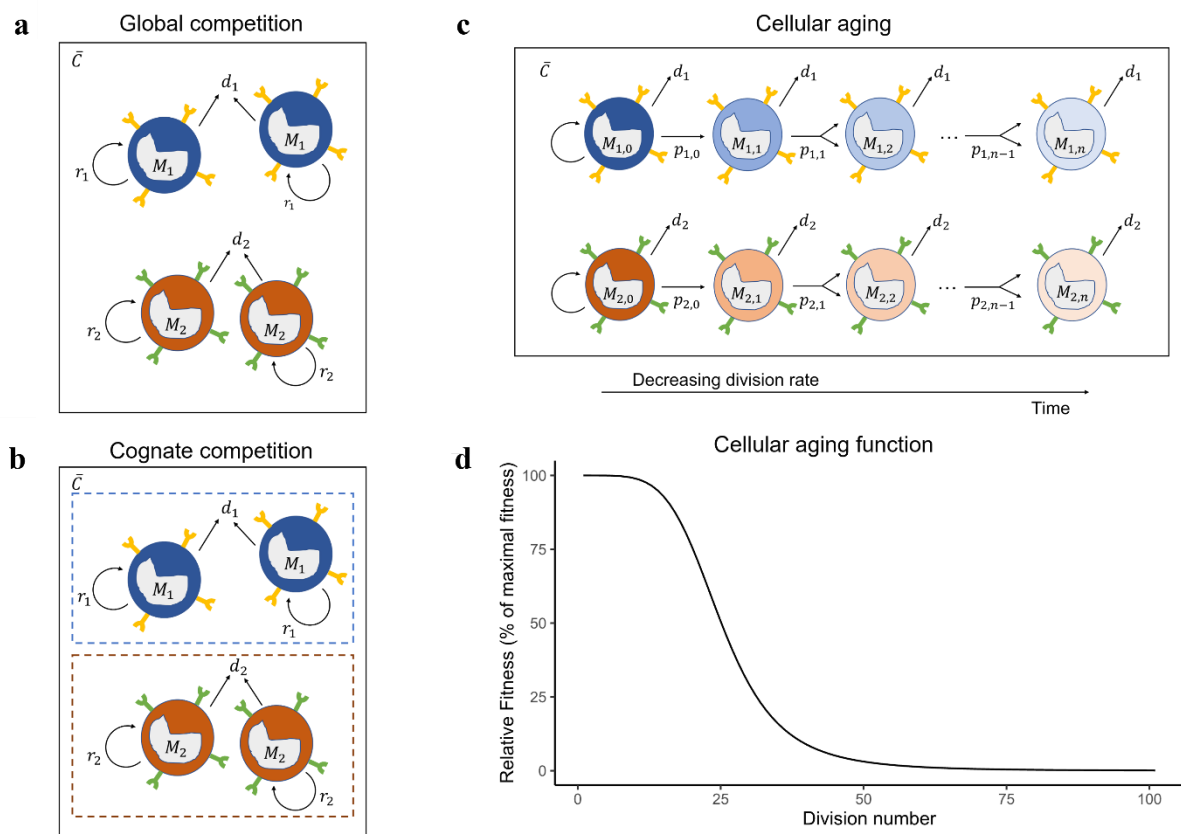


Figure 5.1: Mechanisms of homeostatic maintenance of memory T cells. The cartoons of the (a) global competition, (b) cognate competition, and (c) cellular aging models showing the memory T-cell pool with two immune responses, M_1 and M_2 . The different immune responses can have different division rates, p_i , and death rates, d_i , and share the same cytokines, C . On top of the competition for shared global resources (cytokines) (a), the cells of an immune response either compete with cells of the same specificity, leading to cognate competition (b) or lose their potential to divide with each cell division because of cellular aging (c). The cellular aging function shows the drop in the relative fitness of a T-cell population as it divides (d).

The establishment of new memories became challenging when the memory T-cell pool was nearly saturated. Immune responses with low fitness (e.g., M_{41}) declined immediately upon introduction, due to the competitive pressure exerted by existing, fitter, immune responses

(**Figure 5.2a**). Interestingly, even though existing immune responses went through attrition upon exposure to new antigens, the total memory T-cell pool showed modest growth over time (**Figures 5.2a and S5.1a**). This early signature of an increasing memory T-cell pool is in line with observations from previous studies on specific antigen-free laboratory mice (Huster et al., 2009; Vezys et al., 2008). In the very long run, global competition for cytokines dictated the survival of only the fittest immune response (**Figure S5.1b**). Although such a scenario is disconcerting, competitive exclusion of less fit immune responses need not be achieved in a mouse's lifetime (**Figure 5.2a**), as long as cells are relatively long-lived (>50 days), and fitness differences are small.

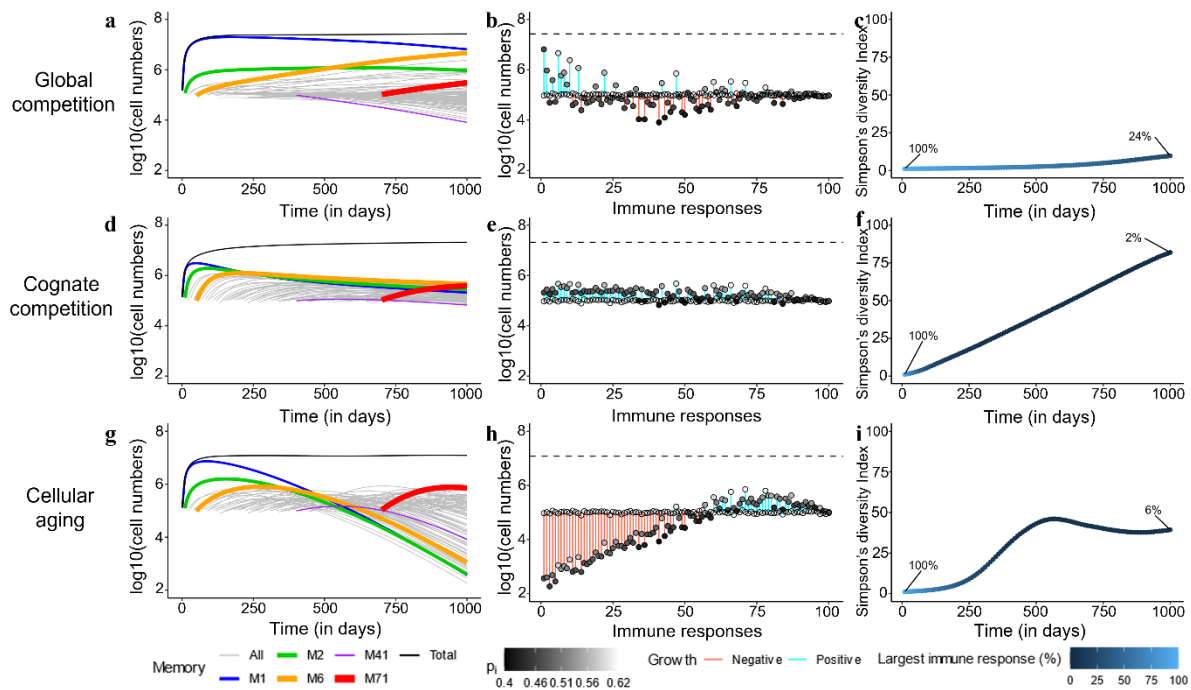


Figure 5.2: Cellular aging improves the diversity of the memory T-cell pool. Comparison of the three mechanisms for homeostatic maintenance of memory T cells showing the temporal dynamics (Panels **a**, **d**, and **g**); the distribution of the sizes of all memory T-cell responses at day 1000, along with their expansion (blue) or contraction (red, indicated by the vertical bars) with respect to their initial value (indicated by the open circles) i.e., $M_i(1000) - M_i(10 \times (i - 1))$, as well as their maximal homeostatic proliferation rate (indicated by the shading of the filled circles) (**b**, **e**, and **h**); and the Simpson's diversity index of the T-cell repertoire over time (**c**, **f**, and **i**). The models were simulated for 1000 days. In panels **a**, **d** and **g**, the thickness of the coloured lines denotes the fitness of the immune response. The dashed lines in panels **b**, **e** and **h** depict the size of the total memory T-cell pool on day 1000. In these simulations, the memory T-cell pool consists of acute immune responses only.

The snapshot of the total memory T-cell pool on day 1000 revealed a clear positive dependence of the size of an immune response on its maximal homeostatic proliferation rate, p_i (**Figure 5.2b**). However, M_1 occupied the largest share (24%) of the memory T-cell pool even with a relatively low p_i , as it was the first immune response. Similarly, the fittest

immune response, M_{71} , formed only a meagre 1% of the total memory T-cell pool, as it was triggered very late in the mouse's life (on day 700). Therefore, under global competition, the size of an immune response is determined not only by its maximal homeostatic proliferation rate but also by the time at which it was generated. The Simpson's diversity index (see **Models**) offers a measure of the diversity of a population by considering both the number and the disparity in the sizes of its constituents. The diversity in the memory T-cell pool barely increased over the course of the mouse's lifetime, evolving from a repertoire with a single immune response on day 0 to one with about 10 dominant responses, and 90 small responses, on day 1000, where the largest immune response made up as much as 24% of the total memory T-cell pool (**Figure 5.2c**). Therefore, global competition gives rise to a skewed memory T-cell pool in which the immunity of a host weakens over time due to the loss of less fit immune responses.

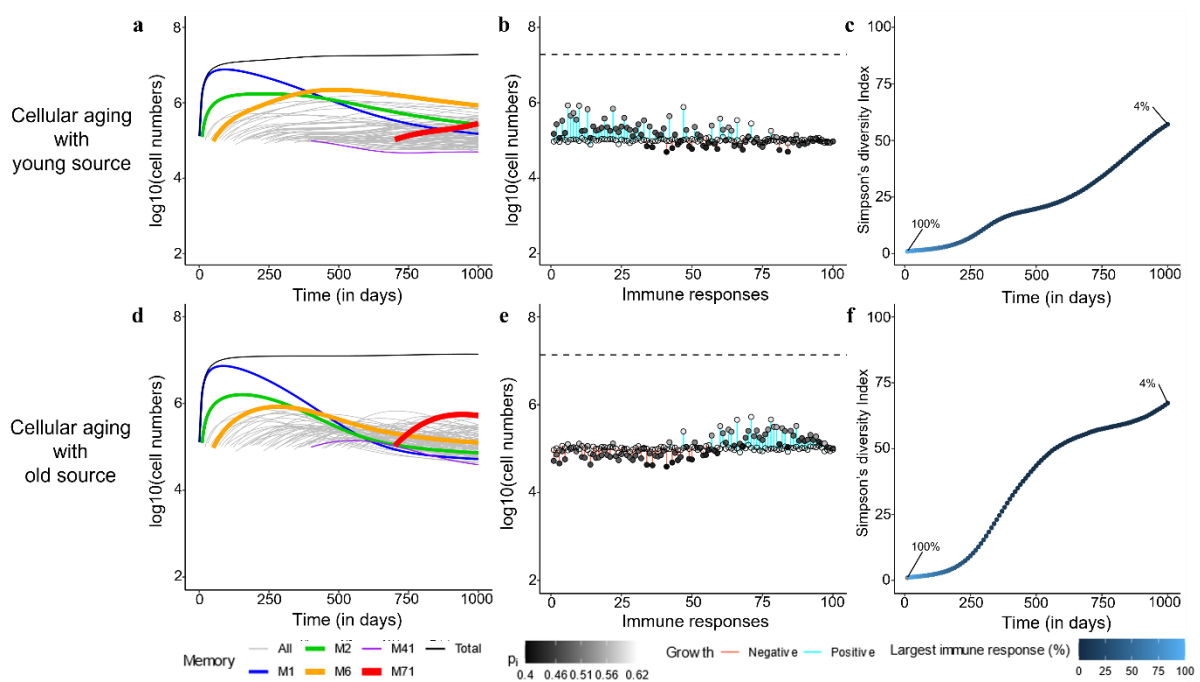


Figure 5.3: A small source helps to achieve the gold-standard diversity within the memory T-cell pool. The dynamics of the cellular aging model along with a source from either a young (upper row) or an old population (lower row). Legends as in **Figure 5.2**. The memory T-cell pool was generated by acute immune responses only.

Cognate competition leads to an evenly distributed memory T-cell pool

Co-existence of multiple species is a well-known phenomenon in ecology. In a stable environment, co-existence can be achieved through intra-specific competition. Based on this idea, previous studies in immunology have suggested the presence of specific competition among the cells participating in the same immune response, because they bind similar (cross-reactive) antigens (Borghans et al., 1999; Freitas and Rocha, 2000; Yates et al., 2005). In this section, we study a similar cognate competition model (despite a lack of experimental

support), which employs competition among cells of an immune response on top of the global competition among all cells in the memory T-cell pool (**Figure 5.1b**; see **Models**).

The additional dependence on cognate resources introduced a strict limit on the size of an immune response. Despite considerable expansion, cognate competition prevented M_1 from taking over the memory T-cell pool, by limiting its size (**Figures 5.2d and S5.1d**). In contrast to what happened in the global competition model, the cytokine was now not depleted (not shown), as inflation of M_1 was avoided. So, upon exposure to new antigens, all new immune responses expanded initially, irrespective of their maximal homeostatic proliferation rate. These expansions came at the expense of the existing immune responses but contributed to the growth of the total memory T-cell pool (**Figure S5.1d**). On day 1000, the memory T-cell pool was composed of many similarly-sized immune responses (**Figure 5.2e**), all of which (except M_{41}) eventually reached non-zero steady state sizes that were proportional to their fitness levels (**Figure S5.1e**). The immune response with the lowest fitness, M_{41} , declined after a short bout of expansion, as its reduced homeostatic proliferation rate (due to global resource sharing) was lower than its death rate (**Figure S5.1e**). The size distribution of the immune responses showed a much stronger dependence on the values of their maximal homeostatic proliferation rate (**Figure 5.2e**), and therefore the size of each immune response depended much less on the time at which the response was generated. In contrast to what was observed in the global competition model, the Simpson's diversity index of the total memory T-cell pool showed an impressive increase over time to a diverse immune repertoire, in which the largest immune response consisted of only 2% of the total memory T-cell pool (**Figure 5.2f**).

Notably, cognate competition among cells of an immune response gives rise to a highly diverse memory T-cell repertoire. Such a repertoire is beneficial, as it offers better protection to the host over its lifetime than the very skewed repertoire that was obtained with the global competition model. Therefore, we refer to the cognate competition model as the 'gold-standard' in the long-term homeostatic maintenance of almost all memories.

Immune memories are sustained for longer periods due to cellular aging

The cognate competition model gave rise to a diverse memory T-cell pool by limiting the size of the individual immune responses. Although competition in antigenic niches has been hypothesized (Agenés et al., 2008; Borghans et al., 1999; Freitas and Rocha, 2000; Yates et al., 2005), experimental evidence for cognate competition in the memory T-cell pool is scarce. Instead, some experimental observations have shown that interactions with cognate resources (antigens) are not required for the survival of memory T cells (Freitas and Rocha, 2000; Murali-Krishna et al., 1999). Therefore, seeking for alternative mechanisms, we hypothesized that cellular aging of T cells may limit the growth of individual memory responses, and thereby generate a diverse memory T-cell repertoire. Here, we discuss the ramifications of cellular aging, in conjunction with global competition as the homeostatic mechanism, on the maintenance of the memory T-cell pool (**Figure 5.1c**; see **Models**).

The unabated expansion of the first immune response, M_1 , was indeed prevented by cellular aging (**Figure 5.2g**). Continued antigen exposures resulted in the growth of the total memory T-cell pool, while existing immune responses underwent 1) moderate erosion due to new antigen exposures (**Figure S5.1g**), and 2) major attrition due to cellular aging (**Figure 5.2g**). The limited consumption of cytokine by the existing immune responses allowed new immune responses to expand. However, on the long term all immune responses eventually declined (**Figure 5.2g**), as they were lost due to cellular aging (**Figure S5.1h**). Interestingly, the maximal homeostatic proliferation rate hardly influenced the size distribution of the immune responses (**Figure 5.2h**). Rather, the sizes were largely determined by the time at which the responses were generated. The most recent responses made up the majority of the memory T-cell pool, as the older a response was, the more it was eroded. The diversity within the memory T-cell pool was much larger than in the global competition model but was only half of that achieved in the cognate competition model (**Figure 5.2i**). The largest immune response on day 1000 occupied a mere 6% of the memory T-cell pool, compared to the inflated 24% in the global competition model. Therefore, although the cellular aging model improves upon the global competition model, it cannot generate a memory T-cell pool as diverse as the ‘gold-standard’ memory T-cell pool that results from cognate competition.

A small source into an aging population helps to maintain a diverse memory T-cell pool

Multiple studies in the recent past have described subsets of memory T cells that have superior potential to generate other memory T-cell subsets (Gattinoni et al., 2011). This self-sustaining population is sometimes referred to as the stem-cell-like memory T-cell population. Stem-cell-like memory T cells, generated during an acute response and residing in stromal niches in the bone marrow, could act as a slow but steady source into the circulating memory T-cell populations. We have seen that cellular aging can limit the expansion of the early memory populations, thereby reducing competition, but that the memory T-cell pool suffers in the long run, due to the eventual loss of all memories by cellular aging. The presence of a lowly-divided stem-cell-like source for each immune response would circumvent this issue. Importantly, this memory-maintaining source could also originate from circulating memory T cells due to repeated infections, from cross-reactions with other antigens, or from activation of new naive T cells (in case of persistent antigens).

Indeed, if each immune response had a small source ($s_i = 100$ cells/day), none of the immune responses would be lost in the long-term (**Figure 5.3**). As the division history of the source might affect the memory T-cell repertoire, we evaluated two different scenarios: one, where the source population turned quiescent early in the expansion phase (‘young’ source, having completed 1 division on average), and the second, where the source population had divided as much as the circulating cells before becoming quiescent (‘old’ source, having completed an average of 20 divisions). A young source sustained the growth of early immune responses for longer periods of time compared to an older source (**Figures 5.3a and 5.3d**).

Remarkably, the size distribution of the memory T-cell pool was completely different in both cases (**Figures 5.3b and 5.3e**). The presence of a young source resulted in a pool dominated (in size) by earlier immune responses, whereas a source from an older population favoured the prevalence of recently generated immune responses. This effect was due to a difference in the ‘effective source’. Although both scenarios have the same source of 100 cells/day, the source from a younger population contributes more daughter cells because of their higher homeostatic proliferation rate. When the source population is old, it expands less and makes for a smaller effective source to the existing memories. Hence, with an old source the later immune responses expand more, due to weaker competition from existing immune responses, compared to the scenario with a young source. Even with such a stark difference in the immune profiles, the diversity within the memory T-cell pool was comparable in both scenarios, as none of the immune responses were lost (**Figures 5.3c and 5.3f**). The Simpson’s diversity index revealed that the diversity achieved by adding a stem-cell-like source to the cellular aging model was comparable to the ‘gold-standard’ diversity achieved with the cognate competition model. Notably, the presence of a source in the global competition model failed to improve its diversity, suggesting that adding a small source is not a trivial solution to maintaining the diversity of a population (figure not shown due to its similarity to **Figure 5.2a-c**). Therefore, we propose that a source into an aging population is a viable alternative to the cognate competition model.

The distribution of the division number in the memory T-cell pool of the global competition model in the absence of cellular aging, i.e., when $p_{i,j} = p_i$, showed a large disparity in the average generation number of the immune responses, with early responses having divided 70 times on average, compared to an average of 25 divisions for recent responses (**Figure 5.4a**). The very first response (like all other responses) had gone through 25 divisions when seeded in the beginning of the memory phase, and subsequently accumulated 50 more divisions throughout the mouse’s life (**Figure 5.4b**). Even though the cells of the first immune response accrued more divisions with time, the size of the first response declined over time due to global competition from successive immune responses (**Figures 5.4b and 5.2a**). The disparity found in the division distribution of the memory T-cell pool dropped considerably in the presence of cellular aging (**Figure 5.4c**). Cellular aging promoted the dominance of recent immune responses, even though they had divided less (**Figures 5.4c and 5.2h**). The number of divisions accrued by an immune response over a mouse’s lifetime was also significantly lower due to cellular aging (**Figure 5.4d**). A continuous source reduced the disparity in the division distribution within the memory T-cell pool even more (**Figures 5.4e and 5.4g**). The average generation number of the first immune response on day 1000 was lower compared to that on day 0 when the source was from a younger population but was higher than that on day 0 in case of an older source (**Figures 5.4f and 5.4h**). Therefore, a small source counteracts the exhaustion of a population by cellular aging and the division history of the source determines the distribution of the division history within the memory T-cell pool.

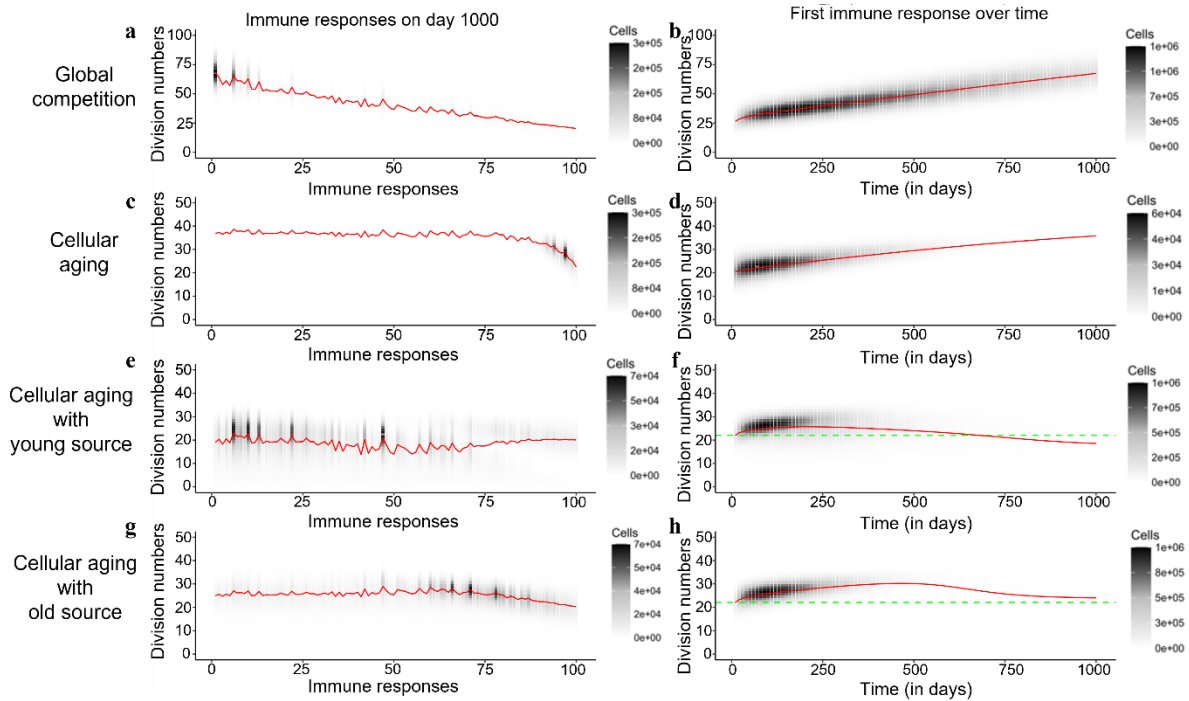


Figure 5.4: The distribution of division numbers in the memory T-cell pool is determined by the age of the source population. Comparison of the distribution of division numbers of all immune responses on day 1000 (Panels a, c, e, and g), and the division history of the first immune response over time (Panels b, d, f, and h), for different mechanisms. The red line plots the average generation number of an immune response. The grey and black shades show the number of cells at different division numbers. The green dotted line marks the starting division number of the first immune response. In these simulations the memory T-cell pool consists of acute immune responses only.

A source into an aging T-cell population maintains immune memories in the long-term even in the presence of chronic responses

Our discussion until now has focused on a memory T-cell pool containing 100 memories to pathogens that were eliminated during the ‘acute’ immune response. However, chronic immune responses to pathogens (or antigens) that persist, may pose a big challenge in maintaining the diversity of the memory T-cell pool, due to their sometimes inflationary properties (Virgin et al., 2009). We assessed whether our novel model, with a memory T-cell pool going through cellular aging in the presence of a source, could maintain T-cell diversity under the competitive pressure from chronic T-cell responses. We considered a host that generated 95 acute responses and 5 chronic responses, even though only 1% of all infections are estimated to lead to chronic responses (Virgin et al., 2009). Chronic responses are maintained in part by homeostatic proliferation due to IL-15, and partly due to repeated stimulation by persistent antigen (see **Models**).

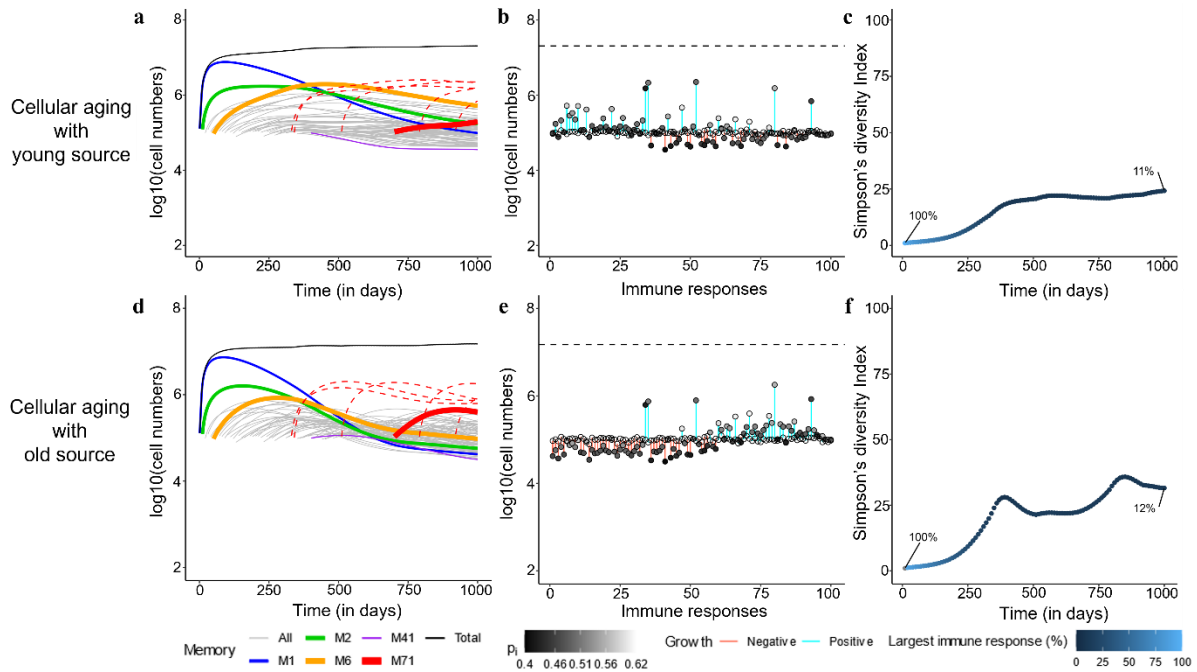


Figure 5.5: Chronic immune responses lower the long-term diversity of the memory T-cell pool. The dynamics of the cellular aging model along with a source from either a young source (upper row) or an old source (lower row). Legends as in **Figure 5.2**. The memory T-cell pool consists of both acute and chronic immune responses.

Chronic responses expanded to occupy a higher proportion of the memory T-cell pool than acute responses (**Figure 5.5**). The immune dynamics of the 95 acute responses were not severely affected by the addition of 5 chronic responses (compare **Figures 5.3a** and **5.3d** with **Figures 5.5a** and **5.5d**). Exposure to chronic antigens expanded the total memory T-cell pool, and the heightened competition reduced the sizes of the acute responses somewhat. The division histories and the prevalence patterns of the immune responses hardly changed (compare **Figures 5.3b** and **5.3e** with **Figures 5.5b** and **5.5e**, and **S5.2**). Like before, the division history showed that the memory T-cell pool became younger with time in the presence of a young source, which resulted in the prevalence of early immune responses. However, the diversity of the memory T-cell pool declined markedly in the presence of chronic responses as the largest immune response now made up only about 10% of the total memory T-cell pool (**Figures 5.5c** and **5.5f**). The cellular aging model along with a source, thus, provides a robust mechanism for the long-term maintenance of memory T cells, even though the diversity in the memory T-cell pool suffers from the presence of chronic responses.

Long-lived memory T cells lower the diversity of the memory T-cell pool

Circulating memory T cells have been shown to be relatively short-lived (Baliu-Piqué et al., 2018), while memory in itself is long-lived (Cendón et al., 2022; “Panum on Measles: Observations Made During the Epidemic of Measles on the Faroe Islands in the Year 1846 (A translation from the Danish) - PMC,” n.d.). In an attempt to understand why memory T cells are relatively short-lived, we studied how the lifespan of memory T cells influences the diversity of memory T-cell repertoires. In our models, the attrition of existing memories was due to the relatively short lifespans of memory T cells. We examined whether memory T cells with longer lifespans would allow for higher diversity in the memory T-cell repertoires. To precisely underline the influence of memory T-cell lifespan (without the effect of a source) on the diversity of the memory T-cell repertoire, we only considered the three basic mechanisms: global competition, cognate competition, and cellular aging, without any source. The model characteristics were compared considering a scenario where memory T cells lived 10 times longer than their estimated lifespans, i.e., $d_i = 0.002/\text{day}$ (**Figure S5.3**). The temporal dynamics corroborated the previous conclusions: M_1 filled up the memory T-cell pool under the influence of global competition, while this was strongly and moderately constrained in the cases of cognate competition and cellular aging, respectively (**Figures S5.3a, S5.3d and S5.3g**). Notably, none of the cases showed the loss of any immune response (**Figures S5.3b, S5.3e and S5.3h**). The degree of inflation of an immune response clearly correlated with how early the response was generated. More importantly, the levels of TCR diversity in the memory T-cell pool were a lot lower when compared to the corresponding cases with short-lived memory T cells (**Figures S5.3c, S5.3f and S5.3i**). When memory T cells were long-lived, the diversity in the global competition and cellular aging models barely improved over time, whereas the index for the cognate competition model was half of that with short-lived memory T cells.

Although maintenance of all encountered immune responses may be advantageous, the inflation of early memories might pose significant challenges for the efficient protection of a host. The recall response to a recent antigen is expected to be delayed when the probability of finding cognate memory T cells decreases due to the presence of inflated early responses in the pool. A considerable delay in the recall response to a large infection may even be detrimental (Huster et al., 2009). Therefore, surprisingly, storing immunological memory in short-lived memory T cells may be more beneficial, as short-lived memory T cells allow for higher diversity in the memory T-cell pool.

Discussion

Here, we showed that cellular aging in the presence of a source population is a mechanism by which long-term maintenance of a diverse memory T-cell pool can be achieved. It preserves acute as well as chronic immune responses in the long-term and generates a diverse memory T-cell repertoire comparable to the gold-standard level of diversity generated with cognate competition. Whereas the occurrence of cognate competition is poorly supported by

experimental evidence, the presence of both cellular aging and a source (from stem-cell-like memory T cells, re-activated memory T cells, cross-reactive memory T cells or newly activated naive T cells) are widely accepted. Therefore, we propose that a source into an aging population is an immunologically viable alternative to the cognate competition model.

The global competition model is prone to competitive exclusion of all but the fittest immune response. Using division and death rates of murine memory CD8⁺ T cells, we showed that although competitive exclusion may not be seen in the lifetime of a mouse, global competition would lead to unrealistically skewed memory repertoires. Moreover, the slow exclusion of memory T-cell responses in our simulations was due to the small differences in the fitness values of the different immune responses. If the fitness values of the immune responses were to differ more than the 10% standard deviation considered in our simulations, the size disparity in the memory T-cell pool would be even higher.

The cellular aging model improves upon the global competition model by limiting the size of each self-renewing memory population, which reduces the competition among them. A source into an aging memory T-cell pool sustains the diversity of the memory T-cell repertoire in the long-term. A young source favours the frequency of early memory responses, while an old source causes recent responses to be more prevalent. The memory T-cell pool eventually turns younger due to the presence of a young source. This could present a potential explanation for the observation that reconstituted T-cell pools have higher proliferation rates after autologous stem-cell transplantation (Baliu-Piqué et al., 2021) as the highly-divided circulating memory T cells were replaced with lowly-divided memory T cells. Moreover, if the acquisition of different memory T-cell phenotypes were correlated with the division history of a cell, cellular aging would have exciting implications. For example, following the linear differentiation pathway (Henning et al., 2018), the absence of a source would predict the accumulation of effector memory T cells over time, whereas the presence of a source would suggest the accumulation of central memory T cells after multiple infections. Previous studies addressing repeated vaccinations (Souquette and Thomas, 2018) have shown diverging results. Some studies showed the enrichment of memory T cells with an effector memory phenotype (Masopust et al., 2006; Minervina et al., 2022), whereas other studies showed the accumulation of central memory T cells after multiple rounds of heterologous, viral vaccinations (Huster et al., 2009). Similar effects of sustained, chronic responses on the phenotypes of both bystander and specific memory T cells have also been discussed (Barnstorf et al., 2019; Snell et al., 2018). Further, the declining fitness of immune responses in older hosts can explain their impaired response to vaccinations (Wherry et al., 2005). In view of such observations, it is extremely interesting to study the mechanisms underlying the phenotypic distribution in memory T-cell pools, and thereby the erosion of protective immunity with age.

In absence of a source, an aging population will eventually be lost. The timescale of this extinction is much longer than the lifetime of a mouse. Interestingly, erosion of early memories could be beneficial for a host to maintain memory and mount responses against recently encountered pathogens, as the relative proportion of recently generated memory T cells would increase. In a changing natural environment, the probability of getting re-exposed

to a pathogen is probably higher for recently encountered pathogens than for those encountered early in life. Therefore, maintenance of recent memories could be beneficial. Along similar lines, we also showed that long-lived memory T cells, or lack of regulation (due to competition or aging) early in life, would lead to a loss of diversity in the memory T-cell pool due to inflation of early memories. Virtual memory T cells are memory-phenotype cells that originate from naive T cells due to homeostatic proliferation in the absence of cognate antigen (Akue et al., 2012; Sosinowski et al., 2013). If virtual memory T cells would be highly inflated due to lack of competition early in life, and/or due to long lifespans, they would severely impair the efficacy of the memory T-cell repertoire against natural infections.

Many laboratory protocols, just like our simulations, use fixed time intervals between antigen introductions, a scheme that is, of course, rather artificial. In reality, a mouse's exposure to antigens is truly a random event. Statistically, random events follow a Poisson distribution, where the time between two consecutive events is exponentially distributed. Therefore, a mouse in its natural environment will be exposed to most unique antigens early on in its life and to relatively fewer novel antigens in its twilight years. For our models, simulations of this real world scenario led to considerably different results from the simulations presented here (**Figure S5.4**). When emulating the real world scenario, the first immune response, M_1 , did not take over the memory T-cell pool in any of the models, due to competition with multiple other immune responses generated early in life. The snapshots of the memory T-cell pool on day 1000 showed a more marked attrition of immune responses, under the influence of global competition and cellular aging but not under cognate competition (**Figure S5.4**). If anything, our simulations showed that random antigenic exposure accelerates the competitive dynamics and reduces the diversity of the memory T-cell repertoire.

Although our simulations were primarily based on murine parameters, the concerns and results discussed here are also applicable to humans. The expected lifespan of human circulating memory CD8⁺ T cells is close to 200 days (Akondy et al., 2017), which is 4 times longer than that in mice. However, the lifespan of a human is 30 times longer than that of a mouse. Thus, based upon our global competition model, one would expect early immune responses to be competitively excluded during a human's lifetime. Both cognate competition and cellular aging with a source would alleviate this problem, the latter providing a more immunologically sound mechanism. Unfortunately, we are not aware of any literature on the effects of cellular aging of memory T cells that could be used to test the prediction of our novel model. Single-cell sequencing studies have described the change in the memory T-cell repertoire with age (Mogilenko et al., 2021). However, these studies have focused on the age of the host rather than the age of the cell, making a comparison of these results and our predictions speculative. Recent studies using the Cre-recombinase technology (Bresser et al., 2022; Reynaldi et al., 2019) do provide an avenue that could be exploited to delineate the age of the cell from the age of its host. Such dedicated experiments would be required to test the predictions of the cellular aging model.

Barring a few studies (Xu et al., 2016), IL-7 is often implicated in the homeostatic maintenance of memory as well as naive T cells (Gao et al., 2015; Sercan Alp et al., 2015; Tan et al., 2002). The competition between naive and memory T-cell populations through IL-

7 has not been taken into account in this study. As the production of new naive T cells declines with age (den Braber et al., 2012; Tong et al., 2020), reduced competition for IL-7 could alleviate some of the ‘global’ competitive pressure on the memory T-cell pool, leading to a larger memory pool size, but not to an alteration in the distribution of clone sizes (i.e., not to a different memory T-cell repertoire). Similarly, a temporal change in the source of homeostatic cytokines (IL-15, IL-7, etc.) e.g., due to aging, would affect the global competition among memory T cells and change the pool size but not the repertoire. IL-15 is produced by multiple tissues (e.g., bone marrow, heart, lung, kidney, thymic epithelium) and cell types (e.g., monocytes/macrophages, blood-derived dendritic cells) (Fehniger and Caligiuri, 2001) that are subject to alterations throughout a host’s life. Since the lifespan of circulating memory T cells has a time scale of months in mice, the division rate is expected to average over such spatial heterogeneities. In our model, the source is considered to be either from naive T cells due to new or recurrent challenges, or from stem-cell-like memory T cells. As the exposure to antigens is random, the source from naive T cells could be stochastic. Further, newly generated stem-cell-like memory T cells in the bone marrow could either increase the source to an immune response (in case of a recurrent infection) (Radbruch et al., 2021; Siracusa et al., 2018), or decrease the source (due to competition among memory T cells for the limited number of stromal niches) (Chang and Radbruch, 2021; Di Rosa, 2016b). Thus, the source need not be constant. It would be interesting to study such model variations in future studies and to quantify their effect on the long-term maintenance of the memory T-cell pool.

The cellular aging model, like existing models for the maintenance of memory T cells, presents a simplified view of the memory T-cell pool and its maintenance. However, unlike the current gold-standard based on cognate competition, cellular aging is well-supported. Therefore, this manuscript puts forth a realistic mechanism that might underlie the observed long-lived large diversity of the CD8⁺ memory T-cell repertoire despite the relatively short lifespan of CD8⁺ memory T cells.

Author contributions

AS performed the mathematical modelling. AS, JB and RdB designed the study. AS, JB and RdB analysed the data and wrote the manuscript. All authors contributed to the article and approved the submitted version.

Funding statement

This work was supported by an NWO grant (ALWOP.265) to RdB and an NWO Vici grant (R5732) to JB.

Supplementary Information

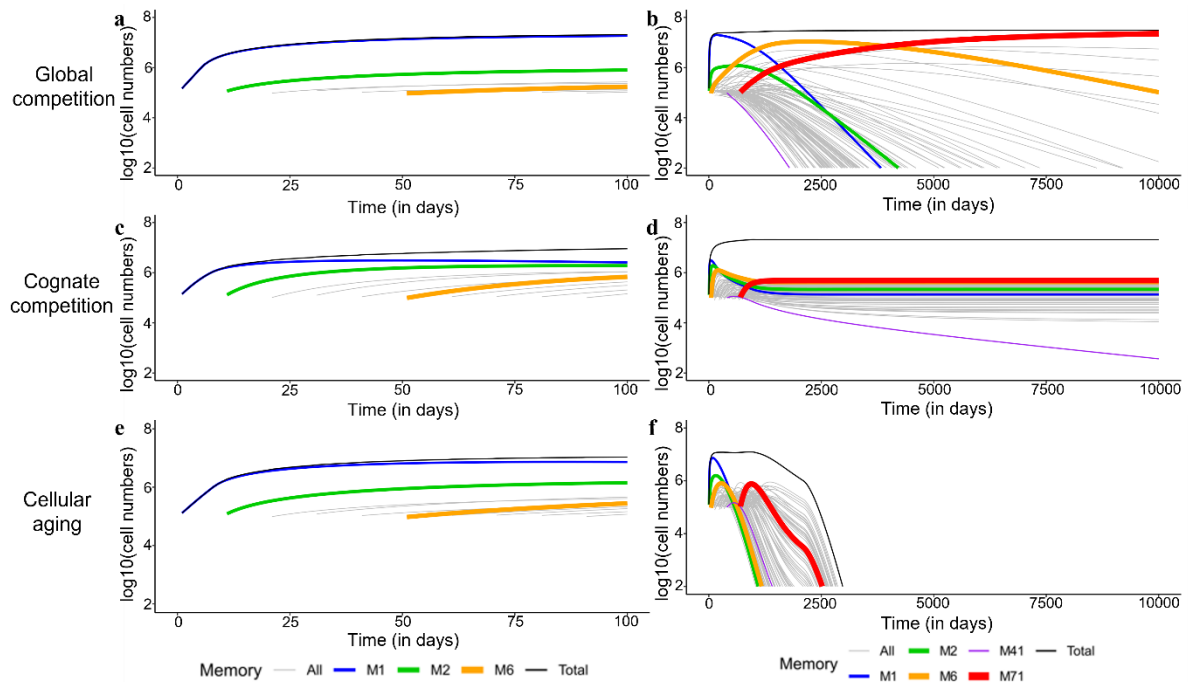


Figure S5.1: Global competition leads to the loss of all but the fittest immune response. Comparison of the three mechanisms (global competition, cognate competition, and cellular aging) for homeostatic maintenance of memory T cells focusing on the short-term (first 100 days in Panels **a**, **c**, and **e**) and long-term (10,000 days in Panels **b**, **d**, and **f**) temporal dynamics of a murine memory T-cell pool. The memory T-cell pool consists of acute immune responses only.

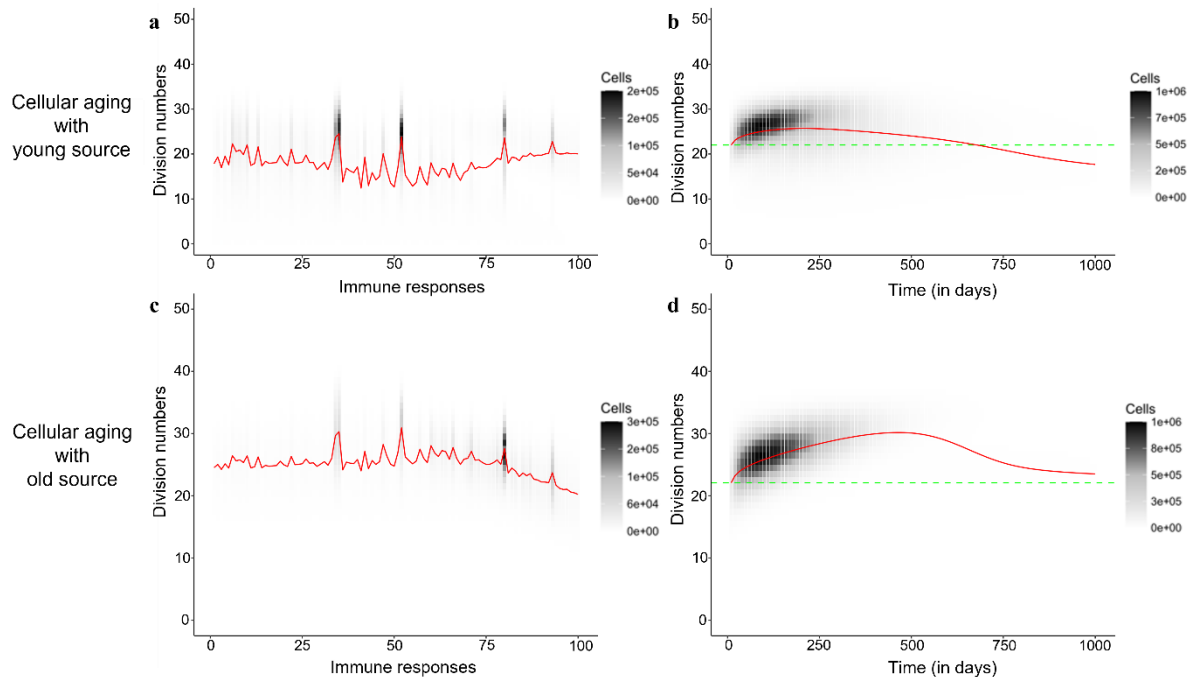


Figure S5.2: Adding chronic responses hardly changed the division distributions. Comparison of the division distributions of all memory T-cell populations on day 1,000, and the division history of

the first memory T-cell population over time. The red line plots the average generation number of an immune response. The grey and black shades show the number of cells at different division numbers. The green dotted line marks the starting division number of the first immune response. The memory T-cell pool consists of both acute and chronic immune responses.

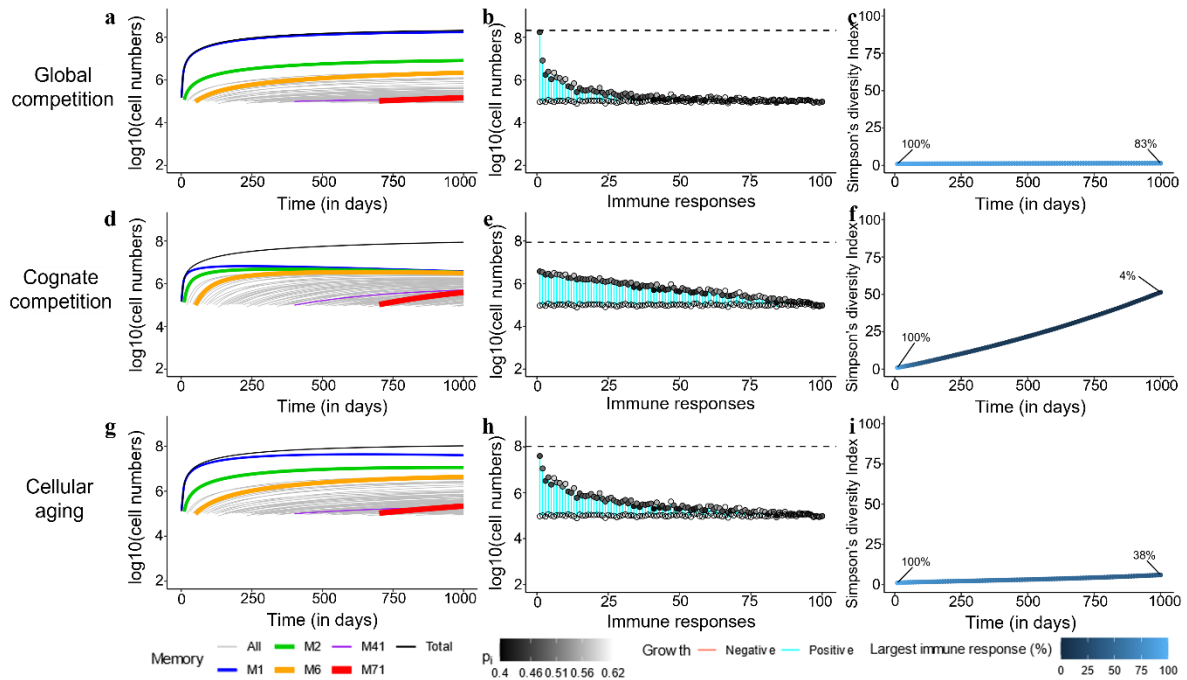


Figure S5.3: Memory T-cell pools with long-lived memory T cells are barely diverse. Comparison of three mechanisms (global competition, cognate competition, and cellular aging, without any source) for homeostatic maintenance of long-lived memory T cells. The expected lifespan of the memory T cells was set to 500 days (which is 10 times longer than their estimated lifespans (Choo et al., 2010)). The memory T-cell pool consists of acute immune responses only.

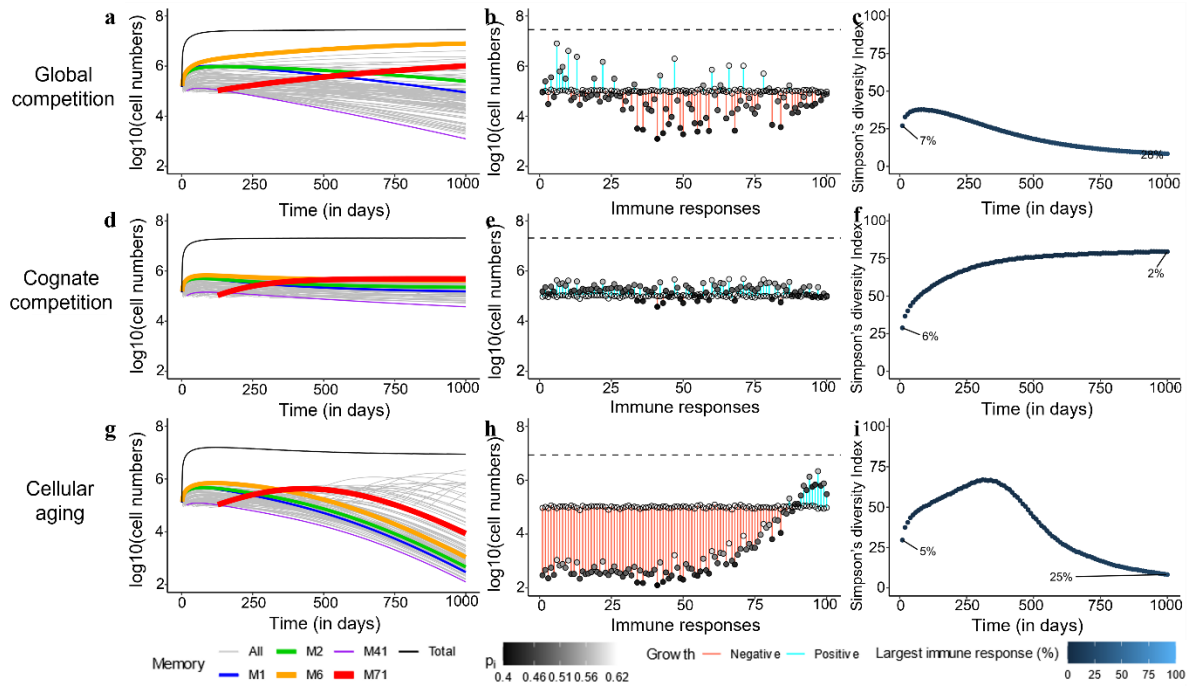


Figure S5.4: Random antigen exposure aggravates the loss of immune memories due to intense competition. Comparison of three mechanisms (global competition, cognate competition, and cellular aging, without any source) for homeostatic maintenance of memory T cells when most novel pathogens appear early in life. The delay between antigen exposures was exponentially distributed, mimicking the random exposure to antigens in real life. The memory T-cell pool consists of acute immune responses only.

Discussion

We raised a few important questions in the introduction to this thesis. Questions that motivated this journey into understanding the formation and longevity of the memory T (T_M)-cell pool. This thesis holds the (partial) answers to those questions. As the previous chapters in this thesis are fairly mathematical, we start this chapter by reiterating the immunological insights. We also take this opportunity to discuss the results of all the chapters together and their contrasts or similarities with other published studies.

Question 1 Do cells of an inflationary T_M -cell response that is maintained during a chronic infection live longer than those of a non-inflationary T_M -cell response? (**Chapter 1**)

It has been suggested that the inflationary property of the MCMV-specific T_M -cell pool is due to the accumulation of long-lived T_M cells (Wallace et al., 2011). We used tetramers for ie2SL, ie2KNL and m45SL, three well-known MCMV epitopes that generate T_M -cell pools with high, medium, and low inflationary properties, respectively, to study this claim. Interestingly, even though the sizes of the tetramer⁺ (i.e., epitope-specific) T_M -cell populations differed considerably between mice infected with different viruses expressing one of these three epitopes, the average *per capita* production rates of the tetramer⁺ T_M cells were similar in all cases. Further, these estimates were not significantly different from the estimated average *per capita* production rates of the bulk T_M -cell populations in the respective mice, as well as in non-infected (i.e., control) mice. We calculated the death rates of the different tetramer⁺ cells by combining the estimated average *per capita* production rates (from deuterium labelling experiments) with the net increases observed in the population sizes of the tetramer⁺ sub-populations. The expected lifespans (i.e., the reciprocal of the calculated death rates) of bulk T_M cells and tetramer⁺ cells were very similar: ~65 days for T_M cells; ~73 days, ~54 days, and ~68 days for tetramer⁺ cells in ie2SL, ie2KNL, and m45SL-immunized mice. Therefore, we did not find any relationship between the inflationary characteristics of a T_M -cell pool and the lifespan of its corresponding T_M cells.

Question 2 How can the label gain rate of a population of cells be higher than its label loss rate? (**Chapter 2**)

CD8⁺ tetramer⁺ T_M cells in MCMV-infected mice (**Chapter 1**) and promyelocytes (neutrophil precursors) in healthy humans generated labelling data that were unexpected for a population of cells at steady state, i.e., the estimated average *per capita* production rate was higher than the estimated loss rate. If the population of interest were heterogeneous, these estimates would intuitively suggest that cells become longer-lived upon division. However, we found that a model where cells become transiently quiescent upon division (i.e., a temporally heterogeneous model) was not sufficient to explain the observed differences in the data. Instead, we propose two separate, alternative mechanisms that can explain why the label gain rates were higher than the label loss rates in these two specific cases. In the case of CD8⁺ T_M cells, the higher estimate of the label gain rate may have been due to the expansion of the T_M -cell population, violating the steady state assumption. As the population expands,

the relative contribution of label from the source to the *per capita* production rate becomes smaller over time, resulting in a slower accrual and loss of label over time. The relatively high label gain rate of neutrophils, in contrast, was most likely due to prolonged (10 hours instead of 5.5 hours) availability of deuterium within the cells in the body of labelled individuals. Due to the sparsity of data points around the peak, i.e., the first data point was at day one, such a longer availability of label can easily be misinterpreted as faster gain of label over an assumed shorter labelling period (5.5 hours), giving rise to a higher estimated label gain rate relative to the label loss rate.

Question 3 Does a population's label gain rate truly reflect its average turnover rate? **(Chapter 3)**

The rate at which a population of cells gains label is generally thought to reflect its turnover rate. We show that strictly speaking this is only true if the population of interest is either solely maintained by proliferation (i.e., does not have a source of cells from a precursor population), or if the precursors of the population of interest turn over rapidly. Thus, whenever it is not safe to make these assumptions, it becomes essential to know the dynamics of the precursors to infer a reliable estimate of the population of interest's true turnover rate solely from the rate at which the population of interest gains label. Depending on the true turnover rates of both the precursors and the population of interest, there can be four different scenarios for the estimated label gain rate, only two of which reflect the true turnover rate of either the precursors or the population of interest. In the other two scenarios, the estimated label gain rate is determined by the true proliferation and turnover rates of both the precursors and the population of interest. Importantly, we found that in three out of the four scenarios, the estimated gain rate is lower than the true turnover rate of the population of interest.

Question 4 Are the protective potential and division history of a T_M cell related? **(Chapter 4)**

Naive T (T_N) cells expand to form T_M cells and T_E cells upon encountering a pathogen. Effector T (T_E) cells are lost after the end of the immune response while T_M cells persist and protect against subsequent pathogen encounters. However, T_M cells are phenotypically heterogeneous, and not all T_M cells are equally protective. We show that in addition to the phenotype, the division history of a T_M cell plays an important role in determining its protective ability during subsequent challenges. Central memory T (T_{CM}) cells, a phenotypic sub-population that is credited to have superior protective abilities, in fact, form a heterogeneous cell population with respect to its division history. T_{CM} cells can be broadly classified into lowly divided and highly divided cells. Lowly divided T_{CM} cells that form a small sub-population (~ 20%) of the T_{CM} cell population are highly enriched in quiescence-related genes, have superior expansion capabilities and are largely responsible for mounting subsequent immune responses to a pathogen. The larger sub-population (~ 80%) of T_{CM} cells that have undergone many more divisions hardly expands upon pathogen re-encounter. Phenotype of a T cell remains important as effector memory T (T_{EM}) cells, which

lay in between lowly divided and highly divided T_{CM} cells in terms of their division history, do not expand upon encountering the pathogen again.

Question 5 Are the relatively short lifespans of T_M cells compatible with a diverse T_M -cell pool? (**Chapter 5**)

Competitive exclusion is a phenomenon that naturally occurs when cells or organisms are competing for a common growth or survival factor. This raises the question how T_M cells, which are all dependent on a shared pool of cytokines, build up a diverse repertoire without outcompeting each other. If T_M cells were quiescent and sufficiently long-lived, they would not be lost due to competition for growth factors. However, since T_M cells are relatively short-lived, our simulations confirm that less fit T_M -cell clones gradually erode over time, which reduces the total TCR diversity of the T_M -cell pool. Interestingly, the simulations also show that competitive exclusion slows down if cells age with cell division, resulting in an increase in the diversity of the T_M -cell pool. In such a cellular aging scenario, the presence of a small source prevents the loss of T_M -cell clones due to competitive exclusion and maintains the diversity of the T_M -cell pool in the long-term. Although the presence of long-lived T_M cells (even in absence of a source) would also prevent competitive exclusion of T_M cells, we show that in such a case the T_M -cell pool would have an extremely low diversity, as the early clones do not erode upon the establishment of new clones and continue to dominate. Therefore, short-lived T_M cells can maintain a long-term, diverse T_M -cell pool, if they age with division and are fed by a source.

Generation of memory T cells

In the introduction, we highlighted the debate around the three different differentiation pathways posited to underlie the development of T_M cells: the circular, the linear and the branched differentiation pathways. Although we did not resolve this debate entirely in this thesis, the data and mathematical modelling in **Chapter 4** suggest that the formation of different T-cell subsets follows a branched differentiation pathway.

The linear and branched differentiation pathways propose that the differentiation of T_{EM} cells from T_{CM} cells occurs during the expansion phase, whereas the circular differentiation pathway proposes that T_{EM} cells differentiate into T_{CM} cells during the memory phase (Henning et al., 2018). We, therefore, believe it is important to distinguish between these phases when discussing T_M -cell differentiation pathways. After all, it is a bit strange to classify $CD27^{hi}KLRG1^{lo}$ activated T cells during the expansion phase as ‘memory’ T cells and use this classification to argue in favour of a linear differentiation pathway. Similarly, referring to activated T cells in the expansion phase as ‘effector’ T cells due to their cytotoxic activity would make the circular differentiation pathway an obvious consequence of the terminology. In our proposed scheme of T_M -cell generation, we, therefore, clearly distinguish between the expansion and memory phases of an immune response.

The proposed memory T-cell generation pathway

In the mathematical model proposed in **Chapter 4**, T_N cells get activated upon recognition of a pathogen, bringing about the expansion phase of an immune response. Throughout the expansion phase, these activated T cells divide rapidly (at a rate of $\sim 1/\text{day}$, see **SI of Chapter 4**), differentiate and switch phenotypes (**Figures D.1 and S4.8a**). Some of the dividing, activated T cells stop dividing and form quiescent T cells, while the rest continue to divide rapidly. The T cells that continue to divide can switch their phenotype by up- or down-regulating several genes. Although we describe the dynamics of two populations ($CD27^{hi}KLRG1^{lo}$ and $CD27^{lo}KLRG1^{hi}$) in **Chapter 4**, it is important to keep in mind that our mathematical model is a simplified representation of the heterogeneity within the dividing pool of activated T cells, which, in reality, is probably made up of a continuum of phenotypes. We further proposed that, during the memory phase of the immune response, these two dividing populations give rise to $CD27^{hi}KLRG1^{lo}$ and $CD27^{lo}KLRG1^{hi}$ cycling T_M phenotypes, respectively, and that the quiescent T cells that were generated during the expansion phase form a $CD27^{hi}KLRG1^{lo}$ quiescent subset in the T_M -cell pool (**Figures D.1 and S4.8a**).

Inferences from the late memory phase

According to the circular differentiation pathway, the T_E cells in the late memory phase, or T_{EM} cells de-differentiate into canonical, T_{CM} cells during the memory phase (Henning et al., 2018; Youngblood et al., 2017). In contrast, it has also been reported that T_{CM} cells differentiate into T_{EM} cells during the memory phase (Caccamo et al., 2005), which is reminiscent of the claims of a linear differentiation pathway during the expansion phase of an immune response (Henning et al., 2018). The data in **Chapter 4** do not provide any evidence of T_{CM} cells differentiating into T_{EM} cells, or *vice versa*, T_{EM} cells de-differentiating into T_{CM} cells during the memory phase. If T_{EM} cells were to differentiate into T_{CM} cells after the peak of the response, the division rate of T_{CM} cells would have to be even faster than the current estimated division rate (which is $0.3/\text{day}$) to attain the observed high average division number of cells in the T_{CM} -cell pool (see **SI of Chapter 4**). We regard this unlikely because, during the memory phase, the average turnover rate of the whole T_M -cell pool (i.e., T_{CM} and T_{EM} cells combined) estimated using the Division Recorder construct (**Chapter 4**) was already markedly higher than that found in deuterium labelling studies (**Chapter 3** and (Westera et al., 2013)) and CFSE experiments (Choo et al., 2010) (see the section **Maintenance of memory T cells** for further discussion on the different lifespan estimates). On the other hand, if T_{CM} cells were to differentiate into T_{EM} cells during the memory phase, the average division number of the T_{EM} -cell pool would have increased more than the marginal increase observed in the T_{EM} -cell pool (**Chapter 4**). Our collective data, therefore, suggest that the generation of T_M cells does not invariably follow a circular or linear differentiation pathway during the memory phase, although T_E cells are formed from T_M cells upon successive challenges. However, based on the data in **Chapter 4**, we cannot exclude the possibility that

a small fraction of the T_{CM} -cell population differentiates into T_{EM} cells and/or that a small fraction of the T_{EM} -cell population de-differentiates into T_{CM} cells.

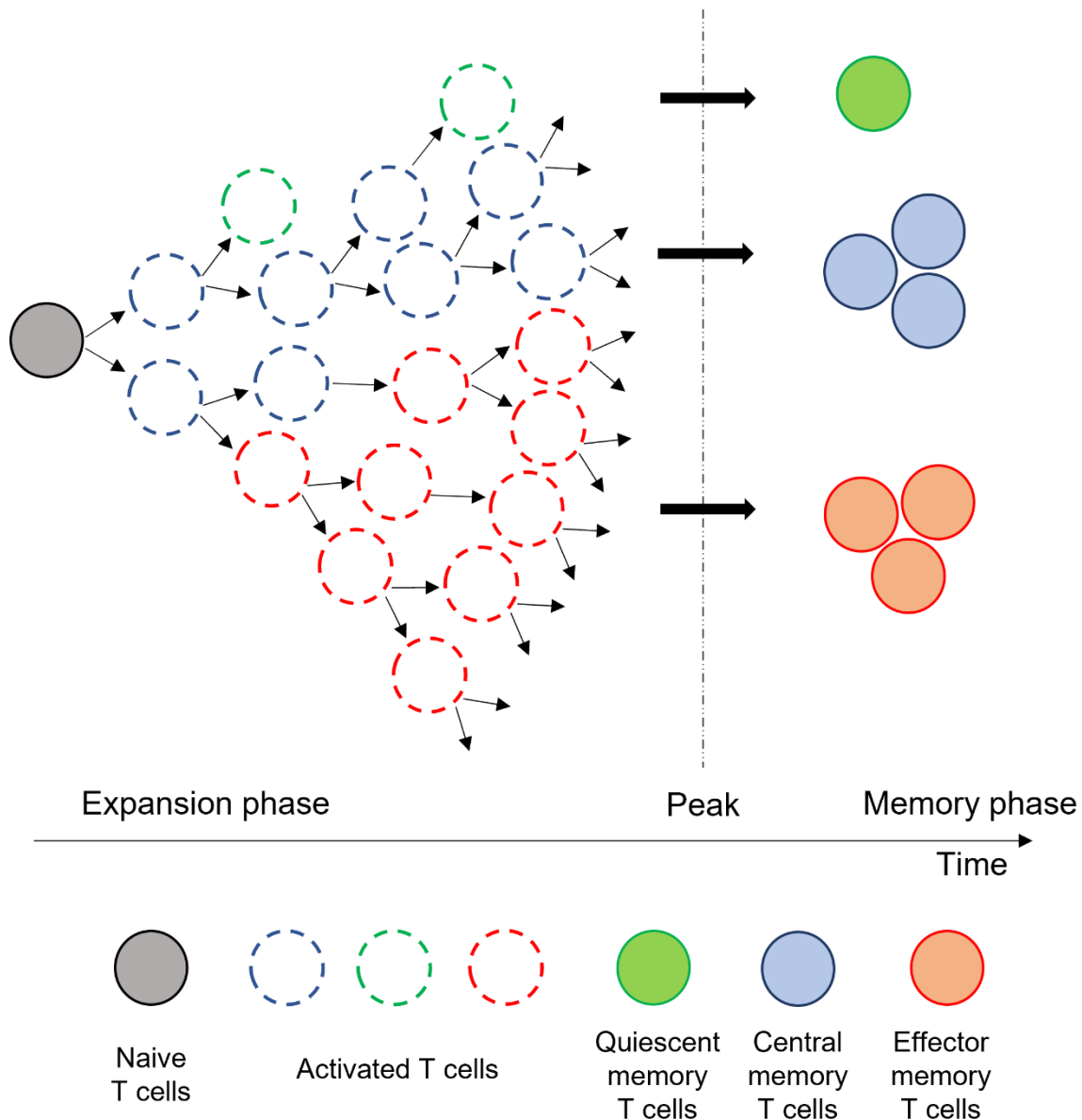


Figure D.1: Our proposed scheme of the development of T cells follows a branched differentiation pathway.

The data in **Chapter 4** showed that T_{CM} cells (defined as $CD27^{hi}KLRG1^{lo}$ cells) are heterogeneous in the number of divisions they have gone through, which is in line with our model, in which the T_{CM} -cell pool consists of a quiescent and a cycling subset. Our modelling suggested that about 20% of the T_{CM} -cell pool, i.e., the quiescent or lowly divided T_{CM} cells, had divided much less than the T_{EM} cells, while the majority (i.e., $\sim 80\%$) of T_{CM} cells were highly divided, and kept on dividing rapidly (much faster than the T_{EM} cells) after the resolution of the infection. Consequently, the division history of the cells, as measured during the late memory phase of the response, showed that T_{CM} cells, on average, had completed

many more divisions than T_{EM} cells (**Chapter 4**). However, if the T_{CM} -cell pool were assumed to be homogeneous, the finding that T_{CM} cells had divided more than T_{EM} cells could be misinterpreted as evidence for highly-divided T_{EM} cells de-differentiating into T_{CM} cells during the memory phase, which would be in line with the circular differentiation pathway (Henning et al., 2018; Youngblood et al., 2017). It is, therefore, important to take the heterogeneity in the division history within the T_M -cell pool into account.

Inferences from the expansion phase

The linear differentiation pathway would predict that the average division number of activated T cells with a memory-phenotype (i.e., $CD27^{hi}KLRG1^{lo}$ T cells) at the end of the expansion phase would be lower than that of activated T cells with an effector-phenotype (i.e., $CD27^{lo}KLRG1^{hi}$ T cells). In contrast, in the branched differentiation pathway, memory- and effector-phenotype activated T cells can undergo a similar number of divisions during the expansion phase, highlighting a key difference between the predictions of these pathways. The data in **Chapter 4** show that the average division numbers of memory- and effector-phenotype activated T cells during the expansion phase are similar, and thus, provide evidence in favour of the proposed branched differentiation pathway during the expansion phase.

Several studies supporting the existence of a linear differentiation pathway have shown that the acquisition of effector markers (for example, TOX) and loss of quiescence markers (like TCF1) are gradual processes (Gonzalez et al., 2021; Kratchmarov et al., 2018; Soerens et al., 2023). Interestingly, the branched differentiation pathway is compatible with these observations as long as the quiescent T_{CM} -cell population is not too large, as the gene expression profile of quiescent T_M cells is similar to that of T_N cells (**Chapter 4**). Our estimates that the quiescent T_M -cell pool occupies $\sim 10\%$ of the total T_M -cell pool is, therefore, compatible with the observed progressive change in the phenotype of T_M cells (Soerens et al., 2023).

TCF1: a surface marker associated with stemness

Several studies have tracked the expression of various transcription factors or the methylation of CpG sites over time to distinguish between the various differentiation pathways in T_M -cell development (Akondy et al., 2017; Henning et al., 2018; Youngblood et al., 2017). However, most of these techniques rely on processes that are reversible. For example, surface markers like CD62L can be re-expressed and CpG sites can be demethylated upon cellular differentiation (Akondy et al., 2017; Youngblood et al., 2017). Recent studies have, therefore, focused on the transcription factor TCF1, the loss of which has been claimed to be irreversible and thus, inheritable (much like the Division Recorder module, see **SI of Chapter 4** and **Box 1** for the similarities in the mathematical description) (Beltra et al., 2020; Kratchmarov et al., 2018; Lin et al., 2016; Nish et al., 2017). TCF1 is associated with cellular

quiescence, stemness and multipotency (**Chapter 4**, (Escobar et al., 2020; Kratchmarov et al., 2018; Pais Ferreira et al., 2020; Wen et al., 2021)). It is thought to be highly expressed in less-differentiated, stem-like T_M cells, which replenish the circulating T_M -cell pool after acute as well as during chronic immune responses (Kratchmarov et al., 2018; Welten et al., 2020).

Current interpretations, based on TCF1, suggest that the T_M -cell generation follows a linear or a branched differentiation pathway. These conclusions hinge on the assumption that the expression of TCF1 is lost asymmetrically and irreversibly, which has primarily been inferred from dilution dye (CFSE/CTV) experiments and the imaging of a few cells sampled from a large population (Lin et al., 2016; Nish et al., 2017). It is important to test whether data from dilution dye experiments are sufficient to infer the asymmetric and irreversible loss of TCF1 expression. For this, we digitized three different datasets (two published (Lin et al., 2016; Nish et al., 2017) and one unpublished, which was kindly provided by Rafi Ahmed) using the ‘Plot Profile’ tool from the software ‘FiJi’ (Schindelin et al., 2012) (see Beatrice Guastella’s Masters’ thesis (Beatrice Guastella, A. C. Swain, 2020)).

The mathematical models that we used to analyse the TCF1 expression data are similar to the models that we used in the Division Recorder study, as both markers are thought to be inheritable and asymmetrically transferred to the next generation of cells (see **Box 1**). We have tested several permutations of reversibility and symmetry of TCF1 expression (see **Figure D.2**) using the digitized datasets (Beatrice Guastella, A. C. Swain, 2020). However, there are several challenges with this approach. The parameters of the mathematical models were not always identifiable, perhaps due to the relatively sparse data. Further, digitization of the figures from the experiments may have introduced noise in the analysed data. For instance, we were surprised to find $TCF1^{lo}$ cells already in the first three divisions (Beatrice Guastella, A. C. Swain, 2020), contradicting the claim that $TCF1^{lo}$ cells are formed only after the first three divisions (Lin et al., 2016). Further studies dedicated to determining the reversibility and symmetry of TCF1 expression are essential to reliably comment on the differentiation pathways of T_M cells based on their expression of TCF1.

Box 1

Model for irreversible and asymmetric loss of TCF1 expression

This box presents the mathematical model for the loss of TCF1 expression, in the case where TCF1 is irreversibly and asymmetrically lost. This describes only one out of all possible permutations of reversibility and symmetry in the loss of TCF1 expression (see (Beatrice Guastella, A. C. Swain, 2020) for in-depth descriptions of all the models). To observe the similarity between this model and the Division Recorder model, compare **equation D.1** to the first two lines of **equation 4.4**.

Consider a population of $TCF1^{hi}$ T_N cells that get activated by encountering an antigen and divide at a *per capita* rate of λ /day and die at a *per capita* rate of d /day. Expression of TCF1 can be lost asymmetrically upon division, i.e., upon division, a $TCF1^{hi}$ cell will make one

TCF1^{hi} daughter cell, while the other daughter cell can either lose TCF1 expression with a probability p , giving rise to a TCF1^{lo} cell, or maintain TCF1 expression with a probability $(1 - p)$, and giving rise to another TCF1^{hi} cell (Lin et al., 2016). If the loss of TCF1 expression is irreversible and asymmetric, then the dynamics of TCF1^{hi} (H) and TCF1^{lo} (L) cells can be expressed in terms of the following ordinary differential equations:

$$\frac{dH}{dt} = \lambda H + (1 - p)\lambda H - (\lambda + d)H$$

$$\frac{dL}{dt} = p\lambda H + 2\lambda L - (\lambda + d)L$$
(D.1)

The above model (**equation D.1**) was extended to a division-indexed form (see (Beatrice Guastella, A. C. Swain, 2020) and **SI of Chapter 4**) to describe the data from dilution dye experiments. This system of equations can also be modified to model different permutations of reversibility and symmetry of TCF1 expression loss (see (Beatrice Guastella, A. C. Swain, 2020) for detailed description of the different models).

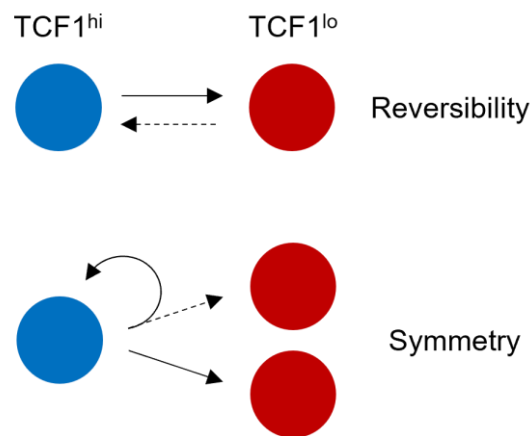


Figure D.2: Schematic for propagation of TCF1 expression. The solid arrows depict the processes modelled in **equation D.1**, while the dashed arrows are other possible processes.

Maintenance of memory T cells

An effective T_M-cell pool must be long-lived and diverse. We showed that T_M cells have to be relatively short-lived for a diverse T_M-cell repertoire to be maintained, as the diversity of the T_M-cell pool suffers if individual T_M cells are long-lived (**Chapter 5**). However, under the threat of competitive exclusion, short-lived T_M cells can only be sustained long-term in the presence of long-lived or self-sustaining precursors (**Chapter 5**). During chronic responses (for example, against MCMV), TCF1⁺ stem-like T_M cells are thought to act as a constant source of cycling T_M cells due to persistent stimulation (Welten et al., 2020). We found that after an acute response, the quiescent subset of T_M cells that expands on successive pathogen encounter is also TCF1⁺ (**Chapter 4**). Our simulations confirmed that if such quiescent T_M cells divide sporadically into short-lived T_M cells, the resulting small source of

short-lived T_M cells can sustain the diversity of the T_M -cell pool in the circulation (**Chapter 5**).

Surprisingly, we found that the small, quiescent T_M -cell pool orchestrates successive immune responses, while the short-lived, cycling T_{CM} and T_{EM} cells that make up $\sim 90\%$ of the T_M -cell pool hardly expand on re-stimulation (**Chapter 4**, see **Figure D.3**). This curious characteristic of the immune system may reflect its safeguards against losing precious memory. By storing the ‘real’ memory in long-lived quiescent T_M cells (in circulation, see **Chapter 4**, or in bone marrow (Okhrimenko et al., 2014)), the immune system may avoid or at least slow down the competitive exclusion of these T_M cells. It would be more difficult to avoid competitive exclusion and to maintain the diversity of the T_M -cell pool if memory was only stored in proliferating (self-sustaining) T_M cells. It is tempting to speculate that stem-like T_M cells may help to avoid competitive exclusion of T_M -cell clones by tuning their own differentiation rate. Such regulation of differentiation has been proposed for hematopoietic stem cells (HSCs) during tissue (re-)generation (Lander et al., 2009), where downstream tissues provide feedback signals to HSCs, which can increase or decrease the differentiation rate of HSCs. In such a scenario, stem-like T_M cells specific for an epitope would need clone-specific (cognate) signals from the circulating cognate T_M cells. Such cognate signals, however, have not yet been identified. Importantly, it is unlikely that successive immune responses in the Division Recorder study originated from T_N cells that failed to become stimulated during the previous response, as the TCR of all the transferred OT-1 T cells had the same high affinity for the peptide, suggesting high (and uniform) recruitment of these cells during an immune response (Leube et al., 2022).

Although it is now well-established that circulating T_M cells are short-lived (Borghans et al., 2018), the estimates of their expected lifespans vary across studies. For example, the (deuterium) labelling curve of MCMV-specific T_M cells could be explained equally well by a population of T_M cells that have an expected lifespan of ~ 65 days (**Chapter 1**) or by a growing population of long-lived T_M cells (**Chapter 2**). The expected lifespan of T_M cells in mice in homeostasis was previously estimated to be ~ 25 days in a deuterium labelling study (Westera et al., 2013) and ~ 50 days in a dilution dye experiment (Choo et al., 2010). Using the Division Recorder construct and mathematical modelling, we found that OT-1 T_M cells can be broadly divided into three sub-groups: cycling T_{CM} cells, which make up $\sim 45\%$ of the circulating T_M -cell population and have an expected lifespan of ~ 3 days (i.e. a turnover rate of 0.3/day), T_{EM} cells, which make up $\sim 45\%$ of the circulating T_M -cell population and have an expected lifespan of ~ 25 days (turnover rate = 0.04/day), and quiescent T_{CM} cells, which make up $\sim 10\%$ of the circulating T_M -cell population (see **SI** of **Chapter 4**). Thus, the average expected lifespan of OT-1 T_M cells was estimated to be roughly 7 days (calculated as the inverse of the average of the turnover rates) using the Division Recorder construct, which is much lower than the 25 days (Westera et al., 2013) and 50 days (Choo et al., 2010) that were previously estimated. Disturbingly, the averaging method itself affects the estimated expected lifespan because the average lifespan of a kinetically heterogeneous population can be calculated in two ways: 1) as the weighted average of the turnover rates, which is then converted into lifespans, or 2) as the weighted average of the lifespans of the sub-populations.

Using the latter method, the estimate of the expected lifespan of T_M cells from the Division Recorder study would be much longer than 7 days, as it would strongly depend on the long expected lifespan of the quiescent T_{CM} cells.

The discrepancies in the estimated expected lifespans of T_M cells could be due to:

1. different experimental conditions, for example, deuterium labelling was done either under homeostatic conditions or during a chronic infection (**Chapters 1-3**), the dilution dye experiments were done with endogenous T cells in BALB/c mice or with P14 cells in C57BL/6 mice (Choo et al., 2010) and OT-1 cells were used in the Division Recorder experiments (**Chapter 4**);
2. different experimental techniques, for example, deuterium is incorporated into the DNA of a cell (Hellerstein and Neese, 1992), while components of the cytoplasm are fluorescently stained in dilution dye experiments (Parish, 1999), and a fluorescent protein is expressed in Division Recorder experiments (Yang and Hughes, 2001); and
3. different assumptions, for example, the assumption of steady state as in **Chapter 1**, as opposed to the non-steady state analysis in **Chapter 2**, or the assumption of heterogeneity in the kinetic heterogeneity model versus the explicit source model as noted in **Chapter 3**. Considering the heterogeneity of the T_M -cell pool could lead to different conclusions, which was also highlighted in the previous section **Generation of memory T cells**.

To truly understand the maintenance of the T_M -cell pool, it is important to understand the differences in the estimated expected lifespans of T_M cells. One way to move towards a unified understanding of T_M -cell maintenance is by analysing (datasets of) multiple markers simultaneously, so that the reliability of the estimates can be strengthened. For example, taking along measurements of cell numbers and of the percentage of cells that are $Ki67^+$ over time, when analysing deuterium labelling of a population that is not at steady state, would provide additional information about (and/or put constraints on) the size of the population and the proportion of cells that are actively dividing (Gossel et al., 2017; Hogan et al., 2017). Datasets on the percentage of $Ki67^+$ cells, unfortunately, do not provide much additional information about the dynamics of the population if the population of interest is at steady state, as a fixed fraction of cells divide when a population is at equilibrium (see the general discussion of Vera van Hoven's PhD thesis ("Lymphocyte dynamics in healthy and lymphopenic conditions (2015) | www.narcis.nl," n.d.) for an in-depth discussion).

Although the exact lifespan of cycling T_M cells remains uncertain, the evidence for their relatively short lifespan is numerous and convincing. Through our simulations, we discovered a benefit of the short lifespans of cycling T_M cells and propose that cellular aging is an immunologically viable mechanism through which the long-term diversity of the T_M -cell repertoire could be maintained.

Overcoming the age gap: a cell versus a cell population

Very recently, Masopust and colleagues, in an impressive decade-long study (Soerens et al., 2023), showed that T_M cells retain their expansion capabilities and protective abilities even when stimulated 51 times over 10 years. Incredibly, T_M cells of the original mouse outlived the mouse itself by many mouse lifetimes, as cells that were transferred from the original mouse after the tertiary infection continued to respond and expand upon 48 re-stimulations in 16 new congenic mice. At first sight, these findings seem to conflict with two of the concepts proposed in this thesis, namely 1) that most T_M cells do not expand upon successive infections (**Chapter 4**), and 2) that T_M cells age upon division (**Chapter 5**).

Masopust's experiments do not exclude the possibility that the expansion of the T_M -cell pool could be due to a small stem-cell-like subset among the transferred T_M -cell population (as shown in **Chapter 4**). Along the same lines, recent studies showed that upon secondary infection new $CD103^+$ tissue-resident T_M cells were formed from $CD103^-$ precursor populations, instead of from expansion of existing $CD103^+$ tissue-resident T_M cells (Fung et al., 2022; von Hoesslin et al., 2022). Masopust and colleagues also concluded that their data do not reject the presence of stem cells (Soerens et al., 2023). Interestingly, they showed that T_M cells expressed medium levels of TCF1, which is associated with stemness of T cells, even after 48 expansions. Therefore, it remains possible that the expansion of the T_M -cell pool was due to the participation of a subset of, and not all, T_M cells.

Hayflick limit proposes that cells, after 50-60 divisions, can no longer divide due to the erosion of their telomeres (Hayflick, 1965; Hayflick and Moorhead, 1961). Does the finding that T cells can go through many more divisions than the Hayflick limit (Soerens et al., 2023), then, argue that a T cell does not age upon division? Interestingly, Soerens et al. (Soerens et al., 2023), showed that the telomere length of expanded T_M cells remained comparable to that of T_N cells even after 33 challenges. This is in contrast to previous studies among healthy individuals in which T_M cells had consistently shorter telomeres than T_N cells (Rufer et al., 1999; Weng, 2008; Weng et al., 1995). A recent study showed that the telomere length of some T cells is extended, before clonal expansion, by the transfer of telomeric DNA from antigen presenting cells to T cells in the immunological synapse (Lanna et al., 2022). This would increase the number of divisions clonally expanding T cells can go through. Further, the enzyme telomerase, which extends telomeres, is activated during synaptic stimulation (Akbar et al., 2004). This suggests that T cells can prevent the erosion of their telomeres and, in turn, extend their ability to divide and prevent cellular aging during clonal expansion, but do erode their telomeres, and hence age, during homeostatic cell divisions.

Several independent lines of evidence suggest that T cells age and lose their proliferative capabilities during homeostasis. Telomerase activation of T cells declines progressively with repeated immune-synaptic interactions (Boraschi et al., 2013; Goronzy and Weyand, 2013; Plunkett et al., 2007; Weng et al., 2009), resulting in shortening of telomeres during T-cell division. Proliferation capability of T cells is associated with their telomere lengths (Lanna et al., 2022). In line with this, we showed a clear negative correlation between the division history and the proliferative capabilities of T cells (**Chapter 4**). Further, T_N cells can expand

considerably more than more differentiated T_M cells (Hinrichs et al., 2009). Therefore, our assumption that T cells age with cell division during homeostasis is supported by several studies, and is not inconsistent with the finding that T cells do not lose their expansion potential upon repeated antigenic stimulation (Soerens et al., 2023).

It is difficult to follow single cells and their progenies over a long period of time. Most studies addressing the aging of the immune system, therefore understandably, focus on either the age of the host (Reynaldi et al., 2019; Rudd et al., 2011) or the average age of the cell population (Reynaldi et al., 2019; Soerens et al., 2023), and not on the age of the individual cells (like in **Chapter 5**). Over the years, a few studies have followed the progeny (or family) of single cells over time (Gerlach et al., 2013; Marchingo et al., 2016; Minervina et al., 2022). These techniques could be used to address questions about the age of individual cells. Excitingly, indirect evidence for cellular aging can also be attained by testing the population level predictions of mathematical models. The Division Recorder system can be harnessed to bridge the age gap of a cell and the age of a population of cells. For instance, if the average generation number of a clone or of several clones in the repertoire can be tracked over time using a Division Recorder system, this can then be compared with the changes in the average generation number over time, as predicted by the cellular aging model (see **Figures 5.4 and S5.2**).

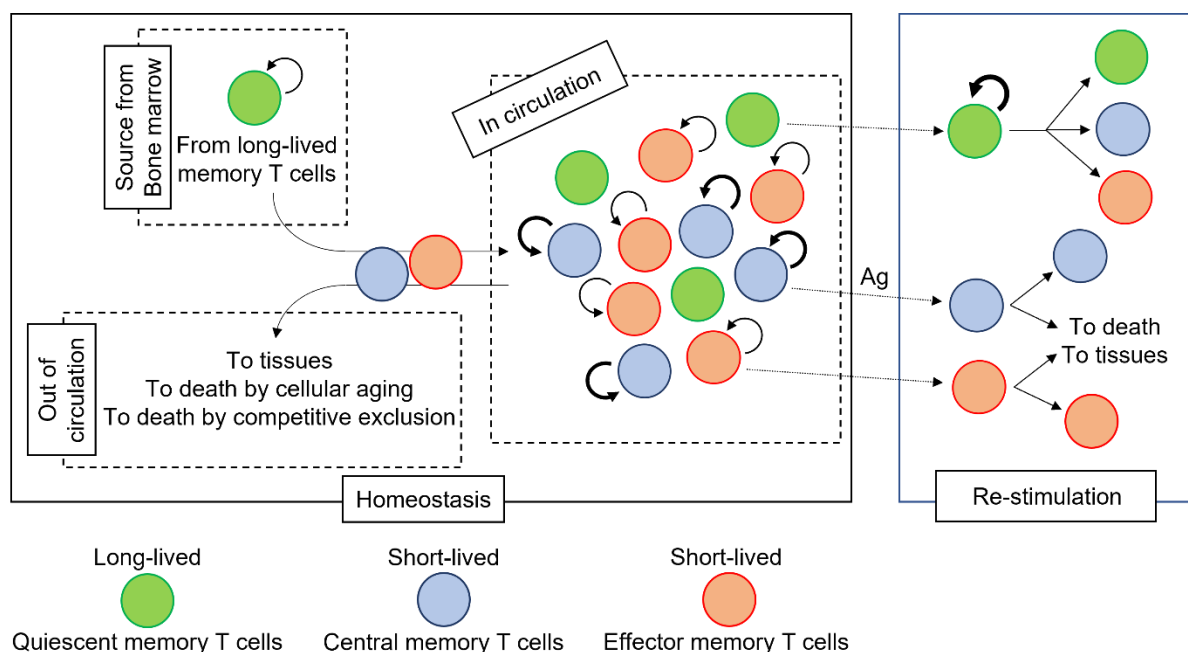


Figure D.3: Maintenance of memory T cells during the memory phase. The homeostatic T_M -cell pool is maintained by proliferation of short-lived T_M cells, and by a small source of short-lived T_M cells from sporadically dividing, long-lived T_M cells in the bone marrow. The source of short-lived T_M cells balances the loss of these cells from the circulation. Quiescent T_M cells are capable of rapidly regenerating all phenotypes of T_M cells, while short-lived T_{CM} and T_{EM} cells hardly divide upon re-encountering a pathogen.

Concluding remarks

This chapter presented our current view on the life of a T_M cell from its birth (generation, **Figure D.1**) to its death (maintenance, **Figure D.3**). We also discussed old and recent experiments that shed light on these processes, and whether these experiments are consistent with our view. Here, at the end, we will summarize the factors that make it difficult to build a coherent view of the generation pathway and the maintenance mechanism of T_M cells:

- ***The absence of an accepted standard definition of various T-cell subsets.*** Since the discovery of different T-cell subsets, studies have continuously updated the definition of these subsets. For example, stem-like T_M cells were first identified as a subset of antigen-experienced T cells with naive-signatures, expressing high levels of CD95 (Gattinoni et al., 2011). Later studies have used TCF1 (Lin et al., 2016) or CD62L (Soerens et al., 2023) as identifiers for stem-like T_M cells. The impact of such definitions is clearly illustrated by the fact that studies that have focused on CD62L have concluded that T_M -cell generation follows a circular differentiation pathway (Akondy et al., 2017; Youngblood et al., 2017), whereas studies that have focused on TCF1 have concluded a linear or branched differentiation pathway underlying T_M -cell generation (Lin et al., 2016; Nish et al., 2017). Further, T_{CM} and T_{EM} subsets that were first differentiated on the basis of CCR7 expression (Sallusto et al., 1999), have also been characterized on the basis of CD62L, TCF1 (Pais Ferreira et al., 2020), CX3CR1 (Gerlach et al., 2016) or CD27 and KLRG1 (**Chapter 4**) expression. The expression of these markers does not necessarily correlate with each other, underscoring the difficulty in comparing different studies. In fact, there is considerable heterogeneity in CD62L and CX3CR1 expression when T_{CM} and T_{EM} subsets are identified on the basis of CD27 and KLRG1 expression (**Figure S4.2d**). It is, therefore, important to come to a unified definition of T-cell subsets.
- ***The scarcity of mathematical theories.*** Defining T-cell subsets based on cell surface markers is tricky, as there are thousands of surface markers, and T cells may gradually change the expression levels of these markers upon migration through the body, during cell division and during cellular aging. We have shown that the division history of T cells is a good predictor of their functional properties (**Chapter 4**). If T cells could be isolated based on their division history, this may provide an alternative way to identify T-cell subsets. Interestingly, the study design of **Chapter 4** was based on a mathematical theory (Weber et al., 2016) that proposed an unambiguous way of determining the division history of a population. Unlike in physics, experimental studies in immunology are hardly ever motivated by mathematical theories. We believe that the development of well-supported mathematical theories and modelling studies will provide novel approaches to study the heterogeneity of T-cell populations and to decode their differentiation pathways and maintenance mechanisms.
- ***The scarcity of corroborative studies.*** Advancement in the field of immunology is extremely fast. Many studies tackling interesting questions are published every

month. The results of such studies do not always match, however. For example, the pathway that underlies the generation of T_M cells and the expected lifespan of T_M cells are still subject of intense debate. Further, researchers studying the effect of serial vaccinations or infections on the diversity of the T_M -cell pool (Selin et al., 1999; Vezys et al., 2008) and its phenotypic composition (Huster et al., 2009; Vezys et al., 2008) find contradictory results. Although several hypotheses for these differences have been proposed (Vezys et al., 2009; Welsh and Selin, 2009), they have not yet been tested. Studies comparing different vaccination strategies (Masopust et al., 2006) and exploring the differences in experiments addressing the same questions (Westera et al., 2013) are rare. We believe such corroborative studies are important to provide a coherent picture of T-cell biology.

Future studies that address the above-mentioned issues should resolve these ambiguities and would help to gain a system-level understanding of the generation and maintenance of the T_M -cell pool.

Bibliography

- Agenés, F., Dangy, J.P., Kirberg, J., 2008. T cell receptor contact to restricting MHC molecules is a prerequisite for peripheral interclonal T cell competition. *J. Exp. Med.* 205, 2735–2743. <https://doi.org/10.1084/JEM.20070467>
- Ahmed, R., Bevan, M.J., Reiner, S.L., Fearon, D.T., 2009. The precursors of memory: models and controversies. *Nat. Rev. Immunol.* 2009 9 9, 662–668. <https://doi.org/10.1038/nri2619>
- Ahmed, R., Miners, K.L., Lahoz-Beneytez, J., Jones, R.E., Roger, L., Baboonian, C., Zhang, Y., Wang, E.C.Y., Hellerstein, M.K., McCune, J.M., Baird, D.M., Price, D.A., Macallan, D.C., Asquith, B., Ladell, K., 2020. CD57+ Memory T Cells Proliferate In Vivo. *Cell Rep.* 33. <https://doi.org/10.1016/J.CELREP.2020.108501>
- Ahmed, R., Westera, L., Drylewicz, J., Elemans, M., Zhang, Y., Kelly, E., Reljic, R., Tesselaar, K., de Boer, R.J., Macallan, D.C., Borghans, J.A.M., Asquith, B., 2015. Reconciling Estimates of Cell Proliferation from Stable Isotope Labeling Experiments. *PLoS Comput. Biol.* 11, 1004355. <https://doi.org/10.1371/journal.pcbi.1004355>
- Aiello, A.E., Chiu, Y.L., Frasca, D., 2017. How does cytomegalovirus factor into diseases of aging and vaccine responses, and by what mechanisms? *GeroScience* 39, 261. <https://doi.org/10.1007/S11357-017-9983-9>
- Akbar, A.N., Beverley, P.C.L., Salmon, M., 2004. Will telomere erosion lead to a loss of T-cell memory? *Nat. Rev. Immunol.* 4, 737–743. <https://doi.org/10.1038/NRI1440>
- Akondy, R.S., Fitch, M., Edupuganti, S., Yang, S., Kissick, H.T., Li, K.W., Youngblood, B.A., Abdelsamed, H.A., McGuire, D.J., Cohen, K.W., Alexe, G., Nagar, S., McCausland, M.M., Gupta, S., Tata, P., Haining, W.N., McElrath, M.J., Zhang, D., Hu, B., Greenleaf, W.J., Goronzy, J.J., Mulligan, M.J., Hellerstein, M., Ahmed, R., 2017. Origin and differentiation of human memory CD8 T cells after vaccination. *Nature* 552, 362–367. <https://doi.org/10.1038/nature24633>
- Akue, A.D., Lee, J.-Y., Jameson, S.C., 2012. Derivation and maintenance of virtual memory CD8 T cells. *J. Immunol.* 188, 2516. <https://doi.org/10.4049/JIMMUNOL.1102213>
- Althaus, C.L., Ganusov, V. V., De Boer, R.J., 2007. Dynamics of CD8+ T cell responses during acute and chronic lymphocytic choriomeningitis virus infection. *J. Immunol.* 179, 2944–2951. <https://doi.org/10.4049/JIMMUNOL.179.5.2944>
- An, Z., Sabalic, M., Bloomquist, R.F., Fowler, T.E., Streelman, T., Sharpe, P.T., 2018. A quiescent cell population replenishes mesenchymal stem cells to drive accelerated growth in mouse incisors. *Nat. Commun.* 9. <https://doi.org/10.1038/s41467-017-02785-6>
- Asquith, B., Debaq, C., Macallan, D.C., Willems, L., Bangham, C.R.M., 2002. Lymphocyte kinetics: The interpretation of labelling data. *Trends Immunol.* 23, 596–601. [https://doi.org/10.1016/S1471-4906\(02\)02337-2](https://doi.org/10.1016/S1471-4906(02)02337-2)
- Austin, W.R., Armijo, A.L., Campbell, D.O., Singh, A.S., Hsieh, T., Nathanson, D.,

- Herschman, H.R., Phelps, M.E., Witte, O.N., Czernin, J., Radu, C.G., 2012. Nucleoside salvage pathway kinases regulate hematopoiesis by linking nucleotide metabolism with replication stress. *J. Exp. Med.* 209, 2215–2228. <https://doi.org/10.1084/jem.20121061>
- Badovinac, V.P., Haring, J.S., Harty, J.T., 2007. Initial T cell receptor transgenic cell precursor frequency dictates critical aspects of the CD8+ T cell response to infection. *Immunity* 26, 827–841. <https://doi.org/10.1016/j.immuni.2007.04.013>
- Baliu-Piqué, M., Drylewicz, J., Zheng, X., Borkner, L., Swain, A.C., Otto, S.A., Boer, R.J. de, Tesselaar, K., Cicin-Sain, L., Borghans, J.A.M., 2022. Turnover of Murine Cytomegalovirus–Expanded CD8+ T Cells Is Similar to That of Memory Phenotype T Cells and Independent of the Magnitude of the Response. *J. Immunol.* 208, 799–806. <https://doi.org/10.4049/JIMMUNOL.2100883>
- Baliu-Piqué, M., van Hoeven, V., Drylewicz, J., van der Wagen, L.E., Janssen, A., Otto, S.A., van Zelm, M.C., de Boer, R.J., Kuball, J., Borghans, J.A.M., Tesselaar, K., 2021. Cell-density independent increased lymphocyte production and loss rates post-autologous hsct. *Elife* 10, 1–22. <https://doi.org/10.7554/ELIFE.59775>
- Baliu-Piqué, M., Verheij, M.W., Drylewicz, J., Ravesloot, L., de Boer, R.J., Koets, A., Tesselaar, K., Borghans, J.A.M., 2018. Short lifespans of memory T-cells in bone marrow, blood, and lymph nodes suggest that T-cell memory is maintained by continuous self-renewal of recirculating cells. *Front. Immunol.* 9, 2054. <https://doi.org/10.3389/FIMMU.2018.02054/BIBTEX>
- Baran, Y., Bercovich, A., Sebe-Pedros, A., Lubling, Y., Giladi, A., Chomsky, E., Meir, Z., Hoichman, M., Lifshitz, A., Tanay, A., 2019. MetaCell: analysis of single-cell RNA-seq data using K-nn graph partitions. *Genome Biol.* 20. <https://doi.org/10.1186/s13059-019-1812-2>
- Barnstorf, I., Borsa, M., Baumann, N., Pallmer, K., Yermanos, A., Joller, N., Spörri, R., Welten, S.P.M., Kräutler, N.J., Oxenius, A., 2019. Chronic virus infection compromises memory bystander T cell function in an IL-6/STAT1-dependent manner. *J. Exp. Med.* 216, 571–586. <https://doi.org/10.1084/JEM.20181589>
- Baumann, N.S., Torti, N., Welten, S.P.M., Barnstorf, I., Borsa, M., Pallmer, K., Oduro, J.D., Cicin-Sain, L., Ikuta, K., Ludewig, B., Oxenius, A., 2018. Tissue maintenance of CMV-specific inflationary memory T cells by IL-15. *PLOS Pathog.* 14, e1006993. <https://doi.org/10.1371/JOURNAL.PPAT.1006993>
- Baumann, N.S., Welten, S.P.M., Torti, N., Pallmer, K., Borsa, M., Barnstorf, I., Oduro, J.D., Cicin-Sain, L., Oxenius, A., 2019. Early primed KLRG1- CMV-specific T cells determine the size of the inflationary T cell pool. *PLOS Pathog.* 15, e1007785. <https://doi.org/10.1371/JOURNAL.PPAT.1007785>
- Beatrice Guastella, A. C. Swain, R.J. de B., 2020. Mathematical modelling of TCF1 expression pattern in proliferating T cells. Vrije Universiteit Amsterdam.
- Becker, T.C., John Wherry, E., Boone, D., Murali-Krishna, K., Antia, R., Ma, A., Ahmed, R., 2002. Interleukin 15 Is required for proliferative renewal of virus-specific memory CD8 T cells. *J. Exp. Med.* 195, 1541–1548. <https://doi.org/10.1084/jem.20020369>
- Beltra, J.C., Manne, S., Abdel-Hakeem, M.S., Kurachi, M., Giles, J.R., Chen, Z., Casella, V.,

- Ngiow, S.F., Khan, O., Huang, Y.J., Yan, P., Nzingha, K., Xu, W., Amaravadi, R.K., Xu, X., Karakousis, G.C., Mitchell, T.C., Schuchter, L.M., Huang, A.C., Wherry, E.J., 2020. Developmental Relationships of Four Exhausted CD8⁺ T Cell Subsets Reveals Underlying Transcriptional and Epigenetic Landscape Control Mechanisms. *Immunity* 52, 825-841.e8. <https://doi.org/10.1016/J.IMMUNI.2020.04.014>
- Berard, M., Tough, D.F., 2002. Qualitative differences between naïve and memory T cells. *Immunology* 106, 127. <https://doi.org/10.1046/J.1365-2567.2002.01447.X>
- Birnie, G.D., 1988. The HL60 cell line: a model system for studying human myeloid cell differentiation. *Br. J. Cancer. Suppl.* 9, 41.
- Blattman, J.N., Antia, R., Sourdive, D.J.D., Wang, X., Kaech, S.M., Murali-Krishna, K., Altman, J.D., Ahmed, R., 2002. Estimating the precursor frequency of naive antigen-specific CD8 T cells. *J. Exp. Med.* 195, 657–664. <https://doi.org/10.1084/jem.20001021>
- Block, K.E., Jameson, S.C., 2021. Inflating the role of stromal cells in CD8⁺ T cell memory. *Nat. Immunol.* 2021 228 22, 942–944. <https://doi.org/10.1038/s41590-021-00974-6>
- Bolinger, B., Sims, S., Swadling, L., O’Hara, G., de Lara, C., Baban, D., Saghal, N., Lee, L.N., Marchi, E., Davis, M., Newell, E., Capone, S., Folgari, A., Barnes, E., Klenerman, P., 2015. Adenoviral Vector Vaccination Induces a Conserved Program of CD8(+) T Cell Memory Differentiation in Mouse and Man. *Cell Rep.* 13, 1578–1588. <https://doi.org/10.1016/J.CELREP.2015.10.034>
- Boraschi, D., Aguado, M.T., Dutel, C., Goronzy, J., Louis, J., Grubeck-Loebenstien, B., Rappuoli, R., Del Giudice, G., 2013. The gracefully aging immune system. *Sci. Transl. Med.* 5. <https://doi.org/10.1126/SCITRANSLMED.3005624>
- Borghans, J.A.M., Taams, L.S., Wauben, M.H.M., De Boer, R.J., 1999. Competition for antigenic sites during T cell proliferation: A mathematical interpretation of in vitro data. *Proc. Natl. Acad. Sci.* 96, 10782–10787. <https://doi.org/10.1073/PNAS.96.19.10782>
- Borghans, J.A.M., Tesselaar, K., de Boer, R.J., 2018. Current best estimates for the average lifespans of mouse and human leukocytes: reviewing two decades of deuterium-labeling experiments. *Immunol. Rev.* 285, 233–248. <https://doi.org/10.1111/IMR.12693>
- Borkner, L., Sitnik, K.M., Dekhtiarenko, I., Pulm, A.-K., Tao, R., Drexler, I., Cicin-Sain, L., 2017. Immune Protection by a Cytomegalovirus Vaccine Vector Expressing a Single Low-Avidity Epitope. *J. Immunol.* 199, 1737–1747. <https://doi.org/10.4049/JIMMUNOL.1602115>
- Borsa, M., Barnstorf, I., Baumann, N.S., Pallmer, K., Yermanos, A., Gräbnitz, F., Barandun, N., Hausmann, A., Sandu, I., Barral, Y., Oxenius, A., 2019. Modulation of asymmetric cell division as a mechanism to boost CD8⁺ T cell memory. *Sci. Immunol.* 4. <https://doi.org/10.1126/SCIIMMUNOL.AAV1730>
- Bouvy, A.P., Kho, M.M.L., Klepper, M., Litjens, N.H.R., Betjes, M.G.H., Weimar, W., Baan, C.C., 2013. Kinetics of homeostatic proliferation and thymopoiesis after ratg induction therapy in kidney transplant patients. *Transplantation* 96, 904–913. <https://doi.org/10.1097/TP.0B013E3182A203E4>
- Bresser, K., Kok, L., Swain, A.C., King, L.A., Jacobs, L., Weber, T.S., Perié, L., Duffy, K.R.,

- de Boer, R.J., Scheeren, F.A., Schumacher, T.N., 2022. Replicative history marks transcriptional and functional disparity in the CD8+ T cell memory pool. *Nat. Immunol.* 23, 791–801. <https://doi.org/10.1038/S41590-022-01171-9>
- Brodin, P., Jovic, V., Gao, T., Bhattacharya, S., Angel, C.J.L., Furman, D., Shen-Orr, S., Dekker, C.L., Swan, G.E., Butte, A.J., Maecker, H.T., Davis, M.M., 2015. Variation in the human immune system is largely driven by non-heritable influences. *Cell* 160, 37–47. <https://doi.org/10.1016/J.CELL.2014.12.020>
- Buchholz, V.R., Flossdorf, M., Hensel, I., Kretschmer, L., Weissbrich, B., Gräf, P., Verschoor, A., Schiemann, M., Höfer, T., Busch, D.H., 2013. Disparate individual fates compose robust CD8+ T cell immunity. *Science (80-.)*. 340, 630–635. <https://doi.org/10.1126/science.1235454>
- Buchholz, V.R., Schumacher, T.N.M., Busch, D.H., 2016. T cell fate at the single-cell level. *Annu. Rev. Immunol.* 34, 65–92. <https://doi.org/10.1146/annurev-immunol-032414-112014>
- Butler, A., Hoffman, P., Smibert, P., Papalexi, E., Satija, R., 2018. Integrating single-cell transcriptomic data across different conditions, technologies, and species. *Nat. Biotechnol.* 36, 411–420. <https://doi.org/10.1038/nbt.4096>
- Caccamo, N., Meraviglia, S., Ferlazzo, V., Angelini, D., Borsellino, G., Poccia, F., Battistini, L., Dieli, F., Salerno, A., 2005. Differential requirements for antigen or homeostatic cytokines for proliferation and differentiation of human Vgamma9Vdelta2 naive, memory and effector T cell subsets. *Eur. J. Immunol.* 35, 1764–1772. <https://doi.org/10.1002/EJI.200525983>
- Callard, R.E., Stark, J., Yates, A.J., 2003. Fratricide: a mechanism for T memory-cell homeostasis. *Trends Immunol.* 24, 370–375. [https://doi.org/10.1016/S1471-4906\(03\)00164-9](https://doi.org/10.1016/S1471-4906(03)00164-9)
- Cannon, M.J., Schmid, D.S., Hyde, T.B., 2010. Review of cytomegalovirus seroprevalence and demographic characteristics associated with infection. *Rev. Med. Virol.* 20, 202–213. <https://doi.org/10.1002/RMV.655>
- Carey, A., Niedernhofer, L., Camell, C., 2022. Telomeres are a life-extending gift. *Nat. Cell Biol.* 2022 2410 24, 1449–1450. <https://doi.org/10.1038/s41556-022-01004-9>
- CARTWRIGHT, G.E., ATHENS, J.W., WINTROBE, M.M., 1964. Analytical Review: The Kinetics of Granulopoiesis in Normal Man. *Blood* 24, 780–803. <https://doi.org/10.1182/BLOOD.V24.6.780.780>
- Cendón, C., Du, W., Durek, P., Liu, Y.C., Alexander, T., Serene, L., Yang, X., Gasparoni, G., Salhab, A., Nordström, K., Lai, T., Schulz, A.R., Rao, A., Heinz, G.A., Stefanski, A.L., Claußnitzer, A., Siewert, K., Dörner, T., Chang, H.D., Volk, H.D., Romagnani, C., Qin, Z., Hardt, S., Perka, C., Reinke, S., Walter, J., Mashreghi, M.F., Thurley, K., Radbruch, A., Dong, J., 2022. Resident memory CD4+ T lymphocytes mobilize from bone marrow to contribute to a systemic secondary immune reaction. *Eur. J. Immunol.* 0, 1–16. <https://doi.org/10.1002/EJI.202149726>
- Chan, S.R.W.L., Blackburn, E.H., 2004. Telomeres and telomerase. *Philos. Trans. R. Soc. B Biol. Sci.* 359, 109. <https://doi.org/10.1098/RSTB.2003.1370>

- Chang, H.D., Radbruch, A., 2021. Maintenance of quiescent immune memory in the bone marrow. *Eur. J. Immunol.* 51, 1592–1601. <https://doi.org/10.1002/EJI.202049012>
- Chang, J.T., Palanivel, V.R., Kinjyo, I., Schambach, F., Intlekofer, A.M., Banerjee, A., Longworth, S.A., Vinup, K.E., Mrass, P., Oliaro, J., Killeen, N., Orange, J.S., Russell, S.M., Weninger, W., Reiner, S.L., 2007. Asymmetric T lymphocyte division in the initiation of adaptive immune responses. *Science* (80-.). 315, 1687–1691. https://doi.org/10.1126/SCIENCE.1139393/SUPPL_FILE/CHANG.SOM.PDF
- Chang, J.T., Wherry, E.J., Goldrath, A.W., 2014. Molecular regulation of effector and memory T cell differentiation. *Nat. Immunol.* 2014 1512 15, 1104–1115. <https://doi.org/10.1038/ni.3031>
- Cheung, T.H., Rando, T.A., 2013. Molecular regulation of stem cell quiescence. *Nat. Rev. Mol. Cell Biol.* 14, 329–340. <https://doi.org/10.1038/nrm3591>
- Chidrawar, S., Khan, N., Wei, W., McLarnon, A., Smith, N., Nayak, L., Moss, P., 2009. Cytomegalovirus-seropositivity has a profound influence on the magnitude of major lymphoid subsets within healthy individuals. *Clin. Exp. Immunol.* 155, 423–432. <https://doi.org/10.1111/J.1365-2249.2008.03785.X>
- Cho, B.K., Wang, C., Sugawa, S., Eisen, H.N., Chen, J., 1999. Functional differences between memory and naive CD8 T cells. *Proc. Natl. Acad. Sci. U. S. A.* 96, 2976–2981. <https://doi.org/10.1073/PNAS.96.6.2976/ASSET/E368D0E9-4C05-4C54-80A2-E14B0F97E368/ASSETS/GRAPHIC/PQ0690157005.JPEG>
- Choo, D.K., Murali-Krishna, K., Anita, R., Ahmed, R., 2010. Homeostatic turnover of virus-specific memory CD8 T cells occurs stochastically and is independent of CD4 T cell help. *J. Immunol.* 185, 3436–3444. <https://doi.org/10.4049/JIMMUNOL.1001421>
- Clayton, E., Doupé, D.P., Klein, A.M., Winton, D.J., Simons, B.D., Jones, P.H., 2007. A single type of progenitor cell maintains normal epidermis. *Nature* 446, 185–189. <https://doi.org/10.1038/nature05574>
- Crotty, S., Ahmed, R., 2004. Immunological memory in humans. *Semin. Immunol.* 16, 197–203. <https://doi.org/10.1016/j.smim.2004.02.008>
- Cui, G., Hara, T., Simmons, S., Wagatsuma, K., Abe, A., Miyachi, H., Kitano, S., Ishii, M., Tani-Ichi, S., Ikuta, K., 2014. Characterization of the IL-15 niche in primary and secondary lymphoid organs in vivo. *Proc. Natl. Acad. Sci. U. S. A.* 111, 1915–1920. <https://doi.org/10.1073/PNAS.1318281111/-/DCSUPPLEMENTAL>
- Cupovic, J., Ring, S.S., Onder, L., Colston, J.M., Lütge, M., Cheng, H.W., De Martin, A., Provine, N.M., Flatz, L., Oxenius, A., Scandella, E., Krebs, P., Engeler, D., Klenerman, P., Ludewig, B., 2021. Adenovirus vector vaccination reprograms pulmonary fibroblastic niches to support protective inflating memory CD8+ T cells. *Nat. Immunol.* 2021 228 22, 1042–1051. <https://doi.org/10.1038/s41590-021-00969-3>
- Davis, F.M., Lloyd-Lewis, B., Harris, O.B., Kozar, S., Winton, D.J., Muresan, L., Watson, C.J., 2016. Single-cell lineage tracing in the mammary gland reveals stochastic clonal dispersion of stem/progenitor cell progeny. *Nat. Commun.* 7. <https://doi.org/10.1038/ncomms13053>

- De Boer, R.J., Noest, A.J., 1998. T Cell Renewal Rates, Telomerase, and Telomere Length Shortening. *J. Immunol.* 160, 5832–5837.
<https://doi.org/10.4049/JIMMUNOL.160.12.5832>
- De Boer, R.J., Perelson, A.S., 2013a. Quantifying T Lymphocyte Turnover. *J. Theor. Biol.* 327, 45. <https://doi.org/10.1016/J.JTBI.2012.12.025>
- De Boer, R.J., Perelson, A.S., 2013b. Antigen-stimulated CD4 T cell expansion can be limited by their grazing of peptide-MHC complexes. *J. Immunol.* 190, 5454–5458.
<https://doi.org/10.4049/JIMMUNOL.1203569>
- De Boer, R.J., Perelson, A.S., 1994. T cell repertoires and competitive exclusion. *J. Theor. Biol.* 169, 375–390. <https://doi.org/10.1006/JTBI.1994.1160>
- De Boer, R.J., Perelson, A.S., Ribeiro, R.M., 2012. Modelling deuterium labelling of lymphocytes with temporal and/or kinetic heterogeneity. *J. R. Soc. Interface.*
<https://doi.org/10.1098/rsif.2012.0149>
- De Boer R.J., N.A., 1998. T cell renewal rates, telomerase, and telomere length shortening. *J Immunol.*
- Dekhtiarenko, I., Jarvis, M.A., Ruzsics, Z., Čičin-Šain, L., 2013. The context of gene expression defines the immunodominance hierarchy of cytomegalovirus antigens. *J. Immunol.* 190, 3399–3409. <https://doi.org/10.4049/JIMMUNOL.1203173>
- del Amo, P.C., Beneytez, J.L., Boelen, L., Ahmed, R., Miners, K.L., Zhang, Y., Roger, L., Jones, R.E., Marraco, S.A.F., Speiser, D.E., Baird, D.M., Price, D.A., Ladell, K., Macallan, D., Asquith, B., 2018. Human TSCM cell dynamics in vivo are compatible with long-lived immunological memory and stemness. *PLoS Biol.* 16.
<https://doi.org/10.1371/JOURNAL.PBIO.2005523>
- den Braber, I., Mugwagwa, T., Vrisekoop, N., Westera, L., Mögling, R., Bregje de Boer, A., Willems, N., Schrijver, E.H.R., Spierenburg, G., Gaiser, K., Mul, E., Otto, S.A., Ruiter, A.F.C., Ackermans, M.T., Miedema, F., Borghans, J.A.M., de Boer, R.J., Tesselaar, K., 2012. Maintenance of Peripheral Naive T Cells Is Sustained by Thymus Output in Mice but Not Humans. *Immunity* 36, 288–297.
<https://doi.org/10.1016/J.IMMUNI.2012.02.006>
- Derhovanessian, E., Larbi, A., Pawelec, G., 2009. Biomarkers of human immunosenescence: impact of Cytomegalovirus infection. *Curr. Opin. Immunol.* 21, 440–445.
<https://doi.org/10.1016/J.COI.2009.05.012>
- Di Rosa, F., 2016a. Two Niches in the Bone Marrow: A Hypothesis on Life-long T Cell Memory. *Trends Immunol.* 37, 503–512. <https://doi.org/10.1016/J.IT.2016.05.004>
- Di Rosa, F., 2016b. Maintenance of memory T cells in the bone marrow: survival or homeostatic proliferation? *Nat. Rev. Immunol.* 2016 164 16, 271–271.
<https://doi.org/10.1038/nri.2016.31>
- DiLoreto, R., Murphy, C.T., 2015. The cell biology of aging. *Mol. Biol. Cell* 26, 4524.
<https://doi.org/10.1091/MBC.E14-06-1084>
- Escobar, G., Mangani, D., Anderson, A.C., 2020. T cell factor 1 (Tcf1): a master regulator of the T cell response in disease. *Sci. Immunol.* 5.

<https://doi.org/10.1126/SCIIMMUNOL.ABB9726>

- Esser, M.T., Marchese, R.D., Kierstead, L.S., Tussey, L.G., Wang, F., Chirmule, N., Washabaugh, M.W., 2003. Memory T cells and vaccines. *Vaccine* 21, 419–430. [https://doi.org/10.1016/S0264-410X\(02\)00407-3](https://doi.org/10.1016/S0264-410X(02)00407-3)
- Fehniger, T.A., Caligiuri, M.A., 2001. Interleukin 15: biology and relevance to human disease. *Blood* 97, 14–32. <https://doi.org/10.1182/BLOOD.V97.1.14>
- Ferrando-Martínez, S., Ruiz-Mateos, E., Hernández, A., Gutiérrez, E., Rodríguez-Méndez, M.D.M., Ordoñez, A., Leal, M., 2011. Age-related deregulation of naive T cell homeostasis in elderly humans. *Age (Dordr)*. 33, 197–207. <https://doi.org/10.1007/S11357-010-9170-8>
- Fraser, K.A., Schenkel, J.M., Jameson, S.C., Vezys, V., Masopust, D., 2013. Preexisting high frequencies of memory CD8+ T cells favors rapid memory differentiation and preservation of proliferative potential upon boosting. *Immunity* 39, 171. <https://doi.org/10.1016/J.IMMUNI.2013.07.003>
- Freitas, A.A., Rocha, B., 2000. Population biology of lymphocytes: the flight for survival. *Annu. Rev. Immunol.* 18, 83–111. <https://doi.org/10.1146/ANNUREV.IMMUNOL.18.1.83>
- Fung, H.Y., Teryek, M., Lemenze, A.D., Bergsbaken, T., 2022. CD103 fate mapping reveals that intestinal CD103- tissue-resident memory T cells are the primary responders to secondary infection. *Sci. Immunol.* 7. https://doi.org/10.1126/SCIIMMUNOL.ABL9925/SUPPL_FILE/SCIIMMUNOL.ABL9925_TABLE_S1.ZIP
- Gaimann, M.U., Nguyen, M., Desponds, J., Mayer, A., 2020. Early life imprints the hierarchy of T cell clone sizes. *Elife* 9, 1–36. <https://doi.org/10.7554/ELIFE.61639>
- Ganusov, V. V., Borghans, J.A.M., De Boer, R.J., 2010. Explicit kinetic heterogeneity: Mathematical models for interpretation of deuterium labeling of heterogeneous cell populations. *PLoS Comput. Biol.* <https://doi.org/10.1371/journal.pcbi.1000666>
- Gao, J., Zhao, L., Wan, Y.Y., Zhu, B., 2015. Mechanism of Action of IL-7 and Its Potential Applications and Limitations in Cancer Immunotherapy. *Int. J. Mol. Sci.* 2015, Vol. 16, Pages 10267-10280 16, 10267–10280. <https://doi.org/10.3390/IJMS160510267>
- Gattinoni, L., Lugli, E., Ji, Y., Pos, Z., Paulos, C.M., Quigley, M.F., Almeida, J.R., Gostick, E., Yu, Z., Carpenito, C., Wang, E., Douek, D.C., Price, D.A., June, C.H., Marincola, F.M., Roederer, M., Restifo, N.P., 2011. A human memory T cell subset with stem cell-like properties. *Nat. Med.* 2011 1710 17, 1290–1297. <https://doi.org/10.1038/nm.2446>
- Gattinoni, L., Zhong, X.S., Palmer, D.C., Ji, Y., Hinrichs, C.S., Yu, Z., Wrzesinski, C., Boni, A., Cassard, L., Garvin, L.M., Paulos, C.M., Muranski, P., Restifo, N.P., 2009. Wnt signaling arrests effector T cell differentiation and generates CD8+ memory stem cells. *Nat. Med.* 15, 808–813. <https://doi.org/10.1038/nm.1982>
- Geginat, J., Lanzavecchia, A., Sallusto, F., 2003. Proliferation and differentiation potential of human CD8+ memory T-cell subsets in response to antigen or homeostatic cytokines. *Blood* 101, 4260–4266. <https://doi.org/10.1182/BLOOD-2002-11-3577>

- Gerlach, C., Moseman, E.A., Loughhead, S.M., Alvarez, D., Zwijnenburg, A.J., Waanders, L., Garg, R., de la Torre, J.C., von Andrian, U.H., 2016. The Chemokine Receptor CX3CR1 Defines Three Antigen-Experienced CD8 T Cell Subsets with Distinct Roles in Immune Surveillance and Homeostasis. *Immunity* 45, 1270–1284. <https://doi.org/10.1016/J.IMMUNI.2016.10.018>
- Gerlach, C., Rohr, J.C., Perié, L., Van Rooij, N., Van Heijst, J.W.J., Velds, A., Urbanus, J., Naik, S.H., Jacobs, H., Beltman, J.B., De Boer, R.J., Schumacher, T.N.M., 2013. Heterogeneous differentiation patterns of individual CD8+ T cells. *Science (80-.)*. 340, 635–639. <https://doi.org/10.1126/science.1235487>
- Gershon, R.K., Krüger, J., Naysmith, J.D., Waksman, B.H., 1971. Cellular Basis for Immunologic Memory. *Nat.* 1971 2325313 232, 639–641. <https://doi.org/10.1038/232639b0>
- Gonzalez, N.M., Zou, D., Gu, A., Chen, W., 2021. Schrödinger’s T Cells: Molecular Insights Into Stemness and Exhaustion. *Front. Immunol.* 12, 3480. <https://doi.org/10.3389/FIMMU.2021.725618/BIBTEX>
- Goronzy, J.J., Fujii, H., Weyand, C.M., 2006. Telomeres, immune aging and autoimmunity. *Exp. Gerontol.* 41, 246–251. <https://doi.org/10.1016/j.exger.2005.12.002>
- Goronzy, J.J., Weyand, C.M., 2019. Mechanisms underlying T cell ageing. *Nat. Rev. Immunol.* 19, 573. <https://doi.org/10.1038/S41577-019-0180-1>
- Goronzy, J.J., Weyand, C.M., 2013. Understanding immunosenescence to improve responses to vaccines. *Nat. Immunol.* 14, 428–436. <https://doi.org/10.1038/NI.2588>
- Gossel, G., Hogan, T., Cownden, D., Seddon, B., Yates, A.J., 2017. Memory CD4 T cell subsets are kinetically heterogeneous and replenished from naive T cells at high levels. *Elife* 6. <https://doi.org/10.7554/ELIFE.23013>
- Gowans, J.L., Uhr, J.W., 1966. THE CARRIAGE OF IMMUNOLOGICAL MEMORY BY SMALL LYMPHOCYTES IN THE RAT. *J. Exp. Med.* 124, 1017. <https://doi.org/10.1084/JEM.124.5.1017>
- Graef, P., Buchholz, V.R., Stemberger, C., Flossdorf, M., Henkel, L., Schiemann, M., Drexler, I., Höfer, T., Riddell, S.R., Busch, D.H., 2014. Serial transfer of single-cell-derived immunocompetence reveals stemness of CD8+ central memory T cells. *Immunity* 41, 116–126. <https://doi.org/10.1016/j.immuni.2014.05.018>
- Grassmann, S., Mihatsch, L., Mir, J., Kazerooni, A., Rahimi, R., Flommersfeld, S., Schober, K., Hensel, I., Leube, J., Pachmayr, L.O., Kretschmer, L., Zhang, Q., Jolly, A., Chaudhry, M.Z., Schiemann, M., Cicin-Sain, L., Höfer, T., Busch, D.H., Flossdorf, M., Buchholz, V.R., 2020. Early emergence of T central memory precursors programs clonal dominance during chronic viral infection. *Nat. Immunol.* 21, 1563–1573. <https://doi.org/10.1038/S41590-020-00807-Y>
- Gratzner, H.G., 1982. Monoclonal antibody to 5-bromo- and 5-iododeoxyuridine: A new reagent for detection of DNA replication. *Science* 218, 474–475. <https://doi.org/10.1126/SCIENCE.7123245>
- Gray, D., Matzinger, P., 1991. T cell memory is short-lived in the absence of antigen. *J. Exp.*

- Med. 174, 969–974. <https://doi.org/10.1084/JEM.174.5.969>
- Hahne, F., LeMeur, N., Brinkman, R.R., Ellis, B., Haaland, P., Sarkar, D., Spidlen, J., Strain, E., Gentleman, R., 2009. flowCore: a Bioconductor package for high throughput flow cytometry. *BMC Bioinforma.* 10. <https://doi.org/10.1186/1471-2105-10-106>
- Handbook of Immunosenescence, 2020. . *Handb. Immunosenescence.* <https://doi.org/10.1007/978-3-319-64597-1>
- Hashimoto, M., Im, S.J., Araki, K., Ahmed, R., 2019. Cytokine-Mediated Regulation of CD8 T-Cell Responses During Acute and Chronic Viral Infection. *Cold Spring Harb. Perspect. Biol.* 11, a028464. <https://doi.org/10.1101/CSHPERSPECT.A028464>
- Hayflick, L., 1965. The limited in vitro lifetime of human diploid cell strains. *Exp. Cell Res.* 37, 614–636. [https://doi.org/10.1016/0014-4827\(65\)90211-9](https://doi.org/10.1016/0014-4827(65)90211-9)
- Hayflick, L., Moorhead, P.S., 1961. The serial cultivation of human diploid cell strains. *Exp. Cell Res.* 25, 585–621. [https://doi.org/10.1016/0014-4827\(61\)90192-6](https://doi.org/10.1016/0014-4827(61)90192-6)
- Haynes, L., Swain, S.L., 2012. Aged-related shifts in T cell homeostasis lead to intrinsic T cell defects. *Semin. Immunol.* 24, 350–355. <https://doi.org/10.1016/J.SMIM.2012.04.001>
- Hellerstein, M., Hanley, M.B., Cesar, D., Siler, S., Papageorgopoulos, C., Wieder, E., Schmidt, D., Hoh, R., Neese, R., Macallan, D., Deeks, S., McCune, J.M., 1999. Directly measured kinetics of circulating T lymphocytes in normal and HIV-1-infected humans. *Nat. Med.* 1999 51 5, 83–89. <https://doi.org/10.1038/4772>
- Hellerstein, M.K., Hoh, R.A., Hanley, M.B., Cesar, D., Lee, D., Neese, R.A., McCune, J.M., 2003. Subpopulations of long-lived and short-lived T cells in advanced HIV-1 infection. *J. Clin. Invest.* 112, 956–966. <https://doi.org/10.1172/JCI17533>
- Hellerstein, M.K., Neese, R.A., 1992. Mass isotopomer distribution analysis: a technique for measuring biosynthesis and turnover of polymers. <https://doi.org/10.1152/ajpendo.1992.263.5.E988> 263. <https://doi.org/10.1152/AJPENDO.1992.263.5.E988>
- Henning, A.N., Roychoudhuri, R., Restifo, N.P., 2018. Epigenetic control of CD8+ T cell differentiation. *Nat. Rev. Immunol.* 18, 340–356. <https://doi.org/10.1038/NRI.2017.146>
- Herndler-Brandstetter, D., Ishigame, H., Shinnakasu, R., Plajer, V., Stecher, C., Zhao, J., Lietzenmayer, M., Kroehling, L., Takumi, A., Kometani, K., Inoue, T., Kluger, Y., Kaech, S.M., Kurosaki, T., Okada, T., Flavell, R.A., 2018. KLRG1+ effector CD8+ T Cells lose KLRG1, differentiate into all memory T cell lineages, and convey enhanced protective immunity. *Immunity* 48, 716–729. <https://doi.org/10.1016/j.immuni.2018.03.015>
- Hinrichs, C.S., Borman, Z.A., Cassard, L., Gattinoni, L., Spolski, R., Zhiya, Y., Sanchez-Perez, L., Muranski, P., Kern, S.J., Logun, C., Palmer, D.C., Yun, J., Reger, R.N., Leonard, W.J., Danner, R.L., Rosenberg, S.A., Restifo, N.P., 2009. Adoptively transferred effector cells derived from naive rather than central memory CD8+ T cells mediate superior antitumor immunity. *Proc. Natl. Acad. Sci. U. S. A.* 106, 17469–17474. <https://doi.org/10.1073/PNAS.0907448106>

- Hogan, T., Nowicka, M., Cownden, D., Pearson, C., Yates, A.J., Seddon, B., 2019. Differential impact of self and environmental antigens on the ontogeny and maintenance of CD4⁺ T cell memory. *Elife* 8. <https://doi.org/10.7554/ELIFE.48901>
- Hogan, T., Shuvaev, A., Commenges, D., Yates, A., Callard, R., Thiebaut, R., Seddon, B., 2013. Clonally Diverse T Cell Homeostasis Is Maintained by a Common Program of Cell-Cycle Control. *J. Immunol.* 190, 3985–3993. <https://doi.org/10.4049/JIMMUNOL.1203213>
- Hogan, T., Yates, A., Seddon, B., 2017. Analysing Temporal Dynamics of T Cell Division in vivo Using Ki67 and BrdU Co-labelling by Flow Cytometry. *Bio-protocol* 7. <https://doi.org/10.21769/BIOPROTOCOL.2649>
- Huster, K.M., Stemberger, C., Gasteiger, G., Kastenmüller, W., Drexler, I., Busch, D.H., 2009. Cutting Edge: Memory CD8 T Cell Compartment Grows in Size with Immunological Experience but Nevertheless Can Lose Function. *J. Immunol.* 183, 6898–6902. <https://doi.org/10.4049/JIMMUNOL.0902454>
- Hwang, L.N., Yu, Z., Palmer, D.C., Restifo, N.P., 2006. The in vivo expansion rate of properly stimulated transferred CD8⁺ T cells exceeds that of an aggressively growing mouse tumor. *Cancer Res.* 66, 1132–1138. <https://doi.org/10.1158/0008-5472.can-05-1679>
- Ito, M., Liu, Y., Yang, Z., Nguyen, J., Liang, F., Morris, R.J., Cotsarelis, G., 2005. Stem cells in the hair follicle bulge contribute to wound repair but not to homeostasis of the epidermis. *Nat. Med.* 11, 1351–1354. <https://doi.org/10.1038/nm1328>
- Johnnidis, J.B., Muroyama, Y., Ngiow, S.F., Chen, Z., Manne, S., Cai, Z., Song, S., Platt, J.M., Schenkel, J.M., Abdel-Hakeem, M., Beltra, J.C., Greenplate, A.R., Ali, M.A.A., Nzingha, K., Giles, J.R., Harly, C., Attanasio, J., Pauken, K.E., Bengsch, B., Paley, M.A., Tomov, V.T., Kurachi, M., Vignali, D.A.A., Sharpe, A.H., Reiner, S.L., Bhandoola, A., Johnson, F.B., Wherry, E.J., 2021. Inhibitory signaling sustains a distinct early memory CD8⁺ T cell precursor that is resistant to DNA damage. *Sci. Immunol.* 6, eabe3702. <https://doi.org/10.1126/sciimmunol.abe3702>
- Kaech, S.M., Wherry, E.J., Ahmed, R., 2002. Effector and memory T-cell differentiation: implications for vaccine development. *Nat. Rev. Immunol.* 2002 24 2, 251–262. <https://doi.org/10.1038/nri778>
- Kalia, V., Sarkar, S., Ahmed, R., 2013. CD8 T-Cell Memory Differentiation during Acute and Chronic Viral Infections.
- Kalia, V., Sarkar, S., Gourley, T.S., Rouse, B.T., Ahmed, R., 2006. Differentiation of memory B and T cells. *Curr. Opin. Immunol.* 18, 255–264. <https://doi.org/10.1016/J.COI.2006.03.020>
- Kallert, S.M., Darbre, S., Bonilla, W. V., Kreutzfeldt, M., Page, N., Müller, P., Kreuzaler, M., Lu, M., Favre, S., Kreppel, F., Löhning, M., Luther, S.A., Zippelius, A., Merkler, D., Pinschewer, D.D., 2017. Replicating viral vector platform exploits alarmin signals for potent CD8⁺ T cell-mediated tumour immunotherapy. *Nat. Commun.* 8. <https://doi.org/10.1038/ncomms15327>
- Karrer, U., Sierro, S., Wagner, M., Oxenius, A., Hengel, H., Koszinowski, U.H., Phillips,

- R.E., Klenerman, P., 2003. Memory inflation: continuous accumulation of antiviral CD8⁺ T cells over time. *J. Immunol.* 170, 2022–2029. <https://doi.org/10.4049/JIMMUNOL.170.4.2022>
- Kedl, R.M., Rees, W.A., Hildeman, D.A., Schaefer, B., Mitchell, T., Kappler, J., Marrack, P., 2000. T Cells Compete for Access to Antigen-Bearing Antigen-Presenting Cells. *J. Exp. Med.* 192, 1105. <https://doi.org/10.1084/JEM.192.8.1105>
- Kim, J., Kim, A.-R., Shin, E.-C., 2015. Cytomegalovirus Infection and Memory T Cell Inflation. *Immune Netw.* 15, 186. <https://doi.org/10.4110/IN.2015.15.4.186>
- Kim, S.-K., Welsh, R.M., 2004. Comprehensive early and lasting loss of memory CD8 T cells and functional memory during acute and persistent viral infections. *J. Immunol.* 172, 3139–3150. <https://doi.org/10.4049/JIMMUNOL.172.5.3139>
- Kinjyo, I., Qin, J., Tan, S.Y., Wellard, C.J., Mrass, P., Ritchie, W., Doi, A., Cavanagh, L.L., Tomura, M., Sakaue-Sawano, A., Kanagawa, O., Miyawaki, A., Hodgkin, P.D., Weninger, W., 2015. Real-time tracking of cell cycle progression during CD8⁺ effector and memory T-cell differentiation. *Nat. Commun.* 6. <https://doi.org/10.1038/ncomms7301>
- Klenerman, P., Oxenius, A., 2016. T cell responses to cytomegalovirus. *Nat. Rev. Immunol.* 16, 367–377. <https://doi.org/10.1038/NRI.2016.38>
- Kok, L., Dijkgraaf, F.E., Urbanus, J., Bresser, K., Vredevoogd, D.W., Cardoso, R.F., Perić, L., Beltman, J.B., Schumacher, T.N., 2020. A committed tissue-resident memory T cell precursor within the circulating CD8⁺ effector T cell pool. *J. Exp. Med.* 217. <https://doi.org/10.1084/JEM.20191711>
- Koole, W., Schäfer, H.S., Agami, R., Van Haften, G., Tijsterman, M., 2013. A versatile microsatellite instability reporter system in human cells. *Nucleic Acids Res.* 41, e158–e158. <https://doi.org/10.1093/nar/gkt615>
- Korotkevich, G., Sukhov, V., Budin, N., Shpak, B., Artyomov, M.N., Sergushichev, A., 2021. Fast gene set enrichment analysis. *bioRxiv* 060012. <https://doi.org/10.1101/060012>
- Kozar, S., Morrissey, E., Nicholson, A.M., van der Heijden, M., Zecchini, H.I., Kemp, R., Tavaré, S., Vermeulen, L., Winton, D.J., 2013. Continuous clonal labeling reveals small numbers of functional stem cells in intestinal crypts and adenomas. *Cell Stem Cell* 13, 626–633. <https://doi.org/10.1016/j.stem.2013.08.001>
- Kratchmarov, R., Magun, A.M., Reiner, S.L., 2018. TCF1 expression marks self-renewing human CD8⁺ T cells. *Blood Adv.* 2, 1685–1690. <https://doi.org/10.1182/BLOODADVANCES.2018016279>
- Kretschmer, L., Flossdorf, M., Mir, J., Cho, Y.L., Plambeck, M., Treise, I., Toska, A., Heinzl, S., Schiemann, M., Busch, D.H., Buchholz, V.R., 2020. Differential expansion of T central memory precursor and effector subsets is regulated by division speed. *Nat. Commun.* 11. <https://doi.org/10.1038/s41467-019-13788-w>
- Krishnamurty, A.T., Turley, S.J., 2020. Lymph node stromal cells: cartographers of the immune system. *Nat. Immunol.* 2020 214 21, 369–380. <https://doi.org/10.1038/s41590->

020-0635-3

- Ku, C.-C., Kappler, J., Marrack, P., 2001. The growth of the very large CD8⁺ T cell clones in older mice is controlled by cytokines. *J. Immunol.* 166, 2186–2193.
<https://doi.org/10.4049/JIMMUNOL.166.4.2186>
- Ku, C.C., Murakami, M., Sakamoto, A., Kappler, J., Marrack, P., 2000. Control of Homeostasis of CD8⁺ Memory T Cells by Opposing Cytokines. *Science* (80-). 288, 675–678. <https://doi.org/10.1126/SCIENCE.288.5466.675>
- Kurd, N.S., He, Z., Louis, T.L., Milner, J.J., Omilusik, K.D., Jin, W., Tsai, M.S., Widjaja, C.E., Kanbar, J.N., Olvera, J.G., Tysl, T., Quezada, L.K., Boland, B.S., Huang, W.J., Murre, C., Goldrath, A.W., Yeo, G.W., Chang, J.T., 2020. Early precursors and molecular determinants of tissue-resident memory CD8⁺ T lymphocytes revealed by single-cell RNA sequencing. *Sci. Immunol.* 5, eaaz6894.
<https://doi.org/10.1126/sciimmunol.aaz6894>
- Lahoz-Beneytez, J., Elemans, M., Zhang, Y., Ahmed, R., Salam, A., Block, M., Niederaalt, C., Asquith, B., Macallan, D., 2016. Human neutrophil kinetics: modeling of stable isotope labeling data supports short blood neutrophil half-lives. *Blood* 127, 3431.
<https://doi.org/10.1182/BLOOD-2016-03-700336>
- Lai, Y., Sun, F., 2003. The relationship between microsatellite slippage mutation rate and the number of repeat units. *Mol. Biol. Evol.* 20, 2123–2131.
<https://doi.org/10.1093/molbev/msg228>
- Lander, A.D., Gokoffski, K.K., Wan, F.Y.M., Nie, Q., Calof, A.L., 2009. Cell lineages and the logic of proliferative control. *PLoS Biol.* 7.
<https://doi.org/10.1371/JOURNAL.PBIO.1000015>
- Lanfermeijer, J., Borghans, J.A.M., van Baarle, D., 2020. How age and infection history shape the antigen-specific CD8⁺ T-cell repertoire: Implications for vaccination strategies in older adults. *Aging Cell* 19. <https://doi.org/10.1111/ACEL.13262>
- Lanfermeijer, J., de Greef, P.C., Hendriks, M., Vos, M., van Beek, J., Borghans, J.A.M., van Baarle, D., 2021. Age and CMV-Infection Jointly Affect the EBV-Specific CD8⁺ T-Cell Repertoire. *Front. Aging* 2, 11. <https://doi.org/10.3389/FRAGI.2021.665637>
- Lanna, A., Vaz, B., D'Ambra, C., Valvo, S., Vuotto, C., Chiurchiù, V., Devine, O., Sanchez, M., Borsellino, G., Akbar, A.N., De Bardi, M., Gilroy, D.W., Dustin, M.L., Blumer, B., Karin, M., 2022. An intercellular transfer of telomeres rescues T cells from senescence and promotes long-term immunological memory. *Nat. Cell Biol.* 2022 2410 24, 1461–1474. <https://doi.org/10.1038/s41556-022-00991-z>
- Laurenti, E., Frelin, C., Xie, S., Ferrari, R., Dunant, C.F., Zandi, S., Neumann, A., Plumb, I., Doulatov, S., Chen, J., April, C., Fan, J.B., Iscove, N., Dick, J.E., 2015. CDK6 levels regulate quiescence exit in human hematopoietic stem cells. *Cell Stem Cell* 16, 302–313. <https://doi.org/10.1016/j.stem.2015.01.017>
- Leube, J., Mühlbauer, A., Andrä, I., Biggel, M., Busch, D.H., Kretschmer, L., Buchholz, V.R., 2022. Single-cell fate mapping reveals widespread clonal ignorance of low-affinity T cells exposed to systemic infection. *Eur. J. Immunol.*
<https://doi.org/10.1002/EJI.202250009>

- Lin, W.H.W., Nish, S.A., Yen, B., Chen, Y.H., Adams, W.C., Kratchmarov, R., Rothman, N.J., Bhandoola, A., Xue, H.H., Reiner, S.L., 2016. CD8⁺ T lymphocyte self-renewal during effector cell determination. *Cell Rep.* 17, 1773–1782. <https://doi.org/10.1016/j.celrep.2016.10.032>
- Loewendorf, A.I., Arens, R., Purton, J.F., Surh, C.D., Benedict, C.A., 2011. Dissecting the Requirements for Maintenance of the CMV-Specific Memory T-Cell Pool. *Viral Immunol.* 24, 351. <https://doi.org/10.1089/VIM.2010.0140>
- Lymphocyte dynamics in healthy and lymphopenic conditions (2015) | www.narcis.nl [WWW Document], n.d. URL [https://www.narcis.nl/publication/RecordID/oai%3Adspace.library.uu.nl%3A1874%2F320830/uquery/lymphocyte dynamics in healthy and lymphopenic conditions/id/1/Language/EN](https://www.narcis.nl/publication/RecordID/oai%3Adspace.library.uu.nl%3A1874%2F320830/uquery/lymphocyte+dynamics+in+healthy+and+lymphopenic+conditions/id/1/Language/EN) (accessed 2.9.23).
- Macallan, D.C., Asquith, B., Irvine, A.J., Wallace, D.L., Worth, A., Ghattas, H., Zhang, Y., Griffin, G.E., Tough, D.F., Beverley, P.C., 2003. Measurement and modeling of human T cell kinetics. *Eur. J. Immunol.* 33, 2316–2326. <https://doi.org/10.1002/EJI.200323763>
- Macallan, D.C., Asquith, B., Zhang, Y., de Lara, C., Ghattas, H., Defoiche, J., Beverley, P.C.L., 2009. Measurement of proliferation and disappearance of rapid turnover cell populations in human studies using deuterium-labeled glucose. *Nat. Protoc.* 4, 1313–1327. <https://doi.org/10.1038/nprot.2009.117>
- Macallan, D.C., Borghans, J.A.M., Asquith, B., 2017. Human T Cell Memory: A Dynamic View. *Vaccines* 5. <https://doi.org/10.3390/VACCINES5010005>
- Macallan, D.C., Busch, R., Asquith, B., 2019. Current estimates of T cell kinetics in humans. *Curr. Opin. Syst. Biol.* <https://doi.org/10.1016/j.coisb.2019.10.002>
- Macallan, D.C., Fullerton, C.A., Neese, R.A., Haddock, K., Park, S.S., Hellerstein, M.K., 1998. Measurement of cell proliferation by labeling of DNA with stable isotope-labeled glucose: Studies in vitro, in animals, and in humans. *Proc. Natl. Acad. Sci. U. S. A.* 95, 708–713. <https://doi.org/10.1073/PNAS.95.2.708>
- Macallan, D.C., Wallace, D., Zhang, Y., De Lara, C., Worth, A.T., Ghattas, H., Griffin, G.E., Beverley, P.C.L., Tough, D.F., 2004. Rapid turnover of effector-memory CD4(+) T cells in healthy humans. *J. Exp. Med.* 200, 255–260. <https://doi.org/10.1084/JEM.20040341>
- Madisen, L., Zwingman, T.A., Sunkin, S.M., Oh, S.W., Zariwala, H.A., Gu, H., Ng, L.L., Palmiter, R.D., Hawrylycz, M.J., Jones, A.R., Lein, E.S., Zeng, H., 2010. A robust and high-throughput Cre reporting and characterization system for the whole mouse brain. *Nat. Neurosci.* 13, 133–140. <https://doi.org/10.1038/nn.2467>
- Marandu, T.F., Oduro, J.D., Borkner, L., Dekhtiarenko, I., Uhrlaub, J.L., Drabig, A., Kröger, A., Nikolich-Zugich, J., Cicin-Sain, L., 2015. Immune Protection against Virus Challenge in Aging Mice Is Not Affected by Latent Herpesviral Infections. *J. Virol.* 89, 11715–11717. <https://doi.org/10.1128/JVI.01989-15>
- Marchingo, J.M., Prevedello, G., Kan, A., Heinzl, S., Hodgkin, P.D., Duffy, K.R., 2016. T-cell stimuli independently sum to regulate an inherited clonal division fate. *Nat. Commun.* 2016 71 7, 1–12. <https://doi.org/10.1038/ncomms13540>

- Masopust, D., Ha, S.-J., Vezys, V., Ahmed, R., 2006. Stimulation history dictates memory CD8 T cell phenotype: implications for prime-boost vaccination. *J. Immunol.* 177, 831–839. <https://doi.org/10.4049/JIMMUNOL.177.2.831>
- Mayer, A., Zhang, Y., Perelson, A.S., Wingreen, N.S., 2019. Regulation of T cell expansion by antigen presentation dynamics. *Proc. Natl. Acad. Sci. U. S. A.* 116, 5914–5919. <https://doi.org/10.1073/PNAS.1812800116>
- Mays Hoopes, L.L., 2010. Aging, Cell Division | Learn Science at Scitable [WWW Document]. Mays Hoopes, L. L. *Aging Cell Div. Nat. Educ.* 3(9)55. URL <https://www.nature.com/scitable/topicpage/aging-and-cell-division-14230076/> (accessed 11.23.21).
- Michie, C.A., McLean, A., Alcock, C., Beverley, P.C.L., 1992. Lifespan of human lymphocyte subsets defined by CD45 isoforms. *Nature* 360, 264–265. <https://doi.org/10.1038/360264A0>
- Miles, D.J.C., Sanneh, M., Holder, B., Crozier, S., Nyamweya, S., Touray, E.S., Palmero, M.S., Zaman, S.M.A., Rowland-Jones, S., Van Der Sande, M., Whittle, H., 2008. Cytomegalovirus infection induces T-cell differentiation without impairing antigen-specific responses in Gambian infants. *Immunology* 124, 388. <https://doi.org/10.1111/J.1365-2567.2007.02787.X>
- Miller, J.F.A.P., Sprent, J., 1971. CELL-TO-CELL INTERACTION IN THE IMMUNE RESPONSE VI. CONTRIBUTION OF THYMUS-DERIVED CELLS AND ANTIBODY-FORMING CELL PRECURSORS TO IMMUNOLOGICAL MEMORY. *J. Exp. Med.* 134, 66–82. <https://doi.org/10.1084/JEM.134.1.66>
- Minervina, A.A., Pogorelyy, M. V., Kirk, A.M., Crawford, J.C., Allen, E.K., Chou, C.H., Mettelman, R.C., Allison, K.J., Lin, C.Y., Brice, D.C., Zhu, X., Vegesana, K., Wu, G., Trivedi, S., Kottapalli, P., Darnell, D., McNeely, S., Olsen, S.R., Schultz-Cherry, S., Estep, J.H., Gaur, A., Hoffman, J., Mori, M., Tang, L., Tuomanen, E., Webby, R., Hakim, H., Hayden, R.T., Hijano, D.R., Bajracharya, R., Awad, W., Van de Velde, L.A., Clark, B.L., Wilson, T.L., Souquette, A., Castellaw, A., Dallas, R.H., Hodges, J., Gowen, A., Russell-Bell, J., Sparks, J., Wittman, D.E., Fabrizio, T.P., Cherry, S., Roubidoux, E.K., Cortez, V., Freiden, P., Wohlgemuth, N., Whitt, K., McGargill, M.A., Wolf, J., Thomas, P.G., 2022. SARS-CoV-2 antigen exposure history shapes phenotypes and specificity of memory CD8⁺ T cells. *Nat. Immunol.* 23, 781–790. <https://doi.org/10.1038/S41590-022-01184-4>
- Mitrović, M., Arapović, J., Jordan, S., Fodil-Cornu, N., Ebert, S., Vidal, S.M., Krmpotić, A., Reddehase, M.J., Jonjić, S., 2012. The NK cell response to mouse cytomegalovirus infection affects the level and kinetics of the early CD8(+) T-cell response. *J. Virol.* 86, 2165–2175. <https://doi.org/10.1128/JVI.06042-11>
- Mittelbrunn, M., Kroemer, G., 2021. Hallmarks of T cell aging. *Nat. Immunol.* 2021 226 22, 687–698. <https://doi.org/10.1038/s41590-021-00927-z>
- Mogilenko, D.A., Shchukina, I., Artyomov, M.N., 2021. Immune ageing at single-cell resolution. *Nat. Rev. Immunol.* 2021 1–15. <https://doi.org/10.1038/s41577-021-00646-4>
- Mohri, H., Perelson, A.S., Tung, K., Ribeiro, R.M., Ramratnam, B., Markowitz, M., Kost, R., Hurley, A., Weinberger, L., Cesar, D., Hellerstein, M.K., Ho, D.D., 2001. Increased

- turnover of T lymphocytes in HIV-1 infection and its reduction by antiretroviral therapy. *J. Exp. Med.* <https://doi.org/10.1084/jem.194.9.1277>
- Mugwagwa, T., 2010. Quantification of T cell dynamics in health and disease. PhD Thesis.
- Munks, M.W., Cho, K.S., Pinto, A.K., Sierro, S., Klenerman, P., Hill, A.B., 2006. Four distinct patterns of memory CD8 T cell responses to chronic murine cytomegalovirus infection. *J. Immunol.* 177, 450–458. <https://doi.org/10.4049/JIMMUNOL.177.1.450>
- Murali-Krishna, K., Lau, L.L., Sambhara, S., Lemonnier, F., Altman, J., Ahmed, R., 1999. Persistence of Memory CD8 T Cells in MHC Class I-Deficient Mice. *Science* (80-.). 286, 1377–1381. <https://doi.org/10.1126/SCIENCE.286.5443.1377>
- Nakrani, M.N., Wineland, R.H., Anjum, F., 2022. Physiology, Glucose Metabolism. StatPearls.
- Nish, S.A., Zens, K.D., Kratchmarov, R., Lin, W.H.W., Adams, W.C., Chen, Y.H., Yen, B., Rothman, N.J., Bhandoola, A., Xue, H.H., Farber, D.L., Reiner, S.L., 2017. CD4+ T cell effector commitment coupled to self-renewal by asymmetric cell divisions. *J. Exp. Med.* 214, 39–47. <https://doi.org/10.1084/JEM.20161046>
- Nitta, T., Takayanagi, H., 2021. Non-Epithelial Thymic Stromal Cells: Unsung Heroes in Thymus Organogenesis and T Cell Development. *Front. Immunol.* 11, 3445. <https://doi.org/10.3389/FIMMU.2020.620894/BIBTEX>
- O'Hara, G.A., Welten, S.P.M., Klenerman, P., Arens, R., 2012. Memory T cell inflation: understanding cause and effect. *Trends Immunol.* 33, 84–90. <https://doi.org/10.1016/J.IT.2011.11.005>
- Obar, J.J., Khanna, K.M., Lefrançois, L., 2008. Endogenous naive CD8+ T cell precursor frequency regulates primary and memory responses to infection. *Immunity* 28, 859–869. <https://doi.org/10.1016/j.immuni.2008.04.010>
- Obar, J.J., Lefrançois, L., 2010. Early signals during CD8 T cell priming regulate the generation of central memory cells. *J. Immunol.* 185, 263–272. <https://doi.org/10.4049/jimmunol.1000492>
- Oduro, J.D., Redeker, A., Lemmermann, N.A.W., Ebermann, L., Marandu, T.F., Dekhtiarenko, I., Holzki, J.K., Busch, D.H., Arens, R., Čičin-Šain, L., 2016. Murine cytomegalovirus (CMV) infection via the intranasal route offers a robust model of immunity upon mucosal CMV infection. *J. Gen. Virol.* 97, 185–195. <https://doi.org/10.1099/JGV.0.000339>
- Okhrimenko, A., Grün, J.R., Westendorf, K., Fang, Z., Reinke, S., Von Roth, P., Wassilew, G., Kühn, A.A., Kudernatsch, R., Demski, S., Scheibenbogen, C., Tokoyoda, K., McGrath, M.A., Raftery, M.J., Schönrich, G., Serra, A., Chang, H.D., Radbruch, A., Dong, J., 2014. Human memory T cells from the bone marrow are resting and maintain long-lasting systemic memory. *Proc. Natl. Acad. Sci. U. S. A.* 111, 9229–9234. <https://doi.org/10.1073/PNAS.1318731111/-/DCSUPPLEMENTAL/PNAS.201318731SI.PDF>
- Olson, J.A., McDonald-Hyman, C., Jameson, S.C., Hamilton, S.E., 2013. Effector-like CD8+ T cells in the memory population mediate potent protective immunity. *Immunity* 38,

- 1250–1260. <https://doi.org/10.1016/j.immuni.2013.05.009>
- Omilusik, K.D., Goldrath, A.W., 2017. The origins of memory T cells. *Nat.* 2021 5527685 552, 337–339. <https://doi.org/10.1038/d41586-017-08280-8>
- P. Chou, J., B. Effros, R., 2013. T cell replicative senescence in human aging. *Curr. Pharm. Des.* 19, 1680–1698. <https://doi.org/10.2174/138161213805219711>
- Pais Ferreira, D., Silva, J.G., Wyss, T., Fuertes Marraco, S.A., Scarpellino, L., Charmoy, M., Maas, R., Siddiqui, I., Tang, L., Joyce, J.A., Delorenzi, M., Luther, S.A., Speiser, D.E., Held, W., 2020. Central memory CD8⁺ T cells derive from stem-like Tcf7hi effector cells in the absence of cytotoxic differentiation. *Immunity* 53, 985-1000.e11. <https://doi.org/10.1016/J.IMMUNI.2020.09.005>
- Panum on Measles: Observations Made During the Epidemic of Measles on the Faroe Islands in the Year 1846 (A translation from the Danish) - PMC [WWW Document], n.d. URL <https://www.ncbi.nlm.nih.gov/pmc/articles/PMC1530953/> (accessed 4.27.22).
- Parish, C.R., 1999. Fluorescent dyes for lymphocyte migration and proliferation studies. *Immunol. Cell Biol.* 77, 499–508. <https://doi.org/10.1046/J.1440-1711.1999.00877.X>
- Patel, A.A., Zhang, Y., Fullerton, J.N., Boelen, L., Rongvaux, A., Maini, A.A., Bigley, V., Flavell, R.A., Gilroy, D.W., Asquith, B., Macallan, D., Yona, S., 2017. The fate and lifespan of human monocyte subsets in steady state and systemic inflammation. *J. Exp. Med.* 214, 1913–1923. <https://doi.org/10.1084/jem.20170355>
- Plunkett, F.J., Franzese, O., Finney, H.M., Fletcher, J.M., Belaramani, L.L., Salmon, M., Dokal, I., Webster, D., Lawson, A.D.G., Akbar, A.N., 2007. The loss of telomerase activity in highly differentiated CD8⁺CD28⁻CD27⁻ T cells is associated with decreased Akt (Ser473) phosphorylation. *J. Immunol.* 178, 7710–7719. <https://doi.org/10.4049/JIMMUNOL.178.12.7710>
- Qiu, Z., 2022. Discovery of T cell memory. *Nat. Res.* 2022.
- Radbruch, A., McGrath, M.A., Siracusa, F., Hoffmann, U., Sercan-Alp, Ö., Hutloff, A., Tokoyoda, K., Chang, H.D., Dong, J., 2021. Homeostasis and Durability of T-Cell Memory—The Resting and the Restless T-Cell Memory. *Cold Spring Harb. Perspect. Biol.* 13, a038083. <https://doi.org/10.1101/CSHPERSPECT.A038083>
- Rane, S., Hogan, T., Seddon, B., Yates, A.J., 2018. Age is not just a number: Naive T cells increase their ability to persist in the circulation over time. *PLOS Biol.* 16, e2003949. <https://doi.org/10.1371/JOURNAL.PBIO.2003949>
- Reinauer, H., Gries, F.A., Hübinger, A., Knode, O., Severing, K., Susanto, F., 1990. Determination of glucose turnover and glucose oxidation rates in man with stable isotope tracers. *J. Clin. Chem. Clin. Biochem.* 28, 505–512. <https://doi.org/10.1515/CCLM.1990.28.8.505>
- Reizel, Y., Chapal-Ilani, N., Adar, R., Itzkovitz, S., Elbaz, J., Maruvka, Y.E., Segev, E., Shlush, L.I., Dekel, N., Shapiro, E., 2011. Colon stem cell and crypt dynamics exposed by cell lineage reconstruction. *PLoS Genet.* 7, e1002192. <https://doi.org/10.1371/journal.pgen.1002192>
- Restifo, N.P., Gattinoni, L., 2013. Lineage relationship of effector and memory T cells. *Curr.*

- Opin. Immunol. 25, 556–563. <https://doi.org/10.1016/J.COI.2013.09.003>
- Reynaldi, A., Smith, N.L., Schlub, T.E., Tabilas, C., Venturi, V., Rudd, B.D., Davenport, M.P., 2019. Fate mapping reveals the age structure of the peripheral T cell compartment. *Proc. Natl. Acad. Sci. U. S. A.* 116, 3974–3981. https://doi.org/10.1073/PNAS.1811634116/SUPPL_FILE/PNAS.1811634116.SD03.XLSX
- Ribeiro, R.M., Mohri, H., Ho, D.D., Perelson, A.S., 2002. Modeling deuterated glucose labeling of T-lymphocytes. *Bull. Math. Biol.* 2002 642 64, 385–405. <https://doi.org/10.1006/BULM.2001.0282>
- Roberts, A.D., Ely, K.H., Woodland, D.L., 2005. Differential contributions of central and effector memory T cells to recall responses. *J. Exp. Med.* 202, 123. <https://doi.org/10.1084/JEM.20050137>
- Roberts, E.T., Haan, M.N., Dowd, J.B., Aiello, A.E., 2010. Cytomegalovirus antibody levels, inflammation, and mortality among elderly Latinos over 9 years of follow-up. *Am. J. Epidemiol.* 172, 363–371. <https://doi.org/10.1093/AJE/KWQ177>
- Rudd, B.D., Venturi, V., Li, G., Samadder, P., Ertelt, J.M., Way, S.S., Davenport, M.P., Nikolich-Žugich, J., 2011. Nonrandom attrition of the naive CD8 + T-cell pool with aging governed by T-cell receptor: pMHC interactions. *Proc. Natl. Acad. Sci. U. S. A.* 108, 13694–13699. <https://doi.org/10.1073/PNAS.1107594108/-/DCSUPPLEMENTAL>
- Rufer, N., Brümendorf, T.H., Kolvraa, S., Bischoff, C., Christensen, K., Wadsworth, L., Schulzer, M., Lansdorp, P.M., 1999. Telomere fluorescence measurements in granulocytes and T lymphocyte subsets point to a high turnover of hematopoietic stem cells and memory T cells in early childhood. *J. Exp. Med.* 190, 157–167. <https://doi.org/10.1084/JEM.190.2.157>
- Sallusto, F., Geginat, J., Lanzavecchia, A., 2004. Central memory and effector memory T cell subsets: function, generation, and maintenance. *Annu. Rev. Immunol.* 22, 745–763. <https://doi.org/10.1146/ANNUREV.IMMUNOL.22.012703.104702>
- Sallusto, F., Lenig, D., Förster, R., Lipp, M., Lanzavecchia, A., 1999. Two subsets of memory T lymphocytes with distinct homing potentials and effector functions. *Nature* 401, 708–712. <https://doi.org/10.1038/44385>
- Sandalova, E., Laccabue, D., Boni, C., Tan, A.T., Fink, K., Ooi, E.E., Chua, R., Schreve, B.S., Ferrari, C., Bertoletti, A., 2010. Contribution of Herpesvirus Specific CD8 T Cells to Anti-Viral T Cell Response in Humans. *PLOS Pathog.* 6, e1001051. <https://doi.org/10.1371/JOURNAL.PPAT.1001051>
- Sarkar, S., Kalia, V., Haining, W.N., Konieczny, B.T., Subramaniam, S., Ahmed, R., 2008. Functional and genomic profiling of effector CD8 T cell subsets with distinct memory fates. *J. Exp. Med.* 205, 625–640. <https://doi.org/10.1084/jem.20071641>
- Schepers, A.G., Vries, R., Van Den Born, M., Van De Wetering, M., Clevers, H., 2011. Lgr5 intestinal stem cells have high telomerase activity and randomly segregate their chromosomes. *EMBO J.* 30, 1104–1109. <https://doi.org/10.1038/emboj.2011.26>
- Schindelin, J., Arganda-Carreras, I., Frise, E., Kaynig, V., Longair, M., Pietzsch, T.,

- Preibisch, S., Rueden, C., Saalfeld, S., Schmid, B., Tinevez, J.Y., White, D.J., Hartenstein, V., Eliceiri, K., Tomancak, P., Cardona, A., 2012. Fiji: an open-source platform for biological-image analysis. *Nat. Methods* 2012 9 7, 676–682. <https://doi.org/10.1038/nmeth.2019>
- Schmidt, N.W., Harty, J.T., 2011. Cutting Edge: Attrition of Plasmodium -Specific Memory CD8 T Cells Results in Decreased Protection That Is Rescued by Booster Immunization . *J. Immunol.* <https://doi.org/10.4049/jimmunol.1003949>
- Schober, K., Voit, F., Grassmann, S., Müller, T.R., Eggert, J., Jarosch, S., Weißbrich, B., Hoffmann, P., Borkner, L., Nio, E., Fanchi, L., Clouser, C.R., Radhakrishnan, A., Mihatsch, L., Lückemeier, P., Leube, J., Dössinger, G., Klein, L., Neuenhahn, M., Oduro, J.D., Cicin-Sain, L., Buchholz, V.R., Busch, D.H., 2020. Reverse TCR repertoire evolution toward dominant low-affinity clones during chronic CMV infection. *Nat. Immunol.* 21, 434–441. <https://doi.org/10.1038/s41590-020-0628-2>
- Selin, L.K., Lin, M.Y., Kraemer, K.A., Pardoll, D.M., Schneck, J.P., Varga, S.M., Santolucito, P.A., Pinto, A.K., Welsh, R.M., 1999. Attrition of T Cell Memory: Selective Loss of LCMV Epitope-Specific Memory CD8 T Cells following Infections with Heterologous Viruses. *Immunity* 11, 733–742. [https://doi.org/10.1016/S1074-7613\(00\)80147-8](https://doi.org/10.1016/S1074-7613(00)80147-8)
- Selin, L.K., Vergilis, K., Welsh, R.M., Nahill, S.R., 1996. Reduction of otherwise remarkably stable virus-specific cytotoxic T lymphocyte memory by heterologous viral infections. *J. Exp. Med.* 183, 2489–2499. <https://doi.org/10.1084/jem.183.6.2489>
- Sercan Alp, Ö., Durlanik, S., Schulz, D., Mcgrath, M., Grün, J.R., Bardua, M., Ikuta, K., Sgouroudis, E., Riedel, R., Zehentmeier, S., Hauser, A.E., Tsuneto, M., Melchers, F., Tokoyoda, K., Chang, H.D., Thiel, A., Radbruch, A., 2015. Memory CD8+ T cells colocalize with IL-7+ stromal cells in bone marrow and rest in terms of proliferation and transcription. *Eur. J. Immunol.* 45, 975. <https://doi.org/10.1002/EJI.201445295>
- Shimamoto, H., Komiya, S., 2000. The turnover of body water as an indicator of health. *J. Physiol. Anthropol. Appl. Human Sci.* 19, 207–212. <https://doi.org/10.2114/JPA.19.207>
- Shlush, L.I., Chapal-Ilani, N., Adar, R., Pery, N., Maruvka, Y., Spiro, A., Shouval, R., Rowe, J.M., Tzukerman, M., Bercovich, D., Izraeli, S., Marcucci, G., Bloomfield, C.D., Zuckerman, T., Skorecki, K., Shapiro, E., 2012. Cell lineage analysis of acute leukemia relapse uncovers the role of replication-rate heterogeneity and microsatellite instability. *Blood* 120, 603–612. <https://doi.org/10.1182/blood-2011-10-388629>
- Siracusa, F., Alp, Ö.S., Maschmeyer, P., McGrath, M., Mashreghi, M.F., Hojyo, S., Chang, H.D., Tokoyoda, K., Radbruch, A., 2017. Maintenance of CD8+ memory T lymphocytes in the spleen but not in the bone marrow is dependent on proliferation. *Eur. J. Immunol.* 47, 1900. <https://doi.org/10.1002/EJI.201747063>
- Siracusa, F., McGrath, M.A., Maschmeyer, P., Bardua, M., Lehmann, K., Heinz, G., Durek, P., Heinrich, F.F., Mashreghi, M.F., Chang, H.D., Tokoyoda, K., Radbruch, A., 2018. Nonfollicular reactivation of bone marrow resident memory CD4 T cells in immune clusters of the bone marrow. *Proc. Natl. Acad. Sci. U. S. A.* 115, 1334–1339. https://doi.org/10.1073/PNAS.1715618115/SUPPL_FILE/PNAS.201715618SI.PDF
- Smith, C.J., Venturi, V., Quigley, M.F., Turula, H., Gostick, E., Ladell, K., Hill, B.J.,

- Himelfarb, D., Quinn, K.M., Greenaway, H.Y., Dang, T.H.Y., Seder, R.A., Douek, D.C., Hill, A.B., Davenport, M.P., Price, D.A., Snyder, C.M., 2020. Stochastic Expansions Maintain the Clonal Stability of CD8⁺ T Cell Populations Undergoing Memory Inflation Driven by Murine Cytomegalovirus. *J. Immunol.* 204, 112–121. <https://doi.org/10.4049/JIMMUNOL.1900455>
- Snell, L.M., MacLeod, B.L., Law, J.C., Osokine, I., Elsaesser, H.J., Hezaveh, K., Dickson, R.J., Gavin, M.A., Guidos, C.J., McGaha, T.L., Brooks, D.G., 2018. CD8 + T Cell Priming in Established Chronic Viral Infection Preferentially Directs Differentiation of Memory-like Cells for Sustained Immunity. *Immunity* 49, 678-694.e5. <https://doi.org/10.1016/J.IMMUNI.2018.08.002>
- Snyder, C.M., Cho, K.S., Bonnett, E.L., van Dommelen, S., Shellam, G.R., Hill, A.B., 2008. Memory inflation during chronic viral infection is maintained by continuous production of short-lived, functional T cells. *Immunity* 29, 650–659. <https://doi.org/10.1016/J.IMMUNI.2008.07.017>
- Soerens, A.G., Künzli, M., Quarnstrom, C.F., Scott, M.C., Swanson, L., Locquiao, J., Ghoneim, H.E., Zehn, D., Youngblood, B., Vezys, V., Masopust, D., 2023. Functional T cells are capable of supernumerary cell division and longevity. *Nature*. <https://doi.org/10.1038/S41586-022-05626-9>
- Soetaert, K., Petzoldt, T., 2010. Inverse Modelling, Sensitivity and Monte Carlo Analysis in R Using Package FME. *J. Stat. Softw.* 33, 1–28. <https://doi.org/10.18637/JSS.V033.I03>
- Soetaert, K., Petzoldt, T., Setzer, R.W., 2010. Solving Differential Equations in R: Package deSolve. *J. Stat. Softw.* 33, 1–25. <https://doi.org/10.18637/JSS.V033.I09>
- Song, K., Rabin, R.L., Hill, B.J., De Rosa, S.C., Perfetto, S.P., Zhang, H.H., Foley, J.F., Reiner, J.S., Liu, J., Mattapallil, J.J., Douek, D.C., Roederer, M., Farber, J.M., 2005. Characterization of subsets of CD4⁺ memory T cells reveals early branched pathways of T cell differentiation in humans. *Proc. Natl. Acad. Sci. U. S. A.* 102, 7916–7921. <https://doi.org/10.1073/PNAS.0409720102>
- Sosinowski, T., White, J.T., Cross, E.W., Haluszczak, C., Marrack, P., Gapin, L., Kedl, R.M., 2013. CD8 α ⁺ dendritic cell trans presentation of IL-15 to naive CD8⁺ T cells produces antigen-inexperienced T cells in the periphery with memory phenotype and function. *J. Immunol.* 190, 1936–1947. <https://doi.org/10.4049/JIMMUNOL.1203149>
- Souquette, A., Thomas, P.G., 2018. Past Life and Future Effects-How Heterologous Infections Alter Immunity to Influenza Viruses. *Front. Immunol.* 9. <https://doi.org/10.3389/FIMMU.2018.01071>
- Sprent, J., 1997. T cells and memory lapses. *Trends Microbiol.* 5. [https://doi.org/10.1016/S0966-842X\(97\)01072-X](https://doi.org/10.1016/S0966-842X(97)01072-X)
- Sprent, J., Miller, J.F.A.P., 1976. Fate of H2-activated T lymphocytes in syngeneic hosts: III. Differentiation into long-lived recirculating memory cells. *Cell. Immunol.* 21, 314–326. [https://doi.org/10.1016/0008-8749\(76\)90059-9](https://doi.org/10.1016/0008-8749(76)90059-9)
- Sprent, J., Surh, C.D., 2003. T Cell Memory. <https://doi-org.proxy.library.uu.nl/10.1146/annurev.immunol.20.100101.151926> 20, 551–579. <https://doi.org/10.1146/ANNUREV.IMMUNOL.20.100101.151926>

- Sugimura, R., He, X.C., Venkatraman, A., Arai, F., Box, A., Semerad, C., Haug, J.S., Peng, L., Zhong, X.B., Suda, T., Li, L., 2012. Noncanonical Wnt signaling maintains hematopoietic stem cells in the niche. *Cell* 150, 351–365. <https://doi.org/10.1016/j.cell.2012.05.041>
- Sun, Y., Yang, K., Bridal, T., Ehrhardt, A.G., 2016. Robust Ki67 detection in human blood by flow cytometry for clinical studies. *Bioanalysis* 8, 2399–2413. <https://doi.org/10.4155/BIO-2016-0194>
- Surh, C.D., Sprent, J., 2008. Homeostasis of Naive and Memory T Cells. *Immunity* 29, 848–862. <https://doi.org/10.1016/J.IMMUNI.2008.11.002>
- Szabo, P., Weksler, M.E., Nikolich-Z, J., Ugich, ?, Potvin, H., Nikolich-Z, D., Dyllal, R., Lemaoult, J., Messaoudi, I., Manavalan, J.S., 2000. Age-Related Dysregulation in CD8 T Cell Homeostasis: Kinetics of a Diversity Loss. *J. Immunol.* 165, 2367–2373. <https://doi.org/10.4049/JIMMUNOL.165.5.2367>
- Tan, J.T., Ernst, B., Kieper, W.C., LeRoy, E., Sprent, J., Surh, C.D., 2002. Interleukin (IL)-15 and IL-7 Jointly Regulate Homeostatic Proliferation of Memory Phenotype CD8+ Cells but Are Not Required for Memory Phenotype CD4+ Cells. *J. Exp. Med.* 195, 1523–1532. <https://doi.org/10.1084/JEM.20020066>
- Tanchot, C., Lemonnier, F.A., Pérarnau, B., Freitas, A.A., Rocha, B., 1997. Differential requirements for survival and proliferation of CD8 naïve or memory T cells. *Science* 276, 2057–2062. <https://doi.org/10.1126/SCIENCE.276.5321.2057>
- Tempany, J.C., Zhou, J.H.S., Hodgkin, P.D., Bryant, V.L., 2018. Superior properties of CellTrace Yellow as a division tracking dye for human and murine lymphocytes. *Immunol. Cell Biol.* 96, 149–159. <https://doi.org/10.1111/imcb.1020>
- Thoma, O.M., Neurath, M.F., Waldner, M.J., 2021. T Cell Aging in Patients with Colorectal Cancer-What Do We Know So Far? *Cancers (Basel)*. 13. <https://doi.org/10.3390/CANCERS13246227>
- Todryk, S.M., 2018. T Cell Memory to Vaccination. *Vaccines* 6. <https://doi.org/10.3390/VACCINES6040084>
- Tofts, P.S., Chevassut, T., Cutajar, M., Dowell, N.G., Peters, A.M., 2011. Doubts concerning the recently reported human neutrophil lifespan of 5.4 days. *Blood*. <https://doi.org/10.1182/blood-2010-10-310532>
- Tong, Q.Y., Zhang, J.C., Guo, J.L., Li, Y., Yao, L.Y., Wang, X., Yang, Y.G., Sun, L.G., 2020. Human Thymic Involution and Aging in Humanized Mice. *Front. Immunol.* 11, 1399. <https://doi.org/10.3389/FIMMU.2020.01399/BIBTEX>
- Utzschneider, D.T., Delpoux, A., Wieland, D., Huang, X., Lai, C.Y., Hofmann, M., Thimme, R., Hedrick, S.M., 2018. Active Maintenance of T Cell Memory in Acute and Chronic Viral Infection Depends on Continuous Expression of FOXO1. *Cell Rep.* 22, 3454–3467. <https://doi.org/10.1016/J.CELREP.2018.03.020>
- van den Berg, S.P.H., Derksen, L.Y., Drylewicz, J., Nanlohy, N.M., Beckers, L., Lanfermeijer, J., Gessel, S.N., Vos, M., Otto, S.A., de Boer, R.J., Tesselaar, K., Borghans, J.A.M., van Baarle, D., 2021. Quantification of T-cell dynamics during latent

- cytomegalovirus infection in humans. *PLOS Pathog.* 17, e1010152.
<https://doi.org/10.1371/JOURNAL.PPAT.1010152>
- van Grinsven, E., 2019. Sources and significance of neutrophil heterogeneity 192.
- Vezy's, V., Yates, A., Casey, K.A., Lanier, G., Ahmed, R., Antia, R., Masopust, D., 2009. Vezy's et al. reply. *Nat.* 2009 4597247 459, E4–E4. <https://doi.org/10.1038/nature08092>
- Vezy's, V., Yates, A., Casey, K.A., Lanier, G., Ahmed, R., Antia, R., Masopust, D., 2008. Memory CD8 T-cell compartment grows in size with immunological experience. *Nat.* 2008 4577226 457, 196–199. <https://doi.org/10.1038/nature07486>
- Vibert, J., Thomas-Vaslin, V., 2017. Modelling T cell proliferation: Dynamics heterogeneity depending on cell differentiation, age, and genetic background. *PLOS Comput. Biol.* 13, e1005417. <https://doi.org/10.1371/JOURNAL.PCBI.1005417>
- Virgin, H.W., Wherry, E.J., Ahmed, R., 2009. Redefining Chronic Viral Infection. *Cell* 138, 30–50. <https://doi.org/10.1016/J.CELL.2009.06.036>
- Voehringer, D., Blaser, C., Brawand, P., Raulet, D.H., Hanke, T., Pircher, H., 2001. Viral infections induce abundant numbers of senescent CD8 T cells. *J. Immunol.* 167, 4838–4843. <https://doi.org/10.4049/JIMMUNOL.167.9.4838>
- Voehringer, D., Liang, H.-E., Locksley, R.M., 2008. Homeostasis and effector function of lymphopenia-induced ‘memory-like’ T cells in constitutively T cell-depleted mice. *J. Immunol.* 180, 4742. <https://doi.org/10.4049/JIMMUNOL.180.7.4742>
- von Hoesslin, M., Kuhlmann, M., de Almeida, G.P., Kanev, K., Wurmser, C., Gerullis, A.K., Roelli, P., Berner, J., Zehn, D., 2022. Secondary infections rejuvenate the intestinal CD103+ tissue-resident memory T cell pool. *Sci. Immunol.* 7. https://doi.org/10.1126/SCIIMMUNOL.ABP9553/SUPPL_FILE/SCIIMMUNOL.ABP9553_TABLE_S1.ZIP
- Vrisekoop, N., Den Braber, I., De Boer, A.B., Ruiters, A.F.C., Ackermans, M.T., Van Der Crabben, S.N., Schrijver, E.H.R., Spierenburg, G., Sauerwein, H.P., Hazenberg, M.D., De Boer, R.J., Miedema, F., Borghans, J.A.M., Tesselaar, K., 2008. Sparse production but preferential incorporation of recently produced naïve T cells in the human peripheral pool. *Proc. Natl. Acad. Sci. U. S. A.* 105, 6115–6120. https://doi.org/10.1073/PNAS.0709713105/SUPPL_FILE/SD3.TXT
- Wallace, D.L., Masters, J.E., De Lara, C.M., Henson, S.M., Worth, A., Zhang, Y., Kumar, S.R., Beverley, P.C., Akbar, A.N., Macallan, D.C., 2011. Human cytomegalovirus-specific CD8(+) T-cell expansions contain long-lived cells that retain functional capacity in both young and elderly subjects. *Immunology* 132, 27–38. <https://doi.org/10.1111/J.1365-2567.2010.03334.X>
- Wallace, D.L., Zhang, Y., Ghattas, H., Worth, A., Irvine, A., Bennett, A.R., Griffin, G.E., Beverley, P.C.L., Tough, D.F., Macallan, D.C., 2004. Direct measurement of T cell subset kinetics in vivo in elderly men and women. *J. Immunol.* 173, 1787–1794. <https://doi.org/10.4049/JIMMUNOL.173.3.1787>
- Weber, T.S., Perié, L., Duffy, K.R., 2016. Inferring average generation via division-linked labeling. *J. Math. Biol.* 73, 491–523. <https://doi.org/10.1007/S00285-015-0963->

3/FIGURES/5

- Weitering, T.J., Melsen, J.E., van Ostaijen-ten Dam, M.M., Weemaes, C.M.R., Schilham, M.W., van der Burg, M., 2021. Normal Numbers of Stem Cell Memory T Cells Despite Strongly Reduced Naive T Cells Support Intact Memory T Cell Compartment in Ataxia Telangiectasia. *Front. Immunol.* 12, 2253. <https://doi.org/10.3389/FIMMU.2021.686333/BIBTEX>
- Welsh, R.M., Selin, L.K., 2009. Attrition of memory CD8 T cells. *Nature* 459. <https://doi.org/10.1038/NATURE08091>
- Welten, S.P.M., Baumann, N.S., Oxenius, A., 2019. Fuel and brake of memory T cell inflation. *Med. Microbiol. Immunol.* 208, 329–338. <https://doi.org/10.1007/S00430-019-00587-9>
- Welten, S.P.M., Yermanos, A., Baumann, N.S., Wagen, F., Oetiker, N., Sandu, I., Pedrioli, A., Oduro, J.D., Reddy, S.T., Cicin-Sain, L., Held, W., Oxenius, A., 2020. Tcf1+ cells are required to maintain the inflationary T cell pool upon MCMV infection. *Nat. Commun.* 11. <https://doi.org/10.1038/S41467-020-16219-3>
- Wen, S., Lu, H., Wang, D., Guo, J., Dai, W., Wang, Z., 2021. TCF-1 maintains CD8+ T cell stemness in tumor microenvironment. *J. Leukoc. Biol.* 110, 585–590. <https://doi.org/10.1002/JLB.5MR1120-778R>
- Weng, N., 2008. Telomere and adaptive immunity. *Mech. Ageing Dev.* 129, 60. <https://doi.org/10.1016/J.MAD.2007.11.005>
- Weng, N. ping, Akbar, A.N., Goronzy, J., 2009. CD28(-) T cells: their role in the age-associated decline of immune function. *Trends Immunol.* 30, 306–312. <https://doi.org/10.1016/J.IT.2009.03.013>
- Weng, N.P., Levine, B.L., June, C.H., Hodes, R.J., 1995. Human naive and memory T lymphocytes differ in telomeric length and replicative potential. *Proc. Natl. Acad. Sci. U. S. A.* 92, 11091. <https://doi.org/10.1073/PNAS.92.24.11091>
- Westera, L., Drylewicz, J., Den Braber, I., Mugwagwa, T., Van Der Maas, I., Kwast, L., Volman, T., Van De Weg-Schrijver, E.H.R., Bartha, I., Spierenburg, G., Gaiser, K., Ackermans, M.T., Asquith, B., De Boer, R.J., Tesselaar, K., Borghans, J.A.M., 2013. Closing the gap between T-cell life span estimates from stable isotope-labeling studies in mice and humans. *Blood* 122, 2205–2212. <https://doi.org/10.1182/BLOOD-2013-03-488411>
- Westera, L., van Hoven, V., Drylewicz, J., Spierenburg, G., van Velzen, J.F., de Boer, R.J., Tesselaar, K., Borghans, J.A.M., 2015. Lymphocyte maintenance during healthy aging requires no substantial alterations in cellular turnover. *Aging Cell* 14, 219–227. <https://doi.org/10.1111/ACEL.12311>
- Wherry, E.J., Blattman, J.N., Ahmed, R., 2005. Low CD8 T-Cell Proliferative Potential and High Viral Load Limit the Effectiveness of Therapeutic Vaccination. *J. Virol.* 79, 8960. <https://doi.org/10.1128/JVI.79.14.8960-8968.2005>
- Wherry, E.J., Teichgräber, V., Becker, T.C., Masopust, D., Kaech, S.M., Antia, R., von Andrian, U.H., Ahmed, R., 2003. Lineage relationship and protective immunity of

- memory CD8 T cell subsets. *Nat. Immunol.* 4, 225–234. <https://doi.org/10.1038/ni889>
- Wilson, A., Laurenti, E., Oser, G., van der Wath, R.C., Blanco-Bose, W., Jaworski, M., Offner, S., Dunant, C.F., Eshkind, L., Bockamp, E., Lió, P., MacDonald, H.R., Trumpp, A., 2008. Hematopoietic stem cells reversibly switch from dormancy to self-renewal during homeostasis and repair. *Cell* 135, 1118–1129. <https://doi.org/10.1016/j.cell.2008.10.048>
- Xu, A., Bhanumathy, K.K., Wu, J., Ye, Z., Freywald, A., Leary, S.C., Li, R., Xiang, J., 2016. IL-15 signaling promotes adoptive effector T-cell survival and memory formation in irradiation-induced lymphopenia. *Cell Biosci.* 6, 1–13. <https://doi.org/10.1186/S13578-016-0098-2/FIGURES/5>
- Yan, K.S., Chia, L.A., Li, X., Ootani, A., Su, J., Lee, J.Y., Su, N., Luo, Y., Heilshorn, S.C., Amieva, M.R., Sangiorgi, E., Capecchi, M.R., Kuo, C.J., 2012. The intestinal stem cell markers *Bmi1* and *Lgr5* identify two functionally distinct populations. *Proc. Natl Acad. Sci. USA* 109, 466–471. <https://doi.org/10.1073/pnas.1118857109>
- Yang, Y.S., Hughes, T.E., 2001. Cre stoplight: a red/green fluorescent reporter of Cre recombinase expression in living cells. *Biotechniques* 31, 1036–1041. <https://doi.org/10.2144/01315ST03>
- Yates, A., Saini, M., Mathiot, A., Seddon, B., 2008. Mathematical Modeling Reveals the Biological Program Regulating Lymphopenia-Induced Proliferation. *J. Immunol.* 180, 1414–1422. <https://doi.org/10.4049/JIMMUNOL.180.3.1414>
- Yates, A.J., Chan, C.C.T., Callard, R.E., 2005. 16 Modelling T cell activation, proliferation, and homeostasis. *Stud. Multidiscip.* 3, 281–308. [https://doi.org/10.1016/S1571-0831\(06\)80020-1](https://doi.org/10.1016/S1571-0831(06)80020-1)
- Yoon, H., Kim, T.S., Braciale, T.J., 2010. The cell cycle time of CD8+ T cells responding in vivo is controlled by the type of antigenic stimulus. *PLoS One* 5, e15423. <https://doi.org/10.1371/journal.pone.0015423>
- Youngblood, B., Hale, J.S., Kissick, H.T., Ahn, E., Xu, X., Wieland, A., Araki, K., West, E.E., Ghoneim, H.E., Fan, Y., Dogra, P., Davis, C.W., Konieczny, B.T., Antia, R., Cheng, X., Ahmed, R., 2017. Effector CD8 T cells dedifferentiate into long-lived memory cells. *Nature* 552, 404–409. <https://doi.org/10.1038/nature25144>
- Ziegler-Heitbroc, H.W.L., Thiel, E., Futterer, A., Herzog, V., Wirtz, A., Riethmüller, G., 1988. Establishment of a human cell line (Mono Mac 6) with characteristics of mature monocytes. *Int. J. cancer* 41, 456–461. <https://doi.org/10.1002/IJC.2910410324>

Summary

Our immune system protects us from new pathogens as well as from the ones that we have already encountered. This immune memory is stored in memory T cells. Memory T cells are generated in large numbers from naive T cells (i.e., T cells that have never seen a pathogen). They are in a higher state of activation than naive T cells and are, thus, capable of faster and much more efficient control of an infection. Although memory T cells have been proposed to be long-lived (lifespan of years in humans), they have always been found to live for only a few months. This has given rise to postulates that long-lived memory T cells perhaps result from specific conditions (infections), and/or reside in particular anatomic locations (for example, bone marrow or skin). Unravelling the fundamental behaviour of memory T cells, including when they are generated, the events throughout their life, and their lifespan will be invaluable, for example, in developing more robust and reliable vaccines.

It is notoriously difficult to study memory T cells without disturbing their natural dynamics within a host. The most natural state-of-the-art technique is to label the DNA of memory T cells to be able to track them in their natural environment; very much like the police flag the IMEI numbers of criminals' phones to track them. Labelling cells generally involves either switching existing atoms with atoms of different weights (for example, during deuterium labelling in Chapters 1, 2 and 3, hydrogen is replaced by deuterium, which is heavier than hydrogen), or marking cells with a fluorescent colour. For example, in Chapter 4, the population of interest had a fluorescent green colour and upon division cells acquired a fluorescent red colour. The labelling information of memory T cells over time is invaluable in deducing their behaviour. Our goal, in the last few years, has been to follow these labelling trails of memory T cells to sketch out the details of their generation and maintenance mechanisms.

It is known that pathogens trigger naive T cells to divide rapidly. In Chapter 5, we show that there is considerable heterogeneity in the number of divisions expanding T-cell populations go through. We found that this heterogeneity in the division history of the cells determines their functional capabilities. Memory T cells with a short division history respond aggressively to successive stimulation by the same pathogen and are responsible for regenerating the immune response. Conversely, memory T cells that have gone through many divisions hardly divide upon re-encountering the pathogen, and perhaps only form a first line of defence through surveillance.

Interestingly, the memory T-cell pools generated by different pathogens also differ in their characteristics. After most viral infections, the number of memory T cells generated are maintained at roughly the same level throughout life. For some viruses, however, the memory T-cell pool keeps on expanding in size. Such memory T-cell populations are called inflationary and can have detrimental effects on other antigen-specific memory T cells, presumably because memory T cells compete for the same resources to survive. Although such inflationary T-cell pools were thought to be a result of accumulation of long-lived T

cells, we show (in Chapter 1) that even the cells of inflationary memory T-cell pools live on average for only a couple of months, comparable to the lifespan of other memory T cells.

The analysis of the ink (or label) trails left behind by memory T cells is anything but straightforward. We devote Chapters 2 and 3 of this thesis to highlight a few challenges. As cells do not change their behaviour during labelling and de-labelling, the trails for cells taking up the label and later losing it, is expected to be symmetrical. In Chapter 2, we share multiple unusual datasets where the trails are not symmetric, and we present two possible interpretations for which we could also provide experimental evidence. We show that the expected symmetry of the trails is broken when the population that is being tracked is either expanding in size (for example, inflationary memory T cells), and when the label remains available from alternate sources (for example, neutrophils gain label for 4 additional hours after the deuterium has been washed away). In Chapter 3, we show that the estimates of memory T-cell lifespans using different models could differ several fold. Using mathematical proofs and through the analysis of a couple of published datasets, we point out that the expected lifespan of cells in a population can easily be mis-estimated if the relative contribution of label from the source population is not considered. Therefore, it is extremely important to know the contribution of label from the source while analysing the labelling trails of cell populations.

Finally, in Chapter 5, we discuss the diversity and longevity of the memory T-cell pool as a whole, not just that of the individual cells. Above, we reported that individual memory T cells are expected to live for a relatively short period of time (a couple of months). As all memory T cells are thought to depend on the same resources, they naturally compete with each other for survival, eventually resulting in a decline in the diversity of the memory T-cell pool. We show, using numerical simulations, that this competition among memory T cells and the loss of diversity can be avoided if cells ‘age’ when they divide (that is, if they divide more slowly after every division). As a consequence, the size of a memory T cell’s progeny remains limited, which in turn reduces the competitive pressure on other memory T cells. Interestingly, we show that cellular aging cannot avoid the loss of diversity in the memory T-cell pool if individual memory T cells are long-lived (a couple of years).

Across the chapters in this thesis, we provide insights into the mechanisms around the generation and maintenance of memory T cells, using experiments and simulations alike. We present not only instances where modelling plays a complementary role to confirm and cement our understanding of the experimental data (Chapter 4), but also instances where modelling is strictly essential as it exposes the missing links in our intuition (Chapters 1-3, 5). This thesis, thereby, also highlights the value of the cross-talk between experimental and theoretical immunology.

Samenvatting

Ons immuunsysteem beschermt ons zowel tegen nieuwe ziekteverwekkers als tegen de ziekteverwekkers die we al eerder zijn tegengekomen. Dit immunologisch geheugen wordt opgeslagen in geheugen-T-cellen. Geheugen-T-cellen worden in grote aantallen gegenereerd uit naïeve T-cellen (d.w.z. T-cellen die nog nooit een ziekteverwekker hebben gezien). Ze zijn in een hogere staat van activatie dan naïeve T-cellen en zijn daardoor in staat om een infectie sneller en veel efficiënter onder controle te krijgen. Hoewel vaak wordt verondersteld dat geheugen-T-cellen minstens even lang leven als naïeve T-cellen (d.w.z. jaren in mensen), hebben meerdere onderzoeken gevonden dat ze maar een paar maanden leven. Dit heeft aanleiding gegeven tot het idee dat langlevende geheugen-T-cellen het gevolg zijn van specifieke omstandigheden (infecties), en/of zich op bepaalde anatomische locaties bevinden (bijvoorbeeld in het beenmerg of in de huid). Het ontrafelen van het fundamentele gedrag van geheugen-T-cellen, inclusief wanneer ze worden aangemaakt, de gebeurtenissen tijdens hun leven en hun levensduur, zal van onschatbare waarde zijn voor bijvoorbeeld de ontwikkeling van robuustere en betrouwbaardere vaccins.

Het is erg moeilijk om geheugen-T-cellen te bestuderen zonder hun natuurlijke dynamiek binnen een gastheer te verstoren. De meest natuurlijke techniek bestaat uit het labelen van het DNA van T-geheugencellen om ze in hun natuurlijke omgeving te kunnen volgen, net zoals de politie de IMEI-nummers van telefoons van criminelen markeert om ze te kunnen volgen. Het labelen van cellen houdt over het algemeen in dat bestaande atomen worden vervangen door atomen met een ander gewicht (in de hoofdstukken 1, 2 en 3 wordt waterstof vervangen door deuterium, dat zwaarder is dan waterstof) of dat cellen worden gemarkeerd met een fluorescerende kleur. In hoofdstuk 4 heeft de populatie van belang een fluorescerende groene kleur en bij deling kregen de cellen een fluorescerende rode kleur. De informatie die we krijgen door gelabelde T-geheugencellen te volgen over de tijd is van grote waarde bij het afleiden van hun gedrag. Ons doel in de afgelopen jaren was het volgen van deze labelingpaden van geheugen T-cellen, om zo inzicht te krijgen in hun generatie- en onderhoudsmechanismen.

Het is bekend dat pathogenen naïeve T-cellen aanzetten tot snelle deling. In hoofdstuk 5 laten we zien dat er grote verschillen zijn in het aantal delingen dat groeiende T-celpopulaties doormaken. We ontdekten dat deze heterogeniteit in de delingsgeschiedenis van de cellen hun functionele vermogen bepaalt. Geheugen T-cellen met een korte delingsgeschiedenis reageren agressief op opeenvolgende stimulatie door dezelfde ziekteverwekker en zijn verantwoordelijk voor het regenereren van de immuunrespons. Geheugen-T-cellen die veel delingen hebben doorgemaakt, delen zich daarentegen nauwelijks wanneer ze de ziekteverwekker opnieuw tegenkomen en vormen wellicht alleen een eerste verdedigingslinie door middel van surveillance.

Interessant is dat de geheugen-T-celpopulaties die door verschillende ziekteverwekkers worden gegenereerd, ook verschillen in hun karakteristieken. Na de meeste virusinfecties

blijft het aantal geheugen-T-cellen dat wordt aangemaakt ongeveer gelijk gedurende het hele leven. Bij sommige virussen blijft de geheugen-T-celpool echter in omvang toenemen. Dergelijke geheugen-T-celpopulaties worden inflatoir genoemd en kunnen nadelige effecten hebben op andere antigeen-specifieke geheugen-T-cellen, vermoedelijk omdat geheugen-T-cellen concurreren om dezelfde signalen voor overleving. Hoewel gedacht werd dat dergelijke inflatoire T-celpopulaties het resultaat zijn van accumulatie van langlevende T-cellen, laten we (in hoofdstuk 1) zien dat zelfs de cellen van inflatoire geheugen-T-celpopulaties gemiddeld maar een paar maanden leven, vergelijkbaar met de levensduur van andere geheugen-T-cellen.

De analyse van de inkt- (of label-)sporen die geheugen-T-cellen achterlaten is allesbehalve eenvoudig. We wijden hoofdstukken 2 en 3 van dit proefschrift aan het belichten van enkele uitdagingen. Omdat cellen hun gedrag niet veranderen tijdens het labelen en de-labelen, wordt verwacht dat de sporen van cellen die het label opnemen en later weer verliezen symmetrisch zijn. In hoofdstuk 2 presenteren we meerdere ongebruikelijke datasets waarbij deze paden niet symmetrisch zijn en stellen we twee mogelijke interpretaties voor waarvoor we ook experimenteel bewijs kunnen leveren. We laten zien dat de verwachte symmetrie van de paden wordt doorbroken wanneer de populatie die wordt gevolgd groeit (bijvoorbeeld inflatoire geheugen-T-cellen) en wanneer het label beschikbaar blijft uit andere bronnen (neutrofielen krijgen bijvoorbeeld nog 4 uur lang label nadat de aanvoer van deuterium is gestopt). In hoofdstuk 3 laten we zien dat de schattingen van de levensduur van geheugen T-cellen op basis van verschillende modellen behoorlijk kunnen verschillen. Met behulp van wiskundige bewijzen en door de analyse van een paar gepubliceerde datasets, laten we zien dat de verwachte levensduur van cellen in een populatie gemakkelijk verkeerd kan worden geschat als de relatieve bijdrage van label uit de voorloper-populatie niet wordt meegenomen in de analyse. Het is daarom uiterst belangrijk om de bijdrage van het label van de voorlopers te kennen bij het analyseren van de labelingtrajecten van celpopulaties.

Tot slot bespreken we in hoofdstuk 5 de diversiteit en levensduur van de geheugen-T-celpopulatie als geheel, niet alleen die van de individuele cellen. Hierboven vermeldden we al dat individuele geheugen-T-cellen een relatief korte verwachte levensduur hebben (een paar maanden). Omdat alle geheugen-T-cellen afhankelijk zijn van dezelfde signalen, concurreren ze van nature met elkaar om te overleven, wat uiteindelijk resulteert in een afname van de diversiteit van de geheugen-T-celpopulatie. We laten met behulp van numerieke simulaties zien dat deze competitie tussen geheugen-T-cellen en het verlies aan diversiteit kan worden voorkomen als cellen 'ouder' worden wanneer ze delen (dat wil zeggen, als hun delingssnelheid na elke deling langzamer wordt). Als gevolg hiervan blijft de grootte van het 'nageslacht' van een geheugen-T-cel beperkt, wat op zijn beurt de competitieve druk op andere geheugen-T-cellen vermindert. Interessant genoeg hebben we gevonden dat cellulaire veroudering het verlies van diversiteit in de geheugen T-celpopulatie niet kan voorkomen als individuele geheugen-T-cellen lang leven (een paar jaar).

In de hoofdstukken van dit proefschrift verschaffen we inzicht in de mechanismen rond de generatie en instandhouding van geheugen-T-cellen, waarbij we zowel experimenten als wiskundige modellering gebruiken. We presenteren niet alleen gevallen waarin modellering

een aanvullende rol speelt om ons begrip van de experimentele gegevens te bevestigen en te versterken (hoofdstuk 4), maar ook gevallen waarin modellering strikt noodzakelijk is omdat het de ontbrekende schakels in onze intuïtie blootlegt (hoofdstukken 1-3, 5). Dit proefschrift benadrukt daarmee ook de waarde van de kruisbestuiving tussen experimentele en theoretische immunologie.

ସାରାଂଶ

ଆମର ପ୍ରତିରକ୍ଷା ପ୍ରଣାଳୀ ଆମକୁ ନୂତନ କ୍ଷତିକାରକ ଜୀବାଣୁ ରୁ ତଥା ଆମେ ପୂର୍ବରୁ ସାମ୍ନା କରିଥିବା ରୋଗରୁ ରକ୍ଷା କରିଥାଏ । ଏହି ପ୍ରତିରକ୍ଷା ପ୍ରଣାଳୀର ଅନୁଭବ ଶରୀରର ସ୍ମୃତି 'ଟି' କୋଷରେ ସାଇତା ହୋଇ ରହିଥାଏ । ସ୍ମୃତି 'ଟି' କୋଷଗୁଡ଼ିକ ବହୁ ସଂଖ୍ୟାରେ ଅନୁଭବ ନଥିବା 'ଟି' କୋଷ (ସେମାନେ କେବେ ରୋଗ ପ୍ରତିରୋଧକ ଯୁଦ୍ଧ ରେ ଭାଗ ନେଇ ନଥାନ୍ତି) ରୁ ଜନ୍ମ ନେଇଥାଏ । ସ୍ମୃତି 'ଟି' କୋଷ ମାନେ ଅନଭିଜ୍ଞ 'ଟି' କୋଷ ଅପେକ୍ଷା ଅଧିକ ସକ୍ରିୟ ଅବସ୍ଥାରେ ଥାନ୍ତି ଏବଂ ଏହିପରି ଏକ ସଂକ୍ରମଣର ଶୀଘ୍ର, ଅଧିକ ଦକ୍ଷ ନିୟନ୍ତ୍ରଣ କରିବାରେ ସମର୍ଥ ଅଟନ୍ତି । ଯଦିଓ ସ୍ମୃତି 'ଟି' କୋଷଗୁଡ଼ିକ ଦୀର୍ଘସ୍ଥାୟୀ (ଅନେକ ବର୍ଷ ଧରି ମାନବ ଶରୀର ରେ) ବୋଲି ପ୍ରସ୍ତାବ ଦିଆଯାଇଛି, ସେମାନେ ସର୍ବଦା ମାତ୍ର କିଛି ମାସ ବଞ୍ଚନ୍ତି ବୋଲି ଜଣା ପଡ଼ିଛି । ଏହା ବିଶ୍ୱାସ ସୃଷ୍ଟି କରିଛି ଯେ ଦୀର୍ଘସ୍ଥାୟୀ ସ୍ମୃତି 'ଟି' କୋଷଗୁଡ଼ିକ ବୋଧହୁଏ ନିର୍ଦ୍ଦିଷ୍ଟ ଅବସ୍ଥା (ସଂକ୍ରମଣ) ରୁ ଆସିଥାଏ, ଏବଂ/କିମ୍ବା ଶରୀର ର ନିର୍ଦ୍ଦିଷ୍ଟ ଅଙ୍ଗ ରେ ରହିଥାଏ (ଉଦାହରଣ ସ୍ୱରୂପ, ଅସ୍ଥି ମଜ୍ଜା ଏବଂ ଚର୍ମ ରେ) । ସ୍ମୃତି 'ଟି' କୋଷଗୁଡ଼ିକର ମୌଳିକ ଆଚରଣକୁ ଆବିଷ୍କାର କରିବା, ତତ୍ ସହିତ ସେମାନଙ୍କର ସୃଷ୍ଟି ପ୍ରକ୍ରିୟା, ଜୀବନସାରା ର ଘଟଣା, ଏବଂ ଜୀବନକାଳ ସମ୍ବନ୍ଧିତ ଜ୍ଞାନ ଏକ ଅମୂଲ୍ୟ ଅଧ୍ୟୟନ । ଯାହା ମାନବ ସମାଜ ଲାଗି ଅଧିକ ଉପଯୋଗୀ ଏବଂ ନିର୍ଭରଯୋଗ୍ୟ ଚିକିତ୍ସା ବିକାଶର ମାଇଲ୍ ଖୁଣ୍ଟ ସାବ୍ୟସ୍ତ ହେବ ।

ଏକ ପ୍ରାକୃତିକ ମଧ୍ୟରେ ସ୍ମୃତି 'ଟି' କୋଷଗୁଡ଼ିକ ର ପ୍ରାକୃତିକ ଗତିଶୀଳତାକୁ ବ୍ୟାଘାତ ନକରି ଅଧ୍ୟୟନ କରିବା କଠିନ ଅଟେ । ସବୁଠାରୁ ପ୍ରାକୃତିକ ଅତ୍ୟାଧୁନିକ କୌଶଳ ହେଉଛି ସ୍ମୃତି 'ଟି' କୋଷଗୁଡ଼ିକର ଡି.ଏନ.ଏ କୁ ସେମାନଙ୍କର ପ୍ରାକୃତିକ ପରିବେଶରେ ଚିହ୍ନଟ କରିବାକୁ ସକ୍ଷମ ହେବା; ଯେମିତି ପୋଲିସ୍ ଅପରାଧୀକୁ ଧରିବା ପାଇଁ ତାଙ୍କ ଫୋନ୍ ର ଆଇ.ଏମ୍.ଇ.ଆଇ ନମ୍ବର କୁ ଚିହ୍ନଟ କରନ୍ତି । କୋଷଗୁଡ଼ିକୁ ଚିହ୍ନଟ କରିବା ଲାଗି ସାଧାରଣତଃ ଉପସ୍ଥିତ ଅଣୁକୁ ଗୋଟେ ଭାଗୀ ଅଣୁ ସହିତ ପରିବର୍ତ୍ତିତ କରାଯାଏ (ଉଦାହରଣ ସ୍ୱରୂପ, ଅଧ୍ୟାୟ ୧, ୨ ଏବଂ ୩ ରେ ଡିୟୁଟେରିୟମ୍ ଲେବଲ୍ କରିବା ସମୟରେ ହାଇଡ୍ରୋଜେନ୍ ଡିୟୁଟେରିୟମ୍ ଦ୍ୱାରା ବଦଳାଯାଇଥାଏ, ଯାହା ହାଇଡ୍ରୋଜେନ୍ ଠାରୁ ଭାରୀ), କିମ୍ବା ପ୍ଲୋରୋସେଣ୍ଟ ରଙ୍ଗ ସହିତ କୋଷଗୁଡ଼ିକୁ ଚିହ୍ନଟ କରାଯାଏ (ଉଦାହରଣ ସ୍ୱରୂପ, ଅଧ୍ୟାୟ ୪ ରେ, ବିଚାରଧନ କୋଷଗୁଡ଼ିକର ପ୍ଲୋରୋସେଣ୍ଟ ରଙ୍ଗ ସବୁଜ ଥିଲା, କୋଷଗୁଡ଼ିକର ବିଭାଜନ ପରେ ଲାଲ୍ ରଙ୍ଗ କୁ ରୂପାନ୍ତରିତ ହେଲା) । ସମୟ ସହିତ ସ୍ମୃତି 'ଟି' କୋଷଗୁଡ଼ିକର ସୂଚନା ସେମାନଙ୍କ ଆଚରଣ ଜାଣିବାରେ ସହାୟକ ହୁଅନ୍ତି । ଆମର ଉଦ୍ଦେଶ୍ୟ, ଗତ କିଛି ବର୍ଷ ମଧ୍ୟରେ, ସ୍ମୃତି 'ଟି' କୋଷଗୁଡ଼ିକର ଚିହ୍ନ ଅନୁସରଣ କରି ସେମାନଙ୍କର ଉତ୍ପାଦନ ଏବଂ ରକ୍ଷଣାବେକ୍ଷଣ ପ୍ରଣାଳୀ ଉପରେ ଗବେଷଣା କରିବା । ଏ ଥିସିସ୍ ରେ ଆମେ ସେହି ପ୍ରୟାସ କରିଛୁ ।

ଏହା ଜଣା ଯେ କ୍ଷତିକାରକ ଜୀବାଣୁଗୁଡ଼ିକ ଅନଭିଜ୍ଞ 'ଟି' କୋଷଗୁଡ଼ିକୁ ସାଂଘାତିକ ଭାବେ ରେ ବିଭାଜନ କରିବା ପାଇଁ ଆକ୍ରମଣ କରିଥାନ୍ତି । ଅଧ୍ୟାୟ ୫ ରେ ଆମେ ଦେଖାଉଛୁ ଯେ, ବିସ୍ତାରିତ 'ଟି' କୋଷର ବିଭାଜିତ ସଂଖ୍ୟାରେ ଯଥେଷ୍ଟ ଭେଦଭାବ ଅଛି । ଆମେ ଜାଣିଲୁ ଯେ କୋଷଗୁଡ଼ିକର ବିଭାଜନ ଲତିହାସରେ ଏହି ଭେଦଭାବ ସେମାନଙ୍କର କାର୍ଯ୍ୟକାରୀତା ନିର୍ଣ୍ଣୟ କରେ । ଅଳ୍ପ ବିଭାଜିତ ସ୍ମୃତି 'ଟି' କୋଷଗୁଡ଼ିକ ସମାନ କ୍ଷତିକାରକ ଜୀବାଣୁକୁ ସମ୍ମୁଖୀନ କରିବା ମାତ୍ରେ ଆକ୍ରମଣାତ୍ମକ ଭାବରେ ପ୍ରତିକ୍ରିୟା କରନ୍ତି ଏବଂ ପ୍ରତିରକ୍ଷା ପ୍ରକ୍ରିୟାକୁ ପୁନଃ ନିର୍ମାଣ କରନ୍ତି । ଅପରପକ୍ଷେ, ଅନେକ ବିଭାଜିତ ସ୍ମୃତି 'ଟି'

କୋଷଗୁଡ଼ିକ ପୁନର୍ବାର ଆକ୍ରମଣର ସମ୍ମୁଖୀନ ହେବା ପରେ ବିଭାଜିତ ନ ହୋଇ କେବଳ ନୀରିକ୍ଷଣ ମାଧ୍ୟମରେ ପ୍ରତିରକ୍ଷା ର ପ୍ରଥମ ଧାଡ଼ି ଗଠନ କରନ୍ତି ।

କୌତୁହଳର ବିଷୟ, ବିଭିନ୍ନ କ୍ଷତିକାରକ ଜୀବାଣୁ ଦ୍ୱାରା ଉତ୍ପନ୍ନ ସ୍ମୃତି 'ଟି' କୋଷଗୁଡ଼ିକ ମଧ୍ୟ ସେମାନଙ୍କର ଗୁଣରେ ଭିନ୍ନ । ଅଧିକାଂଶ ସଂକ୍ରମକ ରୋଗ ର ସଂକ୍ରମଣ ପରେ, ସୃଷ୍ଟି ହୋଇଥିବା ସ୍ମୃତି 'ଟି' କୋଷଗୁଡ଼ିକର ସଂଖ୍ୟା ଜୀବନସାରା ପ୍ରାୟ ସମାନ ସ୍ତରରେ ପରିଚାଳିତ ହୁଅନ୍ତି । କେତେକ ଜୀବାଣୁ ଲାଗି ତଥାପି ସ୍ମୃତି 'ଟି' କୋଷଗୁଡ଼ିକ ଆକାରରେ ବିସ୍ତାର କରିବାରେ ଲାଗେ । ଏହିପରି ସ୍ମୃତି 'ଟି' କୋଷ ସଂଖ୍ୟାକୁ ଇନ୍-ଫ୍ଲେସନାରୀ କୁହାଯାଏ ଏବଂ ଅନ୍ୟ ଆଣ୍ଟିଜେନ୍-ନିର୍ଦ୍ଦିଷ୍ଟ ସ୍ମୃତି 'ଟି' କୋଷ ଉପରେ କ୍ଷତିକାରକ ପ୍ରଭାବ ପକାଇପାରେ, ସମ୍ଭବତଃ ଏହି କାରଣ ରୁ ସ୍ମୃତି 'ଟି' କୋଷଗୁଡ଼ିକ ବଞ୍ଚିବା ଲାଗି ସମାନ ଉତ୍ସ ପାଇଁ ପ୍ରତିସ୍ପନ୍ଦିତା କରନ୍ତି । ଯଦିଓ ଏହିପରି ଇନ୍-ଫ୍ଲେସନାରୀ 'ଟି' କୋଷଗୁଡ଼ିକ ଦୀର୍ଘସ୍ଥାୟୀ 'ଟି' କୋଷର ଫଳାଫଳ ବୋଲି ବିବେଚନା କରାଯାଏ, ଆମେ ଦେଖାଇଅଛୁ (ଅଧ୍ୟାୟ ୧ ରେ) ଯେ ଇନ୍-ଫ୍ଲେସନାରୀ ସ୍ମୃତି 'ଟି' କୋଷଗୁଡ଼ିକ ମଧ୍ୟ ହାରାହାରି ମାତ୍ର ଦୁଇମାସ ବଞ୍ଚନ୍ତି, ଯାହା କି ଅନ୍ୟ ସ୍ମୃତି 'ଟି' କୋଷଗୁଡ଼ିକର ଜୀବନକାଳ ସହିତ ତୁଳନୀୟ ।

ସ୍ମୃତି 'ଟି' କୋଷଗୁଡ଼ିକ ଦ୍ୱାରା ଛାଡ଼ି ଯାଇଥିବା ସମ୍ବାହୀ (କିମ୍ବା ଲେବଲ୍) ଚିହ୍ନଗୁଡ଼ିକର ବିଶ୍ଳେଷଣ ସରଳ ଅଟେ । କିଛି ଆହ୍ୱାନକୁ ଦେଖାଇବାକୁ ଆମେ ଏହି ଥିସିସ୍ ର ଅଧ୍ୟାୟ ୨ ଏବଂ ୩ କୁ ଉତ୍ତର କରୁଛୁ । ଯେହେତୁ ଲେବଲ୍ ଏବଂ ଡି-ଲେବଲ୍ କରିବା ସମୟରେ କୋଷଗୁଡ଼ିକ ସେମାନଙ୍କର ଆଚରଣରେ ପରିବର୍ତ୍ତନ କରନ୍ତି ନାହିଁ, ଲେବଲ୍ ଗ୍ରହଣ କରୁଥିବା ସମୟ ର ଏବଂ ପରେ ଏହାକୁ ହରାଇବା ସମୟ ର ଚିହ୍ନଗୁଡ଼ିକ ସମାନ ହେବ ବୋଲି ଆଶା କରାଯାଏ । ଅଧ୍ୟାୟ ୨ ରେ, ଆମେ ଏକାଧିକ ଅସାଧାରଣ ଡାଟାସେଟ୍ ଉପସ୍ଥାପନ କରୁଛୁ ଯେଉଁଠାରେ ଚିହ୍ନଗୁଡ଼ିକ ସମାନ ନୁହେଁ, ଆମେ ମଧ୍ୟ ଦୁଇଟି ସମ୍ଭାବ୍ୟ ଉତ୍ତର ଉପସ୍ଥାପନ କରୁଛୁ ଯାହା ପାଇଁ ଆମେ ପରୀକ୍ଷାମୂଳକ ପ୍ରମାଣ ପ୍ରଦାନ କରିପାରିଛୁ । ଆମେ ଦେଖାଇଛୁ ଯେ ଚିହ୍ନଗୁଡ଼ିକର ଆଶା କରାଯାଉଥିବା ସମାନତା ଭାଙ୍ଗିଯାଏ ଯେତେବେଳେ ଚିହ୍ନିତ ସଂଖ୍ୟା ଆକାରରେ ବିସ୍ତାରିତ ହୁଏ (ଉଦାହରଣ ସ୍ୱରୂପ, ଇନ୍-ଫ୍ଲେସନାରୀ ସ୍ମୃତି 'ଟି' କୋଷ), ଏବଂ ଯେତେବେଳେ ଲେବଲ୍ ବିକଳ ଉତ୍ତର ଉପଲବ୍ଧ ରହିଥାଏ (ଉଦାହରଣ ସ୍ୱରୂପ, ନିଉଗ୍ରୋଫିଲ୍ ଡ୍ରାପ୍‌ରେସନ୍ ବନ୍ଦ ହେବା ର ୪ ଘଣ୍ଟା ପରେ ବି ଲେବଲ୍ ପ୍ରାପ୍ତ କରେ) । ଅଧ୍ୟାୟ ୩ ରେ, ଆମେ ବିଭିନ୍ନ ମତେଲ୍ ବ୍ୟବହାର କରି ଦେଖାଇଛୁ ଯେ, ସ୍ମୃତି 'ଟି' କୋଷ ମାନଙ୍କର ଜୀବନକାଳର ଆକଳନ ଅନେକ ଗୁଣ ଭିନ୍ନ ହୋଇପାରେ । ଗାଣିତିକ ପ୍ରମାଣ ବ୍ୟବହାର କରି ଏବଂ ପ୍ରକାଶିତ ଦୁଇଟି ଡାଟାସେଟର ବିଶ୍ଳେଷଣ ମାଧ୍ୟମରେ, ଆମେ ସୂଚାଇ ଦେଉଛୁ ଯେ ଉତ୍ସ ସଂଖ୍ୟାରୁ ଲେବଲ୍ ର ଆପେକ୍ଷିକ ଅବଦାନକୁ ବିଚାର ନକଲେ ଏକ କୋଷର ସଂଖ୍ୟାରେ କୋଷଗୁଡ଼ିକର ଆଶା କରାଯାଉଥିବା ଜୀବନକୁ ଭୁଲ୍ ଆକଳନ କରାଯାଇପାରେ । ତେଣୁ, କୋଷଗୁଡ଼ିକର ଲେବେଲିଂ ଚିହ୍ନ ବିଶ୍ଳେଷଣ କରିବାବେଳେ ଉତ୍ତର ଲେବଲ୍ ର ଅବଦାନ ଜାଣିବା ଅତ୍ୟନ୍ତ ଗୁରୁତ୍ୱପୂର୍ଣ୍ଣ ।

ଶେଷରେ, ଅଧ୍ୟାୟ ୪ ରେ, ଆମେ କେବଳ ଗୋଟିଏ ସ୍ମୃତି 'ଟି' କୋଷର ନୁହେଁ ବରଂ କୋଷ ସମୂହ ର ବିବିଧତା ଏବଂ ଦୀର୍ଘାୟତା ବିଷୟରେ ଆଲୋଚନା କରୁଛୁ । ଉପରେ, ଆମେ ଜଣାଇଛୁ ଯେ ଗୋଟିଏ ସ୍ମୃତି 'ଟି' କୋଷ ଅପେକ୍ଷାକୃତ ସ୍ୱଳ୍ପ ସମୟ (ଦୁଇମାସ) ବଞ୍ଚିବାର ଆଶା କରାଯାଏ । ଯେହେତୁ ସମସ୍ତ ସ୍ମୃତି 'ଟି' କୋଷଗୁଡ଼ିକ ସମାନ ଉତ୍ସ ଉପରେ ନିର୍ଭରଶୀଳ ବୋଲି ଚିନ୍ତା କରାଯାଏ, ସେମାନେ ବଞ୍ଚିବା ପାଇଁ ସ୍ୱଭାବିକ ଭାବରେ ପରସ୍ପର ସହିତ ପ୍ରତିସ୍ପନ୍ଦିତା କରନ୍ତି, ଫଳସ୍ୱରୂପ ସ୍ମୃତି 'ଟି' କୋଷଗୁଡ଼ିକର ସଂଖ୍ୟା ଓ ବିବିଧତା ହ୍ରାସ ପାଏ । ସାଂଖ୍ୟିକ ଅନୁକରଣ ବ୍ୟବହାର କରି ଆମେ ଦେଖାଇଛୁ ଯେ ସ୍ମୃତି 'ଟି' କୋଷଗୁଡ଼ିକ ମଧ୍ୟରେ ଏହି ପ୍ରତିଯୋଗିତା ଏବଂ ବିବିଧତା ନଷ୍ଟକୁ ଏଡାଇ ଦିଆଯାଇପାରେ ଯଦି କୋଷଗୁଡ଼ିକ ବିଭାଜିତ

ହେଲେ 'ବୟସ୍କ' ହୋଇଯାନ୍ତି (ଅର୍ଥାତ୍ ଯଦି ସେମାନଙ୍କ ପ୍ରତ୍ୟେକ ବିଭାଜନ ପରେ ତାଙ୍କ ବିଭାଜନ ଗତି କମ ହୋଇଯାଏ) । ଫଳସ୍ଵରୂପ, ଏକ ସ୍ଫୁଟି 'ଟି' କୋଷ ବଂଶର ଆକାର ସୀମିତ ରହିଥାଏ, ଯାହା ଅନ୍ୟ ସ୍ଫୁଟି ଟି କୋଷଗୁଡ଼ିକ ଉପରେ ପ୍ରତିଯୋଗିତାମୂଳକ ଚାପକୁ ହ୍ରାସ କରିଥାଏ । କୌତୁହଳର ବିଷୟ, ଆମେ ଦେଖାଇଛୁ ଯେ କୋଷର ବାର୍ଦ୍ଧକ୍ୟ ସ୍ଫୁଟି 'ଟି' କୋଷଗୁଡ଼ିକର ବିବିଧତା ନଷ୍ଟକୁ ଏତାଇ ପାରିବ ନାହିଁ ଯଦିଓ ବ୍ୟକ୍ତିଗତ ସ୍ଫୁଟି 'ଟି' କୋଷଗୁଡ଼ିକ ଦୀର୍ଘସ୍ଥାୟୀ (ଅନେକ ବର୍ଷ) ରହିଥାନ୍ତି ।

ଏହି ଥିସିସ୍ ର ଅଧ୍ୟୟନଗୁଡ଼ିକରେ, ଆମେ ପରୀକ୍ଷଣ ଏବଂ ଗାଣିତିକ ପ୍ରଣାଳୀ ବ୍ୟବହାର କରି ସ୍ଫୁଟି 'ଟି' କୋଷଗୁଡ଼ିକର ଉତ୍ପାଦନ ଏବଂ ରକ୍ଷଣାବେକ୍ଷଣର ଯାନ୍ତ୍ରିକ କୌଶଳ ବିଷୟରେ ସୂଚନା ପ୍ରଦାନ କରିଛୁ । ଆମେ କେବଳ ସେହି ଉଦାହରଣଗୁଡ଼ିକ ଉପସ୍ଥାପନ କରୁନାହିଁ, ଯେଉଁଠାରେ ପରୀକ୍ଷାମୂଳକ ତଥ୍ୟ ବିଷୟରେ ଆମର ବୁଝାମଣା କୁ ନିଶ୍ଚିତ ଏବଂ ଦୃଢ଼ କରିବା ପାଇଁ ମଡେଲିଂ ଏକ ସଂପୂର୍ଣ୍ଣ ଭୂମିକା ଗ୍ରହଣ କରିଛି (ଅଧ୍ୟାୟ ୪), କିନ୍ତୁ ଏପରି ମଧ୍ୟ ଉଦାହରଣ ଦେଇଛୁ ଯେଉଁଠାରେ ମଡେଲିଂ ଜରୁରୀ ଅଟେ କାରଣ ଏହା ଆମର ଅନ୍ତଃକରଣ ରେ ଲୁଚାଇତ ତଥ୍ୟ ଗୁଡ଼ିକୁ ପ୍ରକାଶ କରିଥାଏ (ଅଧ୍ୟାୟ ୧-୩, ୫) । ଏହି ଥିସିସ୍ ପରୀକ୍ଷାମୂଳକ ଏବଂ ତତ୍ତ୍ଵଗତ ପ୍ରତିରକ୍ଷା ଶକ୍ତି ମଧ୍ୟରେ ଡର୍କ ବିଡର୍କ ର ମୂଲ୍ୟକୁ ମଧ୍ୟ ଆଲୋଚିତ କରେ ।

Curriculum Vitae

Arpit Chandan Swain was born on the 26th of April, 1993 (for all official uses and purposes) in Odisha, India. He grew up in the city Rourkela, where he did his schooling in St. Paul's School (ICSE board) until 2009. For his higher secondary education, he moved to Deepika E.M. School (CBSE board), also in Rourkela. With the intent to never study Biology again, he chose Computer Science as the optional subject. However, in a few weeks, he succumbed to the Indian dream of having an engineer and a doctor in the family and reverted back to Biology, which he managed to scrape by in for the next two years.

He continued his studies in Rourkela, not due to a lack of desire to move out of the city. He chose to study Mathematics (the only subject he mistakenly thought he would not struggle with) in the 5-year Integrated M.Sc. (B.Sc. + M.Sc.) course at National Institute of Technology (NIT), Rourkela from 2011-2016. Looking to dive into the applications of Mathematics, he again found himself in the clutches of Biology when he joined the National Network of Mathematical and Computational Biology (NNMCB) for a summer internship with Dr. Deepayan Sarkar at ISI, Delhi. He found Biology approachable and interesting through the lens of Mathematics. So, after returning from the internship, he took up a project with Dr. Bibekanand Mallick from the Life Sciences department of NIT, Rourkela on ranking competing endogenous RNA (ceRNA) pairs. After his Master's, he (finally) moved out of Rourkela to the National Chemical Laboratory (NCL), Pune to join Dr. Ram Rup Sarkar's lab as a project assistant in 2016, where we worked on epidemiological and immunological models.

In the beginning of 2018, he joined Prof. Rob de Boer to start his PhD in Theoretical Immunology. He was co-supervised by Prof. José Borghans during his PhD years and worked on finding mechanisms underlying the maintenance of memory T cells. In 2022, while still writing his PhD thesis, he joined Prof. José Borghans as a (fake) postdoctoral researcher continuing their work on deuterium labelling and estimating the lifespans of cell populations. He became a real postdoctoral researcher in the beginning of 2023 when he submitted his PhD thesis.

After enjoying his work with Prof. Rob de Boer and Prof. José Borghans and being mildly useful for 5 years, he will be joining Dr. Andrew Yates in Columbia University Irving Medical Center as a postdoctoral researcher from October 2023.

List of Publications

(presented in this thesis)

Mariona Baliu-Piqué, Julia Drylewicz, Xiaoyan Zheng, Lisa Borkner, **Arpit C. Swain**, Sigrid A. Otto, Rob J. de Boer, Kiki Tesselaar, Luka Cicin-Sain, José A. M. Borghans; (2022) Turnover of Murine Cytomegalovirus–Expanded CD8+ T Cells Is Similar to That of Memory Phenotype T Cells and Independent of the Magnitude of the Response. *J. Immunol.* 208 (4): 799–806.

Kaspar Bresser, Lianne Kok, **Arpit C. Swain**, Lisa A. King, Laura Jacobs, Tom S. Weber, Leila Perié, Ken R. Duffy, Rob J. de Boer, Ferenc A. Scheeren, Ton N. Schumacher. (2022) Replicative history marks transcriptional and functional disparity in the CD8+ T cell memory pool. *Nat Immunol.* 23(5):791-801.

Arpit C. Swain, Julia Drylewicz, Elena S. de Dios Panal, Daniela K. Korolova, Kiki Tesselaar, José A. M. Borghans, Rob J. de Boer; Explaining unexpected deuterium labelling curves. *To be submitted.*

Arpit C. Swain, José A. M. Borghans, Rob J. de Boer; How are estimated cellular turnover rates of a population influenced by the dynamics of its precursor population? *In preparation.*

Arpit C. Swain, José A. M. Borghans, Rob J. de Boer; (2022) Effect of cellular aging on memory T-cell homeostasis. *Front. Immunol.* 13:947242.

ସ୍ୟାନ୍ସି ପଥରେଖା

